UNIVERSITAT DE LES ILLES BALEARS
DEPARTAMENT DE FÍSICA
GRUP DE METEOROLOGIA

Programa de Doctorat en Física
Memòria presentada per optar al grau de
Doctor en Física, menció Doctor Europeu

STABLY STRATIFIED ATMOSPHERIC BOUNDARY LAYER: STUDY THROUGH LARGE-EDDY SIMULATIONS, MESOSCALE MODELLING AND OBSERVATIONS

CAPA LÍMIT ESTABLEMENT ESTRATIFICADA: ESTUDI MITJANÇANT SIMULACIONS EXPLICITES DE GRANS REMOLINS, MESOSCALARS I OBSERVACIONS

Maria Antònia Jiménez Cortés
Director del Treball: Dr. Joan Cuxart Rodamilans

Palma de Mallorca, Setembre 2005

UNIVERSITAT DE LES ILLES BALEARS
DEPARTAMENT DE FÍSICA
GRUP DE METEOROLOGIA

Programa de Doctorat en Física
Memòria presentada per optar al grau de
Doctor en Física, menció Doctor Europeu

STABLY STRATIFIED ATMOSPHERIC BOUNDARY LAYER: STUDY THROUGH LARGE-EDDY SIMULATIONS, MESOSCALE MODELLING AND OBSERVATIONS

CAPA LÍMIT ESTABLEMENT ESTRATIFICADA: ESTUDI MITJANÇANT SIMULACIONS EXPLICITES DE GRANS REMOLINS, MESOSCALARS I OBSERVACIONS

Signat autor: Maria Antònia Jiménez Cortés

Signat director del treball: Dr. Joan Cuxart Rodamilans

Palma de Mallorca, Setembre 2005

Al meu pare

Acknowledgements

First of all, I would like to thank my husband Jaume for his constant encouragement and patience. I am also grateful to my family and my friends for the support given. Many thanks to Joan Cuxart for trusting me and introducing me to the boundary layer meteorology studies. All members of the group of meteorology as well as the Physics department of the Universitat de les Illes Balears (UIB) are also acknowledged.

The European Centre for Medium-range Weather Forecasts (Reading, UK) is acknowledged for the access to its computing facilities, through the intermediation of the Spanish Met. Service (INM).

Many thanks as well to the Centre National de Recherches Météorologiques (Toulouse, France) for their support in the use of the Meso-NH model, especially to Patrick Jabouille (deceased), Jeanine Payart and Isabelle Mallet. It is worth mentioning the support given by Juan Escobar (Laboratoire d'Aerologie, Toulouse, France) and by Joan Miquel Torres (group of meteorology, UIB) during the installation of the Meso-NH model in the UIB PC's cluster.

The members of the research projects REN2002-00486/CLI and REN2003-09435/CLI of the Spanish Ministry of Research, as well as the members of the GABLS community are also acknowledged for many fruitful discussions and ideas, especially Larry Mahrt and Josep Antoni Guijarro (INM).

Finally, all members of the committee are also acknowledged: Dr. Sergio Alonso (UIB), Dra. Françoise Guichard (Centre National de Recherches Météorologiques, Meteo France), Dr. Harm Jonker (Delft University of Technology, The Netherlands), Dr. Haraldur Ólafsson (University of Iceland) and Dr. Climent Ramis (UIB). The reserve members of the jury are also acknowledged: Dr. Carlos Yagüe (Universidad Complutense de Madrid), Dr. Josep Antoni Guijarro (INM), Dr. Romualdo Romero (UIB), Dra. Maria Rosa Soler (Universitat de Barcelona) and Dr. Enrique Sánchez (Universidad de Castilla la Mancha).

Financial support

This work has been partially funded by the research fellowship (BOE 18/04/01) of the Instituto Nacional de Meteorologia, an especial action of the Govern de les Illes Balears and the research project REN2002-00486/CLI of the Spanish Ministry of Research.

Resum

La **Capa Límit Atmosfèrica (CLA)** és l'àrea directament influenciada per la presència de la superfície de la terra, que li fa de condició de contorn inferior. Els efectes de la fricció, evaporació, transport de calor i orografia entre d'altres indueixen fluxos de moment, calor o massa que es transporten cap a l'atmosfera superior mitjançant moviments turbulents. Els fluxos turbulents estan formats per remolins de diferent escala i a la CLA poden estar compresos entre 1 mm (o de l'ordre d'1 s) i un parell de quilòmetres (o hores). L'estudi de la CLA és important ja que és el lloc a on tots nosaltres vivim i a on desenvolupam la gran majoria d'activitats.

L'altura de la CLA és d'uns centenars de metres fins a pocs quilòmetres, però damunt el terra és variable en espai i temps. En canvi, damunt els oceans l'altura de la CLA varia relativament poc ja que la temperatura superficial no canvia gaire entre el dia i la nit. Durant el dia, l'escalfament del terra provoca una forta convecció, amb grans moviments ascendents/descendents, i es forma el que es coneix com a Capa Límit Convectiva (CLC). En canvi, durant el vespre, el refredament radiatiu del sòl fa que es desenvolupi el que es coneix com a **Capa Límit Estable (CLE)** o també capa límit establement estratificada. Aquest règim és l'estudiat en aquest treball.

A la CLE, el refredament radiatiu del sòl fa que l'aire que està just en contacte amb el terra sigui molt més fred que l'aire de dalt. Aleshores, l'aire prop del sòl és més estable que l'aire que hi ha més amunt i l'estabilitat decreix a mesura que augmenta l'altura fins a arribar a un punt a on les condicions d'estabilitat són neutres, nivell que es coneix com a l'altura de la inversió. Pel que fa al vent, prop del sòl és zero a causa de la fricció però a mesura que augmenta l'atura també augmenta de forma logarítmica.

Prop de l'altura de la inversió, el vent presenta un màxim amb valors més grans que el geostròfic (fins a 20 m s^{-1} a una altura aproximada d'uns 300 m). Aquest és un fenomen molt característic de la CLE i es coneix com a Low-Level Jet (LLJ, màxim de vent a nivells baixos). Un altre dels fenòmens que es desenvolupen dins la CLE, a les valls i depressions, són els vents catabàtics. Es formen quan l'aire adjacent a les muntanyes es refreda i baixa cap a les valls generant vents de velocitats entre 1 i 5 m s^{-1} a altures entre 2 i 20 m. L'orografia del terreny és un factor important a la CLE com també en la formació i desenvolupament dels vents catabàtics.

Dins la CLE la **turbulència** és un dels factors més importants, juntament amb la radiació, advecció o orografia. En alguns casos la turbulència pot ser contínua i/o forta mentre que en d'altres pot ser dèbil i/o intermitent. A més, la turbulència és anisotròpica, ja que en condicions d'estabilitat forta els moviments verticals estan inhibits, i no ho-

mogènia ja que els efectes locals com l'orografia també són importants. La turbulència dins la CLE bàsicament es genera mecànicament, a causa del fregament del vent prop del sòl o també a nivells més alts a causa de les variacions del vent en altura.

Aleshores, la CLE és un règim complex i difícil d'estudiar per diferents motius:

(i) la **turbulència no és homogènia ni isòtropa** i els moviments verticals tendeixen a estar inhibits sota condicions de forta estabilitat.

(ii) els efectes locals com l'orografia juguen un paper important.

(iii) actualment encara no hi ha mesures de la CLA al llarg de tota l'alçada. Això és una limitació especialment per la CLE ja que els canvis de les variables amb la vertical són importants.

(iv) la modelització també és difícil en aquestes condicions. Quan la superfície es refreda en excés als models, la capa límit es torna molt estable i apareix el fenomen que és conegut com a **runaway cooling**. En aquesta situació el model no experimenta barreja prop del sòl i les condicions de la superfície es desacoblen de la resta.

(v) per estudiar qualsevol variable turbulenta, aquesta se separa en el valor mitjà i la part fluctuant, suposant indirectament que hi ha una separació entre les escales del moviment mitjà i el turbulent. Sota condicions d'estabilitat forta no hi ha evidència que aquestes escales es pugin separar i aquest fenomen es coneix com a **spectral gap**.

(vi) en els models meteorològics, els efectes de les escales menors que la resolució del model es tenen en compte mitjançant l'esquema de turbulència. En la majoria de casos, el procés de dissipació d'energia de les petites escales es fa mitjançant la **teoria de Kolmogorov**, vàlida per situacions isotròpiques i homogènies. Aquesta teoria explica el procés de transferència d'energia de les grans escales a les petites escales a on els remolins són isotròpics. A les escales moleculars, la dissipació viscosa converteix l'energia cinètica del moviment en calor. En condicions fortament estables, l'aplicació d'aquesta teoria pot deixar de ser vàlida, ja que s'està lluny de la isotropia i de la homogeneïtat. Aleshores, es proposen diferents modificacions als esquemes de turbulència però encara no hi ha una teoria amplament acceptada.

Actualment, experiments (tant numèrics com experimentals) i anàlisi de dades serveixen per entendre millor els processos que s'observen a la CLE. En aquest treball ens concentrarem a estudiar la CLE mitjançant simulacions numèriques i anàlisi de dades.

Per poder estudiar la CLE mitjançant simulacions numèriques, totes les escales de moviment han d'estar representades en el model per tenir una bona descripció dels processos. Cal tenir en compte que sota condicions d'estabilitat tant els remolins més petits (de l'ordre d'1 mm) com els més grans (de l'ordre del quilòmetre) són importants. Aleshores, en aquest treball l'estudi de la CLE es fa mitjançant simulacions de grans remolins resolts

explícitament (Large-Eddy Simulations, LES), que ens permeten veure l'efecte de les escales més petites, i també simulacions mesoscalars, a on els efectes de major escala estan representats.

En primer lloc es fa un LES de la CLE per comprovar si el model, que utilitza la teoria de Kolmogorov per la dissipació d'energia, pot treballar sota condicions d'estabilitat. Es troba que el model funciona adequadament quan l'estabilitat és dèbil i moderada. Els casos més estables presenten runaway cooling perquè les condicions tèrmiques imposades a la superfície i el vent geostròfic no compleixen el criteri de Derbyshire.

Per comprovar si són realistes els resultats LES, aquests es comparen amb dades mesurades durant dues campanyes experimentals. Es comprova que el LES pot reproduir aproximadament el comportament mitjà de les dades. Les diferències més grans es troben prop de la superfície a on al LES se li prescriu la **teoria de semblança de Monin-Obukhov** i pareix ser que les dades no es comporten d'aquesta manera. Aquesta teoria s'aplica per poder descriure els perfils verticals d'algunes de les variables prop del sòl en funció d'un paràmetre adimensional, assumint que la CLE és contínua en espai i temps. Aquestes condicions no sempre es compleixen a la CLE i l'aplicació de la teoria de Monin-Obukhov pot ser dubtosa.

Les diferències entre els resultats LES i les dades poden ser degudes al fet que les condicions simulades no corresponen exactament a les observades i aleshores les dades poden incloure informació de forçaments externs que no estan inclosos al LES. A més, quan es fa aquesta comparació se suposa la **hipòtesi d'ergodicitat** (camp homogeni i estacionari) que tant per LES com per les dades podria no complir-se.

Per comprovar com depenen els resultats LES de l'esquema de turbulència, el model LES utilitzat en aquest treball ha participat en una intercomparació del models amb diferents esquemes de turbulència, alguns d'ells modificats. Els resultats depenen fortament de la resolució, però els models amb esquema de turbulència modificats no experimenten millores respecte als que utilitzen la teoria de Kolmogorov, encara que per condicions fortament estables l'aplicació d'aquesta teoria sigui dubtosa.

Per explorar més a fons els resultats LES i estudiar com són les estructures s'han utilitzat les **funcions de distribució de probabilitat** (Probability Density Function, PDF). Aleshores, es fa una anàlisi tenint en compte l'espectre, la forma de la PDF i el tall horitzontal corresponent. Es troba que les PDF son gaussianes però que el camp no és homogeni i aleshores no és ergòdic. També es mostra com les PDF poden ser útils per comparar els resultats LES amb les dades, a on les majors diferències apareixen a les cues, corresponents a valors llunyans del valor mitjà i poc probables.

Una vegada desenvolupades les eines d'estudi es fa un LES més realista, corresponent a

un LLJ observat. Els resultats LES mostren que no hi ha transport a través de la inversió i que damunt del LLJ hi ha un màxim d'energia. Els resultats LES són comparables als perfils mesurats mitjançant un globus sonda i a les sèries temporals obtingudes per una torre. Així i tot, els resultats LES prop de la superfície són bastant sensibles a la condició de contorn inferior, encara que damunt del LLJ els resultats són independents.

Durant tot aquest estudi s'arriba a la conclusió que, per determinar completament els processos que s'observen a la CLE, l'efecte dels forçaments externs és important i aquesta contribució no es pot estudiar mitjançant simulacions LES. Per aquest motiu es recorre a les simulacions mesoscalars, a on els forçaments externs, com l'orografia, estan inclosos. Aleshores, es fa una simulació mesoscalar d'un cas real sobre Mallorca. Durant el vespre es veu com les circulacions locals es desenvolupen a les conques (longitud aproximadament 25 km) formant-se, per exemple, vents catabàtics. Les simulacions es verifiquen amb imatges del satèl·lit NOAA i observacions de les estacions automàtiques en superfície donant resultats semblants.

Actualment els estudis sobre la CLE continuen per millorar-ne la descripció en models numèrics de predicció. Encara no hi ha una teoria amplament acceptada per descriure la turbulència anisòtropa i inhomogenia que funcioni per treballar sota condicions d'estabilitat. Això és la feina del futur, però mentrestant hem d'anar estudiant els processos que s'observen a la CLE mitjançant les eines actuals, en el rang que funcionen correctament.

Contents

Chapter 1

INTRODUCTION

1.1 Description of the Planetary Boundary Layer

The Planetary Boundary Layer (PBL) is the area directly influenced by the presence of the Earth's surface, the atmospheric lower boundary condition. The PBL is also known as Atmospheric Boundary Layer (ABL) or simply Boundary Layer (BL). Within the PBL the surface forcings induce fluxes of momentum, heat or mass, that are transmitted to the upper Atmosphere by turbulent motions. These forcings include frictional drag, evaporation and transpiration, heat transfer, pollutant emission, and terrain induced flow modifications.

Stull (1988) defines the turbulence as the gustiness superimposed on the mean wind, which can be visualized as irregular swirls of motion called eddies. Turbulent flows are presented as a superposition of eddies of different sizes and periods, that for the PBL, range from under the milimetre (or second) to few kilometres (or hours). These eddies can be generated by surface friction or heating but also the orography is playing an important role generating and even destroying them. Turbulence is several orders of magnitude more effective at transporting quantities than is molecular diffusivity. It is the turbulence that allows the boundary layer to respond to changing surface forcings.

The PBL is also the part of the atmosphere in which we live and take place most human activities. Therefore, a deep knowledge of the processes that take place therein will be important in:

(i) Climate and Numerical Weather Prediction (NWP) modelling, where the surface features are included, such as the air-surface exchange, friction, and clouds. No climate model can succeed without some consideration of the boundary layer. For instance, the representation of the clouds in a climate model can be critical, especially concerning the radiation budget at the surface. On the other hand, the PBL has to be properly described

in NWP models to predict the diurnal cycle, low-level winds and convergence, the effects of complex terrain, and so on. Furthermore, the coupling of the atmospheric model to the ocean, ice, land-surface models occurs through the PBL processes.

(ii) Air Pollution and Urban Meteorology: especially when the pollutant dispersal, the interaction of the PBL with mesoscale circulations and the urban heat island effects among others are considered.

(iii) Agricultural meteorology: for instance the prediction of frost, dew and evapotranspiration.

(iv) Aviation: especially in the forecasts of fog formation, strong wind shears, and other situations that can make the flying conditions extremely dangerous.

(v) Remote Sensing: satellite-based measurements of surface winds, skin temperature,... involve the interaction of the PBL and surface, and must often be interpreted in light of a PBL model to be useful for NWP.

The PBL thickness varies between hundreds of meters and a few kilometers although it is quite variable in time and space over land. On the contrary, over the oceans, the PBL depth varies relatively slowly in space and time because the sea surface temperature does not change very much between day and night. During a diurnal cycle, the air over the land heats and cools producing large variations on the buoyant forcings. A typical diurnal cycle of the PBL in a high pressure region over land is shown in Figure 1.1.

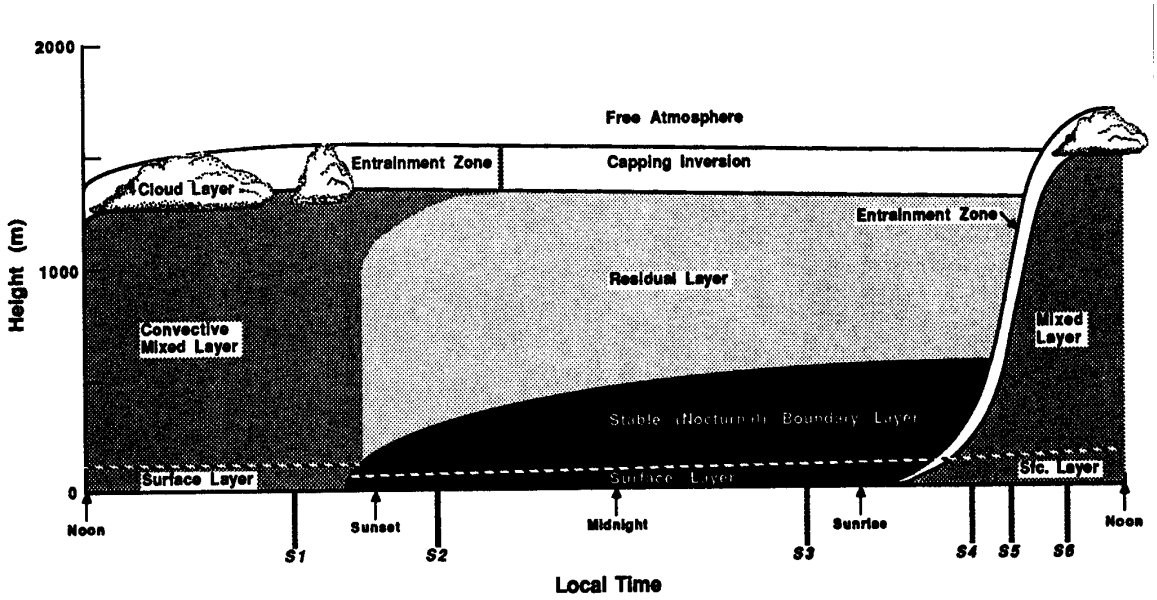

Figure 1.1: A typical diurnal cycle of the PBL in a high pressure region over land (Stull, 1988, Figure 1.7)

The heating of the ground during the day leads to convective mixing and a deep

Convective Boundary Layer (CBL) where the turbulence grows in depth, capped by a statically stable entrainment zone of intermittent turbulence. The CBL is characterized by intense mixing in statically unstable situation where thermals of warm air rise from the ground, reaching a maximum in depth in late afternoon. The resulting turbulence tends to mix heat, momentum and moisture uniformly in the vertical. At sunset, the radiative cooling of the ground leads to a shallow Stable Boundary Layer (SBL). Turbulence also decays, leaving a residual layer in the place of the mixed layer. Finally, after sunrise the CBL develops again destroying the SBL. In the absence of significant cooling or heating the PBL tends to become a Neutral Boundary Layer (NBL). Turbulence is one of the most important features in the PBL and it can be associated with thermal convection and mechanically (shear induced by the friction).

To study a turbulent flow, such as the PBL, the experimental approach is an obvious first step. In addition, some of idealized cases can be study in laboratories (experimental or numerical) in order to understand the basic physics. Nevertheless, the ideal conditions in the laboratory are very rarely presented in real situations. The fast-response turbulence data that are necessary to study the turbulence are not routinely collected by most operational weather services. To do so, special field programs must be conducted.

In this work the attention will be focused on the study of the SBL, where the main features, as well as the processes that take place, are quite different to those observed in other boundary layer regimes.

1.2 The Stable Boundary Layer

The Stably Stratified Atmospheric Boundary Layer (SBL or nocturnal BL) is formed under night-time conditions where the radiative cooling makes the near-the-surface air cooler than the air above. Therefore, the greatest stability is near the ground and decreases towards neutral conditions with height. This layer is known as the inversion layer and the height where the stability becomes neutral is called the inversion height. Regarding the larger scale effects, the SBL is usually formed under high-pressure conditions but also by advection of warmer air over a cooler surface.

Near the ground, the wind speed is approximately zero due to the frictional drag but within the SBL the mean wind profile has a logarithmic shape. Close to the inversion level, the wind speed presents a maximum, with speed values larger than the geostrophic (up to 20 m s^{-1} usually located 100 to 300 m above the ground). This phenomenon is called low-level jet (LLJ) or nocturnal jet and it can be an important source of elevated turbulence due to shear. Investigations have shown that there are many possible causes for

the generation of LLJ, such as the inertial oscillations or the sloping terrain among others although in some situations more than one factor can contribute to the LLJ formation.

Within the SBL, turbulence is one of the most important factors together with the radiation, advection or terrain slope. In some situations, the turbulence can be continuous and strong over the whole depth of the SBL whereas in other situations it can be weak and intermittent. Moreover, the turbulence in the SBL is mainly anisotropic because the statically stable conditions tend to suppress the vertical motions. Therefore, pollutants and other scalar tracers that are emitted into the SBL can spread out horizontally in thin layers. Furthermore, it is not homogeneous since the local effects, such as the orography or the soil uses, play also an important role.

The turbulence within the SBL is mainly generated mechanically, usually by wind shears and the buoyant contribution is much more smaller and it is generally a destruction process. In fact, wind shear can be created near the ground by friction acting on the ambient flow. It can also be generated aloft by variations in the wind speed with height.

The katabatic winds also take place within the SBL, mainly in valleys and depressions. Radiative cooling of the mountain surfaces cools the air adjacent to the surfaces, resulting in cold downslope or katabatic winds. These winds are very shallow (2 to 20 m) and have velocities on the order of 1 to 5 m s^{-1}. This also highlights how the orographical effects can modify the SBL characteristics. Moreover, the inhomogeneites of the terrain (soil uses) also determine the features of the SBL.

Since the statically stable air can support buoyancy (gravity) waves, these are also found within the SBL. On the other hand, the wind shear can also generate Kelvin-Helmholtz instabilities. Waves that propagate upward within the SBL eventually reach the level where their frequency matches the ambient Brunt-Väisälä frequency, at which point they reflect back down toward the ground. Waves are thus trapped between the ground and the neutral layers aloft, resulting in horizontally propagating waves and model oscillations.

To sum up, the SBL is a very complex and turbulent regime difficult to study. Phenomena such as LLJs, katabatic winds or waves further complicate the picture. Nevertheless, the SBL is, at present, one of the atmospheric regimes of the boundary layer receiving especial attention, due to the difficulty of its understanding. Experimental and numerical studies of the SBL are difficult, although the great importance of this regime for numerical climate studies or weather forecasts, and works on pollutant dispersion, fog and dew or frost formation.

1.3 Study of the Stable Boundary Layer

Turbulence was firstly studied by Reynolds (1883) through laboratory experiments. The conditions and the criteria under which the transition from laminar to turbulent flow occurs were analysed. For this purpose, the Reynolds number (Re) was defined as the ratio of inertial to friction forces. Typical Re values for flows near the ground or within the PBL are usually well above the critical values defining the transition to turbulence. Later, the Reynolds decomposition (1895) was proposed to study turbulent flows through the decomposition of the flow into mean and turbulent motions.

The study of the atmospheric turbulence and the PBL started during the XX century. Between 1910 and 1940, Taylor (for instance, Taylor and Green, 1937) developed basic methods for examining and understanding turbulent mixing. In the same period, von Karman and Prandtl were enunciating mixing length hypothesis for the direct application of the atmosphere. Kolmogorov (1941) made an important contribution to the understanding of the small-scale structure turbulence and the energy transfer process from large to small scales. The study of the role of buoyancy in modifying the wind profile and the flux-gradient relations in general give the surface-layer similarity theory of Monin and Obuhkov (1954).

In the 1950s and into the early 1960s major advances took place in the ability to interpret observations. Firstly, measurements were taken over flat uniform terrains but as time advanced the surface properties were more realistic. Nevertheless, accurate observations of a variety of boundary layer types, including convective, stable and trade-cumulus were performed.

The first field campaign took place in the Great Plains of USA during 1953 (Lettau and Davidson, 1957) but data from the Wangara experiment in Australia during 1967 (Clarke et al., 1971) had been further explored. Those field campaigns were devoted to study the SBL and also the CBL and data from them allowed to check the similarity theories previously announced. It is also worth mentioning the 1968 Kansas experiment (Izumi, 1971) which was designed to study the surface layer SBL and to verify the Monin and Obuhkov similarity theory, also in weak to moderately stable conditions. Later, the dynamical processes that take place throughout the whole SBL depth were studied in the Minnesota experiment in 1973 (Izumi and Caughey, 1976).

Meanwhile, the introduction of resolved 3D computer modelling of PBL started with Deardorff (1972) when the first LES was performed. After that, modelling became a complementary tool to better understand the observations. At the same time, laboratory experiments were also conducted to better understand the measurements, such as the works of Willis and Deardorff (1974) where the eddy structures within the CBL were

widely studied.

Since then, the evolution of the tools to study the SBL, as well as the PBL, have largely improved with the major advances on measurements and modelling achieved in the last decade. Regarding the LES, during the eighties the attention was focused on modelling the CBL and in the nineties appeared the first LES of the SBL (Mason and Derbyshire, 1990; Andren, 1995). Since then, the number of numerical studies devoted to the SBL has largely increased. Laboratory experiments of the SBL were also conducted in the nineties (for instance, Thoroddsen and Van Atta, 1992).

Observations have been largely improved because of the new measurement techniques. The first SBL field campaigns were conducted in low to mid latitudes. The first campaign in the mid latitudes was the SABLES-98 campaign (Cuxart et al., 2000b) and took place over the northern Spanish plateau during September 1998. Nevertheless, the CASES-99 campaign (Poulos et al., 2002), that took place in Kansas (USA) during October 1999, has been largely studied because different types of measurements were taken. Nowadays, there are also towers that have been built at permanent sites to measure continuously and produce continuous databases. For instance, in the Ciba site (Valladolid), in Cabauw (The Netherlands), in Boulder (USA) and so on.

The SBL is a complex regime difficult to study, as it is described in the previous section. In fact the stability conditions make it the lesser studied boundary layer regime (and some of the works have been done very recently) for many reasons:

(i) The turbulence is not homogeneous neither isotropic since the vertical motions are suppressed.

(ii) The local effects, such as the orography or the soil uses, are very important and they modify the SBL features.

(iii) Nowadays there are still not available measurements of the PBL over the whole depth. This is mostly important in the SBL because the changes in the vertical are stronger than, for instance, within the CBL. As a result, phenomena such as the elevated turbulence are not well characterized. Therefore, modelling must be used to complement the information that it is not given from measurements.

(iv) Although modelling can be a useful tool to study the SBL, it is also difficult for this regime. If the surface is cooled too much, the boundary layer becomes too stable reducing the downward heat flux and making the surface even colder. In these situations the models do not mix enough at the lowest levels and enter a "decoupled" mode, which can lead to runaway characteristics close to the ground (Viterbo et al., 1999).

(v) Under stably stratified conditions, the Kolmogorov theory for the dissipation of energy might be no longer valid. Therefore, modifications on the turbulence scheme are

considered although there is not still a widely accepted methodology.

(vi) If the flow has a clear gap in the energy spectra, a filter of a scale similar to the gap scale will be adequate enough to perform the separation in mean and fluctuating scales (Reynolds decomposition). In the case that there is no gap, the classical filter allows contributions from larger scales into the statistics of the fluctuations. Since all scales are relevant within the SBL, there is no evidence of the spectral gap, especially under strong stabilities. Nevertheless, the spectral gap is usually supposed about 5 min. A possible improvement is to use a better filter, such as the wavelet transform (Farge, 1992; Cuxart et al., 2002).

1.4 Scientific objectives and methodology

Within this framework, the SBL is studied here to better understand the processes that take place within this regime. Therefore, this work seeks to address several points.

First of all, we analyze if it is possible to run an LES of the SBL using the standard Kolmogorov theory for dissipation. We would also like to know in which stability range the model can work properly without suffering runaway cooling and giving realistic results. The ability of the turbulence scheme to reproduce the main observed features within the SBL is also explored.

Furthermore, we will try to describe how the turbulence is (over the horizontal and vertical) in the presence of increasing the stability as the SBL develops during the night. The relative importance of the processes that take place in the SBL (such as the turbulence, radiation, orography) is also inspected since they can determine the main SBL features.

Although there are different approaches to study the SBL, in this work only LES and mesoscale modelling are taken to understand the main features of the SBL. To proceed, the model and the turbulence scheme used are described in chapter 2.

To start with, an LES of a surface shear-driven SBL is run to see if the model is able to work under stably stratified conditions using the standard Kolmogorov theory. The results are given in chapter 3 as well as a discussion about the situations that suffer runaway cooling. To evaluate how realistic are these runs, they are compared to observations in chapter 4. Furthermore, the results are also evaluated comparing them to others obtained using different turbulence schemes, as it is explained in chapter 5.

To have a complete description of the turbulence within the SBL, the eddy structures are further studied in chapter 6 through the combined use of the Probability Density Functions (PDFs) and the spectra. Therefore, the turbulence is studied in terms of

eddies, beyond the mean profiles obtained classically from the LES results.

Having checked that the model is able to work properly under weakly to moderately stable conditions, a more difficult case than the one in chapter 3 is studied. An LES of an observed LLJ is studied in chapter 7 to analyze the main processes that take place there, especially the mixing across the inversion and the turbulence above the LLJ.

Nevertheless, in the LES the external effects are not included and only the motions up to the resolved scales are described whereas the smallest are parameterized. Therefore, mesoscale modelling is needed to have a complete description of the SBL and this is the purpose of chapter 8. A real observed SBL is studied using mesoscale modelling to evaluate the contribution of the local effects, such as the orography, that are very important within this regime.

Chapter 2

THE USE OF A NUMERICAL MODEL TO STUDY THE STABLE BOUNDARY LAYER

2.1 Available tools to study the Planetary Boundary Layer

The main features of the PBL can be studied through experimental field campaigns, laboratory experiments and numerical modelling. Turbulence is one of the most important processes within the PBL and small scale motions might be present in the flow. Therefore, fast-response turbulence data are necessary to study the PBL but this kind of data is not routinely collected by most operational weather services and special field programs must be conducted on this purpose. One of the limitations of the experimental field campaigns is that observations do not give three-dimensional information for the whole range of scales. Therefore, from the measurements, one can get an idea of the processes that take place near the surface but not for the entire depth of the PBL and other tools are used such as the laboratory and numerical simulations.

Many turbulence studies have been performed in laboratory tanks or wind tunnels where ideal PBL conditions are reproduced to aid understanding of the basic physics through the statistics of the flow (mean values and fluxes). It is worth mentioning the works of Willis and Deardorff (1974), where the eddy structures within the CBL were widely studied, or the Thoroddsen and Van Atta (1992) wind tunnel experiments for SBL varying the Reynolds number. However, the effects of the large scale forcings are difficult to be taken into account in the laboratory experiments.

When a fluid such as water is used to simulate the turbulence in a flow, one must take care to insure that the simulation has the same dimensionless scales as the atmosphere, if this is the object of the study. The Reynolds number can be thought as the ratio of inertial to viscous forcings. In the atmosphere this ratio is expected to be large ($\sim 10^7$) since the molecular diffusion terms are several order of magnitudes smaller than the other terms. However, the dimensions of some laboratory tanks are small enough so that the Reynolds number is not very large, meaning that the viscosity causes the tank flow to differ from the atmospheric flow. Other numbers such as Rayleigh, Richardson or Prandtl numbers should be considered. Wind tunnels have the advantage of using air as the working medium, which overcomes the Reynolds number problem but a disadvantage is that it is difficult to stratify the flow.

Numerical simulations using meteorological models have been very popular since the 1960's. Depending on size of the area of study, different types of meteorological models are used. The General Circulation Models (GCM) are used for climate modelling and weather forecasting and the Limited Area Models (LAM) are used for regional and local weather forecasts. From these models, the synoptical (range of 1000 - 2500 km) and the mesoscale (range of 10 - 1000 km) motions can be studied. Mesoscale models can be used to study the PBL since the main features that take place there correspond to that range of motions whereas synoptical models are not used because the scales of motion are too large to include the PBL processes. Most of the mesoscale models run at resolutions from 1 to 10 km in the horizontal domain and about 50 m in the vertical, with an stretching factor near the ground to better describe the PBL main features. Therefore, the contribution of the largest eddies is taken into account meanwhile the smallest are parameterized through the turbulence scheme.

To focus on the smallest scales, a specific non-hydrostatic model (i.e. because of the small grid scales are involved) is needed to get this lower resolution and this is what a Large-Eddy Simulation (LES) does. The horizontal and vertical domains are smaller than in mesoscale models and this allows to work with resolutions of meters to represent the smallest eddy structures within the PBL. Usually, the LES models run in ideal situations, such as flat homogeneous terrain. Therefore, the orographic effects are not included as in the mesoscale modelling, and not all the external forcings can be taken into account.

Regarding the mesoscale modelling, the horizontal grid size is large enough so that most of the turbulent motions have to be parameterized. Therefore, the turbulence scheme is one-dimensional whereas in the LES models it is three-dimensional since much larger resolutions are considered.

To sum up, the combined inspection of the mesoscale and LES runs can give a picture

of the processes that take place within the PBL, and this methodology is used here to study the SBL.

2.2 Modelling the Planetary Boundary Layer

The complexity of a turbulent flow is so formidable that the description of the flow at all points in space and time is not feasible. Consequently, any study of turbulent flows (either in the form of observations or solution of the conservation equations) is directed towards describing their statistical characteristics, usually in terms of moments and spectra. Following Reynolds (1895), any process s(x,t) can be decomposed into a mean flow component or average $< s >= \overline{s}$ and a rapidly varying turbulent component or fluctuation s' with the following properties,

$$\begin{aligned} s(x,t) &= < s > + s' \\ < s' > &= 0. \\ < ws > &= < w >< s > + < w's' > \\ < u + v > &= < u > + < v > \\ < as > &= a < s > \end{aligned} \tag{2.1}$$

where a is a constant. The mean value $< s >$ is called the first-order moment of s, the variance $< s'^2 >$ is called the second-order moment and the covariance $< w's' >$ is the second-order moment of the joint process w and s. This classical approach is to decompose the variables into a mean part and a perturbation and make a decomposition into the equations governing the flow. Then the averaged equations predict mean values for variables and characterize turbulent process by averaged products of fluctuating values of the variables. However, there are no equations in the original set to account for the averaged fluctuation products which are the turbulent terms. These terms are parameterized using a Subgrid Scale (SGS) scheme or also known as turbulence scheme.

When the Reynolds decomposition is applied to the governing equations of the flow, the remaining unknowns are approximated in terms of known quantities. Such closure approximations or closure assumptions are named by the highest order prognostic equations that are retained.

If a simple parameterization for the turbulent fluxes is used, the main interest is to give formulations for these fluxes that are functions of the prognostic variables of the model (i.e. $\overline{\mu'\beta'} = F(\overline{u_i}, \overline{\theta}, \overline{\beta}, \overline{\mu})$). This approach is commonly called first-order closure,

since the basic equations are the only ones needed. An example of a first-order closure is the one-dimensional K-theory. In this case the fluxes of any quantity β are computed as $\overline{w'\beta'} = -K\frac{\partial\overline{\beta}}{\partial z}$ where K is the so-called eddy diffusivity and the higher order moments should be parameterized.

If time evolution equations are used for the turbulent fluxes, it is called the second-order closure and the higher moments will also be parameterized. It is important to notice that the unknown variables and computing time increase as the order closure does. On the other hand, it is impossible to close the set and there will always be more unknowns than equations. This is the closure problem and to overcome it the higher-order moment terms should be parameterized in terms of known quantities.

Following the 3D K-theory, the Reynolds stresses are assumed proportional to the rates of strain of the resolved flow,

$$\tau_{ij} = K(\frac{\partial\overline{u_i}}{\partial\overline{x_j}} + \frac{\partial\overline{u_j}}{\partial\overline{x_i}}) = KS_{ij} \tag{2.2}$$

where K is the eddy diffusivity and S_{ij} a component of the resolved flow deformation tensor. Smagorinsky (1963) proposed a classical form for the eddy diffusivity: $K = (c\Delta)^2|S_{ij}|$ where Δ is the grid size, $|S_{ij}| = \sqrt{0.5S_{ij}^2}$ is the deformation tensor amplitude and c de Smagorinsky coefficient. This assumption is known as Smagorinsky turbulent model.

Nevertheless, some models use a one-and-a-half-order closure that retains the prognostic equations for the zero-order statistics such as mean wind, temperature and humidity and also retains equations for the variance of those variables. The Turbulent Kinetic Energy (TKE) equation is usually taken in place of the velocity variance equation. One of the advantages of these TKE models is that the prognostic equation provides directly the subgrid contribution of the TKE.

2.3 Eddy sizes and spectra within the Planetary Boundary Layer

Within the PBL, where high Reynolds numbers are typical, the spectrum of turbulent eddies extends over a wide range of sizes (see Figure 2.1). There is a strong interaction between these eddies due to the non-linear and three-dimensional character of the turbulence. To identify the size of the eddies, the energy spectrum of any turbulent variable is inspected as it is seen in Figure 2.2. This spectrum correspond to the range of the high frequencies of the right side of the spectrum in Figure 2.1.

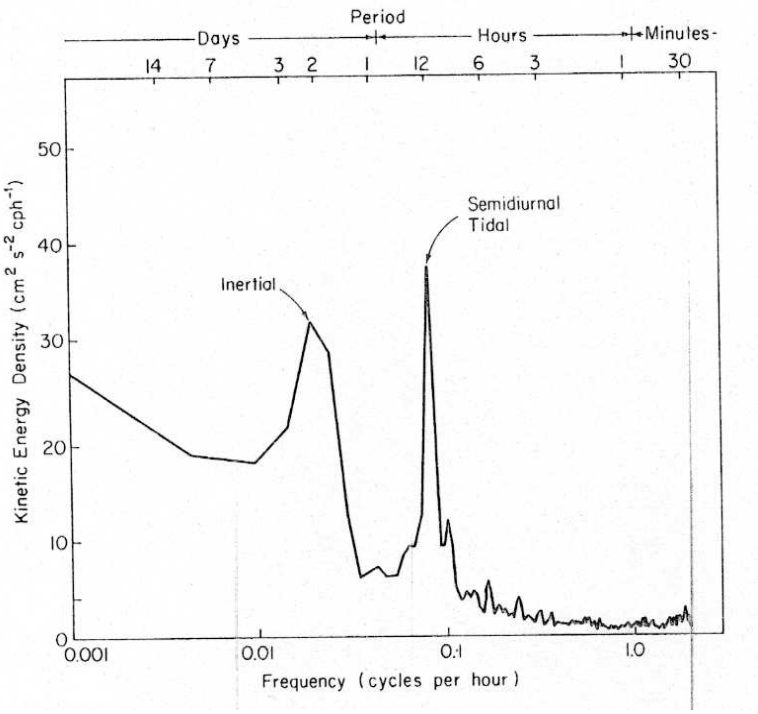

Figure 2.1: Spectrum of energy measured at 13 N. The peaks correspond to the diurnal cycle and to the inertial oscillation corresponding to this latitude (Holton, 1979)

Turbulence energy is gained at the expenses of instabilities in a mean flow, represented by small frequency/wavenumber motions in Figure 2.2. On the other hand, the smallest scales are responsible of viscous dissipation, represented by large frequency/wavenumber motions in Figure 2.2. The spectrum itself is produced by a cascade process, in which smaller and smaller eddies result from the instability of larger ones, continuing down to molecular scales where viscous dissipation converts the kinetic energy of motion into heat.

The Kolmogorov similarity theory of turbulence (Kolmogorov, 1941) explains this *cascade* process and in general the small-scale motions. The large eddies are anisotropic but this anisotropy is lost in the transference of energy to successively smaller and smaller eddies. Finally, the smaller eddies are considered isotropic. Kolmogorov's two main hypotheses state the following:

(i) There exists an equilibrium range in which the average properties of the small-scale components of any turbulent motion at large Reynolds number are determined uniquely by ν and ϵ (kinematic viscosity and rate of dissipation of TKE by viscosity, respectively).

(ii) At large enough Reynolds number, there exists an inertial subrange in which eddy structure is independent of the energy input or viscous dissipation and where only the inertial transfer of energy is important. In this subrange of wavenumbers, average properties are independent of ν and determined solely by ϵ.

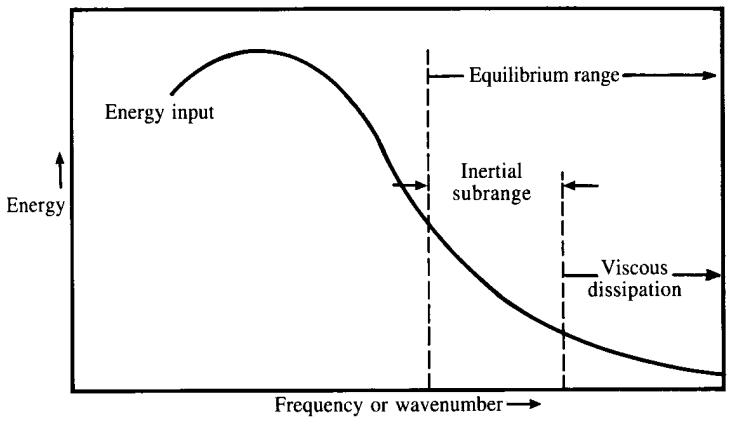

Figure 2.2: Schematic representation of the energy spectrum of any turbulent variable (Garrat, 1992; Figure 2.1)

To identify the size of the most energetic eddies in the flow under stably stratified conditions, the idealized spectra ($S(k)$) for any variable is inspected in Figure 2.3 (Nai-Ping et al., 1983; Stull, 1988).

In $k * S(k)$ space three well defined regions are expected: (1) the scales of the large eddies following a 0 power-law ($k*S(k) \propto k^0$), (2) a buoyancy subrange, where the eddies are quasi-2D because of the suppression of vertical motions by stability, and which obeys a -2 power law ($k * S(k) \propto k^{-2}$) and (3) an inertial subrange, where the turbulence is isotropic and the eddies are 3D, following the -2/3 law ($k*S(k) \propto k^{-2/3}$). Ozmidov (1965) determined the critical length at which buoyancy forces become important in the oceanic boundary layer. He also showed that in such as buoyancy subrange the motion must become anisotropic because not only are the horizontal motions undamped by gravity, but some of the vertical energy is transfered to them.

2.4 Large-Eddy Simulations

In an LES model, the large eddies are explicitly resolved by the grid size of the model and those smaller than the grid size are parameterized (i.e. the equation is replaced with some artificially constructed approximation). It is important to notice that the interactions between the large and small scales are non-linear. Thus, part of the effort in boundary layer meteorology modelling involves the search of adequate turbulence parameterization schemes for the subgrid scale scheme.

The horizontal and vertical domains are smaller than in mesoscale models (for the SBL it is usually about 1 km in each direction) and this allows to work with resolutions of meters to represent the eddy structures within the boundary layer. Typical LES res-

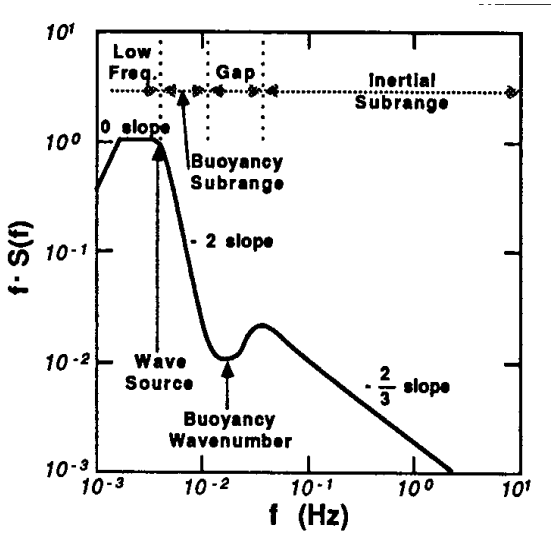

Figure 2.3: Idealized spectral shape of a variable in the SBL conditions (Stull, 1988; Figure 12.22). The frequency f is proportional to the wavenumber k

olutions to study the CBL or the SBL are between meters to tens of meters that aim to resolve explicitly the most energetic turbulence structures.

Classically, LES models use, explicitly or implicitly, the Kolmogorov theory for the dissipation of energy (Kolmogorov, 1941), which applies for homogeneous and isotropic turbulence. Consequently, the grid mesh must be small enough to resolve explicitly the most energetic turbulence structures. On the other hand, the domain must be wide enough to contain a large number of eddies such that the statistics are significant. This makes the computational cost very high and then it has limited the number of LES studies.

LES works started with Deardorff (1972) where a neutral and a convective boundary layer were studied through averaged profiles over a stationary period. Cross-sections were also analyzed to evaluate the eddy structures. Since then, several studies have been made in simulating the convective boundary layer (CBL) (Nieuwstadt et al., 1993; Moeng et al., 1996; Brown et al., 2002...). On the contrary, LES of the SBL has progressed slower.

LES of the SBL started with Mason and Derbyshire (1990), that addressed the study of weakly stratified SBL, and their results were used to check the local scaling theory of Nieuwstadt (1984) and, later, were compared to observations (Derbyshire, 1995). Andrén (1995) continued the study of the weakly stratified SBL, exploring the importance of the SGS scheme, and made a budget analysis of many quantities. Kosović and Curry (2000) made a study for more stable stratification and long steady state conditions in the arctic night, and Saiki et al. (2000) for a windy SBL capped by a strong inversion, where a study of gravity waves was undertaken. Both works use specially adapted SGS scheme for stable stratification. Armenio and Sarkar (2002) studied a range of stably stratified

channel flows using a SGS dynamic model. Cederwall (2002) also used a SGS dynamic model to study the turbulence within the SBL.

Recently, an intercomparison of different SGS has been made for weakly stable stratified conditions (Beare et al., 2005) to check the state of the art. The results and the comparison of the different SGS are further explained in chapter 5.

2.5 Difficulties modelling the Stable Boundary Layer

Near the surface, under stably stratified conditions, the Monin-Obukhov similarity theory (Monin and Obukhov, 1954) is applied to describe the vertical profiles of some variables as a function of the dimensionless group z/L, known as stability parameter. Nevertheless, it assumes that the SBL is continuously turbulent in time and space, with no gaps or patches of non-turbulent air. Since there is evidences from the observations that within the SBL the turbulence can be sporadic, there are some limitations when the Monin-Obukhov similarity theory is applied, especially under strong stable conditions. Most of the LES models use this similarity theory near the surface where it is doubtful to be applied under stable conditions.

The main problem for performing an LES of the SBL is that if the Kolmogorov theory used for the dissipation is to be applied, the grid size must fall within the inertial subrange. Within the stably stratified conditions, the most energetic eddies might be smaller than 1 m because of the suppression of the vertical motions. Therefore, resolutions of about 1 m or smaller are needed to resolve explicitly the most energetic turbulence structures. If such a high resolution is not affordable, often modifications to the SGS scheme are proposed.

Therefore, to perform an LES of the SBL, the domain must be wide enough (1 km) to make the statistics representative but also the resolution must be small (1 m or less) to be close to the inertial subrange and fulfil the conditions to apply the Kolmogorov theory. These facts make the LES of the SBL computationally very expensive.

The LES in this work have been performed at the European Centre for Medium-Range Weather Forecasts (ECMWF) in a cluster system through a special project to get computation time. Some of the LES have been run locally in a PC's cluster. For example, to run 15 min of an LES of the SBL (200×200×200 in the three directions) is needed about 7 hours at the ECMWF and about 6 days at UIB. On the other hand, it is worth mentioning that the computation power is increasing very fast in time and nowadays it is much more larger than during the seventies when the first LES was performed. Deardorff (1972) used 40×40×20 grid points in each of the directions x, y and z respectively and

a time step of 0.2 s. To perform that run, it was needed 150 h of machine time and auxiliary-equipment time distributed over 1.5 years on the CDC 6600 supercomputer of the National Center for Atmospheric Research (NCAR). Over half of this time was spent in reaching the steady state and the rest computing the LES statistics.

2.6 Different approaches to perform an LES of the Stable Boundary Layer

To perform an LES of the SBL, such a high resolutions are usually computationally not affordable. During the last decade, since the initial works of weakly stratified SBL of Mason and Derbyshire (1990) and Andrén (1995), several efforts have been made to overcome this first difficulty, using modified subgrid-scale schemes. Several approaches to the problem appeared in the nineties:

• the backscatter approach (Mason and Thomson, 1992). Fluctuations in the subgrid stress are taken into account in the Smagorinsky model to improve the results near the ground. Therefore, these fluctuations scatter energy randomly from the subgrid scales to the resolved ones. The scales of the smallest resolved motions are the most excited by backscatter. Schumann (1995) pointed out that the backscatter significantly influences the resolved motions since a considerably large eddy viscosity is required to dissipate the extra energy.

• the two-part subgrid scale model (Sullivan et al., 1994) and the non-linear model (Kosović, 1997). These two approaches tend to overcome the difficulties that the subgrid scale models have near the ground. Near the surface, the size of the most energetic eddies becomes proportional to the distance to the wall. Therefore, the smallest resolved eddies may be strongly anisotropic and the inertial subgrange is shifted to smaller scales. Sullivan et al. (1994) splitted the stresses in two terms: isotropic and homogeneous. The isotropic eddy viscosity is a function of the strain rate whereas the inhomogeneous contribution is a function of the mean strain rate. The stress is written as $\tau_{ij} = -2\nu_t\gamma S_{ij} - 2\nu_T < S_{ij} >$ where ν_t and ν_T are the fluctuating and averaged eddy viscosity and γ the anisotropic factor. On the other hand, in Kosović (1997) the backscatter and the anisotropy induced by shear were taken into account.

• the dynamic subgrid scale model (Germano et al., 1991). This model is based on the algebraic identity between turbulent stresses at resolved scales (Γ_{ij}) and subgrid stresses

from velocity fields that are filtered at two different scales (T_{ij} and τ_{ij}) giving $\Gamma_{ij} = T_{ij} - \tau_{ij}$. The basic idea is to use the smallest resolved scales to compute explicitly the stresses and to use this information into the subgrid stresses. The Smagorinsky model is used at each of the filtered scales. However, the Smagorinsky coefficient is not longer constant, but rather is dynamically determined by the flow and it is a function of time and space.

Nevertheless these modifications imply more consumption of computing power and there is not yet a consensus on what is the real solution, because there is not any widely accepted theory on stratified anisotropic turbulence. Moreover, more adjustable constants are needed that sometimes have to be fixed for a particular studied regime.

2.7 The model and the turbulence scheme used

The model used in this work is the Mesoscale Non-Hydrostatic Simulation System (Meso-NH[1] , Lafore et al., 1998) developed jointly by the Centre National de Recherches Météorologiques (Météo-France) and the Laboratoire d'Aérologie. The main objective of this project was to build a model able to simulate the atmospheric motions, ranging from the mesoscale down to the micro-scale and for that the model is non-hydrostatic.

The anelastic approximation is also considered to avoid the use of very small time steps in the integration of the model, due to the very fast propagation of the acoustic waves. In this approach, the acoustic waves are eliminated from the continuous set of equations by the use of a constant density profile instead of the actual fluid density in the continuity equation and in the momentum equation, except for the buoyancy term, which is the leading term of the approximation. The fluid becomes therefore formally incompressible, and the pressure is deduced from the solution of an elliptic equation.

Several parameterizations of physical processes were introduced in the model such as the convection scheme, the radiation scheme, the surface processes scheme, microphysical scheme, turbulence scheme ... In this work, to perform mesoscale runs of real cases, all of these parameterizations are taken into account (see further details in chapter 8). Nevertheless, to run an LES of the SBL here, where ideal situations are considered, just two of these parameterizations have been taken: the turbulence scheme and the dynamics of the model. The rest of the parameterizations are not activated since they are considered not much relevant in the particularly simulated conditions. Moreover, the computational cost increases with the number of schemes that are taken into account.

The ideal LES conditions are introduced using cyclic lateral boundary conditions and a flat (with a fixed roughness length) surface boundary condition. To simplify the runs,

[1] http://www.aero.obs-mip.fr/mesonh/

the SBL is dry and neither moisture variables nor process are activated in the model. Regarding mesoscale modelling, the lateral conditions are open, and come from the analysis of the ECMWF, meanwhile the soil uses as well as the orography are considered, which vary depending on the simulated place.

A flux-corrected second order advection scheme centred on space and time is used for the scalar variables (temperature, TKE, dissipation and scalars). To prevent spurious reflection from the model top boundary, an absorbing layer, in which damping increases with height, occupies the top fraction of the domain.

The turbulence scheme (Cuxart et al., 2000a) is one-and-a-half order and uses a prognostic equation for the Turbulent Kinetic Energy (TKE). A particularity of this scheme is the use of variable turbulent Prandtl and Schmidt numbers, consistently derived from the complete set of second-order turbulent-moment equations. The Turbulent Kinetic Energy (TKE) is defined as: $\overline{e} = 0.5(\overline{u'^2} + \overline{v'^2} + \overline{w'^2})$, where $\overline{u'^2}$, $\overline{v'^2}$ and $\overline{w'^2}$ are the variances of the velocity components. When the flow is laminar TKE is equal to zero and becomes larger when the flow is more turbulent.

The vertical turbulent fluxes can be computed alone, providing an efficient single-column parameterization for the mesoscale configuration of the model, if an appropriate parameterization of the eddy-length scale is used. The one-dimensional version of the turbulence scheme that Meso-NH uses considers only the vertical exchanges with the same system of equations. The mixing length specification and the dimensionality of the scheme are then the only aspects of the scheme which differ from the LES to the mesoscale configuration, and the numerical constants used for the closure terms are the same in both configurations.

Therefore, the fluxes have two contributions: the resolved, computed by the model, and the subgrid (i.e. the contribution of the small scales) computed by the turbulence scheme. Then, the scales greater than the resolution are computed by the model whereas the smallest are parameterized through the SGS. The results obtained from a Meso-NH run in LES mode, as in any other LES, are statistical values, such as means and fluxes, apart from other supplementary and useful diagnostics (spectra, time series, budgets...). These statistics are usually computed at each level averaged over the horizontal domain and then over a period of time where the fields are supposed to be stationary. Some diagnostics, particularly used in the SBL conditions, have been introduced in the model on purpose for this work, as well as the development of the computation of the Probability Density Functions (PDFs) from LES outputs (see chapter 6).

In the three-dimensional model of the turbulence scheme, the fluxes are computed in each point, leading to

$$\overline{u_i' u_j'} = \frac{2}{3}\delta_{ij}\, e - \frac{4}{15}\frac{l}{C_m} e^{\frac{1}{2}} \left(\frac{\partial \overline{u_i}}{\partial x_j} + \frac{\partial \overline{u_j}}{\partial x_i} - \frac{2}{3}\delta_{ij}\frac{\partial \overline{u_m}}{\partial x_m}\right) \tag{2.3}$$

$$\overline{u_i'\xi'} = -\frac{2}{3}\frac{1}{C_\xi}\, l e^{\frac{1}{2}}\, \frac{\partial \xi}{\partial x_i} \underbrace{\left[1 - \delta_{i3}\frac{g}{\theta_{v\,ref}}\frac{\overline{\theta_v'\xi'}}{e\frac{\partial \xi}{\partial x_i}}\right]}_{f^{\xi,i}} \tag{2.4}$$

where u_i are the velocity components, ξ is any scalar (including the potential temperature θ), θ_v is the virtual potential temperature, l a characteristic length and e is the subgrid turbulence kinetic energy. E will be used to denote the total (resolved + subgrid) turbulence kinetic energy. C_m, C_ξ are constants of the scheme and $f^{\xi,i}$ are proportional to the inverse turbulent Prandtl and Schmidt numbers that can be expressed as a function of the spatial gradients of the scalars. In these equations the subscripts follow the standard summation convention but not the superscripts. The index ref refers to reference values for the domain. The primes indicate sub-grid scale perturbations whereas the over-bars stand for grid-scale averages. The variances and correlations can be written, in a general expression, as (C_a, C_b being generic constants of the scheme).

$$\overline{\xi'\chi'} = C_a l^2 \left(\frac{\partial \overline{\xi}}{\partial x_m}\frac{\partial \overline{\chi}}{\partial x_m}\right)\left(f^{\xi,m} + f^{\chi,m}\right) \tag{2.5}$$

$$\overline{\xi'^2} = C_b l^2 \left(\frac{\partial \overline{\xi}}{\partial x_m}\frac{\partial \overline{\xi}}{\partial x_m}\right) f^{\xi,m} \tag{2.6}$$

The system is closed by the use of the mixing length, which is taken as

$$l = min\left[(\Delta x\, \Delta y\, \Delta z)^{1/3}, 0.76\sqrt{\frac{e}{\frac{g}{\theta_{v\,ref}}\frac{\partial \theta}{\partial z}}}\right] \tag{2.7}$$

the second term being the proposed by Deardorff (1980) for stably stratified layers. To obtain this system, several hypotheses are made on the complete second-order system. The more relevant and critical for the SBL are the assumption of stationarity between the subgrid and resolved motions (neglecting advection and time derivatives), the neglect of the third-order terms, and the neglect of the buoyancy contribution to the anisotropic part of the Reynolds stresses. However, the isotropic part of the Reynolds stresses is kept complete and it is the classical Turbulence Kinetic Energy (e or TKE) equation.

$$\begin{aligned}\frac{\partial e}{\partial t} &= -\frac{\partial}{\partial x_k}(\overline{u_k}e) - \overline{u_i' u_k'}\frac{\partial \overline{u_i}}{\partial x_k} + \frac{g}{\theta_{v\,ref}}\delta_{i3}\overline{u_i'\theta_v'} \\ &\quad -\frac{\partial}{\partial x_j}(-C_e l e^{\frac{1}{2}}\frac{\partial e}{\partial x_j}) - C_\epsilon \frac{e^{\frac{3}{2}}}{l} \end{aligned} \tag{2.8}$$

In this equation, classical parameterizations are used (Deardorff, 1973). The most questionable for the SBL is to impose homogeneous and isotropic turbulence for the dissipation terms, where the Kolmogorov proposal is applied with $C_\epsilon = 0.7$. A unique characteristic length is used for the mixing in all directions and the same length is retained for the dissipation term. These choices for the length scales might also be reviewed for stable stratification. However, in this work, the standard scheme will be used with no modifications.

2.8 Regimes previously simulated with this turbulence scheme

Several boundary layer regimes have been previously simulated in LES mode using the Meso-NH model and the turbulence scheme described in the previous section. When this SGS was introduced in the Meso-NH model, it was validated running 3 different boundary layer regimes (Cuxart, 1997; Cuxart et al., 2000a): an intercomparison case of dry convective boundary layer with no mean winds (Nieuwstadt et al., 1993), a smoke cloud case intercomparison (Bretherton et al., 1999a), which emulated a radiative boundary layer by the cooling at the top of the planetary boundary layer and a neutrally stratified shear driven boundary layer (Andrén et al., 1994). The model was able to reproduce well those three cases.

Later, this SGS participated in other intercomparisons exercises where different LES models (i.e. different SGS) ran at the same conditions from different convective boundary layer regimes: stratocumulus boundary layer (Duynkerke, 1999a), shallow cumulus convection (Siebesma et al., 2003), a transition from stratocumulus-capped marine boundary layer into a cumulus capped boundary layer (Bretherton et al., 1999b) and a trade cumulus in strong inversion (Stevens et al., 2001).

The turbulence scheme was also run in single-column mode using the non-local mixing length of Bougeault and Lacarrère (1989) for the same three validation cases (Cuxart, 1997; Cuxart et al., 2000a) and the results compared well to those obtained from LES. A new moist mixing length has been tested for a cloudy boundary layers regimes (Sánchez

and Cuxart, 2004 and widely in Sánchez, 2002). Furthermore, an observed LLJ during a moderately stable night in SABLES-98 experimental field campaign has been simulated in 1D mode (Conangla and Cuxart, 2005) giving comparable results.

The model has recently participated into an intercomparison exercise of a moderately stable shear-driven boundary layer case (Kosović and Curry, 2000). It was run in both configurations: LES mode (Beare et al., 2005) and 1D mode (Cuxart el al., 2005). In each mode, the results were comparable to those of the other participant models but a widely explanation is found in chapter 5.

Regarding the mesoscale modelling using the Meso-NH model, several works are found in the web page of the model but, for example, it is worth mentioning the works of Flamant et al. (2002), that studied the föhn effect in the Wipp valley (Wipptal, Austria), and later Jaubert et al. (2005) in the Rhine valley.

Chapter 3

MEAN CHARACTERISTICS OF THE SBL OBTAINED FROM THE LES MODEL[1]

The main objective in this chapter is to see if the model, which uses the standard Kolmogorov theory, is able to work fine under stably stratified conditions. In the SBL the turbulence is not homogeneous neither isotropic and this makes that the Kolmogorov theory for dissipation is questionable. Some modifications on the turbulence scheme are proposed in the literature but there is not a widely accepted theory.

A surface shear-driven SBL is considered over a flat and uniform terrain. Near the surface the Monin-Obukhov similarity theory is used. Several runs have been performed changing the geostrophic wind and the surface cooling conditions. The turbulence within the boundary layer, as well as the eddy structures, are analysed depending on the parameter space to better understand the processes that take place within the SBL. Besides, some sensitivity tests are performed (such as the resolution, surface forcings and radiation) to evaluate the dependency on the results. Furthermore, the next chapter is devoted to check how realistic are these LES results through the comparison to data from two experimental field campaigns.

[1]This chapter is based on: Jiménez, M.A., and Cuxart, J., 2005: Large-eddy Simulations of the Stable Boundary Layer: study of applicability using experimental data, *Boundary-Layer Meteorology*, **115**, 241-261.

3.1 Model setup for an LES of the Stable Boundary Layer

The first exercise consists on a series of simulations of a surface shear-driven SBL varying the external forcings. The Meso-NH model is run in LES configuration, taking a domain size of 600×400×1431 m, using 96×96×128 grid points in the x, y, and z directions, respectively. The horizontal grid spacing is 6.25 m in x, and 4.17 m in y. A horizontally anisotropic grid has been chosen to better resolve the streamwise streak-like structures present near the wall in shear-driven boundary layers (Andrén et al., 1994). To obtain the better representation of the SBL, a large domain and a high resolution have been chosen, limited by the computational power. The vertical grid spacing changes with height; it is constant (5.21 m) from the surface to 500 m, then a 9 % stretching factor is applied until the top of the model, where the resolution is 82 m. Since most of the significant turbulent motions take place below 500 m in these simulations, this vertical grid configuration should provide sufficient resolution of the turbulence while minimizing the effect of the upper boundary condition.

All the experiments are made at a latitude of 45°, imposing a geostrophic balance above the ABL during all the run. The terrain is flat with a roughness length z_0 of 0.1 m and the moist effects are not considered. This set of conditions are very similar to what Garratt (1992) describes as a stationary SBL.

Twenty different simulations have been performed varying the external forcings: the geostrophic wind (G) and surface vertical temperature flux ($< w'\theta' >_s$). With regard to the wind speed, a well developed neutrally stratified turbulence field is generated for 4 different geostrophic balances G = 13 m s^{-1}, 10 m s^{-1}, 8 m s^{-1}, 5 m s^{-1}, all with potential temperature constant with height and equal to 289 K. Each case is initialized using a steady state mean wind profile for neutrally stratified conditions, and a small random perturbation is added to all velocity components to initiate the resolved motions. The methodology followed is from Andrén et al. (1994) who proposed to run 100000 s at which point the flow regime is considered essentially stationary. LES statistics are computed for the last 30000 s of each case.

Afterwards, cooling is applied using constant negative surface heat flux for two hours and then the value of the heat flux used is changed to the next value, such that all four values of ($< w'\theta' >_s$ = -0.005, -0.010, -0.025, -0.050 K m s^{-1}) are tested over a period of 8 hours for a given G. Monin-Obukhov similarity theory is imposed pointwise as a surface boundary condition, using the Businger-Dyer flux profile relationships (Businger et al., 1971; Dyer, 1974) which consider $\phi_M = 1 + 4.7z/L$ and $\phi_H = 0.74 + 4.7z/L$. The LES

statistics are computed during the last hour of each section. The simulations cannot be considered stationary, similarly to the real SBL. However, the ability of LES to properly describe the turbulent effects resulting from evolving surface heat flux has been shown for the case of the diurnal cycle of the shallow cumulus by Brown et al. (2002).

We believe that this simulation strategy will represent approximately the cooling in a flat location in clear nights with different winds and dry soil and air conditions. Furthermore, these simulations create the beginnings of our LES statistics data base with which we plan a comprehensive, systematic comparison to observations.

3.2 Classification of the simulations

To see whether the chosen parameter space (G and $< w'\theta' >_s$) corresponds to an observable range of the mid-latitude SBL, the formulation of Derbyshire (1990) it is used. Derbyshire fixed the stable limit of the vertical temperature flux ($< w'\theta' >_s$) that can be sustained as:

$$(< w'\theta' >_0)_{max} = \frac{\theta_0 \, R_{fc}}{g\sqrt{3}} |f| G^2 \tag{3.1}$$

where R_{fc} is the critical flux Richardson number, f is the Coriolis parameter ($1.025{\cdot}10^{-4} s^{-1}$ in our case), g the gravitational acceleration, and θ_0 is a reference value for the temperature. Equation 3.1 means that the dynamical effects of the static stability, combined with the earth's rotation, limit the downward surface heat flux which turbulence can support. This formula must be taken as a first approximation, since some of the hypotheses used in the derivation are (i) quasi-steady state, (ii) to consider the SBL a closed system, (iii) inertial equilibrium and (iv) a constant R_{fc} through the layer.

Table 3.1: **Maximum surface cooling flux (K m s^{-1}) derived from Derbyshire's formula (Equation 3.1) for each G, considering different values for R_{fc}**

G	R_{fc}=0.2	R_{fc}=0.25	R_{fc}=1
13 m s^{-1}	-0.056	-0.071	-0.287
10 m s^{-1}	-0.032	-0.042	-0.170
8 m s^{-1}	-0.022	-0.027	-0.109
5 m s^{-1}	-0.008	-0.011	-0.042

In Table 3.1 there are the possible maximum values for the surface heat flux according to Equation 3.1 for each imposed geostrophic wind, varying the value for R_{fc}. The values obtained from Equation 3.1 are different depending on the chosen value for R_{fc}. Canuto

(2002) suggests the value of 0.25 for the transition from laminar to turbulent, but takes 1 for the transition from a turbulent to a laminar state.

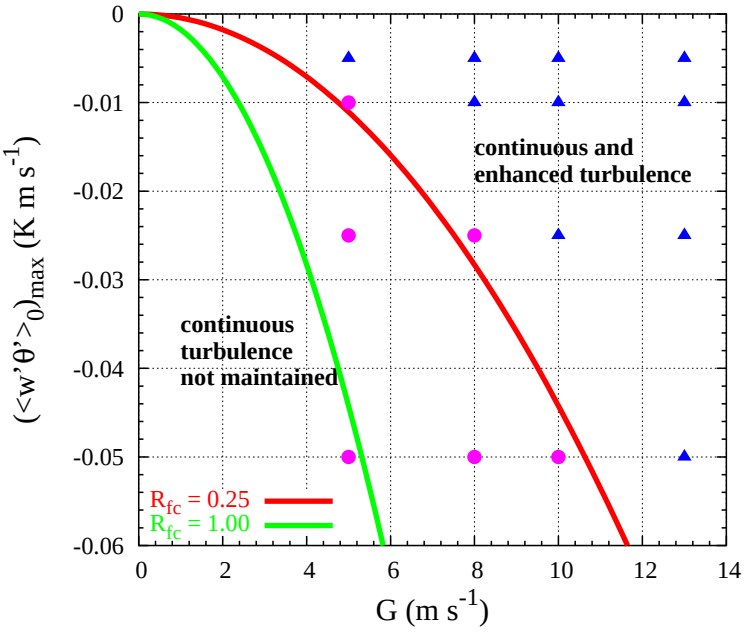

Figure 3.1: External forcings used (points) in the LES of the shear-driven SBL case and two different criteria that specify limiting forcings that support turbulence following Derbyshire (1990). In circles simulations that suffer from runaway cooling and in triangles the rest of the runs

The pairs of forcings used in the LES of the SBL as well as the maximum surface temperature flux predicted by Derbyshire (1990) are shown in Figure 3.1 for R_{fc} equal to 0.25 and 1. Combinations of G and $< w'\theta' >_s$ can be collected in two different zones, as Figure 3.1 indicates. It is seen that almost the whole range of simulated conditions would be observable for $R_{fc} = 1$. However, for smaller R_{fc}, some simulations might never correspond to observed conditions since $< w'\theta' >_s$ is only larger than the one predicted by Derbyshire when external forcings are taken into account but this is not the case of the LES results. Similar results are found in Cederwall (2002) for smaller geostrophic winds.

When $R_{fc} = 0.25$ the simulations that do not follow the Derbyshire criterion coincide with the ones that suffer from runaway cooling as Figure 3.2 indicates. Since the surface vertical temperature flux applied as a surface boundary condition is negative, the surface boundary layer is cooling, as the temperature value in the first computation level shows in Figure 3.2 for a given G. It is observed that the surface temperature decreases for the consecutive increasing cooling fluxes. Runaway cooling appears when the temperature near the ground presents drastic changes, as in Viterbo et al. (1999). Then, the simulations that suffer from runaway cooling have a prescribed $< w'\theta' >_s$ larger than the one

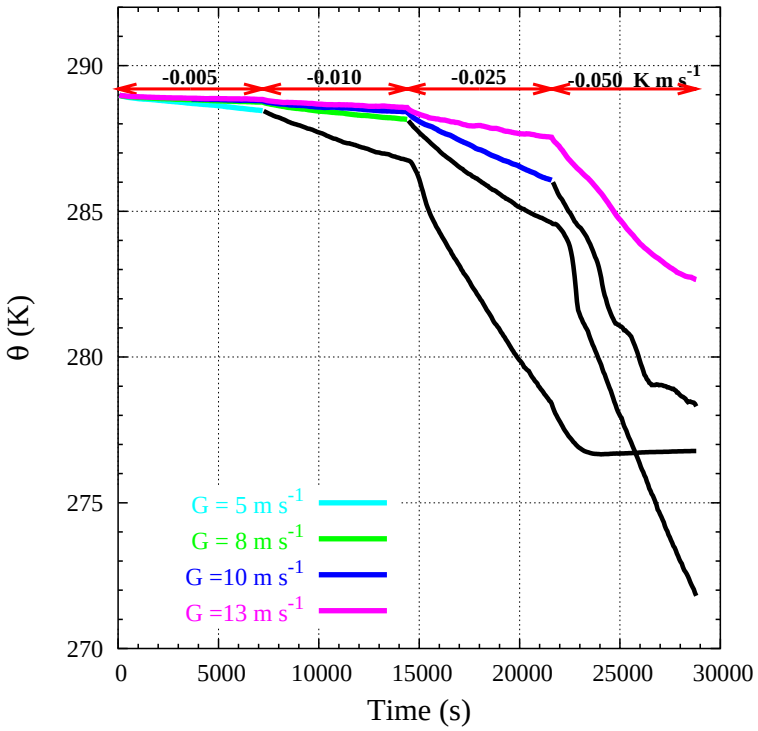

Figure 3.2: Time series of the horizontally-averaged potential temperature at 2.6 m for each geostrophic wind (black-line: simulations with $< w'\theta' >_s$ larger than the one predicted by Derbyshire (1990))

predicted by formulation of Derbyshire (1990) which means that these conditions are not sustained in the atmosphere.

For a given $< w'\theta' >_s$, the cooling increases when G decreases. Therefore, the shear generated by the wind is smaller allowing the increase of the stability until runaway cooling appears. For instance, when $< w'\theta' >_s$ = -0.025 K m s^{-1}, the case with $G = 13$ s^{-1} is stable but do not suffer from runaway cooling but the $G = 5$ s^{-1} does, because this second case is less stable due to the shear.

To inspect the strength of the stability of stratification of each simulation, the values of the stability parameter z/L are used, where

$$L = -\frac{\overline{\theta_v} {u_*}^3}{kg\overline{w'\theta'}} \tag{3.2}$$

$${u_*}^2 = \sqrt{\overline{u'w'}^2 + \overline{u'w'}^2} \tag{3.3}$$

L is the Obukhov length and u_* is the friction velocity. To compute the stability parameter

z is taken at 13 m since it is the nearest computation value to 10 m, the level used by Mahrt et al. (1998) to classify the SBL regimes (see Figure 3.3).

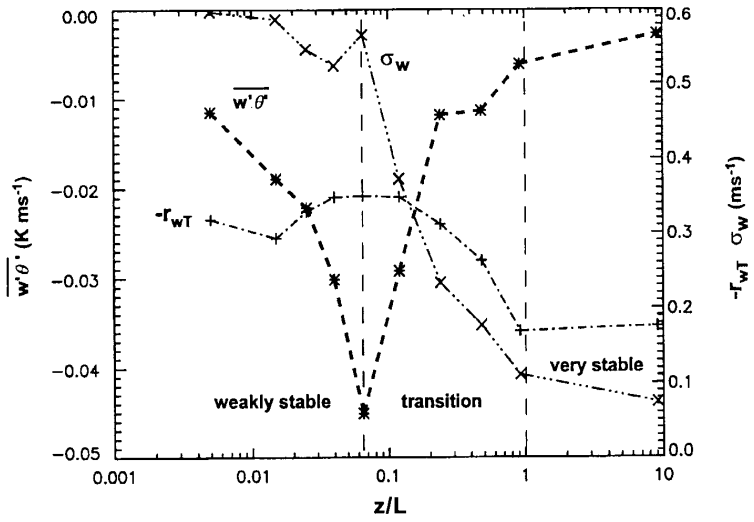

Figure 3.3: Classification of the SBL regimes according to the stability parameter (z/L) (Mahrt et al., 1998, Figure 1.a)

In this classification $z/L < 0.06$ corresponds to a weakly stable regime, $0.06 < z/L < 1$ to a transition and $z/L > 1$ to a very stable. Finally, if $z/L < 0$ means that the regime is unstable. Following Table 3.2, the simulations that suffer from runaway cooling have values of z/L larger than 1 whereas the rest of the runs have values up to 0.6. This confirms that the model, in this particular configuration of parameters (G and $< w'\theta' >_s$), is able to simulate from weakly to moderately stable conditions according to the classification of Mahrt et al. (1998).

Table 3.2: **Stability parameter (z/L) for each simulation at $z = 13.025$ m. In bold and italics simulations with decreasing e/E with increasing stabilisation; those in bold suffer runaway cooling**

	13 m s^{-1}	10 m s^{-1}	8 m s^{-1}	5 m s^{-1}
-0.005 K m s^{-1}	0.006	0.013	0.027	0.202
-0.010 K m s^{-1}	0.016	0.038	0.098	*1.626*
-0.025 K m s^{-1}	0.059	0.321	*0.877*	**0.989**
-0.050 K m s^{-1}	0.485	**1.491**	**1.574**	**-3.619**

3.3 Eddy structures within the Stable Boundary Layer

To see how the eddy structures are within the simulated SBL, some horizontal and vertical cross-sections for the u-component of the wind are shown in Figures 3.5 and 3.6, respectively. Furthermore, the eddy structures under neutral conditions are also analysed in Figure 3.4. From the cross-sections it is possible to study the evolution of the structures as the stability increases (or $< w'\theta' >_s$ for a given G) and also the effect of the shear on the eddy sizes.

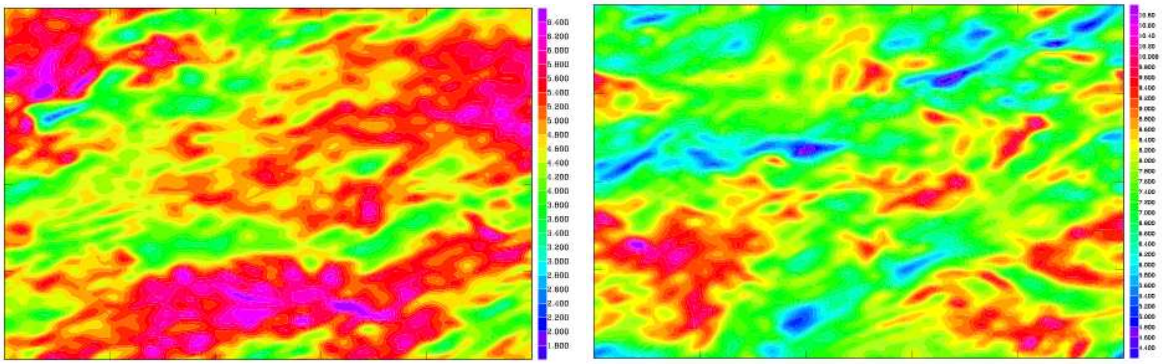

Figure 3.4: u-component (m s^{-1}) horizontal cross-section at z = 50 m for the neutral run. (Left) G = 8 m s^{-1} and (right) G = 13 m s^{-1}

Deardorff (1972) found that, near the ground in the neutral case, the downstream velocity component (u) eddies were organized into distinct "bands" or "strikes" oriented 15 degrees right of the surface wind (northern hemisphere). Moreover, the length of the band was much larger than its width because of the wind shear effect. A similar picture is found in Figure 3.4.

The eddy structures under stable conditions are shown in Figures 3.5 and 3.6. The horizontal cross-section (Figure 3.5) shows that within the SBL the structures are characterized by the appearance of alternating streaks of high and low speed aligned with the mean flow direction, similarly to the ones obtained under neutral conditions (Figure 3.4). On the other hand, the size of the eddies is smaller as the stability increases (for any G) since the stably stratified conditions tend to suppress the turbulence. When shear increases, the flow is more turbulent and less stable. Therefore, the eddy sizes are larger for G = 13 m s^{-1} than for lower G. This is much clearly seen when the highest cooling is considered in Figure 3.5.

Besides, near the surface the eddies are smaller than in the middle or in the top of the SBL, as Figure 3.6 reveals. For weak stable conditions the turbulent motions occupy the whole domain (Figure 3.6 top) whereas for stronger stability the turbulence is confined

to levels close to the ground (Figure 3.6 bottom). Since the conditions are more stable for $G = 8$ m s^{-1} than for $G = 13$ m s^{-1} the boundary layer height is also lower. This also confirms that under very stable conditions shear is small and then the turbulence, mainly generated by shear in the SBL, is weak.

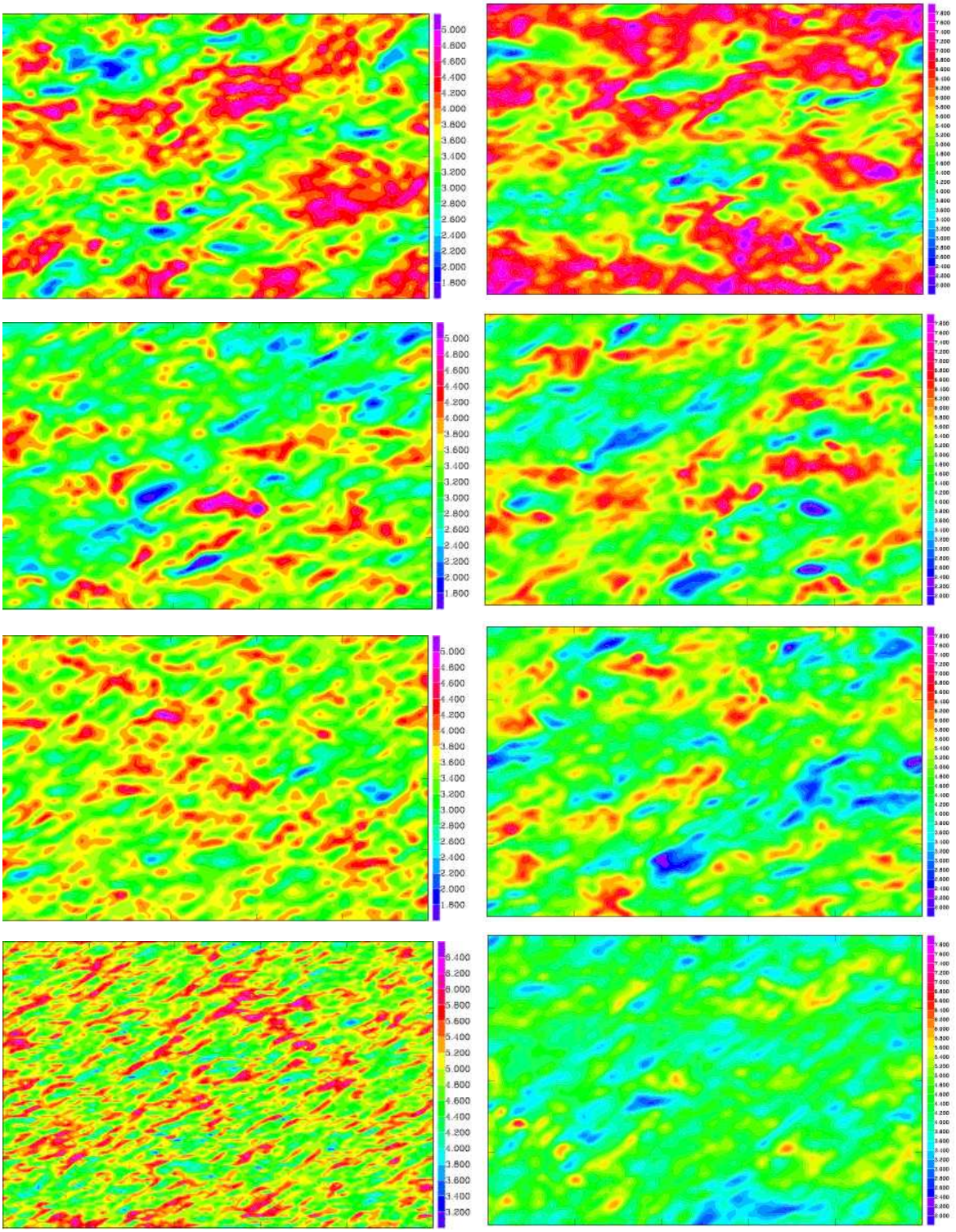

Figure 3.5: u-component (m s^{-1}) horizontal cross-section at z = 50 m for (left) G = 8 m s^{-1} and (right) G = 13 m s^{-1} as the surface cooling increases (intervals = 0.2 m s^{-1}). (First row) $< w'\theta' >_s$ = -0.005 K m s^{-1}, (Second row) $< w'\theta' >_s$ = -0.010 K m s^{-1}, (Third row) $< w'\theta' >_s$ = -0.025 K m s^{-1}, (Last row) $< w'\theta' >_s$ = -0.050 K m s^{-1}

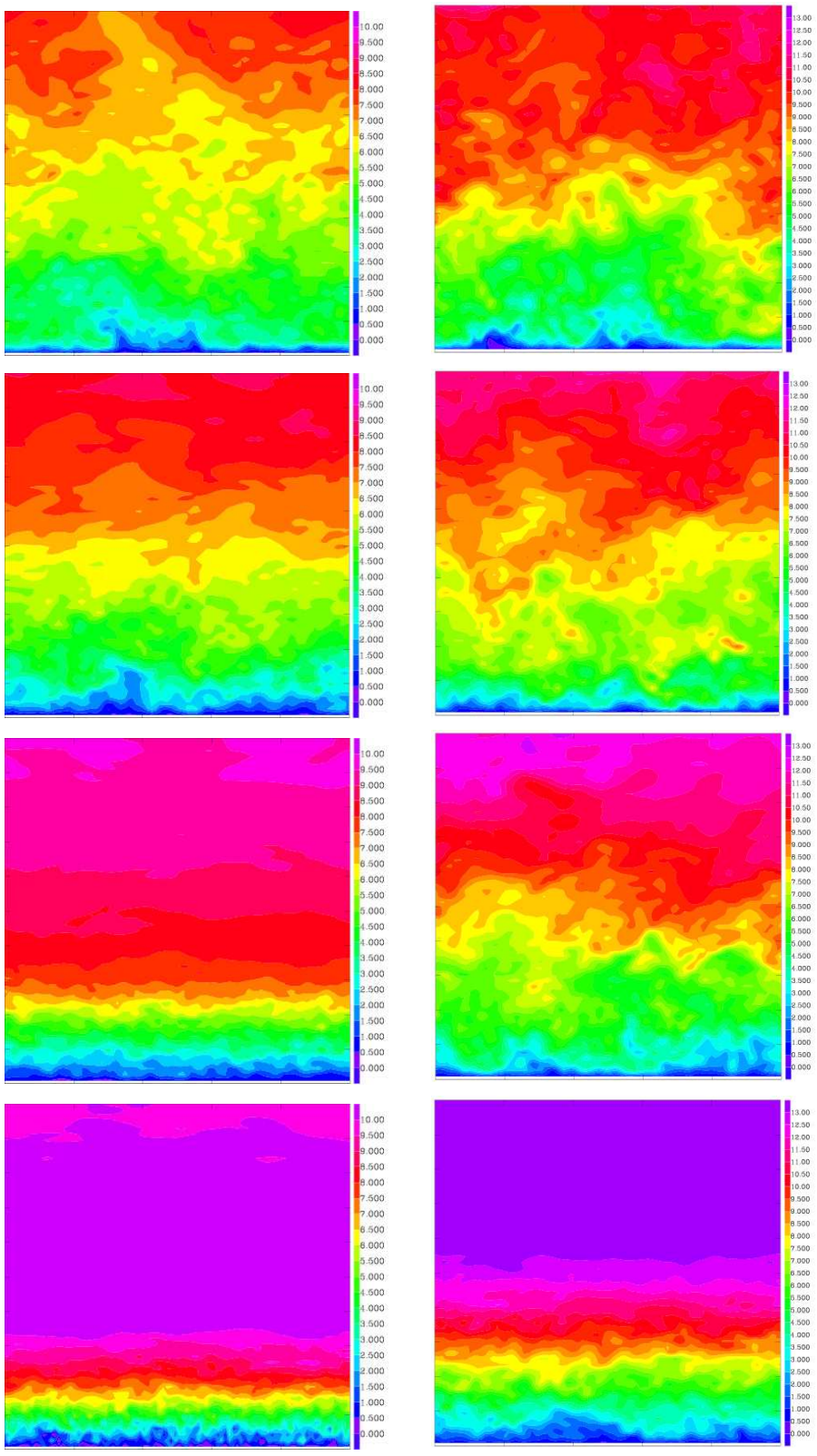

Figure 3.6: u-component (m s^{-1}) vertical cross-section at y = 200 m for (left) $G = 8$ m s^{-1} and (right) $G = 13$ m s^{-1} as the surface cooling increases (as in Figure 3.5). There is one colour each 0.5 m s^{-1} and the x-axis corresponds to the x-domain whereas the y-axis to the z-domain

3.4 Mean structure of the Stable Boundary Layer

From the eddy structures, like the ones obtained in Figures 3.5 and 3.6, the LES models can compute statistics such as mean values and higher order moments. These statistics are usually computed in vertical levels from the all horizontal domain and then averaged over a period of time where the fields are supposed to be stationary. The averaged profiles for the second hour of each section are presented in Figures 3.7, 3.8, 3.9 and 3.10 for each G = 5, 8, 10 and 13 m s^{-1}, respectively. Therefore, some profiles are inspected such as the potential temperature (θ), the wind speed (M), the Brunt-Väisälä frequency (N_{BV}), the flux Richardson number (Ri_f), the total Turbulent Kinetic Energy (TKE_{TOT}) and the ratio between the subgrid and total contribution of the TKE ($\frac{TKE_{SBG}}{TKE_{TOT}}$).

The initial temperature for the neutral case is constant and equal to 289 K. While the consecutive increasing fluxes are applied to stratify the layer, the temperature near the ground cools down (Figures 3.7.a, 3.8.a, 3.9.a and 3.10.a). This means that the strength of the inversion increases with the surface cooling flux for a fixed G. Moreover, the most stable case correspond to the smaller wind (G = 5 m s^{-1}) because the shear is reduced allowing a larger cooling of the surface.

As the stratification increases, for a given G, it appears a maximum of the wind at the inversion level. Since the vertical motions are suppressed under stable conditions, the height of the inversion is smaller for G = 5 m s^{-1} than G = 13 m s^{-1}, for a given surface cooling. Therefore, the maximum of the wind is located at 50 m for G = 5 m s^{-1} and about 200 m for G = 13 m s^{-1}. This maximum is possibly related to the development of an inertial oscillation, similarly to Kosović and Curry (2000), because the wind tends to the geostrophic value at higher levels.

Following Table 3.2, the most stable cases present drastic changes in the potential temperature and wind speed profiles, experiencing runaway cooling as Figure 3.2 indicates, since it is not fulfilling the Derbyshire criterion for R_{fc} up to 0.25.

To go further, two useful parameters to describe what happens within the SBL are computed: the Brunt-Väisälä frequency (N_{BV}) and the flux Richardson number (Ri_f) which are defined as

$$\begin{aligned} N_{BV} &= \sqrt{\frac{g}{\overline{\theta_v}}\frac{\partial\overline{\theta_v}}{\partial z}} \\ Ri_f &= \frac{(\frac{g}{\overline{\theta_v}})\overline{w'\theta'}}{\overline{u'w'}\frac{\partial\overline{U}}{\partial z} + \overline{v'w'}\frac{\partial\overline{V}}{\partial z}} \end{aligned} \tag{3.4}$$

where θ_v is the potential temperature, g the gravitational acceleration and $\overline{u'w'}$, $\overline{v'w'}$ and

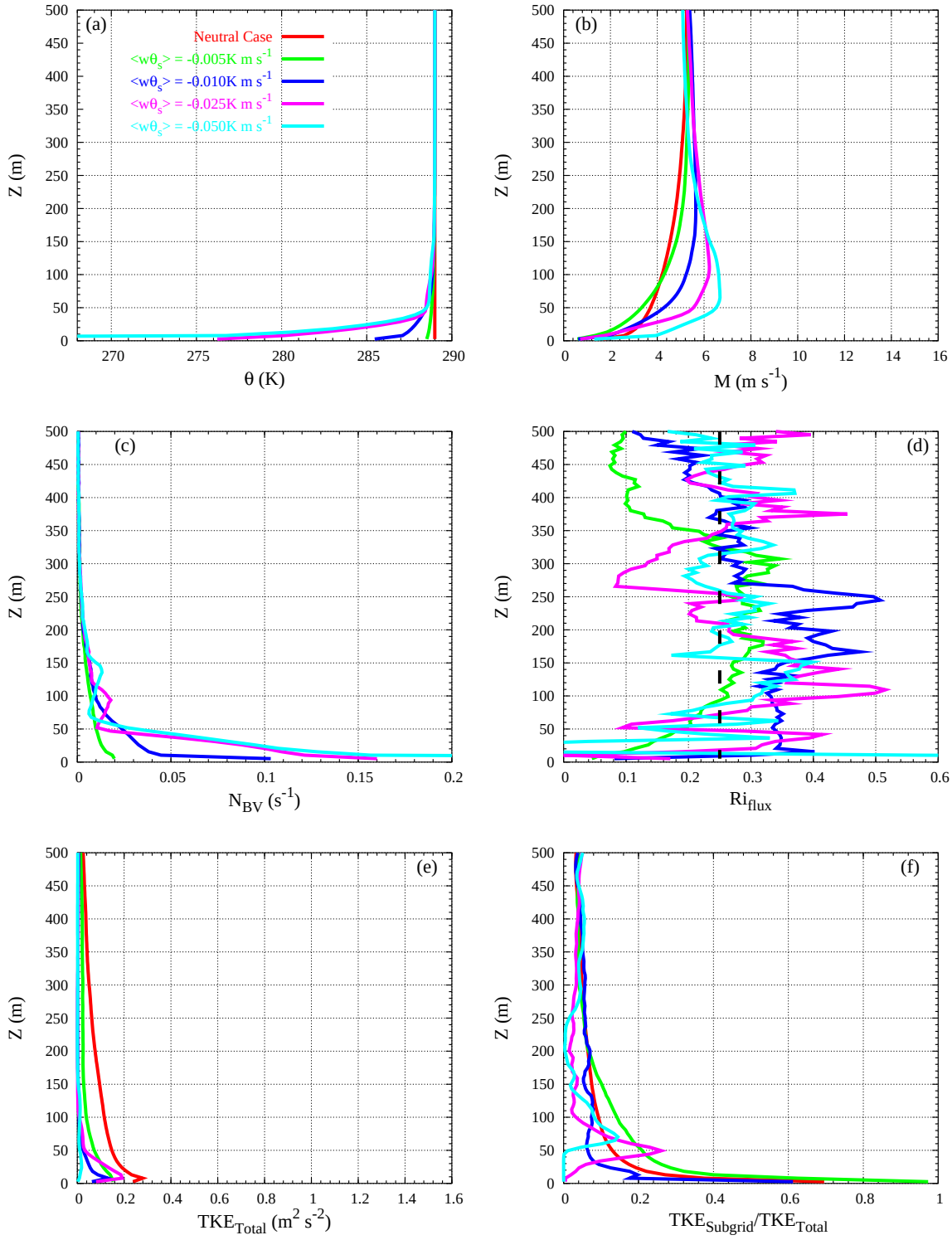

Figure 3.7: Mean profiles for $G = \mathbf{5\ m\ s^{-1}}$ as the surface cooling increases. (a) Potential temperature (K), and (b) Wind speed (m s^{-1}) (c) Brunt-Väisälä frequency (s^{-1}), (d) Flux Richardson number (adimensional), (e) Total (resolved + subgrid) Turbulent Kinetic Energy (TKE) (m^2 s^{-2}) and (f) ratio between $TKE_{Subgrid}$ and TKE_{Total}

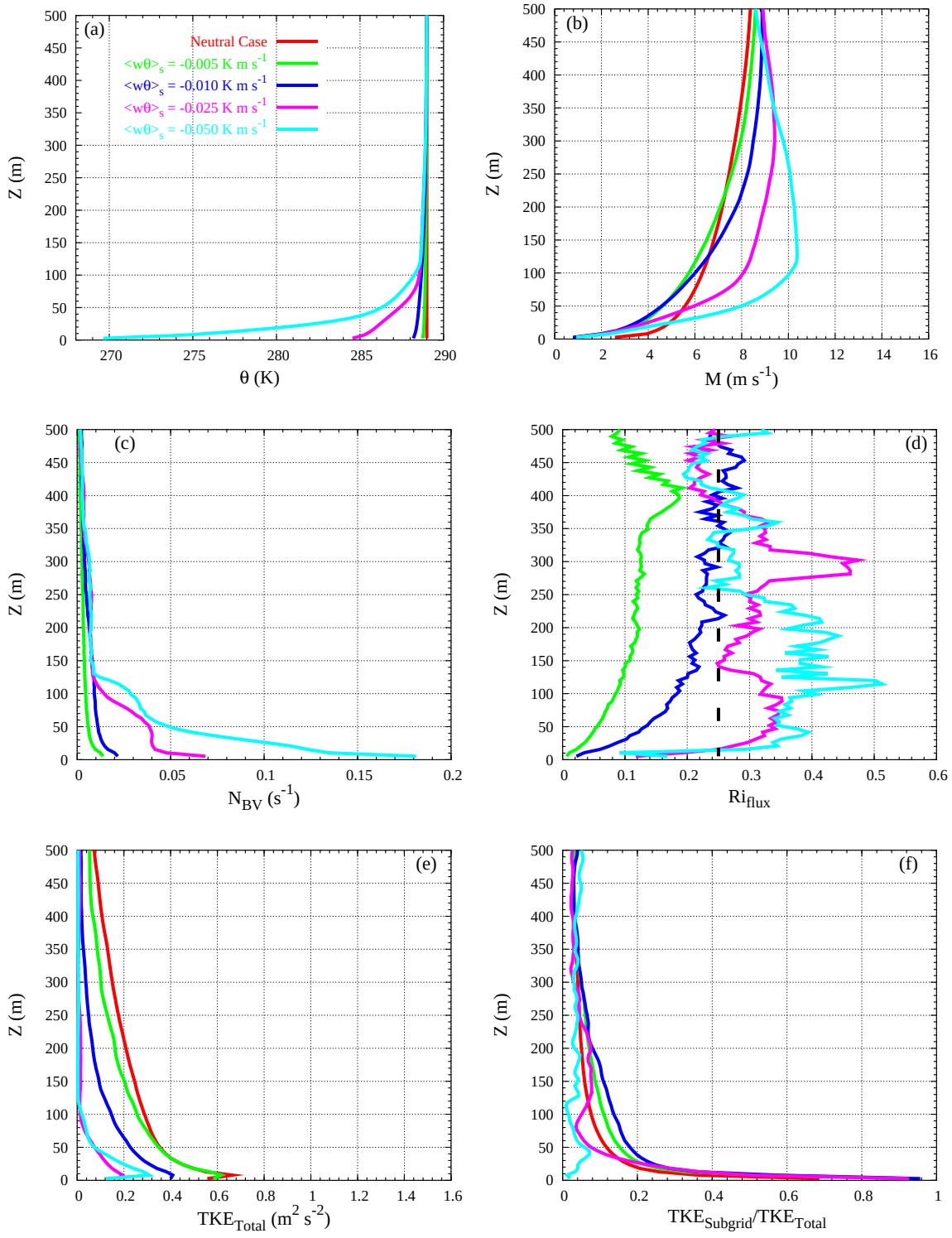

Figure 3.8: Mean profiles for $G = \mathbf{8\ m\ s^{-1}}$ as the surface cooling increases (as in Figure 3.7)

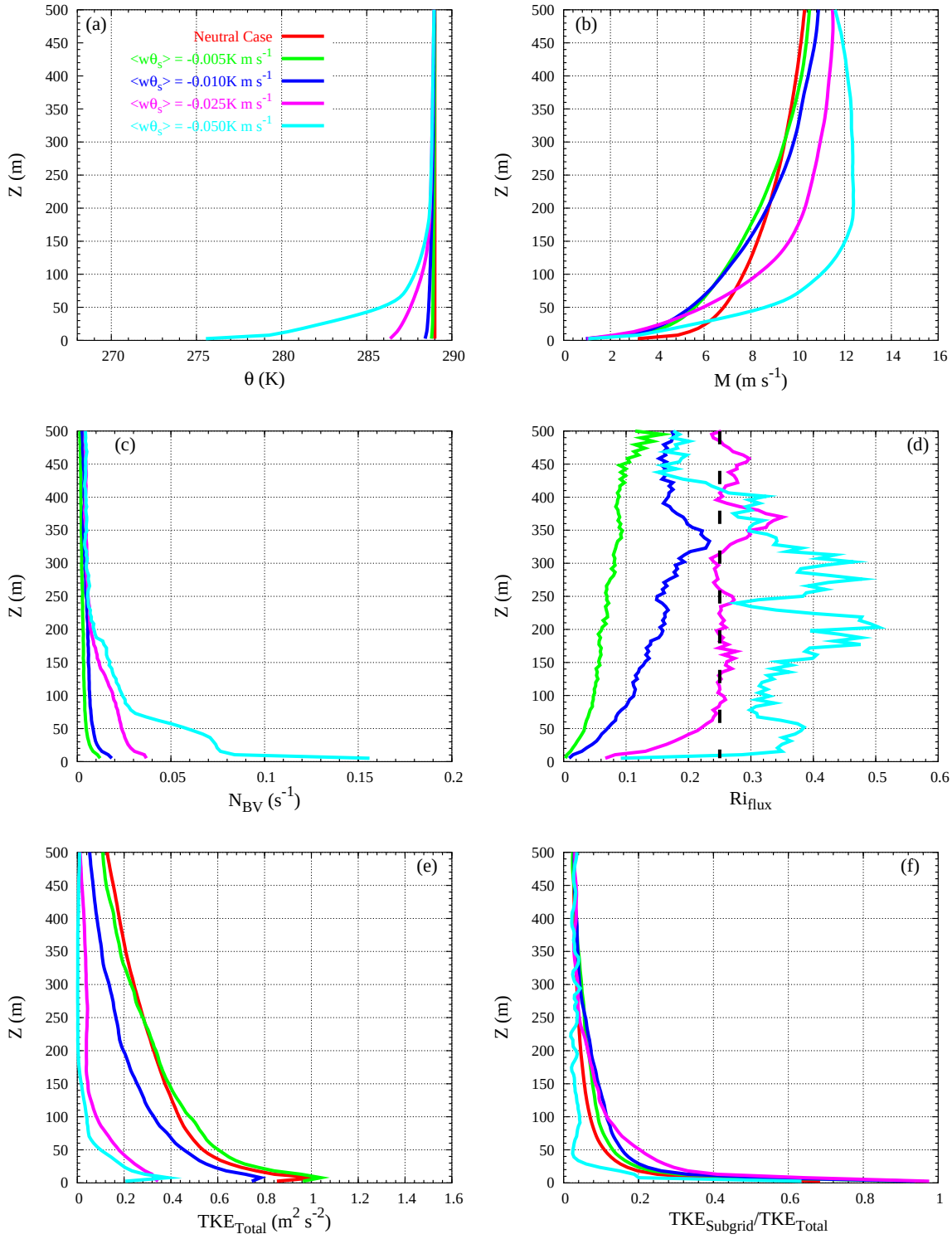

Figure 3.9: Mean profiles for $G = \mathbf{10\ m\ s^{-1}}$ as the surface cooling increases (as in Figure 3.7)

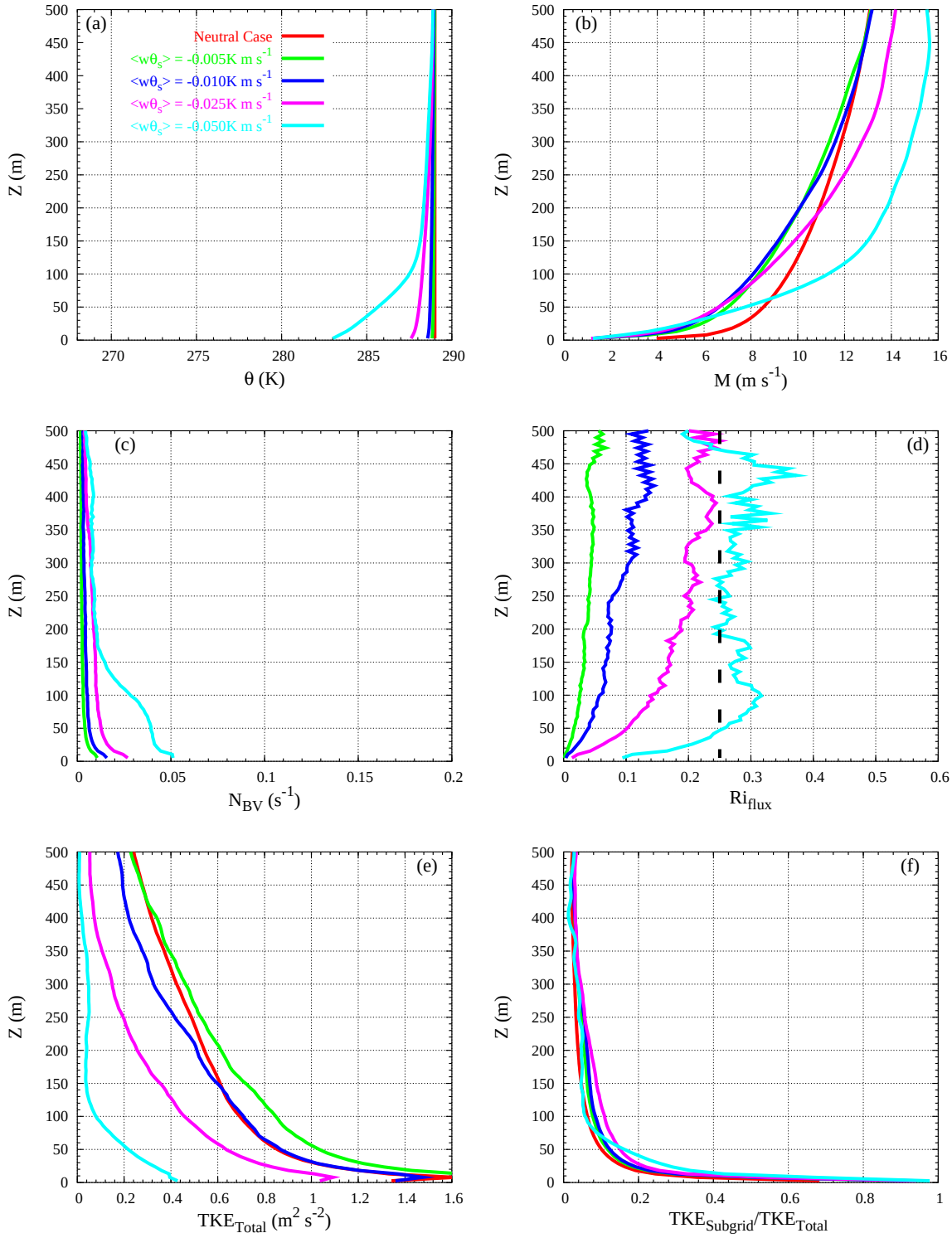

Figure 3.10: Mean profiles for $G = \mathbf{13\ m\ s^{-1}}$ as the surface cooling increases (as in Figure 3.7)

$\overline{w'\theta'}$ the total fluxes.

The Brunt-Väisälä frequency (N_{BV}) is defined as the maximum frequency that waves can have in these conditions. Higher stabilities near the surface support a larger range of frequencies than those higher in the SBL. In a residual layer of neutral stratification, vertically propagating waves are not supported. Waves that propagate upward within the SBL eventually reach the level where their frequency matches the ambient Brunt-Väisälä frequency, at which point they reflect back down toward the ground. Waves within the SBL are thus trapped between the ground and the neutral layers above, resulting in horizontally propagating waves. In the simulations, N_{BV} is maximum near the ground decreasing with height (Figures 3.7.c, 3.8.c, 3.9.c and 3.10.c). Above the inversion layer N_{BV} is close to zero. Consequently, the waves will propagate within the SBL but not above it. On the other hand, N_{BV} increases when the stability is stronger since the turbulence activity is larger. The sensitivity of the shear on the Brunt-Väisälä frequency is also inspected. Since the most stable conditions correspond to smaller G (for a given cooling) the Brunt-Väisälä frequency is larger for these cases. It is worth mentioning that runs that suffer from runaway cooling have large Brunt-Väisälä frequency, especially near the ground.

The flux Richardson number (Ri_f) is the fraction between the buoyant and mechanical terms from the TKE equation and it is an indicator of the turbulence. If $Ri_f < Ri_{fc}$ the flow is turbulent whereas when $Ri_f > Ri_{fc}$ it becomes laminar. For a given G, Ri_f increases with the stratification, becoming closer to Ri_{fc}. Runs that suffer from runaway cooling have Ri_f values larger than Ri_{fc} meaning that the flow becomes laminar.

Regarding the turbulent quantities, for a given G, it is found that the total TKE is maximum near the ground because of the shear but decreases with height. It is also important to notice that in the first computation level $TKE_{TOT} = TKE_{SBG}$ because all the contribution is coming from the turbulence scheme. TKE_{TOT} and TKE_{SBG} decreases as the stability increases, corresponding to and increase of $< w'\theta' >_s$ for a fixed G or to a decrease of G for a fixed $< w'\theta' >_s$.

For the strongest stability TKE_{SBG} is equal to zero because the model is not able to sustain those forcings and then the SGS collapses. This is in good agreement with the behaviour of Ri_f since the turbulence is completely destroyed and the flow becomes laminar.

On the other hand, the profiles for $< w'\theta' >_s$ = -0.010 K m s^{-1} as G varies are shown in Figure 3.11. When the geostrophic wind decreases, the shear is reduced and consequently the SBL is more stable. Then the surface temperature decreases with G. The height of the inversion layer also decreases with the stability because of the suppression of the

motion in stably stratified conditions (see Figures 3.5 and 3.6).

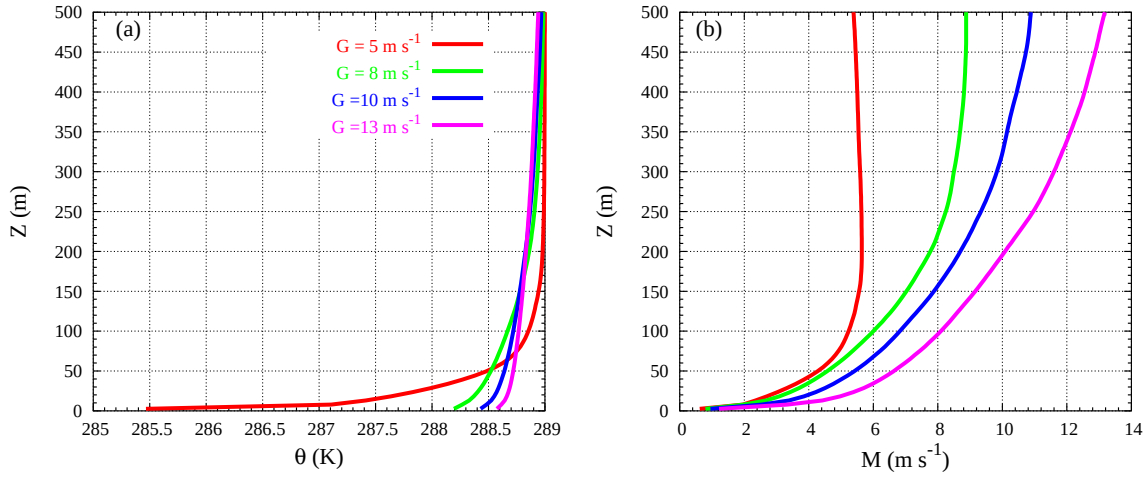

Figure 3.11: Mean values for $< w'\theta' >_s$ = -0.010 K m s^{-1} as the geostrophic wind increases. (a) Potential temperature (K), and (b) Wind speed (m s^{-1})

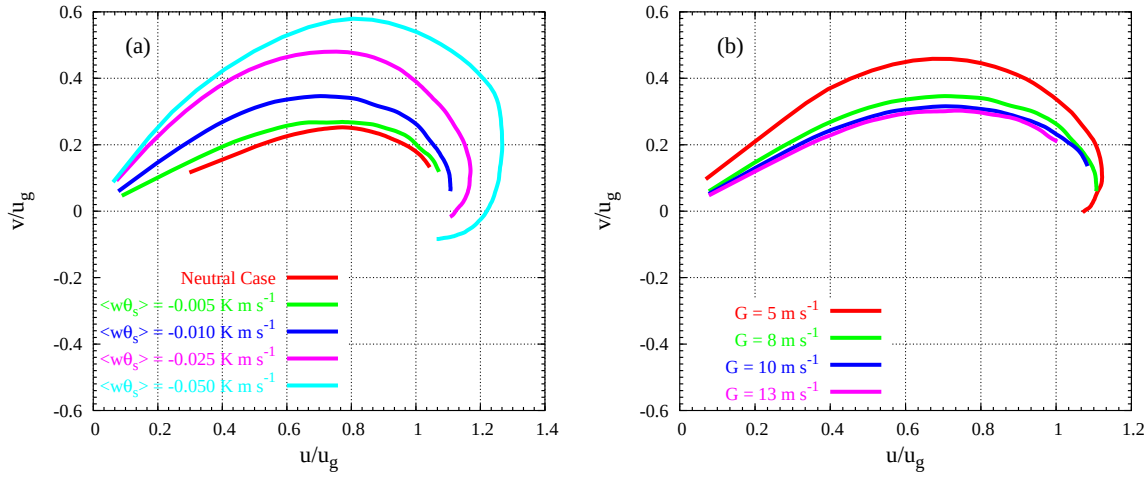

Figure 3.12: Normalized Ekman spirals for (a) G = 8 m s^{-1} as the vertical temperature flux increases and (b) $< w'\theta' >_s$ = -0.010 K m s^{-1} as the geostrophic wind increases

The Ekman spirals obtained for G = 8 m s^{-1}, as cooling increases and those obtained for a fixed $< w'\theta' >_s$ = -0.010 K m s^{-1} as the geostrophic wind changes are shown in Figure 3.12. As for the LES of the SBL results in Kosović and Curry (2000), the angle between the low-level wind vector and the geostrophic wind is approximately 30°, smaller than the angle of 60° that was predicted by Nieuwstadt (1985). Nevertheless, when the stability increases (Figure 3.12.a) this angle tends to the one predicted by Nieuwstadt's model. Within the SBL, when the shear is stronger near the ground, the boundary layer

height decreases and the angle between the low-level wind vector and the geostrophic wind is larger. Similar results are found in Svensson and Holtslag (2005, Figure 4) for 1D modelling. On the other hand, this angle does not change significantly when the geostrophic wind increases, for a given surface vertical temperature flux (Figure 3.12.b).

3.5 Turbulence within the Stable Boundary Layer

The total and subgrid TKE can be an indicator of the turbulence within the SBL. The percentage between the vertically integrated subgrid and total TKE (e/E) is computed for each simulation (Table 3.3). As a percentage, this ratio is expected to increase as the stability is stronger for a fixed resolution, since then the turbulent eddies will be of smaller size (Figures 3.5 and 3.6). Here this would correspond to a decrease in the geostrophic wind (reducing shear production of TKE) and to an increase of the surface cooling flux (increasing stratification). The values in italics and in bold correspond to a decrease in this percentage whereas the ones in bold correspond to cases that suffer runaway cooling (Figure 3.2) and not fulfil the Derbyshire criterion.

Table 3.3: **Percentage of the vertically integrated TKE_{SBG} divided by the TKE_{TOT} for each simulation. In bold and italics simulations with decreasing e/E with increasing stabilisation; those in bold suffer runaway cooling**

	13 m s^{-1}	10 m s^{-1}	8 m s^{-1}	5 m s^{-1}
Neutral	8.67	9.63	10.31	12.20
-0.005 K m s^{-1}	11.47	13.13	15.44	19.59
-0.010 K m s^{-1}	12.39	15.84	20.57	*13.55*
-0.025 K m s^{-1}	16.48	21.88	*20.83*	**6.19**
-0.050 K m s^{-1}	22.12	**12.15**	**3.82**	**4.41**

The resolved and subgrid contributions for a weakly and a moderately stable case are shown in Figure 3.13. As Table 3.3 indicates, the relative contribution of the subgrid part for TKE and $< w'\theta' >$ increases with stratification. This is because the eddies are smaller when the stability increases and consequently the subgrid contribution is also larger.

From the TKE budget it is possible to explain physically the contribution of each term of the Equation 2.8. In Figures 3.13.a and 3.13.b there are the resolved contribution of the TKE budget terms for a weakly and a moderately stable case. The terms in Equation 2.8 mean: (1) the tendency of TKE, (2) the shear production, (3) the turbulent transport, (4) the buoyancy production or destruction depending whether the heat flux is positive or negative, (5) the pressure correlation term that describes how TKE is redistributed by pressure perturbations and (6) the residual. The normalized resolved TKE budgets

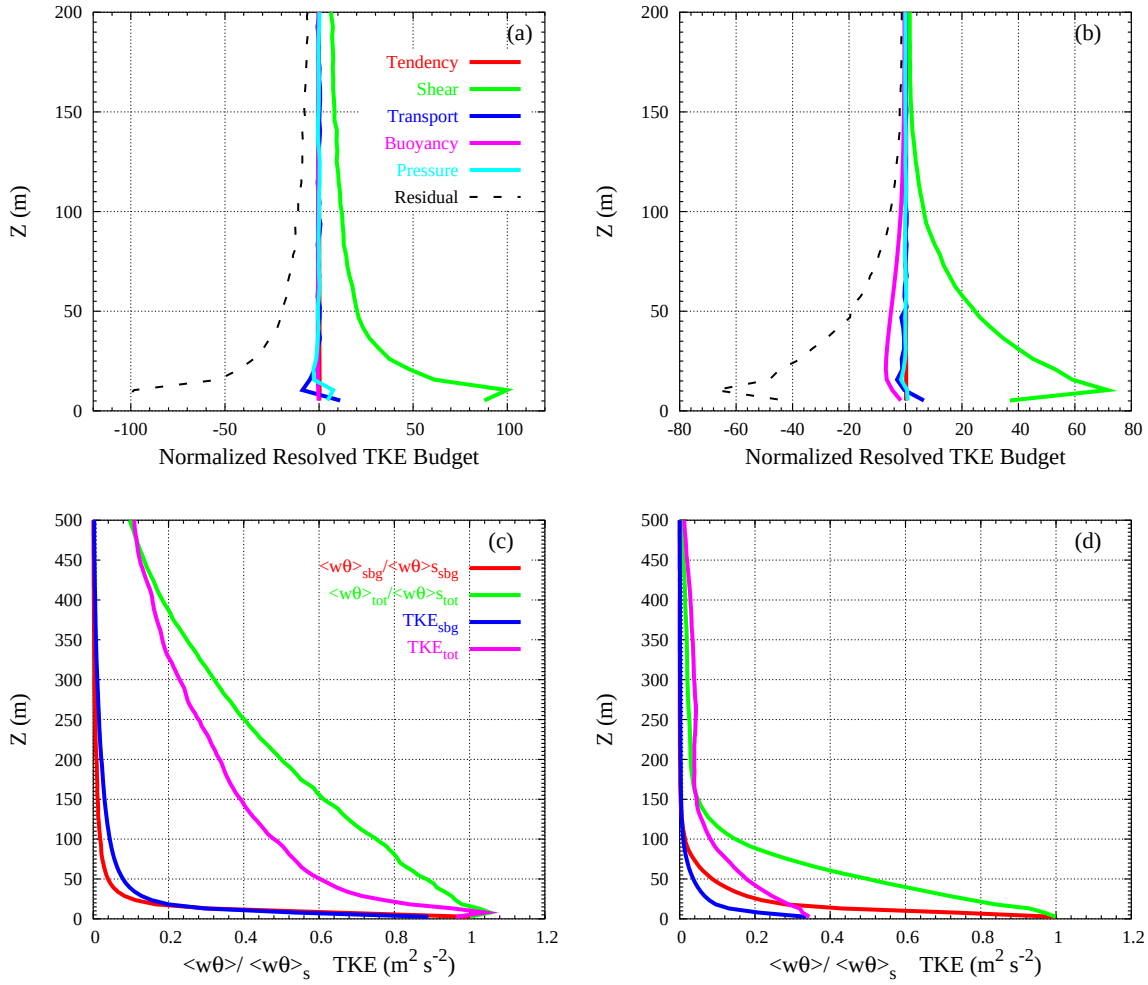

Figure 3.13: (a) Resolved TKE budget (normalized by u_*^3/h_{BL}) for $z/L = 0.013$, (b) same as (a) for $z/L = 0.321$. (c) Total and subgrid TKE and vertical heat fluxes (normalized by the surface value, $< w\theta >_s$) for $z/L = 0.013$, (d) same as (c) for $z/L = 0.321$

show that the only production factor of turbulence in both cases is the shear production, and the destruction is mainly performed by the dissipation (here approximated by the residual). The buoyancy destruction is only significant for the moderately stable case. This destruction factor makes the energy smaller as the stability is stronger (Figures 3.7.e, 3.8.e, 3.9.e and 3.10.e).

3.6 Testing the resolution

One fundamental question in the LES modelling of the SBL is to know if an increase of the resolution would imply a better behaviour of the model, just by shifting the characteristic grid size closer or into the inertial subrange. A higher resolution run (HR) (450×300×1439 m in x, y and z directions with 128×128×168 points; resolution of 3.52×2.34×2.9 m in each direction) has been made for the case with imposed geostrophic wind at 5 m s^{-1}.

The results for a HR (Figure 3.14) are very close to the ones obtained in the lower resolution (LR). Figures 3.1 and 3.2 show that all the different cooling runs for the case of $G = 5$ m s^{-1} suffer from runaway cooling, due to the inadequate prescribed surface boundary condition, except the first section ($< w'\theta' >_s$ = -0.005 K m s^{-1}). The same behaviour is found when the resolution increases and the cases that present runaway cooling at LR still suffer from it at HR.

Nevertheless, the HR generates more stable conditions near the surface than the LR (i.e. $z/L = 0.280$ for the HR instead of the value for LR, $z/L = 0.202$) because the cooling in the first level is slightly larger (Figure 3.14.a). The HR run have larger shear and also a more intense maximum of the wind (Figure 3.14.b). Besides, the TKE_{TOT} for the HR is smaller than for the LR since the stability is larger (Figure 3.14.c). The TKE_{SBG} is also smaller because the contribution of the smaller scales is reduced when the resolution is increased (Figure 3.14.d).

The mechanism of failure of the model seems to be related with an increase of the buoyancy destruction which is not compensated by any production factor (either resolved or subgrid), and although the dissipation is reduced the prescribed Kolmogorov theory could be of no application for this range of stabilities. Nevertheless, the imposed surface flux is slightly above the value of Derbyshire for R_{fc} up to 0.25, and this may indicate that the model is forced with inappropriate lower boundary conditions. Furthermore, the spectral analysis described in the next section show that even for the HR the inertial subrange is beyond the resolution considered.

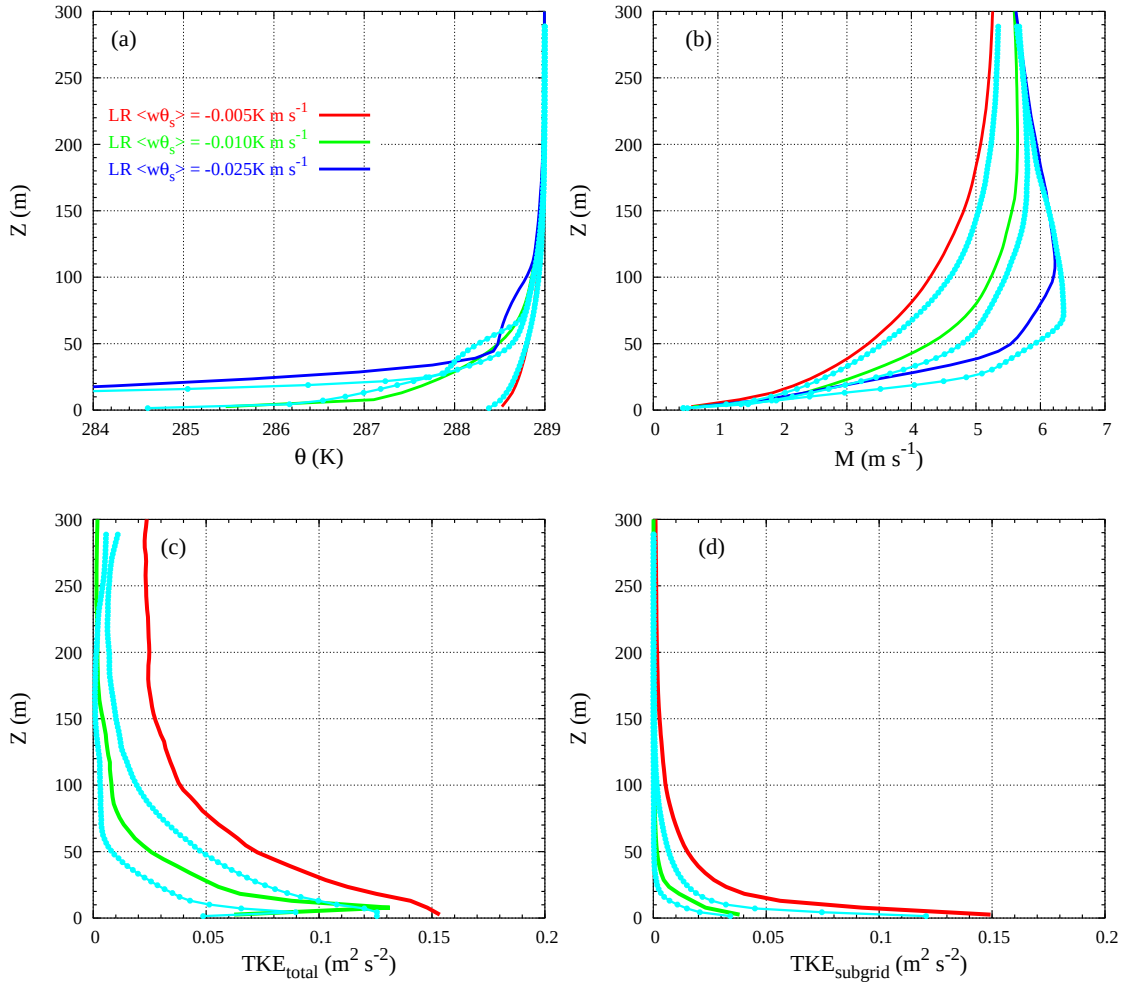

Figure 3.14: Mean values for the LR (lower resolution, $\Delta = 5$ m) and HR (high resolution, $\Delta = 3$ m, lines and points in light blue) for $G = 5$ m s^{-1} as the surface cooling increases. (a) Potential temperature (K), (b) wind speed (m s^{-1}) and (c) total and (d) subgrid Turbulent Kinetic Energy (TKE) (m^2 s^{-2})

3.7 Spectral analysis

To generate spectra, data from the entire horizontal domain are used. The analysed spectra are computed at a height of 40 meters, located inside the surface cooling inversion.

As discussed by Adams and Stoltz (2002), in the spectra of the LES models an approximation error of order unity exists for wavenumbers close to the Nyquist wavenumber K_N. Therefore, spectra should only be inspected until a cut-off wavenumber K_c, for which the error can be considered small enough; they obtain it through comparison between LES and DNS (Direct Numerical Simulations). A value of $K_c/K_N = 1/2$ is suggested. For our standard resolution simulations (LR), with $K_N = 48$, we have $K_c = 24$ corresponding to 25 m in the downwind direction and to 16.7 m in the crosswind direction. Therefore,

below these numbers it is better not to extract conclusions from the spectra.

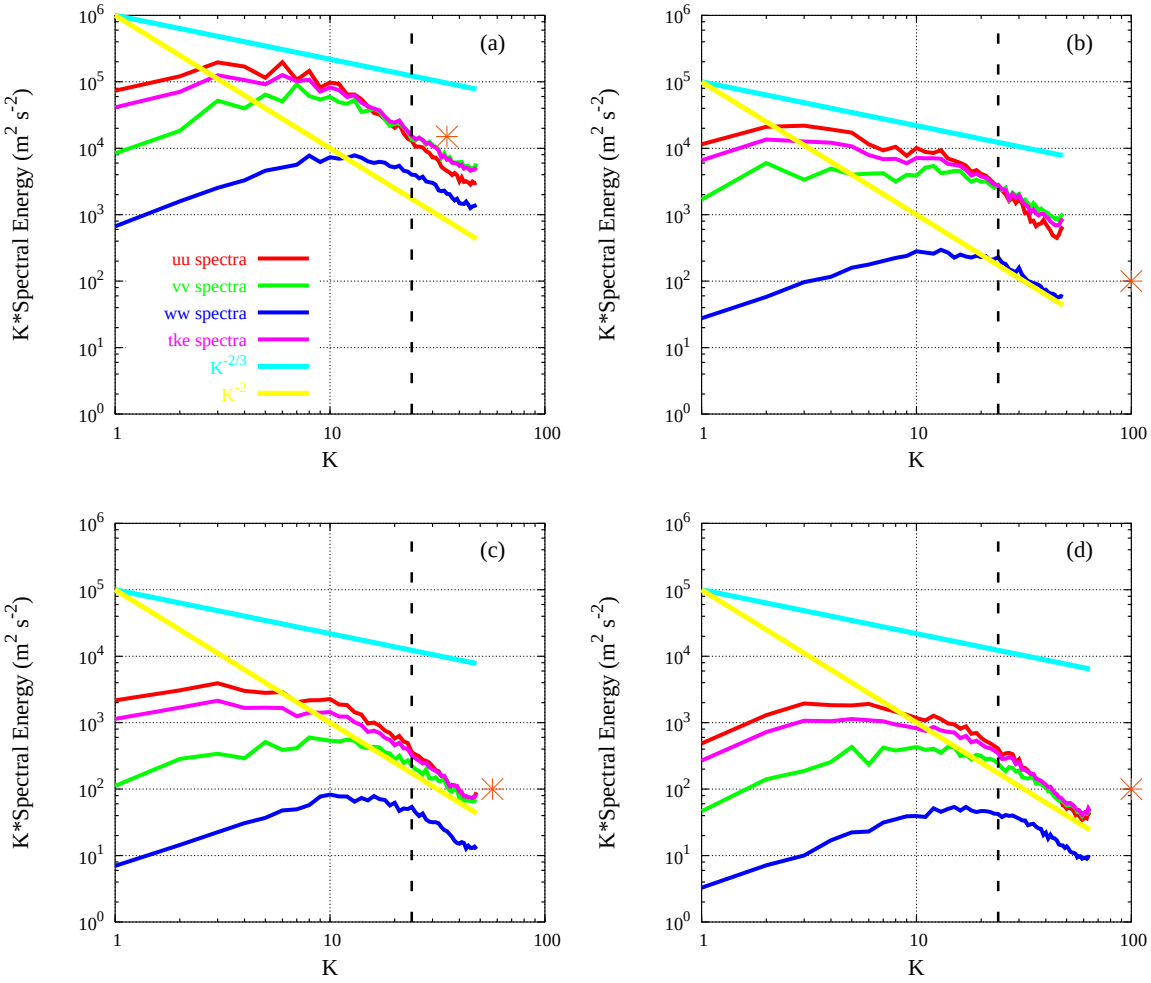

Figure 3.15: Crosswind spectra of resolved $< u'u' >$,$< v'v' >$,$< w'w' >$, and TKE at 40 m. The asterisk represents the Ozmidov scale and the vertical discontinuous line the cut-off wavenumber.(a) $z/L = 0.059$, (b) $z/L = 0.321$, (c) $z/L = 0.202$ (LR) and (d) $z/L = 0.280$ (HR). The buoyancy and the inertial subranges are also indicated with the (-2) and (-2/3) slopes respectively

In Figure 3.15 the spectra for a weakly stable case ($z/L = 0.059$) and a more stable case ($z/L = 0.321$), as well as the spectra for the LR and HR are shown. No sign of the inertial subrange is found, and the slope is closer to the characteristic value of the buoyancy subrange (-2). However, at a height of 40 m, with strong shear generation of turbulence, it is difficult to find a pure buoyancy subrange (Garratt, 1992). The asterisk indicates the estimated value of the Ozmidov scale (L_{oz}) (Ozmidov, 1965), used here as an indication of the upper limit of the inertial subrange. It is defined as:

$$L_{oz} = \sqrt{\frac{\epsilon}{N_{BV}^3}} \tag{3.5}$$

where ϵ is the dissipation and N_{BV} is the Brunt-Väisälä frequency. For the weakly stable case (Figure 3.15.a), L_{oz} is closer to the cut-off wavenumber, but it is definitely out of reach for the more stable cases, even if a substantial increase of the resolution was performed.

The spectral energy of the eddies in the weakly stable case is larger than in the more stable cases where the motions are suppressed. This is in good correspondence with Table 3.3. The spectra also highlight the anisotropy of the field. The spectra for $< u'u' >$ or $< v'v' >$ is much more energetic than the spectra for $< w'w' >$, for a given stability. This is especially found in the most stable cases since the anisotropy is larger.

3.8 Testing the prescribed surface boundary condition

The previous discussion has been valid only for the case of fixed surface heat flux. The fact that no feedback is allowed between the soil and the atmosphere may raise the question of the representativeness of these simulations. There is observational evidence that turbulent bursts during the nocturnal SBL can reduce or eliminate statically stable layers, accompanied by a temperature change in the near-surface soil (Soler et al., 2002). This behaviour was linked to a change in the value of the surface heat fluxes.

A sensitivity study has been made using a very simple energy budget equation, the same as in Van der Wiel et al. (2002), where the three terms that balance are the turbulent heat flux (H_0), the flux from the soil and the longwave radiative flux (Q_{net}).

$$\frac{\partial T_s}{\partial t} = \frac{1}{C_v}[Q_{net} - H_0 - \frac{\lambda_m}{\delta_m}(T_s - T_M)] \tag{3.6}$$

This equation needs the dynamic input of the air temperature and the wind provided by the LES, uses a deep soil temperature (T_M) of 300 K, and a bulk conductance (λ_m/δ_m) of 3.5 W m^{-2} K^{-1}. These values provide a flux around -0.025 K m s^{-1}, when $G = 10$ m s^{-1}. The equation set solves iteratively for surface temperature. Further details of Equation 3.6 are found in Van der Wiel et al. (2002).

By this method, the heat flux balance is calculated for every point of the domain. Then, the average value of the flux is used as a single value for the whole domain. In Figure 3.16.a, the temporal evolution of the horizontally-averaged heat flux at the first model level is shown for the run with the energy budget equation and the run with surface

heat flux prescribed to -0.025 K m s^{-1}, both starting from the same initial conditions and G = 10 m s^{-1}. It can be seen that both simulations converge after about half-an-hour. The spectra (Figure 3.16.b) also point out that the structures in both simulations are very close.

Figures 3.16.c, 3.16.d and 3.16.e show the hour-2 average profiles for the potential temperature, the wind speed and TKE for the energy budget equation run and the prescribed surface heat flux run. The averaged profiles are also very close to each other.

If this run using an energy budget equation is extended two more hours instead of applying the next cooling flux ($< w'\theta' >_s$ = -0.050 K m s^{-1}) there is not runaway cooling (Figure 3.17.a). This is because in the energy budget equation run $< w'\theta' >_s$ is never larger than the one predicted by Derbyshire. Besides, the model seems to reach a stationary state with a surface cooling about $< w'\theta' >_s$ = -0.024 K m s^{-1} far above than the maximum predicted by Derbyshire for G = 10 m s^{-1} (Figure 3.1).

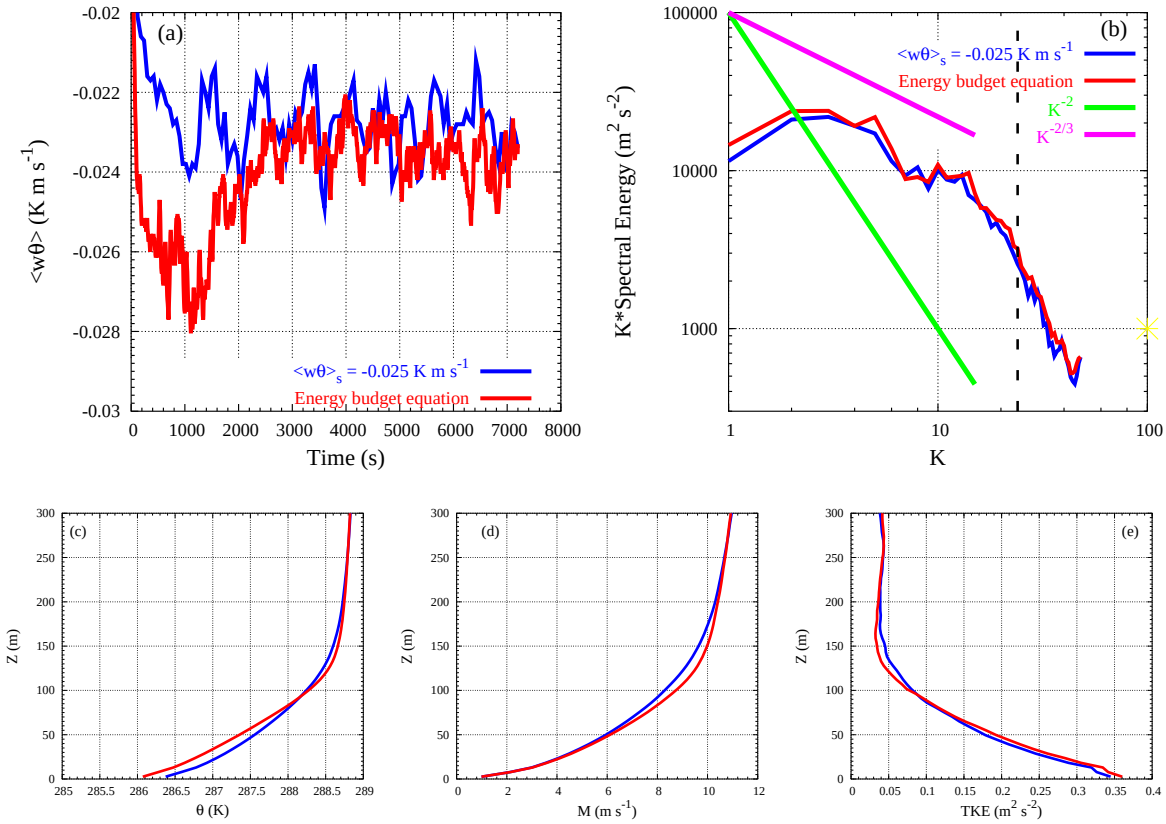

Figure 3.16: Comparison for the energy budget equation run and the simulation with G = 10 m s^{-1} and $< w'\theta' >_s$ = -0.025 K m s^{-1}. (a) $< w'\theta' >_s$ time series, (b) TKE spectra (symbols as in Figure 3.15) and profiles for (c) potential temperature (K), (d) wind speed (m s^{-1}) and (e) TKE (m^2 s^{-2}). The energy budget equation runs are plot using red lines whereas the runs for a prescribed surface vertical temperature flux of -0.025 K m s^{-1} are in blue lines

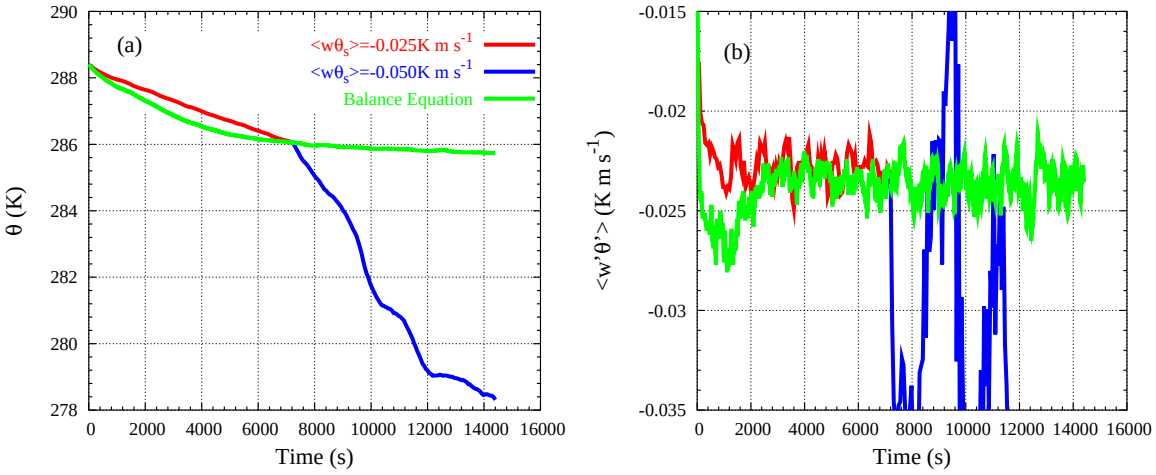

Figure 3.17: Comparison for the energy budget equation run and the simulation with G = 10 m s^{-1} and $< w'\theta' >_s$ = -0.025 K m s^{-1} and -0.050 K m s^{-1}. (a) Potential temperature at the first computation level (K) and (b) vertical temperature flux (K m s^{-1}) at the first computation level. Prescribed surface boundary condition runs are in blue and red whereas those obtained using an Energy budget equation in green

Thus, we conclude that the use of fixed $< w'\theta' >_s$ does not diminish significantly the applicability of the results if the imposed flux is observable according to the Derbyshire's formula. Nevertheless, further tests would be needed in order to explore the behaviour of the model at stronger fluxes, close or beyond Derbyshire's limits, as well as different forcings to reach more stable conditions.

3.9 Testing the radiation

In previous sections it was shown that the surface temperature cools down in stably stratified conditions. This near-the-surface cooling can be influenced by the radiative flux divergence through the upward and downward longwave fluxes, as it was shown in Mahrt et al. (1979), Garratt and Brost (1981) or in André and Mahrt (1982) using data from Wangara (Clarke et al., 1971). More recently, Duynkerke (1999b) studied the contribution of the cooling (due to turbulence or radiation) using data from Cabauw (The Netherlands) and Nakanishi (2000) reproduced the results through LES.

The cooling rate at the surface is dominated by radiative effects, and controlled by the surface energy balance equation. Likewise, the cooling rate at the top of the SBL and above, where the turbulence is negligible, is mainly determined by radiative cooling. Therefore, Garratt and Brost (1981) suggest that the SBL has a three-layer structure so far as cooling is concerned:

(i) the first, or bottom, layer coincides with the surface layer ($z < 0.1h$ where h is the boundary layer height) and it is dominated by radiation;

(ii) throughout most of the SBL ($0.1h < z < 0.8h$), turbulent cooling dominates and the potential temperature profile is nearly linear;

(iii) the uppermost part of the SBL ($0.8h < z < h$) is dominated by radiative cooling.

Furthermore, when the radiation is not considered, the $< w\theta >$ profile is linear. In presence of radiation, when the longwave flux divergence cannot be ignored, constancy of total cooling with height, particularly near the surface where radiative cooling increases rapidly upwards, may actually require turbulent warming near the surface. The result is a low-level maximum in $< w\theta >$, as revealed in both model simulations (Garratt and Brost, 1981) and observations (Izumi, 1971).

When the radiation is considered, the SBL is less stable since the surface temperature does not cool down as much as before. As a result the boundary layer height increases about 25% (Mahrt et al., 1979). Moreover, the radiation is more important when the winds are weak since the shear is reduced and therefore the turbulence. In these cases, the radiation contribution might be much more important than the turbulent one. For instance, Estournel et al. (1986) found that in situations with moderate wind (about 5 m s^{-1}) the contribution of radiative cooling was more important than for higher winds.

Meso-NH uses the same radiation scheme as the European Medium-Range Weather Forecast (ECMWF) model and a further description is found in Morcrette (1990). When the radiation scheme is activated, there is a new term in the temperature tendency equation:

$$\frac{\partial \theta}{\partial t} = ... - \frac{\partial \overline{w'\theta'}}{\partial z} + \frac{1}{\rho c_p} \frac{\partial F_N}{\partial z} \tag{3.7}$$

where $\overline{w'\theta'}$ is the vertical temperature flux and F_N is the net longwave radiation (computed as the sum of the upward and downward radiation fluxes).

The sensitivity of the LES results on the radiation scheme are shown in Figures 3.18, 3.19 and 3.20 for the $G = 5$ m s^{-1} case and the first two coolings: $< w\theta >_s$ = -0.005 and -0.010 K m s^{-1} (the last one corresponds to a run that fulfils the Derbyshire criterion). When the radiation effects are considered, the wind speed almost does not change (Figure 3.18.a) whereas the layer is less stable as the temperature profile (Figure 3.18.b) points out. Similar results were found in André and Mahrt (1982) and in Garratt and Brost (1981) where radiative contribution was similar to the turbulent contribution near the surface.

The total TKE is larger within the SBL but the subgrid contribution does not change

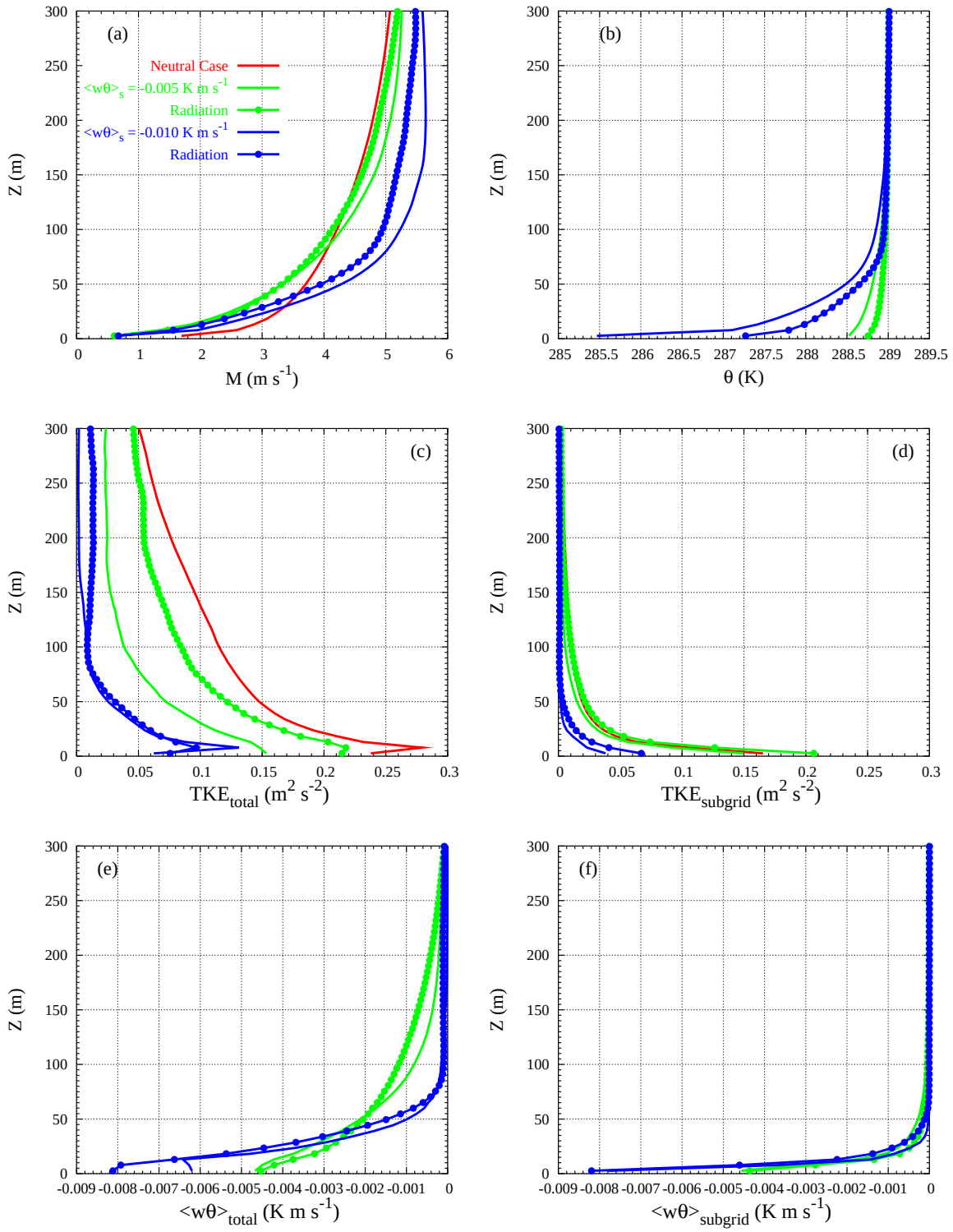

Figure 3.18: Comparison of the profiles considering the radiation scheme (lines and points) and without it (lines) for the G = 5 m s^{-1} case and $< w\theta >_s$ = -0.005 K m s^{-1} and $< w\theta >_s$ = -0.010 K m s^{-1}. The last one suffers from runaway cooling due to the wrong prescribed surface boundary condition according to Figure 3.1. (a) Potential temperature (K), (b) wind speed (m s^{-1}), (c) total and (d) subgrid Turbulent Kinetic Energy (TKE) (m^2 s^{-2}) and (e) total and (f) subgrid $< w\theta >$ (K m s^{-1})

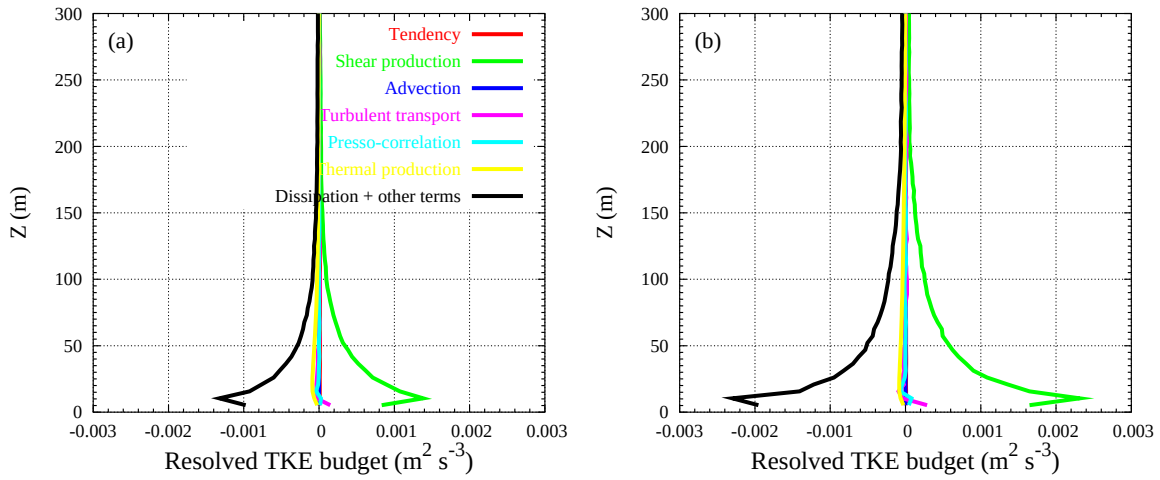

Figure 3.19: Resolved TKE budgets for G = 5 m s^{-1} and $< w\theta >_s$ = -0.005 K m s^{-1}. (a) without considering the radiation and (b) considering the radiation

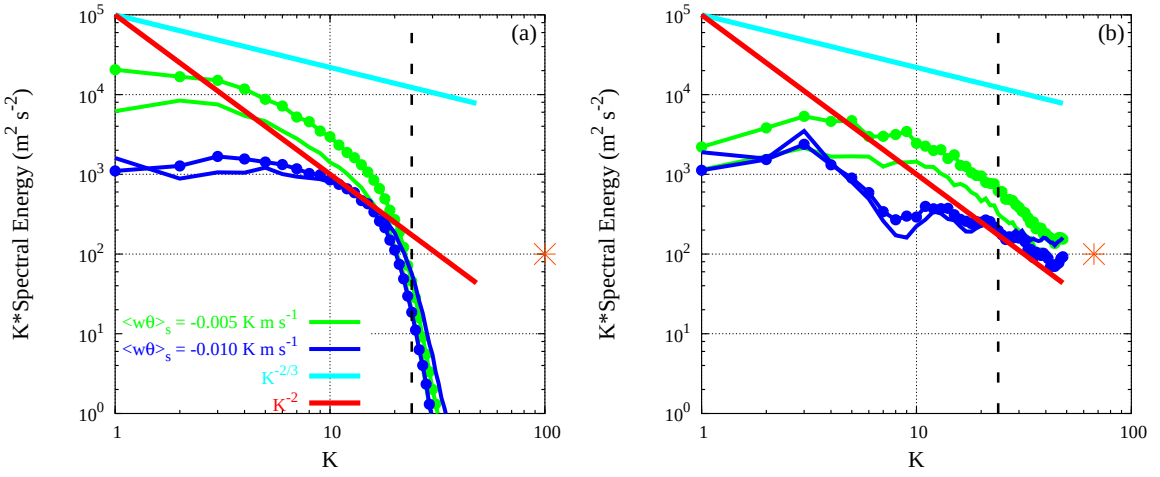

Figure 3.20: TKE spectra at 40 m for the (a) downwind and (b) crosswind directions. The results considering the radiation scheme are plotted in lines and points. The asterisk represents the Ozmidov scale and the vertical discontinuous line the cut-off wavenumber. The buoyancy and the inertial subranges are also indicated with the (-2) and (-2/3) slopes respectively

significantly, although is slightly larger near the surface (see Figures 3.18.c and 3.18.d). Since the profile is less stable when the radiation effects are considered, the turbulence is more intense and therefore there is more TKE. Regarding the vertical temperature flux, the decreasing along the SBL is slower and the major differences occur near the inversion level where there is more vertical temperature flux due to the radiative effects (Figure 3.18.e). This fact might be due to the turbulent cooling is confined within the SBL meanwhile the radiative one is transported through the boundary layer up to the inversion level.

It is also important to notice that the failed simulations according to the Derbyshire criterion still fail when the radiation is considered.

Figure 3.19 shows the sensitivity to the radiation scheme on the resolved TKE budget. There is more resolved energy when the radiation is considered (Figure 3.18.c) and therefore the shear and dissipation to lower scales contributions are larger. Since the radiation effects are also important near the inversion layer the resolved TKE budget tends through the boundary layer to zero much more slowly. Moreover, the turbulent transport becomes relatively important when the radiation is considered.

The TKE spectra for the downwind and crosswind directions are shown in Figure 3.20 as well as the comparison to those obtained when the radiation is not considered. As Figure 3.18.c points out, when the radiation is considered the TKE slightly increases, giving eddies with more spectral energy for any of the directions. Nevertheless, the TKE spectra do not significantly change when the radiation is taken into account.

3.10 Conclusions

To see if the model that uses the standard Kolmogorov theory is able to work under stably stratified conditions, an LES of SBL has been inspected through a surface shear-driven SBL over a flat terrain varying the geostrophic wind and the surface cooling. It is found that the turbulence is mainly generated by shear and that the cases with the greatest stability correspond to weak geostrophic winds and strong cooling.

Following this simulation setup, the model works properly from weakly to moderately stable conditions. When the prescribed surface boundary conditions (geostrophic wind and surface cooling) are not adequate according to the Derbyshire criterion, the model suffers from runaway cooling. When the surface conditions are very stable, the turbulence scheme collapses and the subgrid TKE tends to zero and the model experiences runaway cooling.

From the spectral analysis it is found that, under strong stabilities, the vertical motions

are suppressed and eddies can be very small. Therefore, the chosen resolution is still far away of the inertial subgrange and the application of the Kolmogorov theory is doubtful. Therefore, resolutions of about centimetres should be used here but this is computationally very expensive and nowadays still not affordable. Besides, the largest scales of motion are not included in the LES and for that reason in chapter 8 the SBL is also studied through mesoscale modelling.

It is found that the radiation processes can be important during night conditions. When the radiation is taken the SBL is less stable and the SBL height increases. This is because the radiation transports the cooling from the surface to upper levels, and this effect is more important under more stable conditions.

The LES results of the SBL are highly dependent on the turbulence scheme used. Nevertheless, this sensibility is further explored in chapter 5 were different LES models (some of them use modified turbulence schemes) are run under the same conditions. Finally, to see how realistic are these runs, in chapter 4 they are compared to data from two experimental field campaigns.

Chapter 4

COMPARISON OF THE LES RESULTS TO EXPERIMENTAL FIELD CAMPAIGNS[1]

The LES results of the SBL obtained in the previous chapter here are compared to data from two experimental field campaigns (SABLES-98 and CASES-99). The main objective is to check how realistic these runs are and also to understand better the observations within the SBL.

Since the simulated conditions are simpler than the observed ones, data from the whole campaign are classified into categories. Therefore, the LES profiles are compared to the observed ones for each classification through the inspection of several parameters. The comparison also highlights how difficult is to compare the LES results to observations. Furthermore, all eddy structures and larger scale structures are included in the observations whereas in the LES just a range of the scales are considered (the resolved ones) and only two forcings are applied (the geostrophic wind and the surface cooling).

4.1 The SABLES-98 and CASES-99 campaigns

The Stable Atmospheric Boundary Layer Experiment in Spain-1998 (SABLES-98, Cuxart et al., 2000b) took place during September 1998 on the Northern Spanish Plateau. This region comprises the Duero River Basin, a broad, flat region almost completely surrounded by mountain ranges over 100 km distant. The main objective of this campaign was

[1]This chapter is based on:Jiménez, M.A., and Cuxart, J., 2005: Large-eddy Simulations of the Stable Boundary Layer: study of applicability using experimental data, *Boundary-Layer Meteorology*, **115**, 241-261.

to study the SBL of mid-latitudes. During the 14 experimental days, different static stabilities were sampled, ranging from near neutral to very stable during the 12 hour-long nights. In this work, data from the 100 meter tower are used for intercomparison purposes, mainly using 5-minute averages of temperature, wind and turbulent correlations (in the latter case data are available only at 6, 13 and 32 m). In Figure 4.1 the levels of measurements are plotted.

The second experiment, the Cooperative Atmosphere-Surface Exchange Study-1999 (CASES-99, Poulos et al., 2002) was held in October 1999 in southeastern Kansas, in the Great Plains of the USA. The objective of this campaign was to study the dynamics of the SBL and its transition with a large number of instruments: array of towers, aircraft, tethered balloons... The nights were about 13 hour-long, and the winds were, in general, stronger than for the SABLES-98 campaign. The tower was 60 meter high and very densely instrumented (see Figure 4.1). As for SABLES-98, standard on-line 5-minute averages are taken for our comparison purposes.

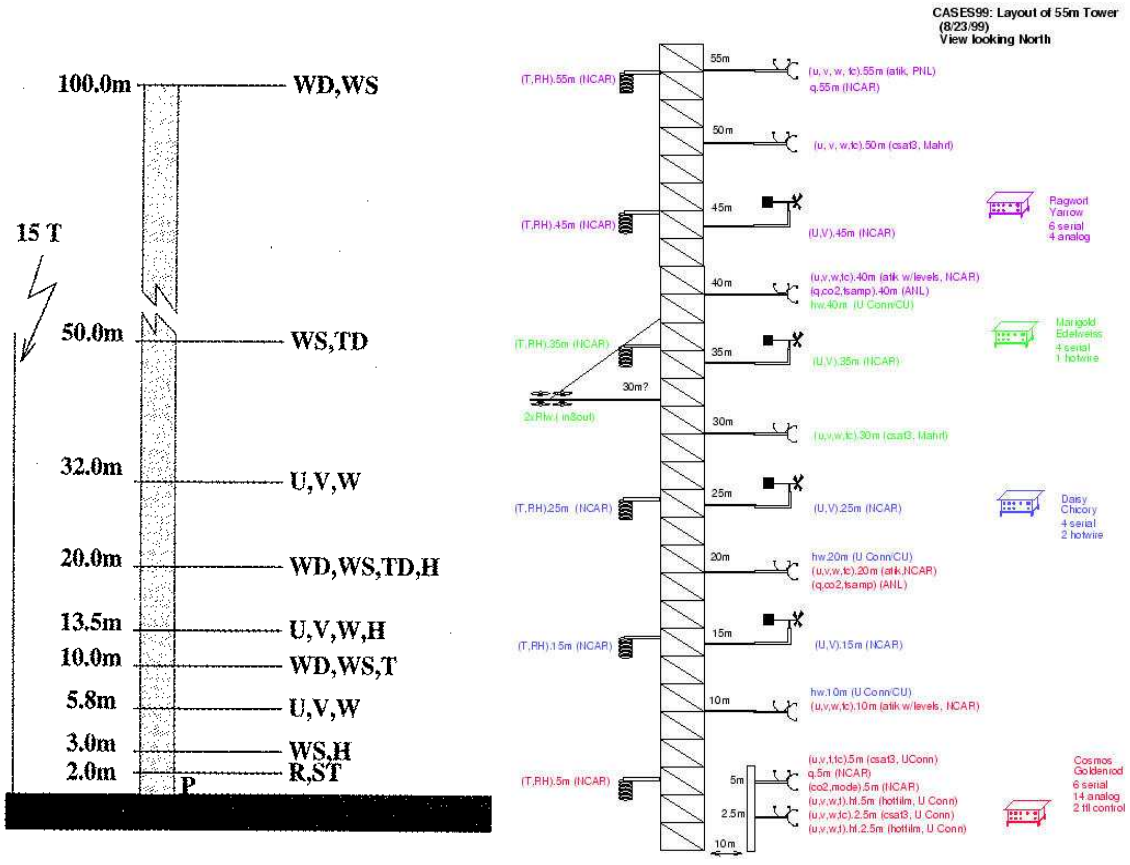

Figure 4.1: Schematic diagram of the levels where the data are captured for the SABLES-98 (left) and the CASES-99 (right) campaigns

4.2 Classification of the data for the comparison purposes

Only the data comparable to the simulated conditions are extracted from the data base: night-time conditions, no rain with humidity below 60 %. Data voids, rainy periods (three days at the end of both campaigns) or questionable data periods are not included in the statistics. Using these criteria, we obtain 1920 5-minute averages from the SABLES-98 data base and 2460 5-minute averages from the CASES-99 dataset.

It is important to notice that these data from the two considered campaigns are single point measurements, usually averaged over 5 minutes. On the contrary, the LES statistics represent an average over the horizontal domain and then over a period of time (in this case, the LES results are averaged over 1 hour). Then, we are trying to compare 5-minute averaged data to 1 hour and horizontal domain averaged data. On the other hand, these LES results do not exactly represent the observed conditions, where the effects of all scales are present, since the observed external forcings are not included. Very often, low-level jets, gravity currents, internal waves and other phenomena are present in the atmosphere and change the characteristics of the SBL. Usually these phenomena imply the existence of turbulence generated at upper levels (Mahrt, 1999) and intermittency. In the LES runs described in the previous chapter, no external forcings other than the geostrophic one are applied, but the data includes other forcings such as the topographic effects, which depend strongly on the location.

Considering the limitations to compare the LES results to observations, the whole data from both campaigns are classified through two different classification parameters. In the first one, the data are classified according the vertical temperature flux in the first computation level and the wind at 50 m, since the geostrophic wind value is not directly available in any of the two data bases. In the other one, data are classified according to the stability parameter z/L.

4.2.1 Wind and vertical temperature flux classification

In this case, data from the CASES-99 and SABLES-98 experiments have been classified within our sampled parameter space (the geostrophic wind and the surface vertical temperature flux). First of all, the 5-minute average surface heat fluxes (at 1.5 m for CASES-99 and at 6 m for SABLES-98) are classified in ranges of $< \overline{w'\theta'} >$ according to Table 4.1.

To complete the classification, a separation has to be made according to the value of

Table 4.1: **Surface cooling flux ($< w\theta >_s$) ranges considered to classify the data from the SABLES-98 and CASES-99 campaigns according to the forcings used in the LES runs**

Runs	range of $< w\theta >_s$
Neutral	(- 0.001, 0.001) K m s^{-1}
- 0.005 K m s^{-1}	(- 0.007, - 0.001) K m s^{-1}
- 0.010 K m s^{-1}	(- 0.015, - 0.007) K m s^{-1}
- 0.025 K m s^{-1}	(- 0.035, - 0.015) K m s^{-1}
- 0.050 K m s^{-1}	below - 0.035 K m s^{-1}

Table 4.2: **Wind speed at 50 m ranges (in m s^{-1}) considered to classify the data from the SABLES-98 and CASES-99 campaigns according to the values obtained from the LES results. In bold and italics as in Table 3.3**

G (m s^{-1})	Neutral	-0.005 K m s^{-1}	-0.010 K m s^{-1}	-0.025 K m s^{-1}	-0.050 K m s^{-1}
14	$u > 10$	$u > 8$	$u > 7.5$	$u > 7.5$	$u > 9$
13	$7.5 < u \leq 10$	$6.5 < u \leq 8$	$6 < u \leq 7.5$	$6 < u \leq 7.5$	$7.5 < u \leq 9$
10	$6 < u \leq 7.5$	$5 < u \leq 6.5$	$5 < u \leq 6$	$5 < u \leq 6$	$\mathbf{6 < u \leq 7.5}$
8	$4.5 < u \leq 6$	$4 < u \leq 5$	$4 < u \leq 5$	*$4 < u \leq 5$*	$\mathbf{4.5 < u \leq 6}$
5	$3 < u \leq 4.5$	$2.5 < u \leq 4$	*$2.5 < u \leq 4$*	$\mathbf{2.5 < u \leq 4}$	$\mathbf{2.5 < u \leq 4.5}$
3	$1.5 < u \leq 3$	$1 < u \leq 2.5$	$1 < u \leq 2.5$	$1 < u \leq 2.5$	$1 < u \leq 2.5$
2	$1.5 \leq u$	$1 \leq u$	$1 \leq u$	$1 \leq u$	$1 \leq u$

the wind. The geostrophic wind value each 5-minute is not directly available in any of the two data bases, so we make use of the observed wind at 50 m in both campaigns. Then, the observed wind at 50 m is compared to the simulated wind at the same level, following Table 4.2. It is worth mentioning that runs suffering from runaway cooling might have wrong wind speed values at 50 m. Nevertheless, this value is considered for the classification of the observations and then in the comparison.

Therefore, the classification of the CASES-99 and the SABLES-98 data according to (M_{50m}, $< \overline{w'\theta'} >_s$) is given in Tables 4.3 and 4.4.

The observations of winds at 50 m not corresponding to the simulations (larger or smaller, see Table 4.2) are not included. It can be seen that the number of cases that fall in the categories where LES suffers from runaway cooling is not very large. These situations correspond to the percentages in bold and italics in Tables 4.3 and 4.4 and they are not observed very often, in comparison to the other situations, as Derbyshire (1990) predicted.

Therefore, performing this classification of the data, the simulated conditions correspond to the 73% of the observations in SABLES-98 and 52% of the observations in CASES-99. The cases with lighter winds (8% for SABLES-98 and 6% for CASES-99) or

Table 4.3: **Percentage of the number of observed events in CASES-99 that have been simulated. In bold and italics as in Table 3.3**

	13 m s^{-1}	10 m s^{-1}	8 m s^{-1}	5 m s^{-1}
Neutral	1.96	8.31	6.43	5.33
-0.005 K m s^{-1}	17.87	17.00	5.72	4.31
-0.010 K m s^{-1}	15.91	3.60	1.41	*1.80*
-0.025 K m s^{-1}	5.88	0.94	*0.94*	**0.39**
-0.050 K m s^{-1}	1.88	**0.24**	**0.00**	**0.08**

Table 4.4: **As in Table 4.3 for SABLES-98 data**

	13 m s^{-1}	10 m s^{-1}	8 m s^{-1}	5 m s^{-1}
Neutral	0.36	3.02	3.66	4.45
-0.005 K m s^{-1}	8.54	10.41	8.76	6.82
-0.010 K m s^{-1}	16.30	8.04	3.10	*1.29*
-0.025 K m s^{-1}	17.16	3.81	*0.57*	**0.29**
-0.050 K m s^{-1}	2.23	**1.15**	**0.07**	**0.00**

stronger winds (19% for SABLES-98 and 42% for CASES-99) are not considered in this comparison. However, as it is described in chapter 3, it would be relatively straightforward to expand the simulated parameter space (make more runs with G larger than 13 m s^{-1}) to include cases with higher wind speed. Nevertheless, following this setup, it is not possible to decrease more the geostrophic wind than 5 m s^{-1} because the simulated conditions are not realistic according to the Derbyshire criterion, as it is described in the previous chapter. Therefore, it is possible to simulate about 95% of the experimental periods of SABLES-98 and CASES-99, where the surface heat flux is negative.

If the stability parameter (z/L) is computed for each classified category, the spread of the results is very large. z/L can be between 0 and 3 for each category but the simulations have values up to 0.6 (see the range of z/L of the simulations in Table 3.2). This spread is too large for practical purposes and to overcome this problem another classification is tried using z/L as a parameter.

4.2.2 z/L parameter classification

This classification is taken because z/L is a widely used parameter and it avoids having to choose a wind parameter (wind at 50 m) that substitutes the geostrophic wind. For the LES runs z is taken at 13 m since it is the nearest computation value to 10 m, the level used by Mahrt et al. (1998) to classify the SBL regimes. z/L is computed at 10 m for SABLES-98 and CASES-99 experiments and this value is compared to the one obtained from the LES runs.

Table 4.5: **Percentage of the 5-minute observations in SABLES-98 and CASES-99 data with the stability parameter (z/L) at 10 m smaller than 1. Only observations with z/L less than 1 are considered**

	SABLES-98	CASES-99
$0.00 < z/L \leq 0.03$	13	12
$0.03 < z/L \leq 0.07$	11	6
$0.07 < z/L \leq 0.15$	12	10
$0.15 < z/L \leq 0.25$	11	9
$0.25 < z/L \leq 0.40$	16	18
$0.40 < z/L \leq 0.60$	18	18
$z/L > 0.60$	19	27

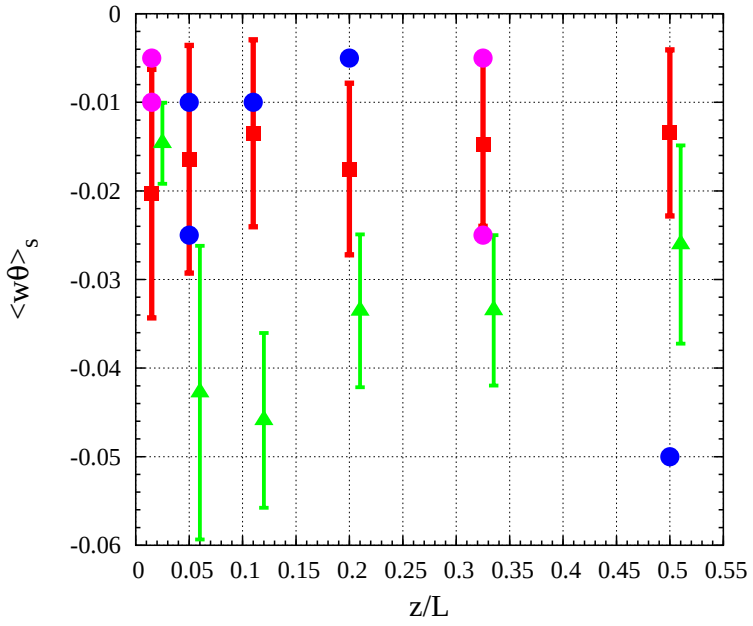

Figure 4.2: Range of surface flux temperature for SABLES-98 (squares), CASES-99 (triangles) and simulation (circles) for each z/L. Non-filled circles represent the simulations that will be shown in the comparison to observations

Since the successful simulations have values of z/L below 0.6, we will only consider cases $0 \leq /L \leq 1$. The rest of the runs have z/L larger than 1 but suffer from runaway cooling and they are not considered realistic according to the Derbyshire criterion. In Table 4.5 the selected 5-minute averages are classified according to the values of z/L at 10 m. Records corresponding to z/L above 1 have not been considered since they are beyond our range of application. The 56 % of the selected records of SABLES-98 and the 40 % of those of CASES-99 are used in this section. From this information and the percentages given in Table 4.5 it is obvious that the surface layer is often in a more stable

conditions for CASES-99 than for SABLES-98.

Using z/L as a classifying parameter implies that each category can contain a wide range of combinations of geostrophic wind forcing or surface cooling flux and several simulations can fall in the same category. Consequently, in the first classification the dispersion of the z/L values for each category were very large as this one are the values of geostrophic wind and surface temperature flux (see Figure 4.2). To overcome this problem, both classifications will be considered for the comparison purposes.

4.3 Comparison of the LES runs and data through parameters

The comparison of the LES results to data is made for each category of wind at 50 m and surface vertical temperature flux (Tables 4.3 and 4.4) and the parameter z/L (Table 4.5) through three parameters: two related to the mean structure of the SBL (temperature gradient and wind shear parameters) and last one to a turbulence quantity (the vertical heat flux parameter). The parameters are normalized by the value closer to the ground, except the shear parameter. These parameters are defined as

$$T_{par} \equiv \frac{(\theta(z) - \theta_{top})}{(\theta_{top} - \theta_{bottom})} \tag{4.1}$$

$$Sh_{par} \equiv \sqrt{(\frac{\Delta U}{\Delta Z})^2 + (\frac{\Delta V}{\Delta Z})^2} \tag{4.2}$$

$$VHF \equiv \frac{< w\theta >}{< w\theta >_s} \tag{4.3}$$

The vertical heat flux parameter has been computed using data from sonic anemometers for SABLES-98 and CASES-99, and the total (resolved + subgrid contributions) fluxes from the simulations. The parameters for each of the classified categories are shown in Figures 4.3, 4.4, 4.5 and 4.6 for the simulations of $G = 5$ m s^{-1}, $G = 8$ m s^{-1}, $G = 10$ m s^{-1} and $G = 13$ m s^{-1}, respectively, as the surface cooling increases. Those computed for the z/L classification are shown in Figures 4.7, 4.8 and 4.9. For the weakly stable case (Figure 4.7), there are only two 5-minute records for CASES-99 and they are not kept due to the weak statistical representativeness. For the more stable categories, both the SABLES-98 and CASES-99 records are used for the comparison.

From both classifications the results obtained are very close to those simulated. For any of the considered parameters, the simulations fall within the error bars, taken as

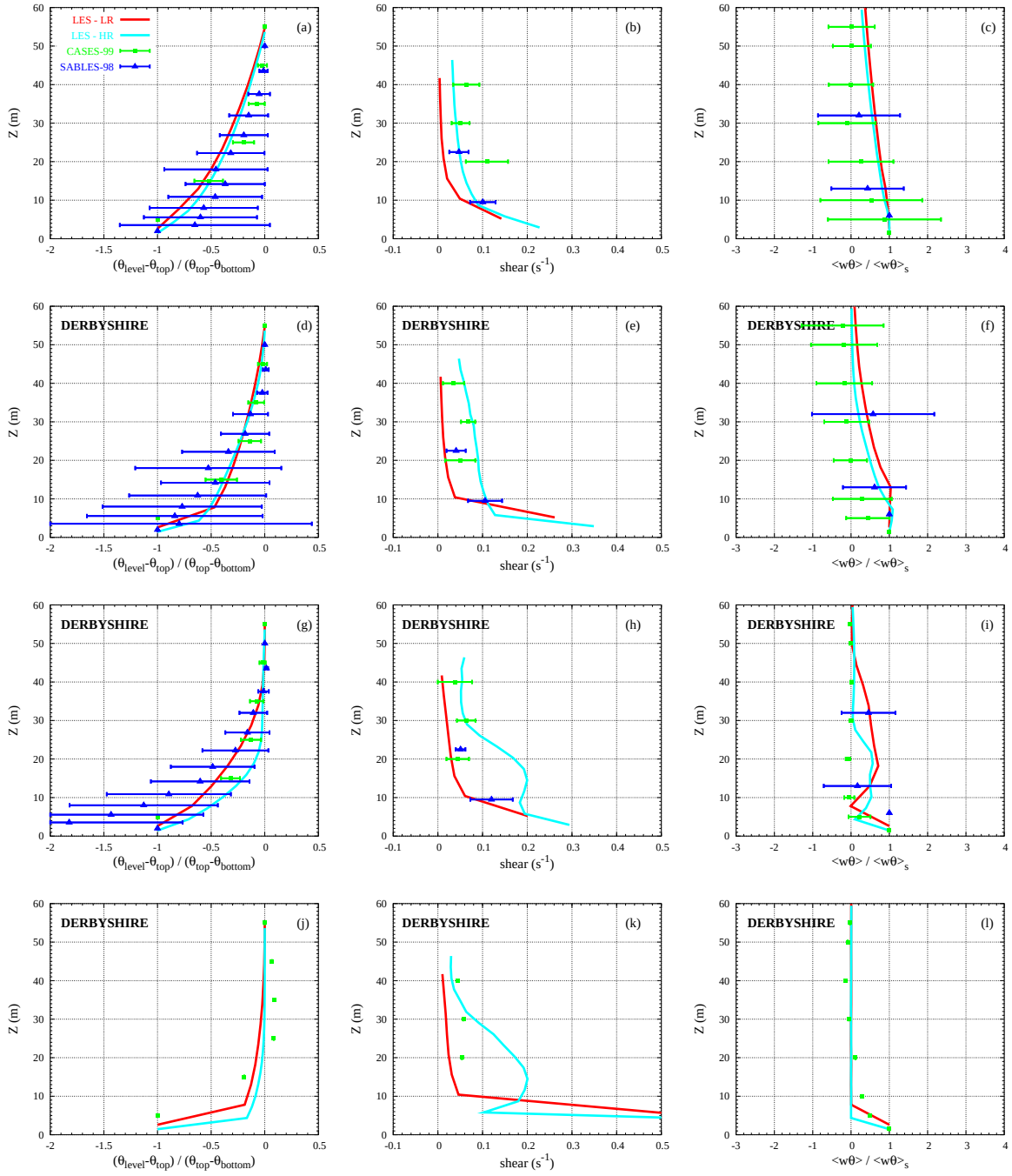

Figure 4.3: **Comparison to observations (wind at 50 m and $< w\theta >_s$ classification) for $G = 5$ m s^{-1}.** (Left) Temperature parameter, (Middle) wind shear and (Right) vertical temperature flux parameter as cooling increases: (a), (b) and (c) $< w\theta >_s$ = -0.005 K m s^{-1} ; (d), (e) and (f) $< w\theta >_s$ = -0.010 K m s^{-1} ; (g), (h) and (i) $< w\theta >_s$ = -0.025 K m s^{-1} ; (j), (k) and (l) $< w\theta >_s$ = -0.050 K m s^{-1}. The triangles for SABLES-98 and squares for CASES-99 are the mean values and the bars the standard deviation. LR stands for low resolution whereas HR high resolution (see more details in chapter 3). The runs that suffer runaway cooling are labelled as **DERBYSIRE**

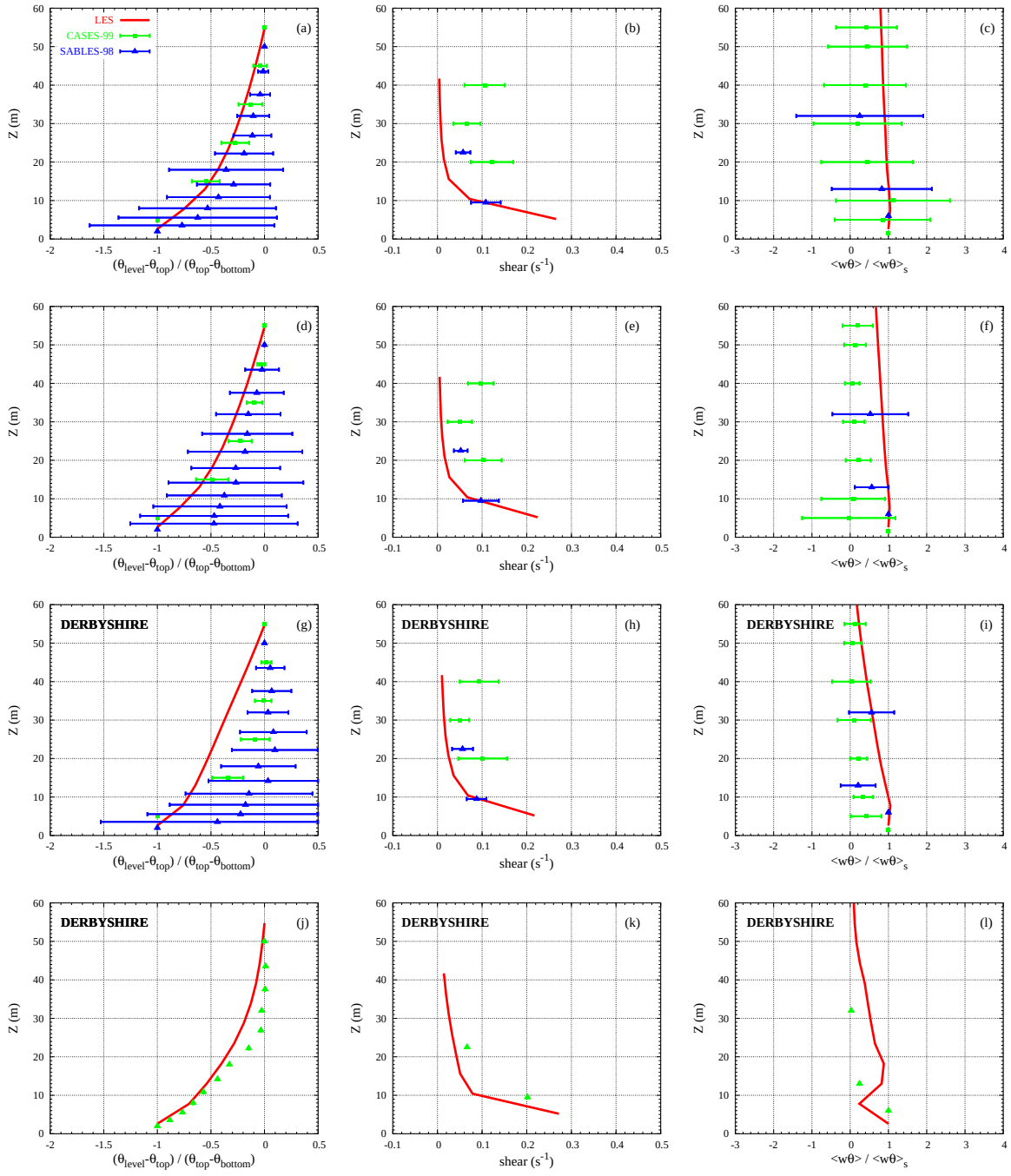

Figure 4.4: **Comparison to observations (wind at 50 m and $< w\theta >_s$ classification) for $G = 8$ m s^{-1}.** Plots as in Figure 4.3

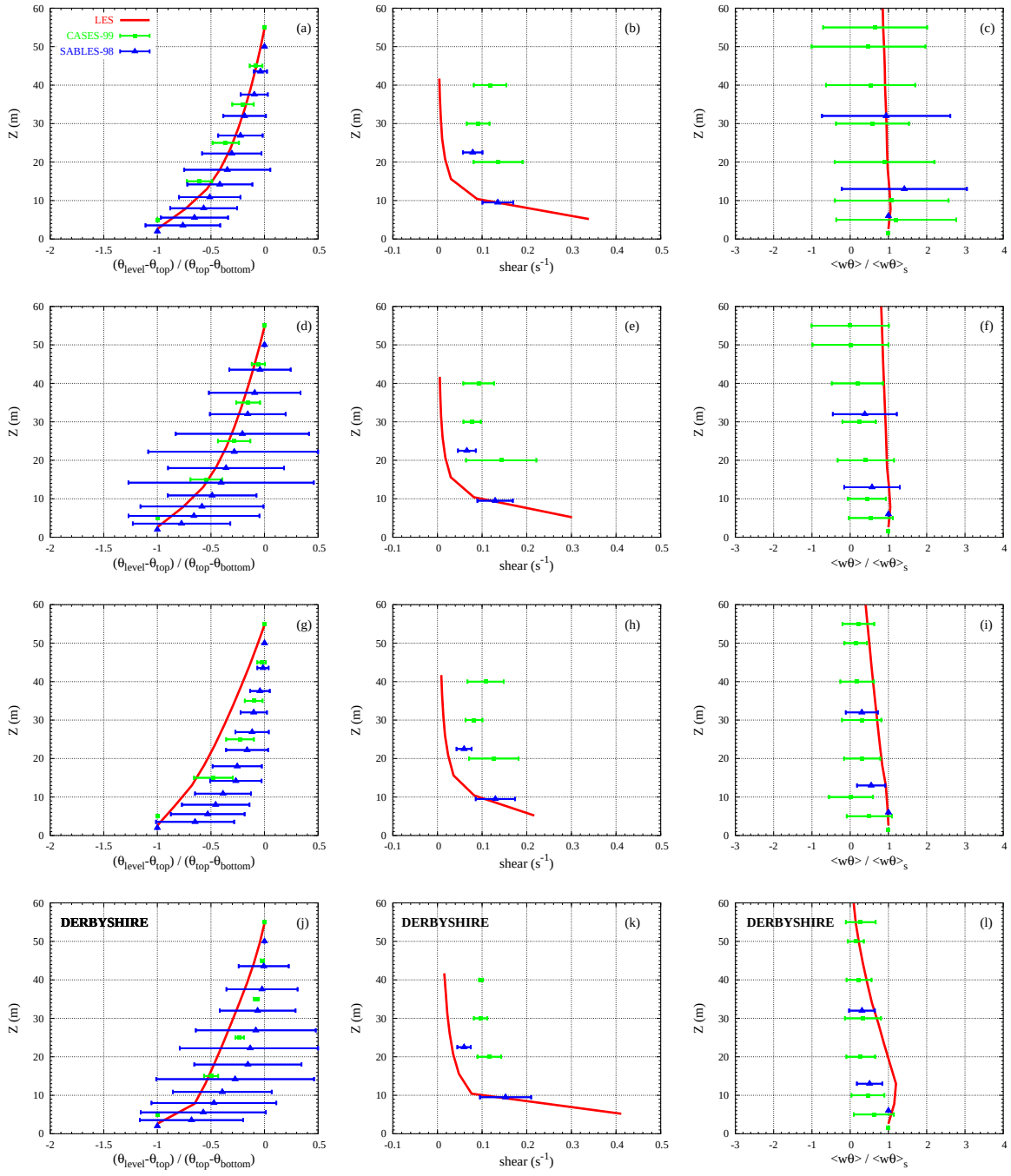

Figure 4.5: **Comparison to observations (wind at 50 m and $< w\theta >_s$ classification) for $G = 10$ m s^{-1}.** Plots as in Figure 4.3

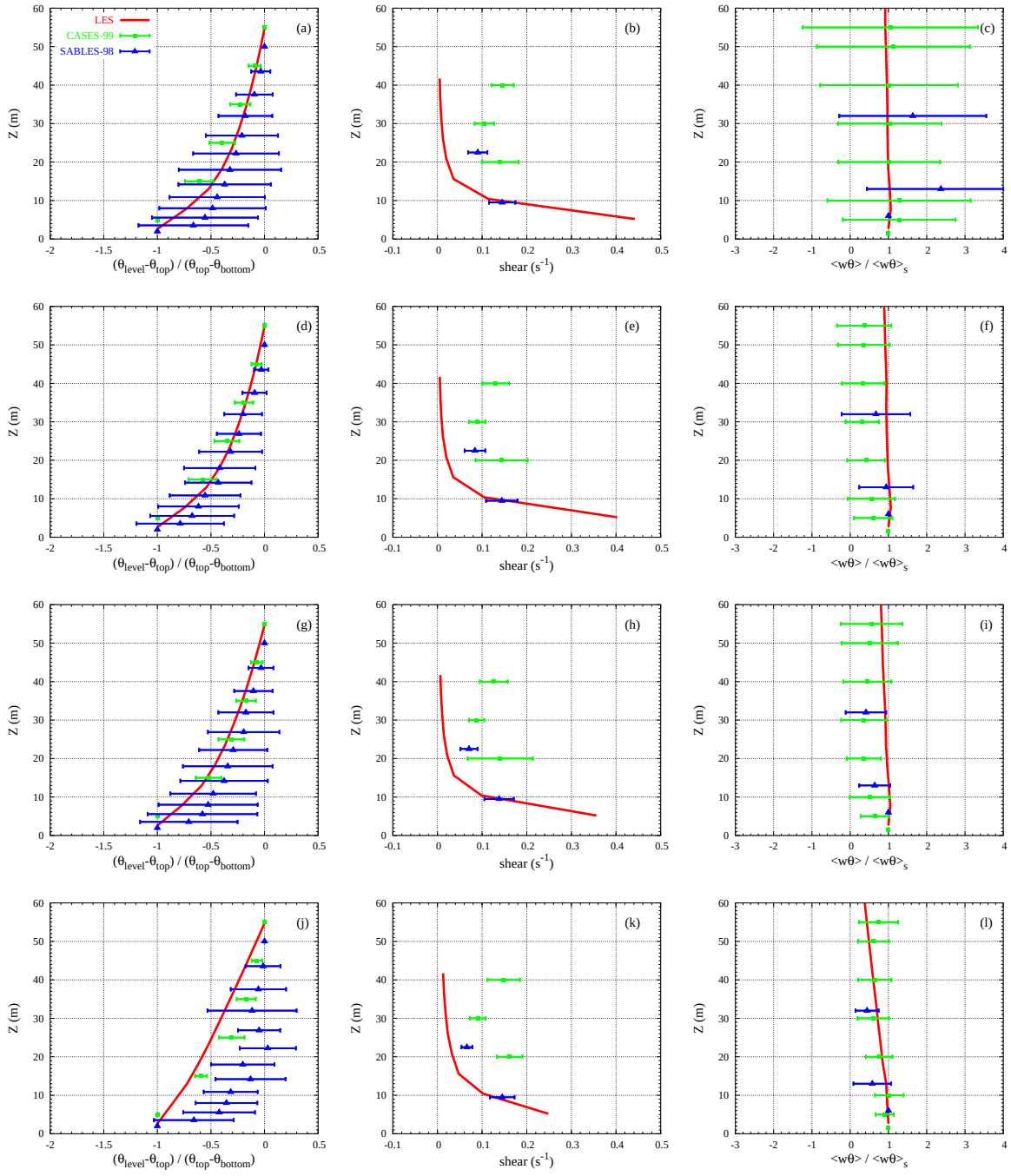

Figure 4.6: **Comparison to observations (wind at 50 m and $< w\theta >_s$ classification) for $G = 13$ m s^{-1}.** Plots as in Figure 4.3

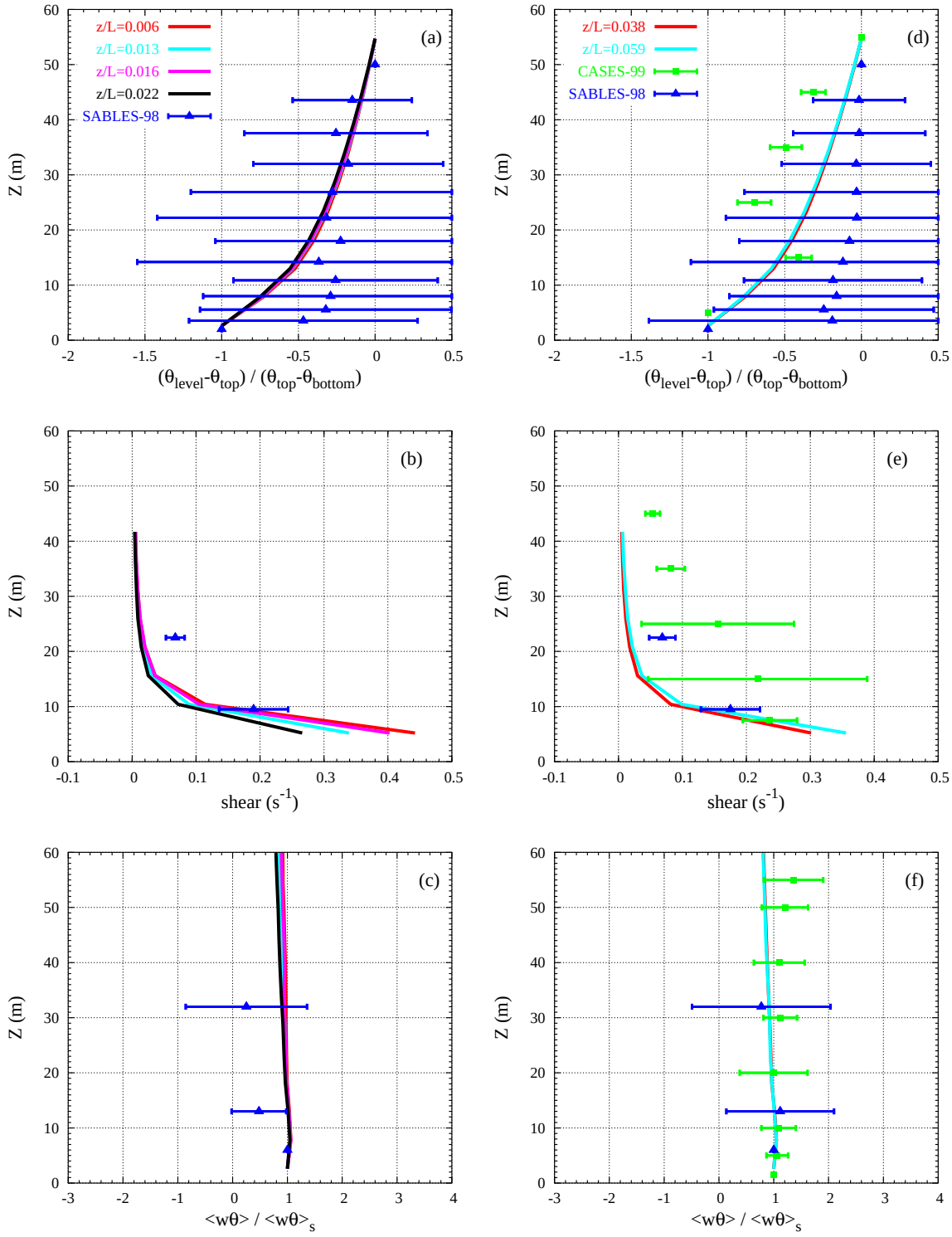

Figure 4.7: **Comparison to observations (z/L classification): (Left) $0 \leq z/L \leq 0.03$ and (Right) $0.03 \leq z/L \leq 0.07$** for (a) and (d) temperature parameter; (b) and (e) shear; (c) and (f) vertical temperature flux parameter. The triangles for SABLES-98 and squares for CASES-99 are the mean values and the bars the standard deviation. HR stands for high resolution (see more details in chapter 3). In the $0 \leq z/L \leq 0.03$ case data from CASES-99 is not plotted since there is only one observational record within these conditions

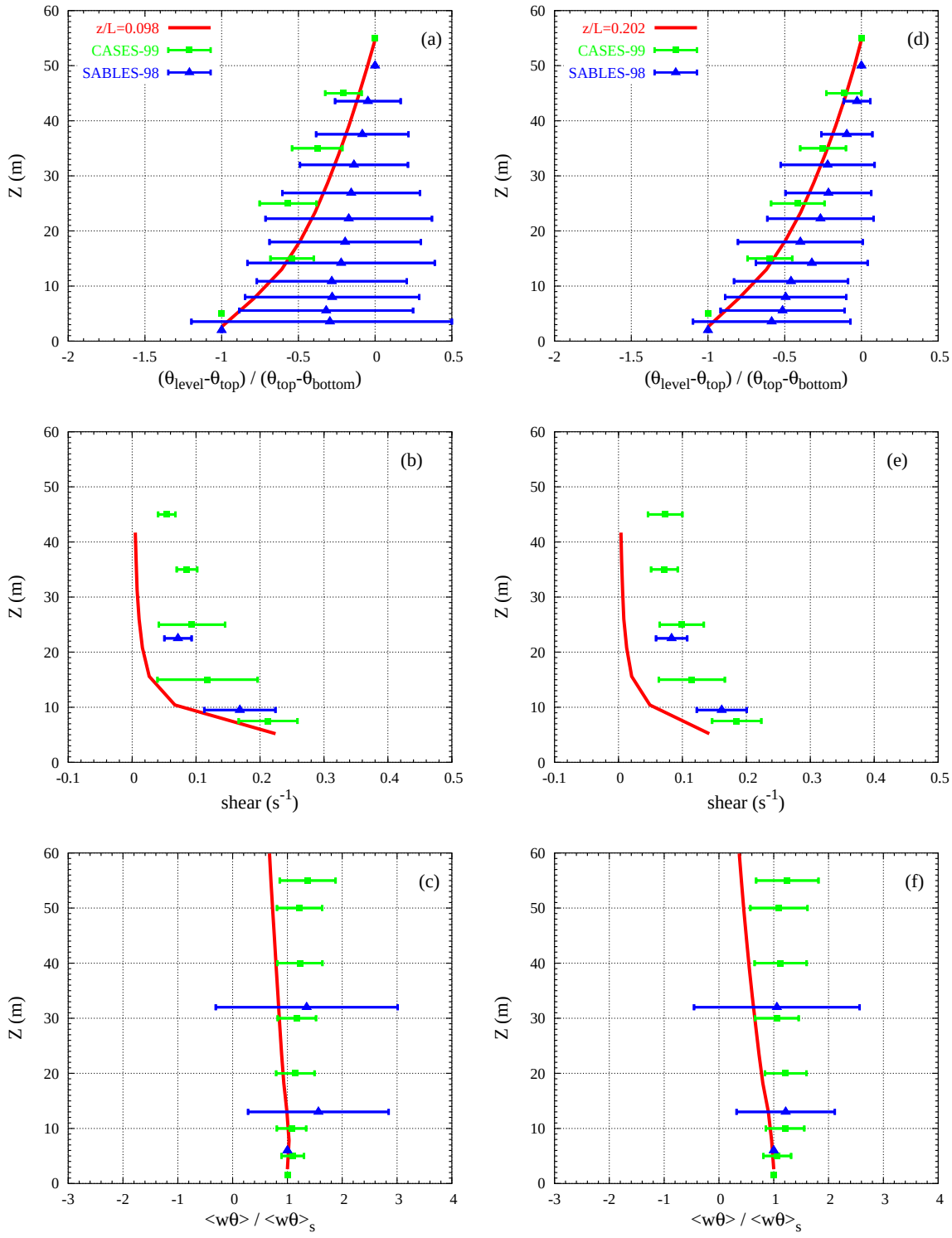

Figure 4.8: **Comparison to observations (z/L classification): (Left) $0.07 \leq z/L \leq 0.15$ and (Right) $0.15 \leq z/L \leq 0.25$.** Plots as in Figure 4.7

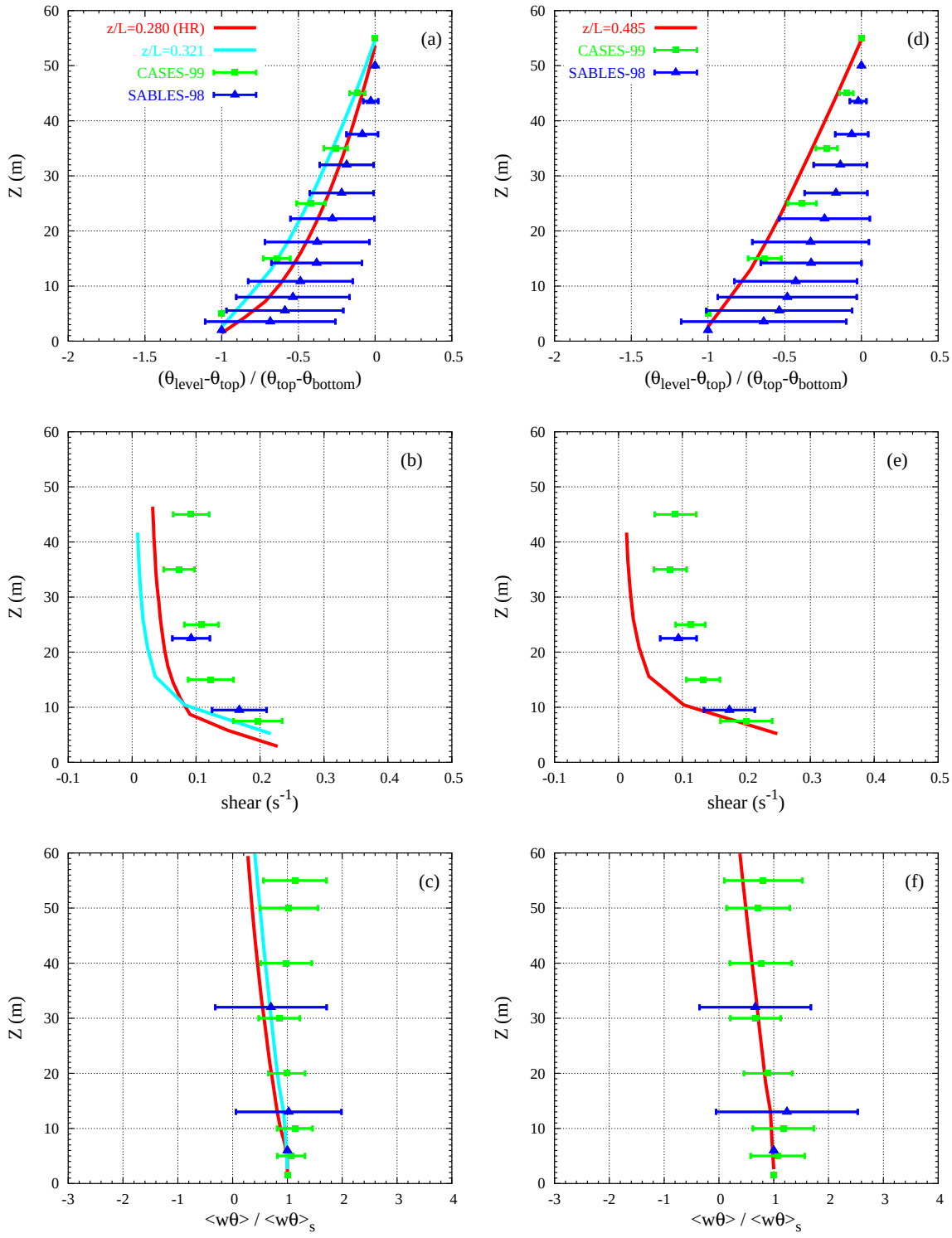

Figure 4.9: **Comparison to observations (z/L classification): (Left) $0.25 \leq z/L \leq 0.40$ and (Right) $0.40 \leq z/L \leq 0.60$.** Plots as in Figure 4.7

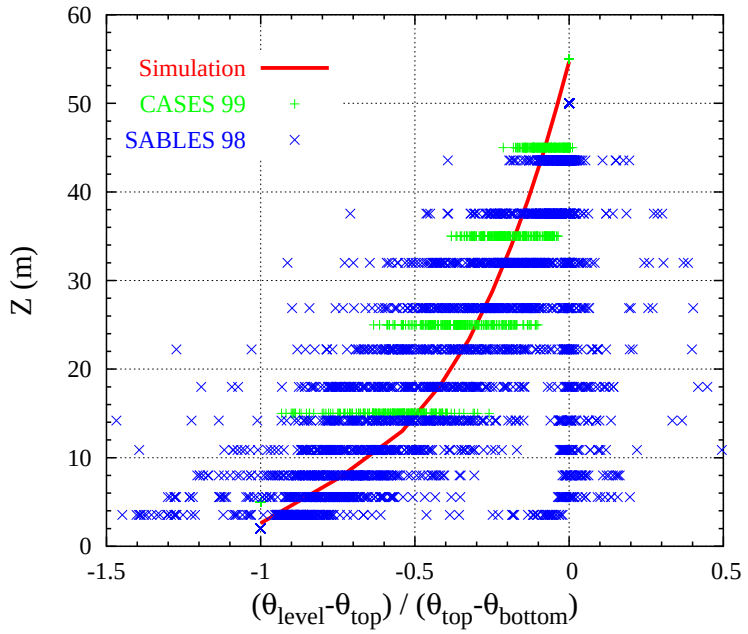

Figure 4.10: Temperature parameter for the most observed case in the wind at 50 m and surface vertical temperature flux classification corresponding to ($< w\theta >_s$ = -0.010 K m s^{-1} u_g = 13 m s^{-1}). The green colour for CASES-99 and the blue one for SABLES-98

one standard deviation. The CASES-99 error bars are smaller than those computed for SABLES-98. This is because the SABLES-98 data are more spread than in CASES-99 as shown in Figure 4.10. It is seen that for SABLES-98 the points gather together in two well defined clusters (Figure 4.10), one corresponding to different situations not taken into account in the previous LES.

For any of the two classifications, the LES results for the higher resolution simulation (HR) tend to be closer to the observations, as it is seen in Figures 4.4 and 4.9. Although the resolution is still far away of the inertial subrange (i.e. the Kolmogorov theory is under question) the mean structure of the SBL is better captured than at lower resolution (LR).

The simulations that suffer runaway cooling have been also considered in the classification of the wind at 50 m and the surface vertical temperature flux (see Figures 4.3, 4.4 and 4.5 for the geostrophic winds of 5, 8 an 10 m s^{-1} respectively). These situations are not very common as Tables 4.3 and 4.4 indicate since some of these events are observed during a very short period of time (there is only one register of the 5-minute time series) and others can be due to the arrival of an external forcing. Nevertheless, within these situations the mean profiles, especially the temperature parameter, are close to the observations.

Regarding the temperature parameter and considering any of the classifications, the

major differences between the data and the simulations are in the layer closer to the ground, below 15 m, where the simulation generates larger gradients than those observed. Nevertheless, the results fall within the error bars. It is worth mentioning that the LES results are closer to the observations for the 50 m wind and $< w\theta >_s$ classification, since they are the parameters that have been used to perform the simulation. In this case, the LES results tend to be closer to the observations especially for larger values of G and smaller values of $< w\theta >_s$, corresponding to a weakly stable conditions (see, for instance Figure 4.6.a). On the other hand, when the z/L classification is taken, the error bars are less spread for higher z/L values (Figure 4.9.a) but the LES results are closer to the observations for the moderately stable conditions (Figure 4.9.a).

For any of the two classifications, the simulations tend to underestimate the shear, especially above 15 m, while the parameter compares better below. Mahrt and Vickers (2002, Figure 3a) show a similar plot based also on CASES-99 data, averaged over 1 hour, and the results are similar to those obtained here from the LES. The deviation in the levels above 20 m might be due to upside-down turbulence events, not considered in our simulation setup. Nevertheless, this is the only parameter that has not been normalized by its surface value and the values are not shifted as in the other parameters. The 50 m wind and $< w\theta >_s$ classification shows that the model has larger shear as the geostrophic wind increases (Figure 4.6.b) and that it is reduced when the stability increases (Figure 4.6.k) because the conditions are more stable. This behaviour is not found in the observations where the shear remains approximately constant for each category. From the z/L classification the values of shear are much more spread than in the 50 m wind and $< w\theta >_s$ classification. This might be explained because the wind is not considered in the z/L classification and the values are more spread, as Figure 4.2 points out.

It is worth mentioning that the Monin-Obukhov similarity is applied in the runs near the surface. The results tend to behave worse near the surface than at upper levels probably because the observations do not behave as the Monin-Obukhov similarity predicts.

The weakly stable case tends to have larger heat fluxes in the upper part of the surface layer than close to the surface. This is consistent with the behaviour of the mean parameters, since the gradient of temperature is overestimated and the shear is underestimated. The more stable category shows that the observed fluxes are approximately constant with height, whereas the simulations show a decrease. Nevertheless, the simulation results fall within the error bars, except at heights above 50 m. Mahrt and Vickers (2002, Figure 3c) show as well that upside-down turbulence has constancy or an increase with height of the absolute value of the heat fluxes, contrarily to the traditional thin boundary layers. The CASES-99 data that are used in these figures do not diminish with height, whereas the

SABLES-98 data do.

4.4 Conclusions

It is difficult to find a parameter to classify the data to perform the comparison to the LES results. Within the observed SBL all scales of motion are included, as well as more forcings than in the LES, and this makes difficult to classify data accurately. Nevertheless, similar results are found from the two classification parameters showed here.

The thermal structure is well represented by the model but the shear is stronger. The surface Monin-Obukhov similarity is applied in the LES but it seems that the observations do not exactly behave in this way. On the other hand, no evidence of the runaway cooling is found from the observations. Then, runaway cooling can be a numerical artifact that the numerical models suffer from when they are dealing with strong stabilities. However, the simulated conditions are closer to CASES-99 campaign than to SABLES-98 one, where a larger number of events were measured than in CASES-99.

Several reasons can explain the differences between the LES results and the observations:

(i) the LES only consideres the information up to the resolved scales meanwhile in the observations all scales of motion are included. A further discussion on the eddy structures is shown in chapter 6.

(ii) the LES results depend on the resolution and when the resolution is higher the results are closer to the observations.

(iii) not all the forcings observed are included in the model. For instance, the orographic effects are quite important within the SBL, as it is seen in chapter 8, but in this LES they are not considered.

(iv) in the LES results the Monin-Obukhov similarity theory is applied in the surface layer and the observations seem not to behave in this way.

It is worth mentioning that the highest measurement level of the turbulent quantities is 50 m for CASES-99 and 32 m for SABLES-98. Turbulent measurements at higher levels are needed in the future to fully characterize the turbulence within the SBL.

Chapter 5

AN INTERCOMPARISON OF DIFFERENT LES MODELS IN STABLE CONDITIONS[1]

Previous chapters show that the LES model, which uses the standard Kolmogorov theory for dissipation, is able to work properly from weakly to moderately stable conditions. This is also confirmed when the LES results are compared to observations (chapters 3 and 4).

Since the Kolmogorov theory is no valid under stably stratified conditions (the turbulence is not homogeneous either isotropic), modifications on the turbulence scheme can be done. Here, different LES models are run in the same prescribed conditions to evaluate the sensibility of the results on the turbulence scheme used. Then, the LES model used in this work is evaluated through the comparison to other LES models. An LES of the SBL, similar to those described in chapter 3, is performed.

The comparison of the results of different models is made through the inspection of mean profiles and time series. The sensitivity of the results to the resolution or the advection scheme among others is explored to evaluate the results.

[1]This chapter is based on: R. J. Beare, M.K. MacVean, A.A.M Holtslag, J. Cuxart, I. Esau, J.-C. Golaz, M.A. Jiménez, M. Khairoutdinov, B. Kosovic, D. Lewellen, T.S. Lund, J.K. Lundquist, A. McCabe, A.F. Moene, Y. Noh, S. Raasch and P. Sullivan, 2005: An intercomparison of Large-Eddy simulations of the Stable Boundary Layer, *Boundary-Layer Meteorology*, in Press.

5.1 The aim of the intercomparison of different LES models

The Meso-NH model has participated to the first GABLS intercomparison exercise where different LES models ran at stably stratified conditions. The GABLS [1] (GEWEX Atmospheric Boundary Layer Study) is a branch of the GEWEX (The Global Energy and Water Cycle Experiment) Modelling and Prediction Panel, from the World Meteorological Organization (WMO). The GEWEX is a program initiated by the World Climate Research Programme (WCRP) to observe, understand and model the hydrological cycle and energy fluxes in the atmosphere, at land surface and in the upper oceans. GABLS, initiated in 2002, is one of the activities within the GEWEX Modelling and Prediction Panel.

The overall objective of the GABLS is to improve the understanding and the representation of the atmospheric boundary layer in regional and large scale climate models. The first focus of GABLS is on the representation of the SBL (Holtslag, 2003). It appears that much of the warming predicted by climate models occurs during stable conditions over land (either in winter or at night). At the same time, it is realized that the understanding and parameterization of the SBL is still poor.

To evaluate the state of art, a simple case (similar to Kosović and Curry, 2000) was selected inspired by the BASE (Beaufort Sea Arctic Status Experiment) arctic observations. In this first GABLS intercomparison, a moderately stable shear-driven case with an imposed surface cooling rate has been chosen. To start with, a simple case is considered because as the stability increases most of the SGS have some well-known limitations (see chapter 2, section 2.4).

11 different LES models and 19 1D models have participated in this first intercomparison exercise. Regarding the LES models, the list of participants, as well as a brief summary of the main features of the subgrid scale scheme and the advection scheme, are shown in Tables 5.1 and 5.2.

As it was described in chapter 2, the turbulence in stably stratified conditions is not homogeneous either isotropic and several approaches are taken. The different SGS that have participated in the intercomparison can be divided in four categories, depending on each treatment of the SGS to run in stable conditions:

• Smagorinsky models (NRL) without modiffications

• Dynamic Smagorinsky models (CORA, LLNL, NCAR, NERSC) where an extra term is added in the eddy viscosity to include the contribution from the mean flow and to reduce

[1] http://www.gabls.org/

the contributions from the turbulent fluctuations near the surface.

• 1.5 order TKE models (CSU, IMUK, UIB, WU, WVU) but some of them include especial modifications. For instance UIB uses the Prandtl and Schmidt numbers consistently derived from the complete set of second-order turbulent-moment equations. WU also changes the dissipation formulation to improve the results and in WVU the rotation effects are included.

• Backscatter (MO) where the large scales are randomly forced through non-linear interaction with subgrid-scale eddies. LLNL also included the backscatter as well as the extra term in the viscosity.

Table 5.1: **Participants in the first LES intercomparison of GABLS**

Model	Institution	References
CORA	Colorado Research Associates	The same as NCAR
CSU	Colorado State University	Khairoutdinov and Randall (2003)
IMUK	University of Hannover, Yonsey University	Raasch and Schröter (2001)
LLNL	Lawrence Livermore National Laboratory	Kosović (1997)
MO	Met Office, UK	Brown et al. (1994)
NCAR	National Center for Atmospheric Research	Sullivan et al. (1994), Moeng (1984)
NERSC	Nansen Env. and Remote Sensing Center	Esau (2004)
NRL	Naval Research Laboratory	Hodur (1997)
UIB	Universitat de les Illes Balears	Cuxart et al. (2000b)
WU	Wageningen University	Cuijpers and Duynkerke (1993)
WVU	West Virginia University	Lewellen and Lewellen (1998)

Table 5.2: **Brief summary of the participant models in GABLS**

Model	Subgrid Model	Advection Scheme
CORA	Dynamic smagorinsky	the same as NCAR
CSU	TKE	monotonic and positive definite
IMUK	TKE	Piacsek and Williams (1970)
LLNL	Non-linear + Two-part	spectral horizontal/monotone vertical
MO	Smagorinsky + Backscatter	Piacsek and Williams (1970)
NCAR	Two-part smagorinsky	spectral horizontal/monotone vertical
NERSC	Dynamic smagorinsky	central differencing not monotonic
NRL	Smagorinsky	positive definite
UIB	TKE	centered and positive definite
WU	TKE + dissipation modified	Piacsek and Williams (1970)
WVU	TKE with rotation effects	central and monotone

Nonetheless, the advection scheme might also explain the differences of the results obtained for each model, as it will be described later. Regarding the advection scheme,

the models can be divided in three groups:

• A second order method in space and time that conserves variances: (1) IMUK, MO, WU use Piacseck and Williams (1970) and (2) CSU, NRL, UIB, WVU use Smolarkiewicz and Grabowski (1990).

• Pseudo-spectral method (Fox and Orszag, 1973) in the horizontal and second order centered in the vertical (CORA, LLNL, NCAR).

• Non-monotonic (NERS) where the numerical solution of the advective part might produce oscillations and negative values.

5.2 Description of the first LES intercomparison

The Stable GABLS LES first case consists on a shear boundary layer driven by an imposed uniform geostrophic wind $(u_G,\ v_G) = (8,\ 0)$ m s^{-1} at a latitude of 73°N. A constant surface cooling rate (0.25 K h^{-1}) is prescribed for 9 hours so that a quasi-equilibrium state is approached. The initial wind profile is equal to the geostrophic whereas the potential temperature profile consists of a mixed layer up to 100 m ($\theta = 265$ K) with an overlying inversion increasing at $\Delta\theta/\Delta z = 0.01$ K m^{-1} to the top of the domain where the temperature is $\theta = 268$ K. To activate the resolved motions, the initial temperature field is perturbated with a random noise of ± 0.1 K of amplitude for $0 < z < 50$ m.

The Monin-Obukhov similarity is also applied at the bottom boundary with prescribed constants:

$$\phi_M = 1 + 4.8\frac{z}{L} \tag{5.1}$$

$$\phi_H = 1 + 7.8\frac{z}{L} \tag{5.2}$$

where z/L is the stability parameter and L the Monin-Obukhov length.

The domain size is set to 400×400×400 m and an isotropic grid is used with different grid lengths: 1 m, 2 m, 3.125 m, 6.25 m, and 12.5 m, depending on the computer power of the participants. In fact, most of participants can run at 6.25 m resolution whereas just two of them can afford to run the LES model at 1 m resolution. In our case, we have run all the grid lengths except 1 m resolution due to the high computational cost. The comparison of the results is made through vertical profiles, averaged over the horizontal domain and over the last hour of the run, as well as time series of some magnitudes.

It is important to notice that this SBL LES case is very similar to the one described in chapter 3. The only difference is that in the stable GABLS case the cooling rate is

imposed (0.25 K h^{-1}) whereas in the stable case described in chapter 3 it was imposed the vertical temperature flux ($< w\theta >_s$).

5.3 Behaviour of the different models

A more detailed description of the LES results is shown in Beare et al. (2005) but here the main points are discussed.

The potential temperature, the wind speed and the vertical temperature flux averaged profiles during the last hour of the run and over the horizontal domain, are shown in Figures 5.1 and 5.2, for each of the chosen resolutions (2 m, 3.125 m, 6.25 m and 12.5 m).

As the time advances, the surface temperature is decreasing due to the prescribed cooling rate (Figures 5.1.a, 5.1.b, 5.2.a and 5.2.b). After 9 h of integration, the boundary layer depth, defined in this intercomparison as the height at which $\sqrt{uw^2 + vw^2}$ falls to 5% of its surface value (u_*) divided by 0.95, is between 150 and 220 m, depending on the model. Elevated inversions within the SBL, similar to the ones here, have been found by Kosovic and Curry (2000) on the Arctic sea, by Garratt and Ryan (1989) in a warm advection over sea nearby Australia and by Lapworth (2003) over a UK site in the middle of the night.

The results are quite sensitive to the chosen resolution, especially near the inversion level, since the surface boundary conditions are prescribed. Figures 5.1 and 5.2 highlight that the results are much more spread for the coarser resolution whereas they tend to be more concentrated when the resolution increases. Nevertheless, the intensity of the maximum of the wind developed near the inversion does not depend on the chosen resolution. This maximum is related to the development of the inertial oscillation because the wind tends to the geostrophic value at higher levels and these conditions are independent of the resolution. The intensity of this wind is independent of the model and even of the resolution but not the height where it takes place that coincides with the inversion layer and it changes for each model.

Since the surface cooling is prescribed, the models tend to different surface vertical heat fluxes as it is seen in the profiles of Figures 5.1.e, 5.1.f, 5.2.e and 5.2.f or in the time series of the surface vertical temperature flux in Figure 5.3. Some models, such as CORA, CSU or LLNL, have larger surface vertical heat fluxes ($< w\theta >_s$ about -0.013 K m s^{-1}) than, for instance, MO or WVU models ($< w\theta >_s$ about -0.009 K m s^{-1}). Therefore, some models introduce more mixing and the inversion can grow more. Nevertheless, all models present a linear profile of the vertical temperature flux within the SBL. The surface vertical temperature flux, at which each model converges, depends on the chosen

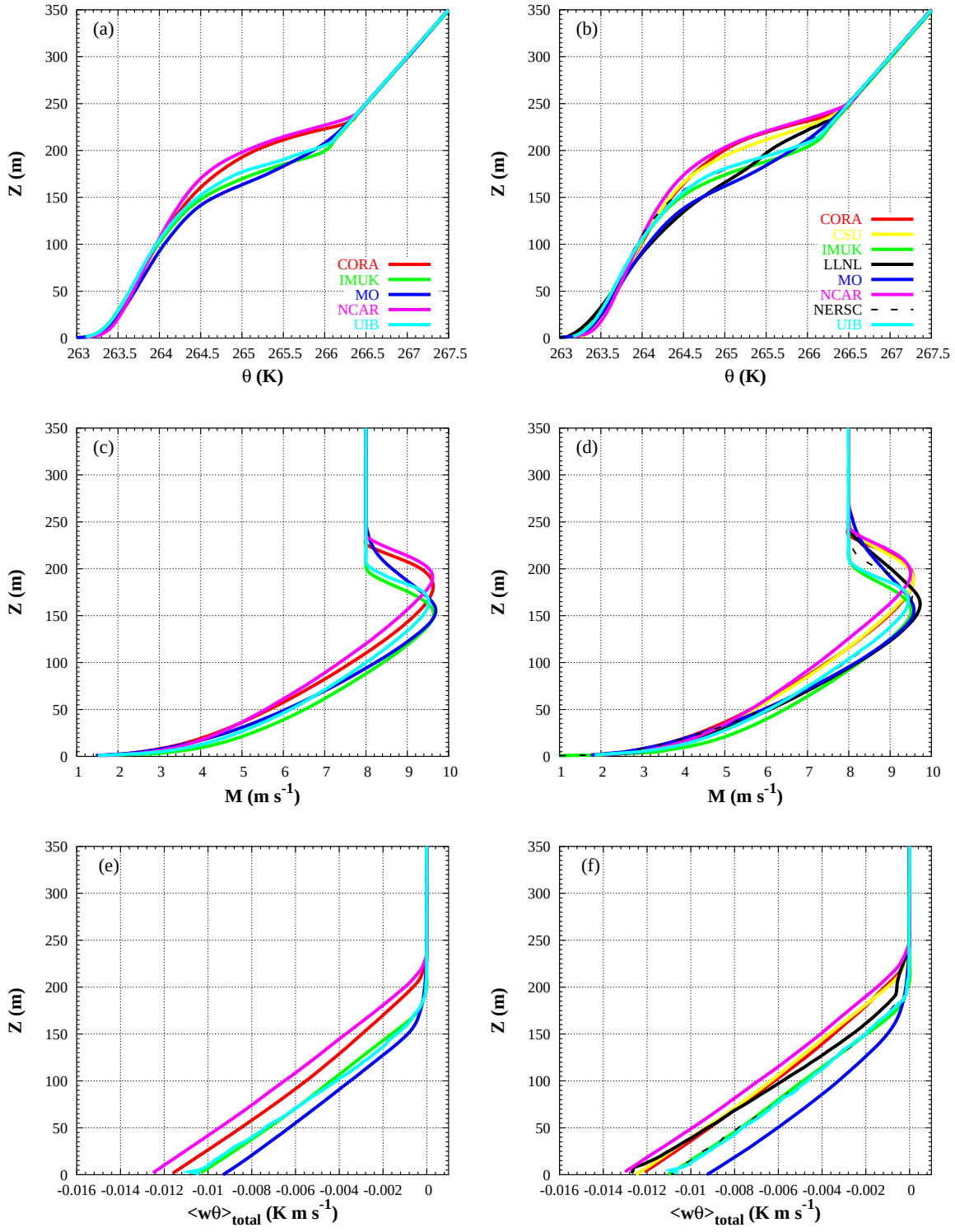

Figure 5.1: GABLS intersomparison profiles averaged over the last hour for the **2 m** runs (left) and **3.125 m** (right). (a) and (b) potential temperature (K), (c) and (d) wind speed (m s^{-1}) and (e) and (f) vertical temperature flux (K m s^{-1}). Description of the models in Tables 5.1 and 5.2

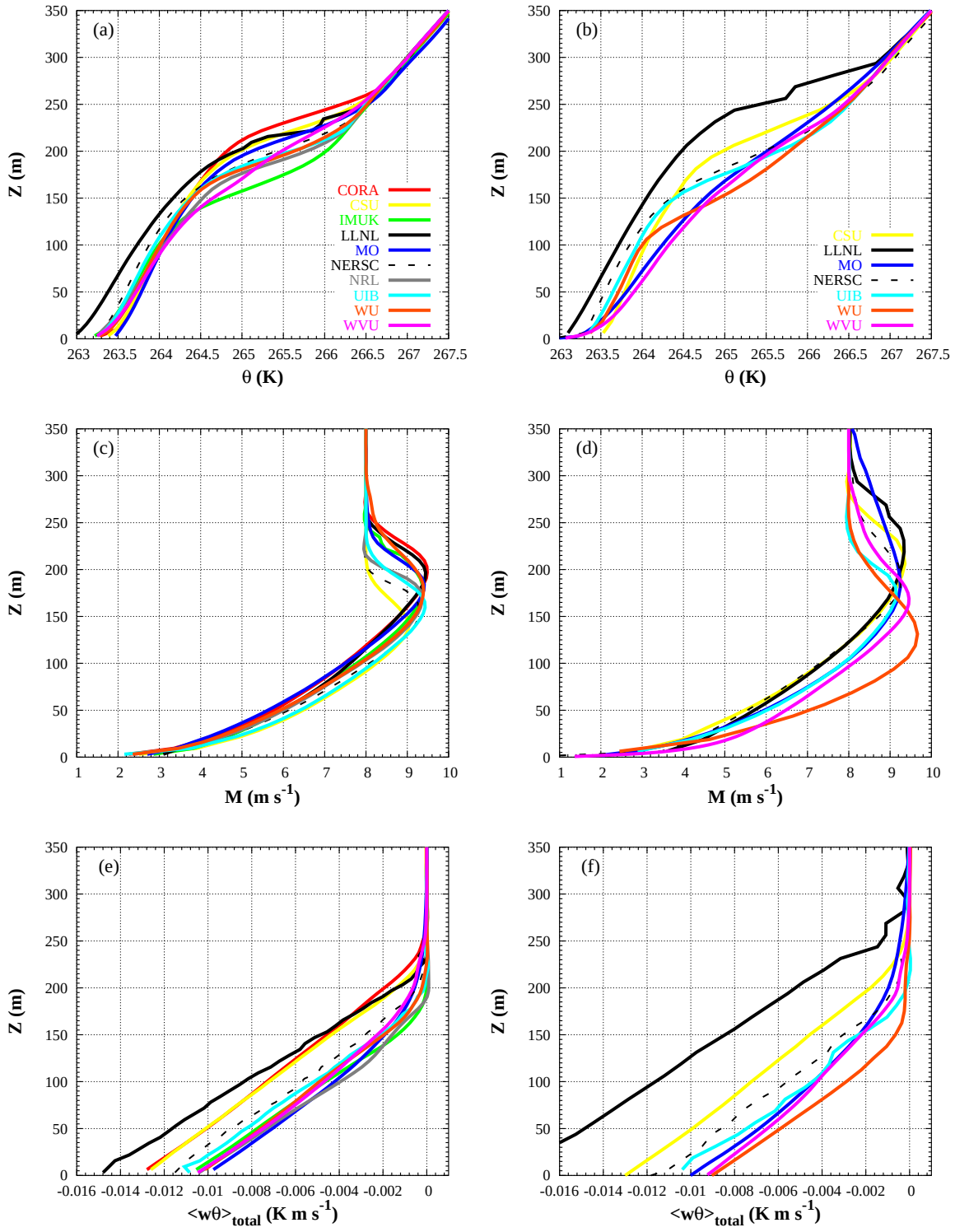

Figure 5.2: GABLS intersomparison profiles averaged over the last hour for the **6.25 m** runs (left) and **12.5 m** (right). Plots as in Figure 5.1

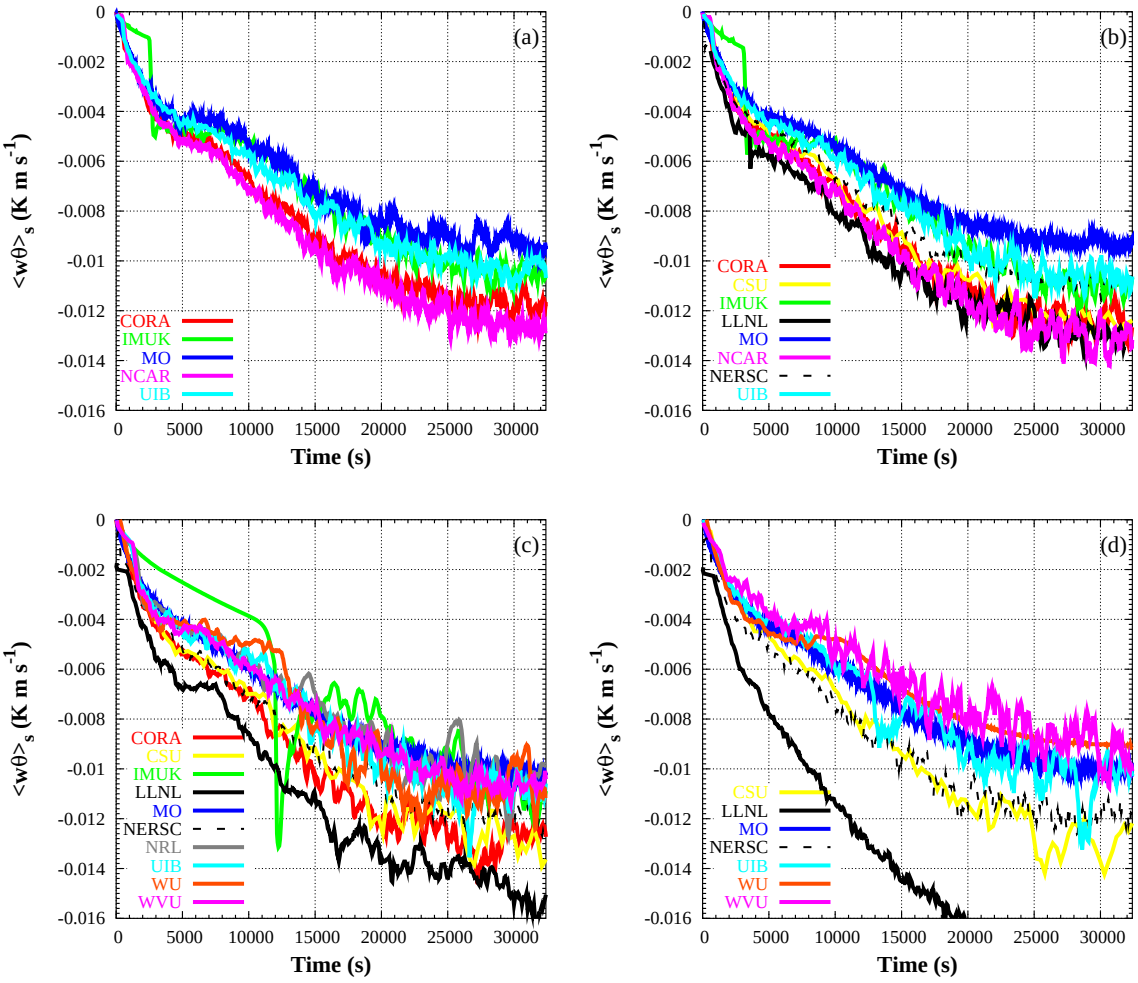

Figure 5.3: Vertical temperature flux time series at the first computation level for each of the resolutions considered: (a) 2 m, (b) 3.125 m, (c) 6.25 m and (d) 12.5 m

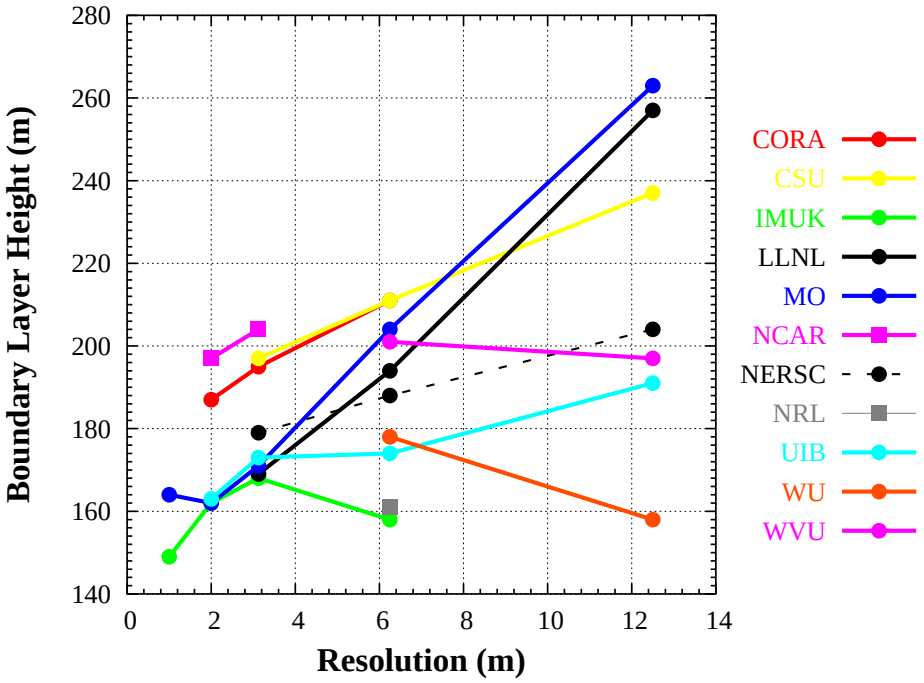

Figure 5.4: Boundary layer heights obtained from each model averaged over the last hour of simulation

resolution as Figure 5.3 points out. Again, the results for the coarser resolution are much more spread but at higher resolutions they tend to concentrate.

The sensitivity to the resolution of the boundary layer height averaged over the last hour of integration is shown in Figure 5.4. This Figure highlights that the results are much more spread when the resolution decreases. For instance, at 12.5 m resolution the values are spread about 100 m whereas at 1 m or 2 m resolution the spread is smaller, between 20 m and 40 m. It is important to notice that there are less models running at such lower resolutions and then it is not possible to determine the behaviour of all models at lower resolutions.

Nevertheless, most of the models have similar results for higher resolutions and present a sharp increase on the boundary layer height at 12.5 m resolution, except WU and WVU that present a smooth decrease. There are also some models that do not experience this sharp increase and the boundary layer height is almost independent of the resolution, such as CORA, IMUK, NERSC or UIB. In these models the difference between the boundary layer height computed from the lower and higher resolution is about 20 m.

The total turbulent kinetic energy (TKE_{total}) as well as the ratio between the subgrid versus the total are shown in Figures 5.5 and 5.6, respectively, for each of the resolutions. The TKE_{total} is larger near the surface and decreases linearly with height up to the top

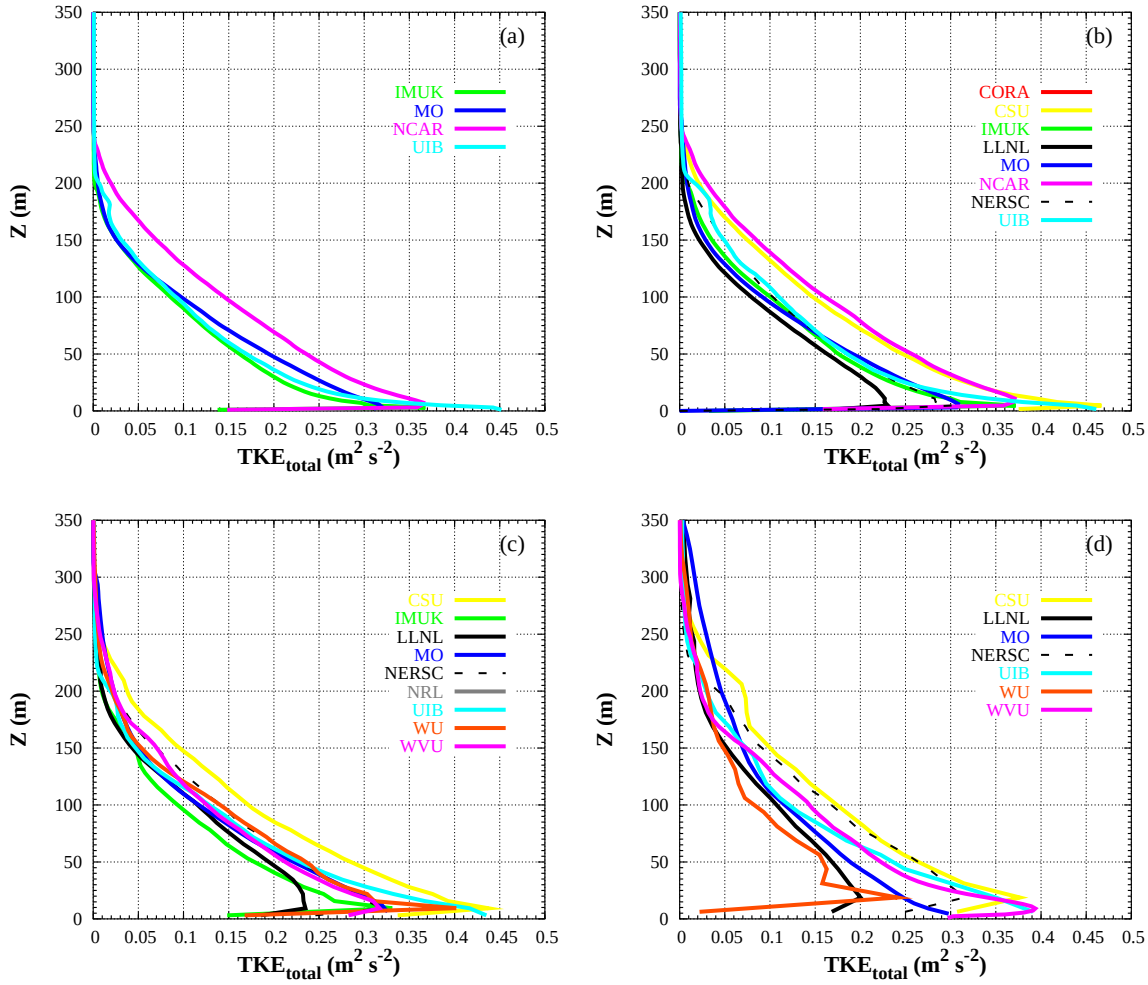

Figure 5.5: Total TKE profiles averaged over the last hour for each of the resolutions considered: (a) 2 m, (b) 3.125 m, (c) 6.25 m and (d) 12.5 m. Since there is no available data for the subgrid contribution of NCAR, this model has not been taken into account in the plots

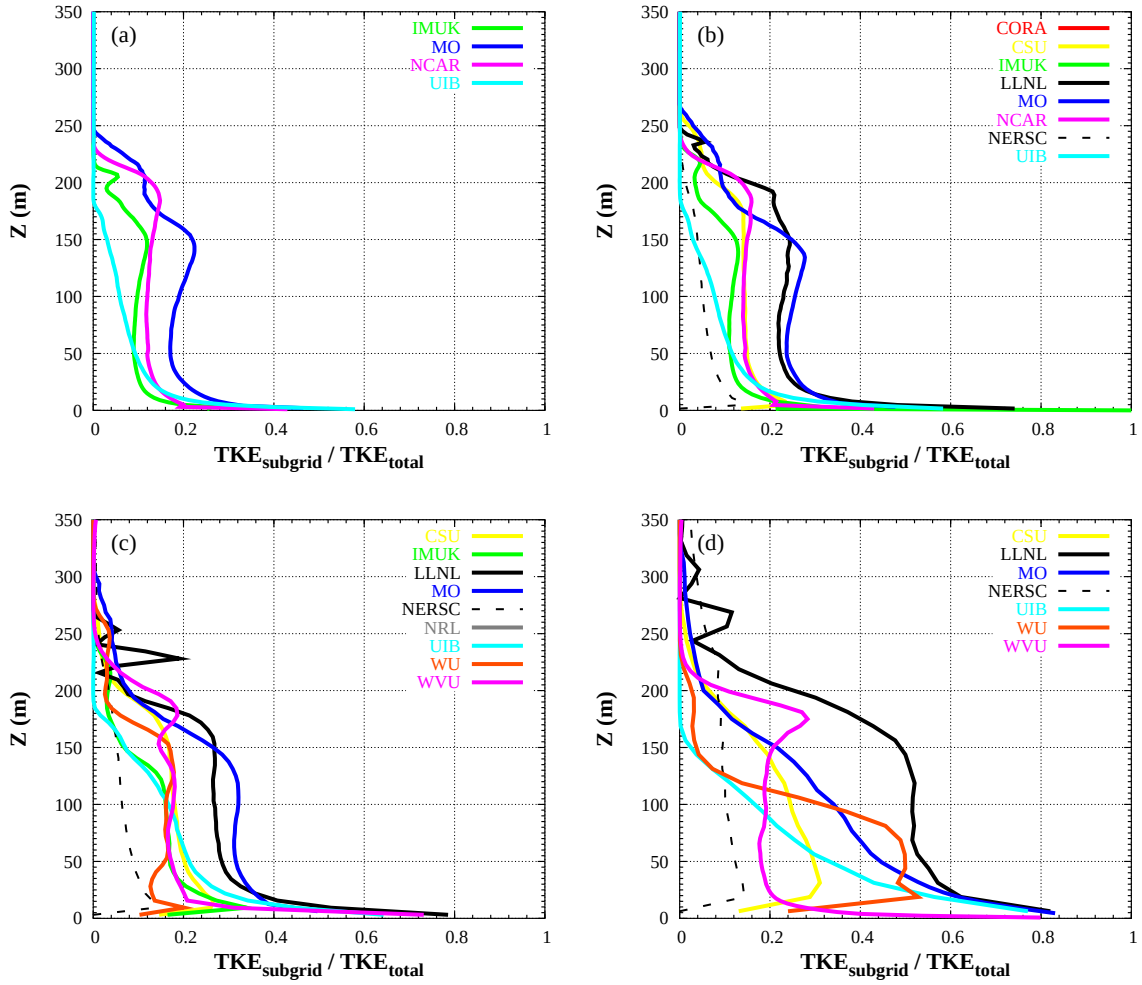

Figure 5.6: Ratio between the sudgrid TKE and the total TKE. Profiles averaged over the last hour for each of the resolutions considered: (a) 2 m, (b) 3.125 m, (c) 6.25 m and (d) 12.5 m

of the boundary layer. Nevertheless, when the resolution decreases, the values are more spread, especially near the surface, but the TKE still decreases linearly with height up to the top of the boundary layer.

On the other hand, for any of the resolutions considered, the subgrid contribution ($TKE_{subgrid}$) is larger near the surface, where the most energetic eddies are smaller. Some models also present a secondary maximum of the ratio $TKE_{subgrid}/TKE_{total}$ near the inversion whereas in others models, such as UIB, this ratio decreases progressively with height. $TKE_{subgrid}$ is also larger when the resolution is coarser as the ratio $TKE_{subgrid}/TKE_{total}$ points out, since there are more "small" eddies that have to be parameterized by the turbulence scheme. On the contrary, this ratio decreases for larger resolutions and also the values are more concentrated.

To sum up, each participant model uses a different turbulence scheme and therefore the results are sensitive to it. The main differences between models occur towards the top of the boundary layer, since in the bottom the surface cooling rate and wind are prescribed. These differences are not reduced when the resolution increases due to the different surface vertical temperature flux that each model converges to (see Figure 5.3), since the models that introduce more mixing allow that the inversion layer can grow more. Nevertheless, models with similar SGS (Table 5.2) do not have the same behaviour.

To explain these differences of the results near the inversion, the attention must be focused on the advection scheme as well, besides the turbulence scheme. In previous LES intercomparisons (Bretherton et al., 1999a) it was found that there was a large sensitivity in the results on the advection schemes used, mostly near the inversion. Some advection schemes can be very diffusive and they will allow growing the inversion. On the contrary, some of them are less diffusive and the inversion can not grow easily. A further discussion regarding the advection schemes is done in the next section.

The Meso-NH results are usually between the high and low diffusive models. Nevertheless, the Meso-NH model belongs to the cluster of models for which the surface vertical temperature flux is smaller and then the boundary layer reaches smaller heights. Further results are described in the next section, as well as some sensitivity tests.

5.4 Sensitivity tests using Meso-NH model

Furthermore, some sensitivity tests using the Meso-NH model are performed. The effect on the resolution is inspected as well as the machine dependency, the advection scheme of the scalars, some parameters of the SGS and finally the surface cooling rate.

5.4.1 Testing the resolution

First of all, we have checked how the model is behaving when the resolution increases. The Meso-NH model has little sensitivity to the resolution (see Figure 5.7), although the major changes are observed in the module of the wind at the upper inversion. Nevertheless, not all the models behave in this way (see Figures 5.1, 5.2 and 5.4). Figure 7 in Beare et al. (2005) compares the sensitivity to the results on the resolution for models with three or more simulations down to 2 m or less. CORA and MO have more spread results than IMUK and UIB and therefore the results depend on the resolution considered. The boundary layer height is slightly larger for the coarser resolution since the surface vertical temperature flux is larger than in higher resolutions.

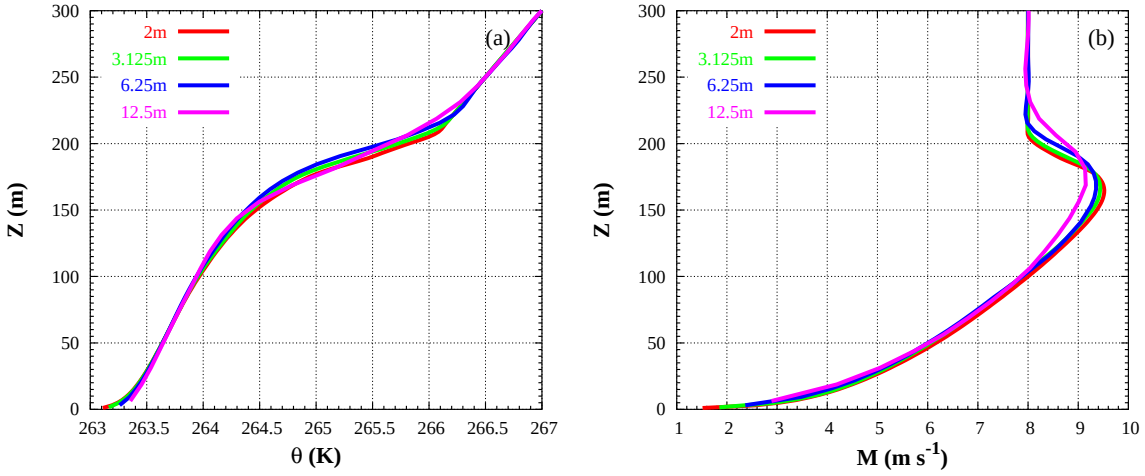

Figure 5.7: (a) Mean potential temperature (K) and (b) module of the wind (m s^{-1}) profiles averaged over the horizontal domain and over the last hour of integration for the GABLS case at: 2 m, 3.125 m, 6.25 m and 12.5 m resolution

The effect on the vertical temperature flux and on the resolved TKE budget when the resolution decreases is shown in Figure 5.8. The total vertical temperature flux is nearly independent of the resolution, but for the coarser resolution the proportion of the subgrid part increases dramatically and the total profile is less linear. Similar results were found in Figure 5.5 for the rest of the models. Then, the resolved contribution decreases and

the results are more dependent to the SGS. In the coarser resolution the model dissipates more to the smaller scales and the SGS contribution is larger. However, it is seems that Meso-NH works well since the SGS tries to supply the resolved contribution properly and keep the total contributions approximately constant.

The resolved TKE budget also points out that shear is the main factor to generate turbulence whereas the energy is lost by the dissipation to lower scales. The buoyancy is much weaker than shear but within these conditions might be an important mechanism of destruction, especially within the boundary layer. The resolved TKE budget for the coarser resolution also highlights that the resolved motions are very small. Nevertheless, the main factor to generate turbulence is still shear.

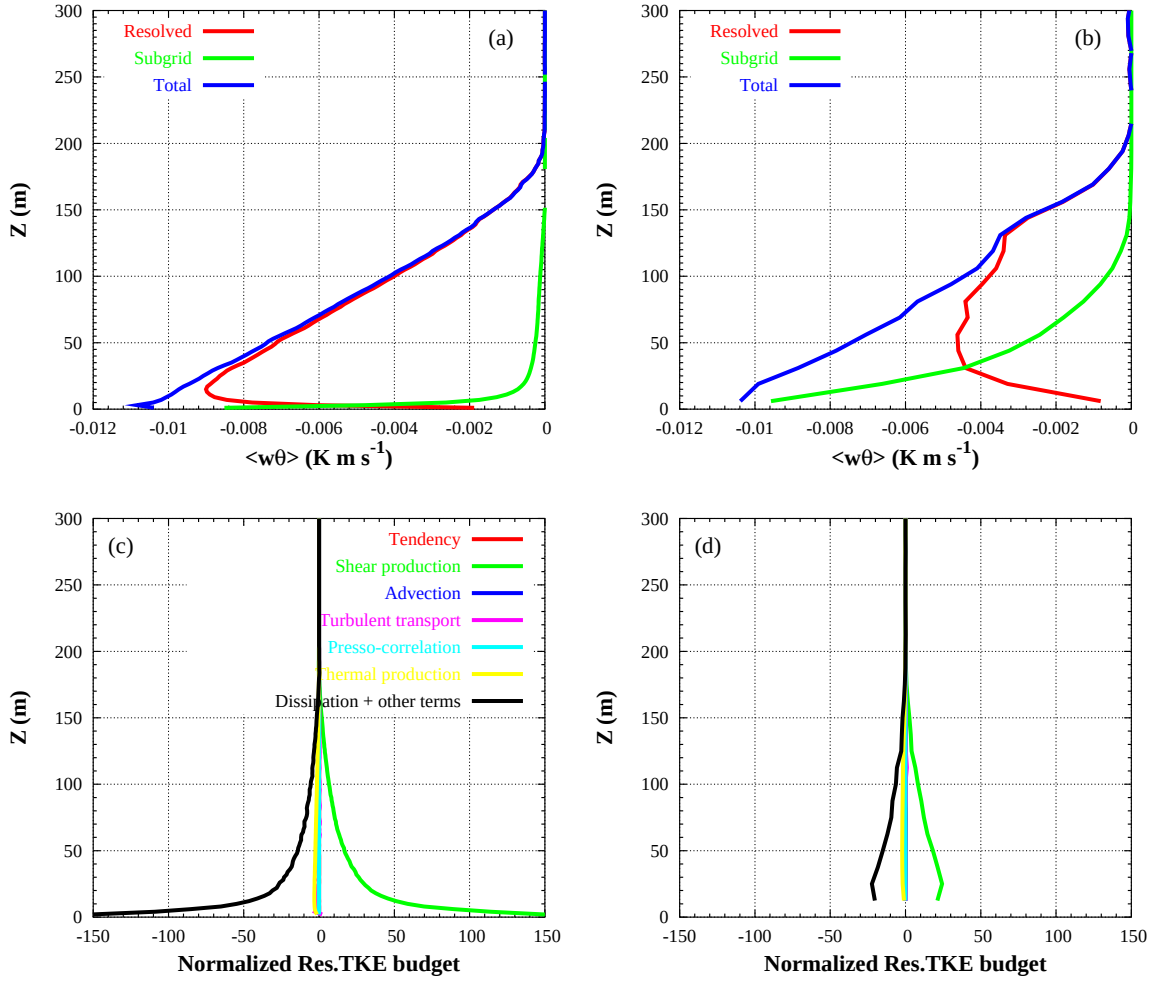

Figure 5.8: Resolved, subgrid and total contributions of the vertical temperature flux profiles (K m s^{-1}) for (a) 2 m and (b) 12.5 m resolution, and the resolved TKE budget (normalized by u_*^3/h_{BLH}, where h_{BLH} is the boundary layer height) for (c) 2 m and (d) 12.5 m resolution, averaged over the horizontal domain and over the last hour of integration

5.4.2 Machine dependency

To see whether the results depend on the computation machine, the runs have been done at the European Centre for Medium-range weather Forecasts (ECMWF) and locally, at the UIB-PC's cluster. The same model version is used and the only difference of these runs is the computer. The mean temperature, wind and vertical temperature flux profiles, as well as the vertically integrated resolved TKE, are shown in Figure 5.9. The mean profiles and time series at 6.25 m resolution are not dependent on the machine whereas the results at 12.5 m are very sensitive to it.

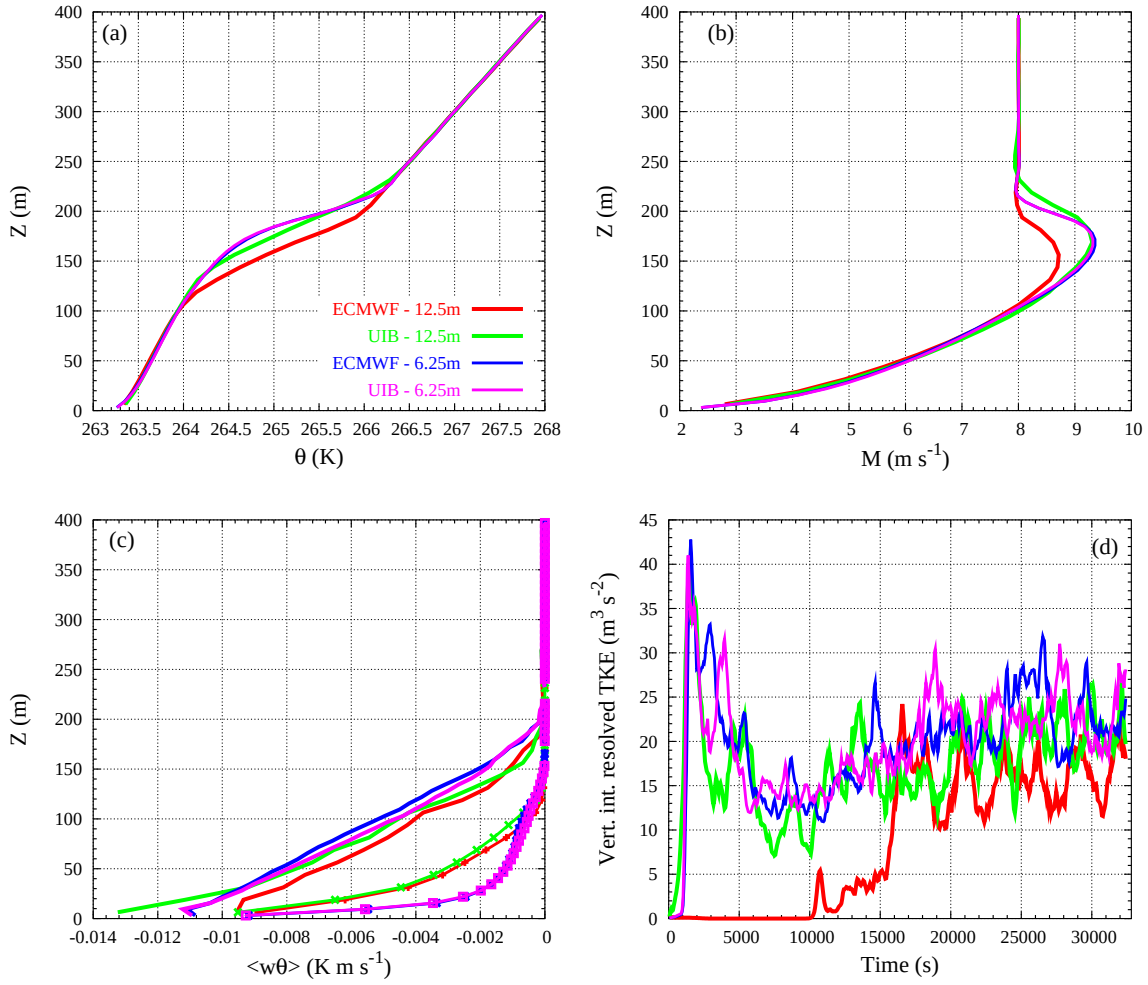

Figure 5.9: (a) Mean potential temperature (K), (b) module of the wind (m s^{-1}) (c) total (lines) and subgrid (lines and points) vertical temperature flux profiles (K m s^{-1}) for the 12.5 m and 6.25 m resolution GABLS case. (d) Time series of the vertically integrated resolved Turbulent kinetic Energy (TKE) (m^2 s^{-2})

For the 12.5 m resolution ECMWF runs, the model converges to a smaller energy and consequently the boundary layer height is smaller contrarily to those obtained at the

UIB-PC's cluster where the vertical temperature flux is larger as well as the boundary layer height. Moreover, the SGS contribution is larger for the ECMWF runs than for the UIB-PC's cluster. This is due to the fact that the length of the word is different in each computer. Then, at the ECMWF the length of the word is larger than at the UIB-PC's cluster and the gradients (computed as the differences of two variables) are smaller at the ECMWF than at UIB-PC's cluster. Since the fluxes are computed from the gradients, they are larger UIB-PC's cluster than at the ECMWF. Furthermore, the resolved motions at the ECMWF are activated later than at the UIB-PC's cluster (Figure 5.9.d). Since the gradients are smaller at the ECMWF, the resolved motions are not activated as soon as in the UIB-PC's cluster. During the beginning of the run (0-15000 s) the SGS contribution is equal to the total and this means that the model is not working properly, although the SGS is supplying it.

All of this differences disappear when the resolution increases, for instance at a 6.25 m resolution, since the profiles and time series are not dependent on the machine.

5.4.3 Advection scheme

In the Meso-NH model the advection scheme is used to simulate the advective transport of quantities such as temperature, water substances, turbulent kinetic energy, dissipation of turbulent kinetic energy and scalars (chemical species). The results send in the intercomparison (from now standard) were made using a positive definite centered second order scheme (FCT) but here the advection scheme is changed to a first order upstream scheme (MPDATA). Nevertheless, FCT and MPDATA are second-order accurate on space and time. The effects of varying the advection scheme on the mean profiles are shown in Figure 5.10.

Using the advection scheme MPDATA instead of FCT has a large impact at the boundary layer top, since the later is much more diffusive for the temperature (Figure 5.10.a). To overcome this problem, the number of iterations of MPDATA can be increased although the computer time also increases. Nevertheless, the maximum of the wind near the inversion still appears but it is weaker and higher than in the standard case due to the larger diffusion (Figure 5.10.b). The sensitivities to the advection scheme are not as large as to the turbulent scheme but they should be taken into account to explain the spread of the intercomparison results near the inversion (Figures 5.1 and 5.2). Moreover, the sensitivity of the results to the advection scheme is larger when the resolution is coarser. This might explain the differences between the models when the resolution is about 1 m or 2 m since the turbulence scheme contribution is very small at these resolutions. Regarding the turbulence, the subgrid contribution within the boundary layer and close

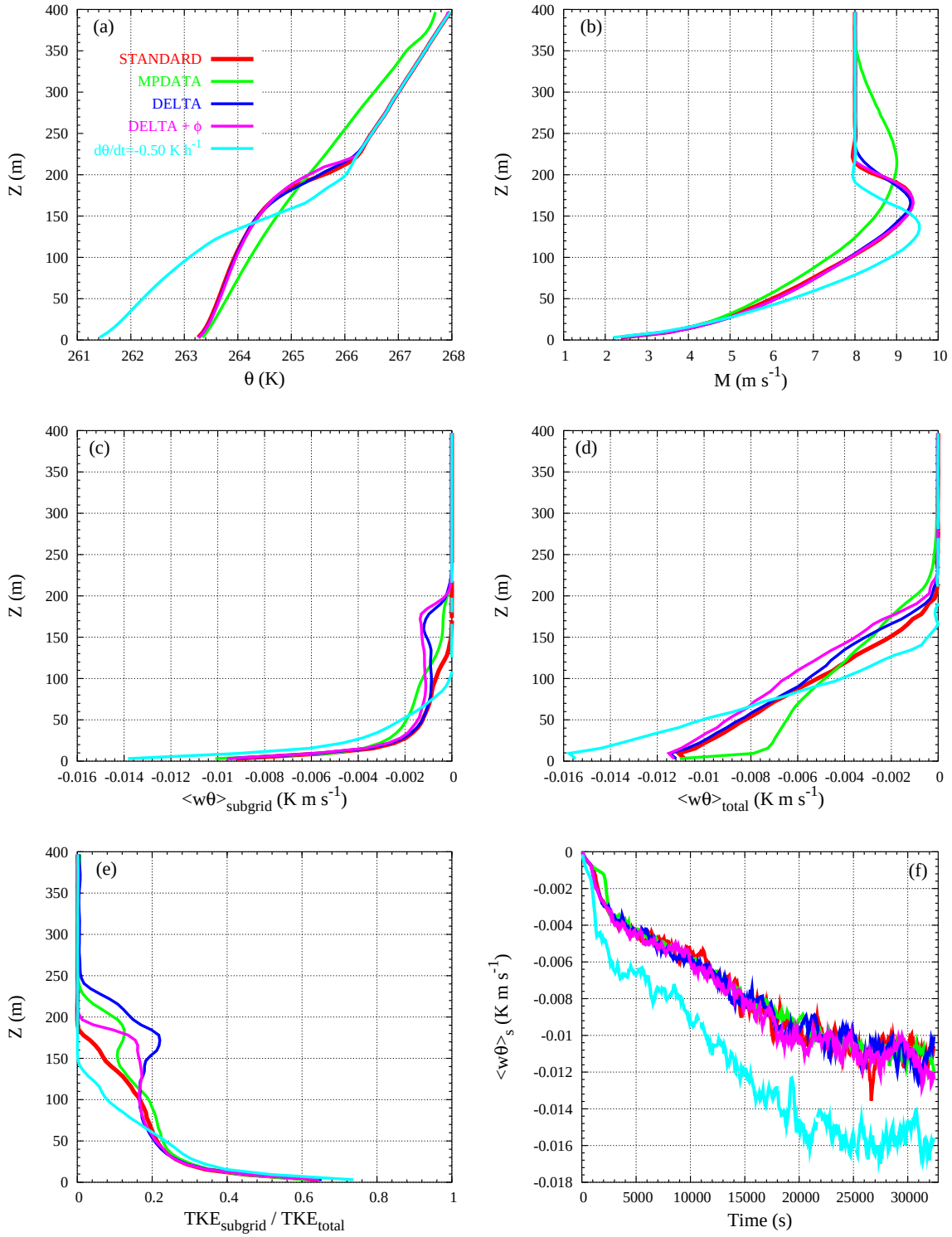

Figure 5.10: Profiles and times series obtained from the sensitivity tests: (a) Mean potential temperature (K), (b) wind speed (m s^{-1}), (c) subgrid and (d) total vertical temperature flux (K m s^{-1}), (e) ratio between the subgrid and total TKE and (f) vertical temperature flux, at the first computation level, time series (K m s^{-1}). These sensitivity tests have been done for the 6.25 m resolution case. The labels stand for: **STANDARD**: results submitted in the intercomparison, **MPDATA**: sensitivity to the advection scheme, **DELTA** and **DELTA+ϕ**: sensitivity to the subgrid scale scheme parameters and $\frac{d\theta}{dt}$ **= -0.50 K h^{-1}**: doubling the cooling rate

to the inversion slightly increases (Figures 5.10.c and 5.10.e) whereas the total vertical temperature profile presents a sharp slope within the boundary layer, as Figure 5.10.d shows. Nevertheless, near the surface the results are very close to the standard case as Figure 5.10.f points out.

5.4.4 SGS parameters

The sensitivities to some SGS parameters are also analyzed. In the Meso-NH SGS (Cuxart et al., 2000a) the fluxes are computed as Equation 2.3, but they can shorten as,

$$\begin{aligned} \overline{u_i\theta_i} &= -K\phi_i \frac{\partial\overline{\theta_i}}{\partial x_i} \\ K &= \frac{2}{3}\frac{\ell}{C_s}e^{1/2} \end{aligned} \tag{5.3}$$

where ϕ_i is the stability parameter ($\phi_i \neq 0$ when $i = 3$), ℓ the mixing length, e the turbulent kinetic energy and C_s a constant equal to 0.7. In the standard case $\phi_3 < 1$ and the considered mixing length is the proposed by Deardorff (see Equation 2.7). The parameters ϕ_i and ℓ have been modified to increase $K\phi_i$ and consequently the fluxes $\overline{u_i\theta_i}$ are larger since the subgrid mixing is more efficient.

First of all, the mixing length ℓ has been increased considering the Delta mixing length equal to the cube root of the grid size ($\ell = (\Delta x\Delta y\Delta z)^{1/3}$). The Delta mixing length is larger than the one proposed by Deardorff (1972) used in the standard case. These results are plotted in Figure 5.10 labelled as DELTA. The parameter $K\phi_i$ is increased more imposing ϕ_3=1, that is the maximum value that ϕ can have, as well as the mixing length equal to Delta ($\ell = (\Delta x\Delta y\Delta z)^{1/3}$). This result is labelled as DELTA+ϕ in Figure 5.10.

When $K\phi_i$ increases the value of the fluxes ($\overline{u_i\theta_i}$) are also larger and then the boundary layer can grow more (see Figures 5.10.a and 5.10.b). Although this effect is not very large, there are some sensitivity to the SGS parameters. The subgrid contribution increases, especially near the inversion where $\partial\overline{\theta_i}/\partial x_i$ in Equation 5.3 becomes larger (see Figures 5.10.c and 5.10.e). Therefore the total contribution of the flux is also slightly larger (Figure 5.10.e). Nevertheless, the surface vertical temperature flux does not change significantly near the surface as the time series in Figure 5.10.f indicates. It is worth mentioning that the sensitivity of the SGS parameters is large near the inversion, as the ratio between the subgrid and total TKE show (Figure 5.10.c), but the mean profiles do not significantly change (Figures 5.10.a and 5.10.b). Therefore, the turbulence properties change within the boundary layer whereas the mean profiles are not as much affected. These facts are

further discussed in the next chapter where the attention is focused in the analysis of the eddy structures.

5.4.5 Cooling rate

Finally, the effect of doubling the prescribed cooling rate is inspected, considering $d\theta/dt = 0.5$ K h^{-1} instead of the standard case ($d\theta/dt = 0.25$ K h^{-1}). With a double cooling rate, the boundary layer is shallower and colder as well as the inversion height is smoother (see Figure 5.10.a). In the same way, the maximum of the wind reaches lower levels and it is also more intense (Figure 5.10.b). The subgrid contribution is also larger (Figure 5.10.c) as well as the total (Figure 5.10.d). However, the ratio between the subgrid and total contribution is smaller (Figure 5.10.e) near the inversion because it is less sharp than in the standard case.

The stability parameter z/L, computed at 10 m according to the classification of Mahrt et al. (1998), is about 0.1 for the standard case and 0.2 when the surface cooling is doubled. Although this is a more difficult case because it is more stable, the model seems to behave properly because there is not a clear evidence of runaway cooling. In fact, both cooling rates give surface vertical temperature fluxes smaller than the one predicted by Derbyshire. For instance, if $R_{fc} = 1$ then $(< w'\theta' >_0)_{max}$ = -0.100 K m s^{-1} whereas $(< w'\theta' >_0)_{max}$ = -0.025 K m s^{-1} for $R_{fc} = 0.25$. These values are very large in comparison to the surface vertical temperature fluxes obtained after 9 hours: $< w'\theta' >_s$ = -0.012 K m s^{-1} for (dT/dt = 0.25 K h^{-1}) and $< w'\theta' >_s$ = -0.016 K m s^{-1} when the cooling rate is doubled.

5.5 Conclusions

Similar qualitative results are found for all the models that have participated in the intercomparison exercise. All models present a maximum of the wind speed at the inversion level and a decrease in the surface temperature. Nevertheless, the strength of the maximum of the wind, as well as the inversion height, is not equal for all models. In fact, the major differences occur near the inversion level, where the results are much spread. The sensitivity to the results on the resolution shows that when the resolution is larger the results obtained from different models tend to be more concentrated. On the contrary, near the surface the conditions are prescribed and all models converge to the same values.

Although the results depend on the turbulence scheme used, they are also sensitive to the advection scheme, especially when the resolution is smaller. Then, some models

have advection schemes that allow more mixing than others giving larger boundary layer heights.

To improve the knowledge of the LES model that we are using, some sensitivity tests have been performed such as to the advection scheme, the turbulence scheme parameters, the resolution and the prescribed surface cooling. Again, the results near the inversion are quite sensitive to any of the considered tests. Nevertheless, it is worth mentioning that the mean profiles do not significantly change when the resolution is increased or when the turbulence scheme parameters are adjusted to allow more mixing.

Although this is a simple LES of the SBL (only shear and surface cooling are considered) the results are very spread near the inversion. Is there any proposition more realistic? A comparison of the LES results showed here to observations, as the one described in chapter 4, can be used to find an answer but further work is still needed.

Chapter 6

FURTHER DIAGNOSTICS: PROBABILITY DENSITY FUNCTIONS[1]

Up to now, the LES results have been studied in terms of mean profiles averaged over the horizontal and over a period of time where the fields are stationary. In fact, this is a very common way to show the LES results. Nevertheless, from them it is not possible to get information about the eddy structures. The spectra computed from the LES give information about the energetical distribution of the eddies but we are also interested in studying how the eddy structures are organized in the SBL.

From the Probability Density Functions (PDFs) the probability of occurrence of each value is considered (whereas from the LES profiles each value has assumed to have the same probability). Since the mean values can be studied directly from the LES mean profiles, we are interested in the tails of the PDFs, which correspond to extremes events with low probability. To evaluate the performance of this methodology, the PDFs of a zero-mean wind Convective Boundary Layer (CBL) are computed and compared to those in the literature. Then, the PDFs of the LES described in the previous chapter are computed.

Through the combined inspection of the horizontal cross-sections, the spectra and the PDFs we can get a more complete picture of the physical processes that take place within the SBL. Moreover, the sensitivity of the shape of the PDFs on the resolution is also explored as well as the Gaussianity and the ergodocity (the field is stationary and

[1]This chapter is based on: Jiménez, M.A., and Cuxart, J., 2005b: Study of the probability density functions from a Large-eddy simulation for a stably stratified boundary layer, *Boundary-Layer Meteorology*, in Press.

homogeneous at the same time).

6.1 Introduction

Turbulent flows can be studied through the inspection of their eddy structures, in the laboratory, in numerical models at very high resolution, and in real geophysical flows. To summarise the turbulence characteristics of the flow, some statistical approach must be taken. Usually the Reynolds decomposition to a mean value and fluctuations is made, and the turbulence is often described through the variances and the covariances of the fluctuations.

If the flow has a clear gap in the energy spectrum, a spatial filter of a scale similar to the gap scale will be adequate to perform the separation into mean and fluctuating scales. As explained in Monin and Yaglom (1971), space, time or space-time averaging are very convenient for practical applications, but an adequate filter function has to be used. They propose another method that has simpler properties, the probability-theory treatment of the variables in a turbulent flow as random fields. It requires considering the flow under study as a statistical ensemble of all similar flows under some fixed external conditions. This is difficult to make for real natural turbulence, because the external conditions vary constantly, but it is possible for a laboratory experiment (either physical or numerical). The key parameter in this study is the probability density function (PDF), which can be constructed for each variable or combination of variables (joint PDF). In this framework, the Reynolds axioms are satisfied exactly.

From the pioneering works of Kampé de Fériet (1939) and the Kolmogorov school (Millionshchikov, 1939), several authors have illustrated the applicability of this approach (see references in Monin and Yaglom, 1971). More recently, several studies have been made using observations and physical laboratory experiments. Mahrt and Paumier (1984) used the joint PDFs to explain the basic features of the cloudy boundary layer. Deardorff and Willis (1985) studied a convective mixed layer in a laboratory tank and compared the joint PDFs to those obtained by Mahrt and Paumier (1984), finding comparable results. Thoroddsen and Van Atta (1992) made a similar experiment in a wind tunnel for a stably stratified regime varying the Reynolds number, and the PDFs were nearly Gaussian for the density. Chu et al. (1996) studied the Gaussianity of the PDFs for three different observed atmospheric stability conditions. It is interesting to mention that Wang and Stevens (2000) computed the Joint PDFs from two cloudy Large-Eddy Simulations (LES) and used them to study the differences between the convective circulations in a shallow cumulus and a stratocumulus regime.

Here, an attempt to compute PDFs from a high resolution LES of a stably stratified boundary layer (SBL) is made. The number of large structures might not be very large, as pointed out Larson et al. (2001), but this limitation is shared by other non-LES studies such as Deardorff and Willis (1985) or Chu et al. (1996). Since the LES structures depend significantly on the subgrid scheme that is used, the comparison of PDFs could be a supplementary output in LES intercomparisons, beyond the classical comparison of averaged values. Furthermore, the PDFs can be a supplementary tool to compare the LES results to observations, as it will be described in chapter 7.

The methodology followed in the construction of the PDFs from the LES results is explained and it is evaluated with an LES of a CBL. Then, this methodology will be applied in the computation of the PDFs from a stably stratified case (the first stable LES GABLS case described in the previous chapter). The shapes of the PDFs will be explained through the inspection of the observed structures, the spectra and the statistical moments.

Another important issue to be addressed is that of ergodicity. If the data analysed are all for a single instant or for a time series of a single location, the hypothesis of ergodicity is implicitly made, that is, that the turbulence statistics obtained from a time or space PDF are supposedly equivalent to those obtained from an ensemble PDF of many instants and locations considered together. The LES methodology provides means to investigate this point for some regimes.

Finally, the sensitivity to the PDFs on the resolution is studied. Therefore, the PDFs are computed from the same simulation at two smaller resolutions over the same domain. It is found that the degradation of the resolution affects the PDFs and the moments obtained from them.

6.2 Construction of the Probability Density Functions from an LES

The PDFs of any field x (for instance the three components of the wind - u, v, w, where u is aligned with the geostrophic wind - or the potential temperature, θ) are computed taking one horizontal field every minute during the period of interest. B(x) is the probability of finding x between x and $x \pm \Delta x$, where Δx is the bin or interval size, and it is normalized as $\int_{-\infty}^{\infty} B(x)dx = 1$. The graphical representation of B(x) is usually $\sigma_x B(x')$ where $x' = \frac{x-\overline{x}}{\sigma_x}$, $\overline{x}$ the mean value and σ_x the standard deviation. This allows a better comparison of different PDFs. To inspect the tails, a logscale is chosen for the y-axis.

From the PDFs it is possible to compute some statistics such as the mean value and

higher order moments (Tennekes and Lumley, 1972) as

$$\overline{x} = \int_{-\infty}^{\infty} xB(x)dx \tag{6.1}$$

$$\sigma_x^2 = \overline{x^2} = \int_{-\infty}^{\infty} (x-\overline{x})^2 B(x)dx \tag{6.2}$$

$$S_x = \frac{\overline{x^3}}{\sigma_x^3} = \frac{1}{\sigma_x^3}\int_{-\infty}^{\infty} (x-\overline{x})^3 B(x)dx \tag{6.3}$$

$$K_x = \frac{\overline{x^4}}{\sigma_x^4} = \frac{1}{\sigma_x^4}\int_{-\infty}^{\infty} (x-\overline{x})^4 B(x)dx \tag{6.4}$$

The second order moment is the variance σ_x^2 and its square root the standard deviation σ_x. The third moment divided by σ_x^3 is the skewness (S_x), which gives a dimensionless measure of the asymmetry, and the fourth moment divided by σ_x^4 is the kurtosis or flatness factor (K_x). A Gaussian distribution has zero skewness and a kurtosis value of 3.

It is important to note that the shape of the PDFs changes depending on the bin size considered (Δx). Therefore, there is also a dependency of the moments computed from them, as it will be shown later.

From previous works (Deardorff and Willis, 1985, for instance), it is known that the shape of the PDFs depends on the structure of the analyzed field. In an LES, the structure of the large eddies depends to some extend on the characteristics of the subgrid scheme and the conclusions must always be subject to caution. This might explain some differences with the PDFs obtained from observations, especially in the extreme values. Moreover, the resolution chosen can also modify the shape of the PDF. This will be further explored in the next sections.

6.3 Evaluation of the procedure for a Convective Boundary Layer

6.3.1 Description of the case

As mentioned in the introduction, the convective boundary layer has received special attention in the study of the statistical approach of the turbulence. A zero-mean wind CBL (ZW-CBL) LES case, based on the intercomparison proposed by Nieuwstadt et al. (1993), is studied here as an initial evaluation case. The horizontal domain is 6400 m $\times$ 6400 m, and 2400 m in the vertical with grid sizes of 160 m $\times$ 160 m $\times$ 50 m in x, y and z directions. The convection is driven by a constant temperature flux at the surface of

$< w'\theta' >_s = 0.06$ K m s^{-1}. The temperature inversion is at a height of about $z_{i0} = 1.6$ km, where z_{i0} is the boundary layer height. Four scaling parameters are introduced:
(i) the scaling height (z_{i0})
(ii) the convective velocity scale (w_*) defined as,

$$w_* = ((\frac{g}{\theta_0}) < w'\theta' >_s z_{i0})^{\frac{1}{3}} \tag{6.5}$$

where g is the gravitational acceleration, θ_0 the reference temperature ($\theta_0 = 300$ K)
(iii) the time scale ($t_* = z_{i0}/w_*$).
(iv) the temperature scale ($\theta_* = \frac{<w'\theta'>_s}{w_*}$)

Considering $z_{i0} = 1.6$ km and $< w'\theta' >_s = 0.06$ K m s^{-1}, the typical turnover time (t_*) is of 15 min, the velocity scale (w_*) is equal to 1.46 m s^{-1} and the temperature scale is 0.041 K.

The initial profiles are taken as:
• for $z < z_{i1} = 0.844\ z_{i0}$

$$\theta = \theta_0 + 0.1r(1 - \frac{z}{z_{i1}})\theta_* \tag{6.6}$$
$$w = 0.1r(1 - \frac{z}{z_{i1}})w_* \tag{6.7}$$
$$u = v = 0 \tag{6.8}$$

• for $z > z_{i1}$

$$\theta = \theta_0 + (z - z_{i1})\Gamma \tag{6.9}$$
$$u = v = w = 0 \tag{6.10}$$

where r stands for a random number uniformly distributed between -0.5 and 0.5 and the constant temperature gradient above the boundary layer is $\Gamma = 0.003$ K m^{-1}. Furthermore, the roughness length is taken to be $z_0 = 0.16$ m. We explore the simulation already made in Cuxart et al. (2000a) using the MESO-NH model.

The averaged profiles for the last hour and over the horizontal domain (Figure 6.1), after reaching a quasi-stationary state ($10t_*$), are similar to those obtained by Nieuwstadt et al. (1993). Within the boundary layer, the temperature profile is nearly constant (Figure 6.1.a) whereas the vertical temperature flux is maximum near the ground and decreases with height (Figure 6.1.b) up to the top of the boundary layer where it is negative because of the entrainment flux. As Nieuwstadt et al. (1993) pointed out, the

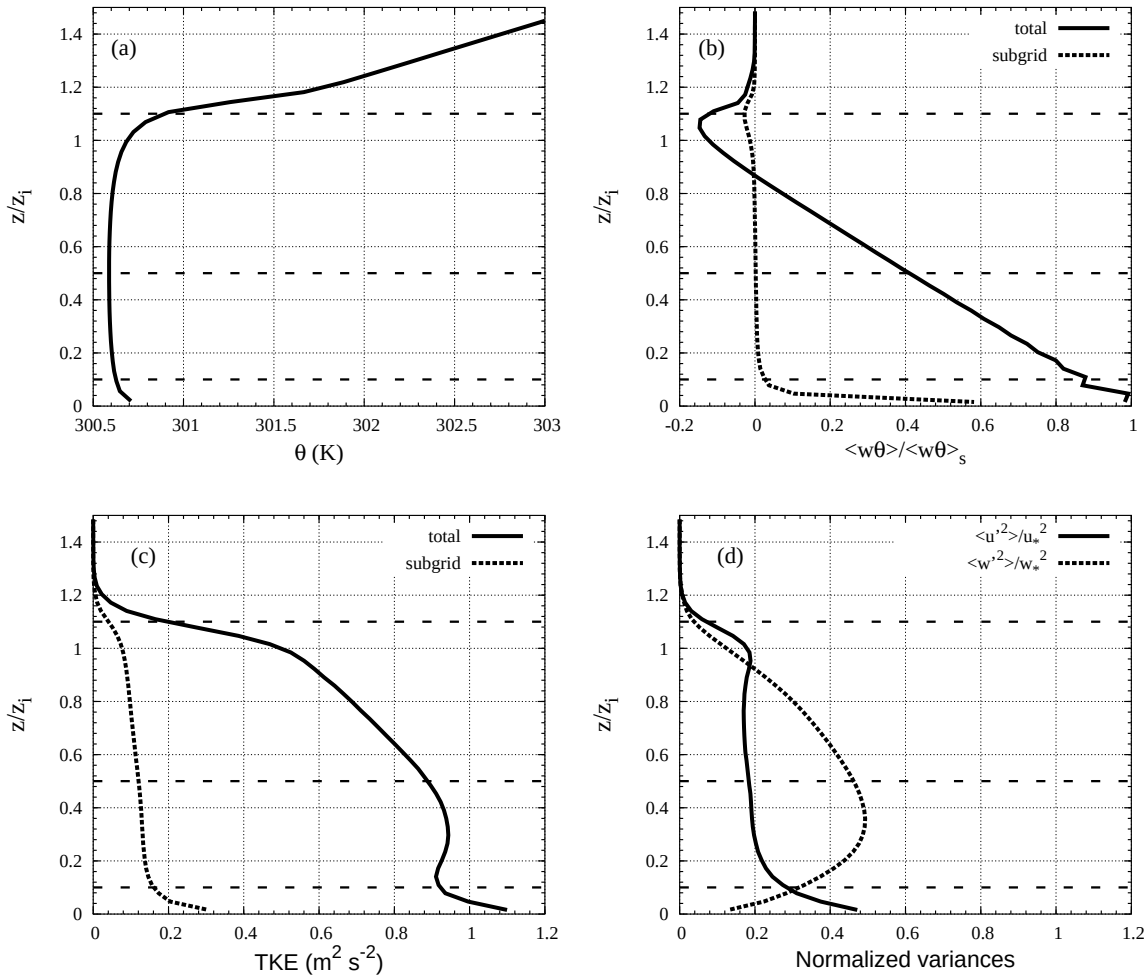

Figure 6.1: Mean profiles for the zero-mean wind CBL LES case: (a) Mean potential temperature (K), (b) total and subgrid vertical temperature flux (normalized by its surface value), (c) total and subgrid TKE (m^2 s^{-2}) and (d) normalized variances of $< u'^2 >$ and $< w'^2 >$. The horizontal discontinuous lines indicate the levels where the PDFs have been computed

contribution by the subgrid vertical temperature flux is small except near the surface where the eddies are smaller. These simulated conditions are similar to those measured in Deardorff and Willis (1985) as Nieuwstadt et al. (1993; Figures 3 and 4) point out.

Near the ground, the major contribution of TKE is from the variance of u because the ground acts as a rigid lid changing the circulations when arriving close to it. Moreover, the ground is the source of the heated updrafts that force circulations as well. On the other hand, the inversion level is not a boundary condition as rigid as the surface since it is deformed by thermals. Within the boundary layer, the variance of w is larger corresponding to the levels where the plumes are formed.

The horizontal and vertical cross-sections for w at the heights indicated in Figure 6.1

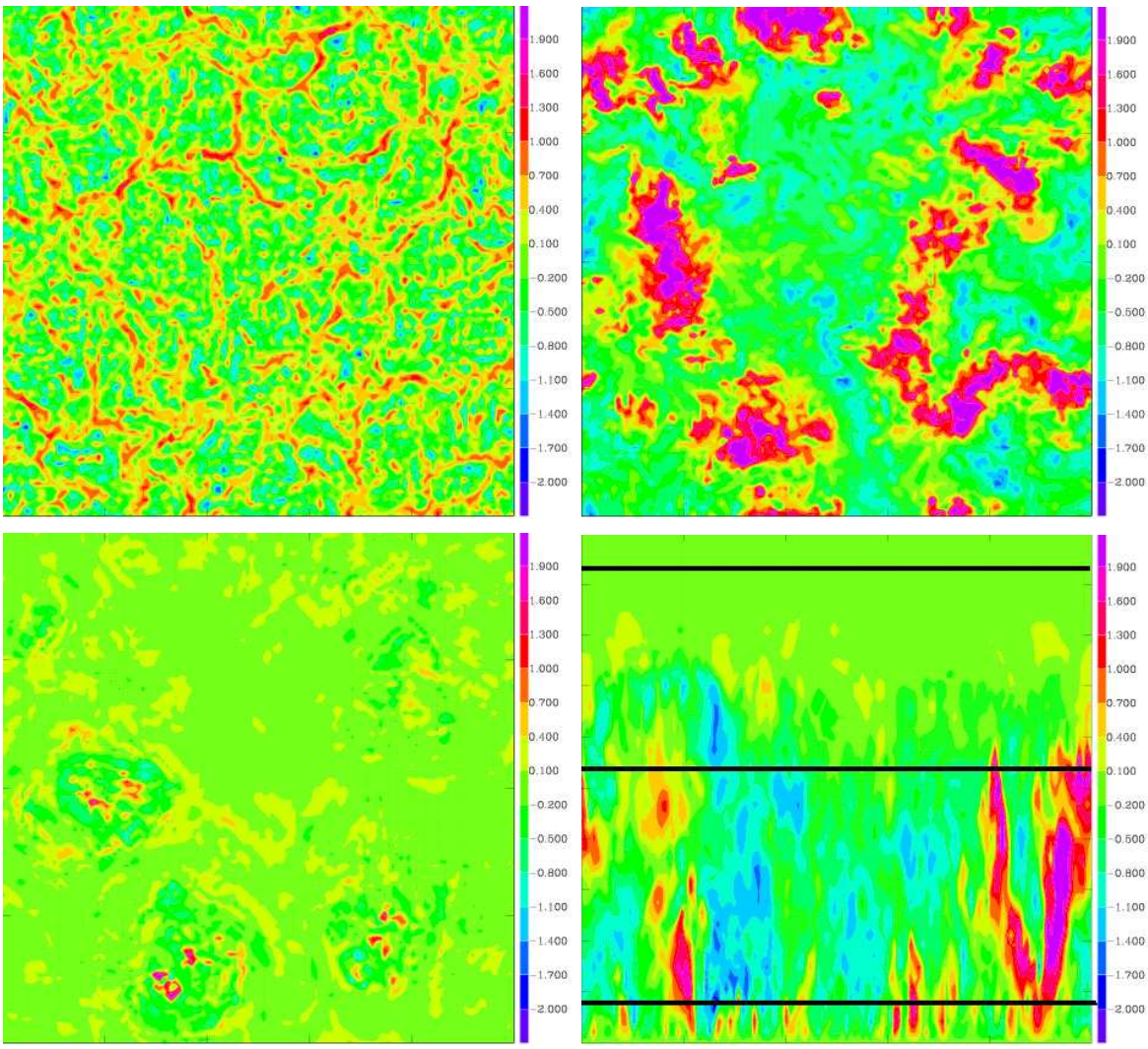

Figure 6.2: Horizontal cross-sections for w (m s^{-1}) for the zero-wind CBL case at: (top left) z/z$_i$=0.1, (top right) z/z$_i$=0.5, (bottom left) z/z$_i$=1.1 (interval: 0.3 m s^{-1}). In (bottom right) a vertical cross-section for w in the transversal direction. Horizontal black lines indicate the levels where the horizontal cross-sections are plotted

are shown in Figure 6.2. Since this is a zero-wind CBL, the structures are not aligned with the mean flow, as it was shown previously in chapter 3 for stable runs (see cross-sections in Figures 3.5 and 3.6). If a shear-driven CBL is considered, the eddy structures are aligned with the mean flow direction as Moeng and Sullivan (1994) point out. Near the ground, the flow structure is determined by some powerful updrafts surrounded by weak downdrafts. The eddy structures grow in height up to the top of the boundary layer where the updrafts are weak surrounded by strong downdrafts. Above the boundary layer height (z/z_i =1.1) there are still some structures corresponding to the plumes that can cross the inversion. The vertical structures tend to span the vertical domain (Figure 6.2) but when the wind is considered the structures tend to be concentrated at scales roughly one-half of the boundary layer height.

6.3.2 Probability Density Functions computed from a zero-mean wind Convective Boundary Layer

The PDFs are computed at three levels: near the ground ($z/z_i = 0.1$), the middle ($z/z_i = 0.5$) and the top of the boundary layer ($z/z_i = 1.1$), corresponding to the horizontal cross-sections in Figure 6.2, taking one field every minute during 1 hour. The PDFs of the vertical wind (w) and the potential temperature (θ) are shown in Figure 6.3. The results in the surface layer are compared to those found by Chu et al. (1996) using observational data (a time series of 900 s at a height of 3 m for an unstable case with a mean wind velocity of 1.87 m s^{-1}).

Near the ground, the shape of the PDFs is similar to Chu et al. (1996) and the values of skewness and kurtosis for w and θ are slightly underestimated (Figure 6.4). It is important to notice that the measured conditions are not exactly equal to those simulated in the LES. All scales of motions are present in the observations whereas the PDFs and moments computed here from LES results only contain the explicitly resolved contribution. This fact might explain the differences in the PDFs obtained from LES and observations. Furthermore, an ensemble average from the LES is compared to a time average from a single observational location, which implies that the hypothesis of ergodicity is made for observations. This will be further explained later.

As Moeng and Rotunno (1990; Figure 1) point out, near the ground there is a good agreement between S_w computed from LES (Moeng and Wyngaard, 1988) and measurements (Lenschow et al., 1980; Wyngaard, 1988). Within the boundary layer, the LES indicates a further increase of S_w with height up to z/z_i =0.9 where it is maximum and decreases sharply up to z/z_i =1. On the other hand, the observations show a nearly

constant value of S_w along the boundary layer, decreasing slightly at z/z_i =1. LeMone (1990) suggests that this difference between LES and observations are due to the presence of clouds, precipitation or larger scale forcings that are not taken into account in the model. Nevertheless, our LES results have similar behaviour for S_θ and S_w as Moeng and Rotunno (1990).

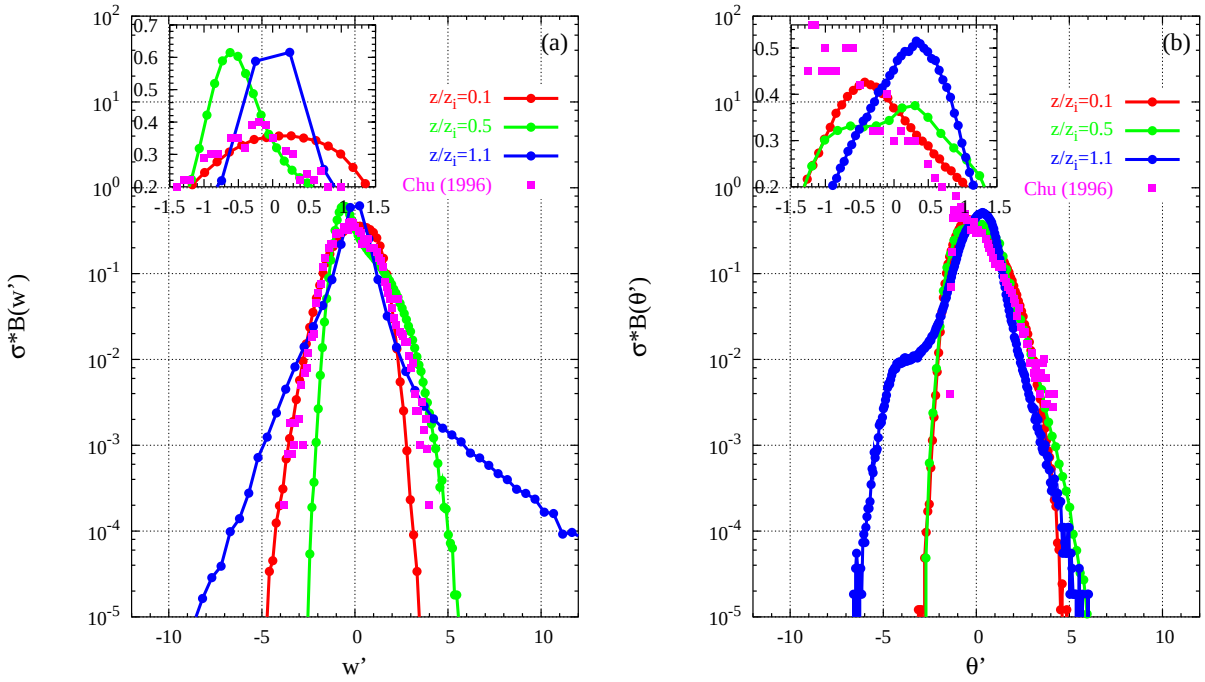

Figure 6.3: Normalized PDFs for (a) w and (b) θ obtained from the zero-mean wind CBL LES case near the ground (z/z_i=0.1), in the middle (z/z_i=0.5) and in the top (z/z_i=1.1) of the boundary layer. The PDFs computed from observations near the ground by Chu et al. (1996) are indicated in squared points. In the top left of both figures there is a zoom of the upper part of the PDFs

The kurtosis behaviour is similar to Deardorff and Willis (1985); K_w and K_θ increase with height since the values are more clustered around the mean ones at the top boundary layer.

The PDFs for the horizontal velocity components appear relatively Gaussian as in Deardorff and Willis (1985). Nevertheless, B(w) and B(θ) are only Gaussian near the ground, as it was found in Chu et al. (1996), since the skewness and kurtosis values are close to the Gaussian ones. At higher levels (z/z_i = 0.5 and z/z_i =1.1) the strong plumes made the PDFs less symmetric and therefore the skewness and kurtosis values depart more to the Gaussian values.

To sum up, the PDFs of a zero-wind CBL are comparable to those computed previously from LES and measurements of the CBL. From the PDFs it is possible to determine

the intensity of the pair of updrafts/downdrafts. Furthermore, the shape of the PDFs depends on the eddy structures present in the flow. This test case encourages to apply this methodology to a stably stratified LES case to further study the runs than using mean profiles.

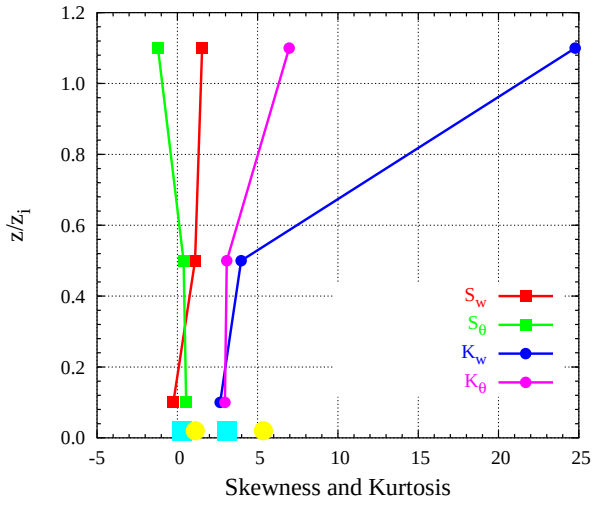

Figure 6.4: Skewness and kurtosis values computed from the zero-mean wind CBL LES case for w (squares) and θ (circles) at each considered level. Separated points indicate the values obtained by Chu et al. (1996) at 3 m

6.4 Application of the methodology to the GABLS stable LES case

6.4.1 Probability Density Functions of a stable case

The PDFs for the stable GABLS LES case at 3.125 m resolution are described in this section but later a further discussion on the sensitivity to the PDFs on the resolution chosen is shown. The PDFs have been computed at three levels: one near the surface (z/z_i=0.1), another in the interior of the SBL (z/z_i=0.5) and another one at the upper part of the inversion ($z/z_i = 1.1$). Here z_i is the value of the boundary layer height during the stationary part of the run, defined as in the intercomparison case (the height at which $(\overline{u'w'}^2 + \overline{v'w'}^2)^{1/2}$ falls to 5% of its surface value (u_*^2), divided by 0.95). However, we take the upper level at 1.1 z_i because there are still turbulence motions above z_i and it is a level where upper-air entrainment in the SBL takes place. These levels are indicated in Figure 6.5 by horizontal discontinuous lines, and the corresponding horizontal cross-

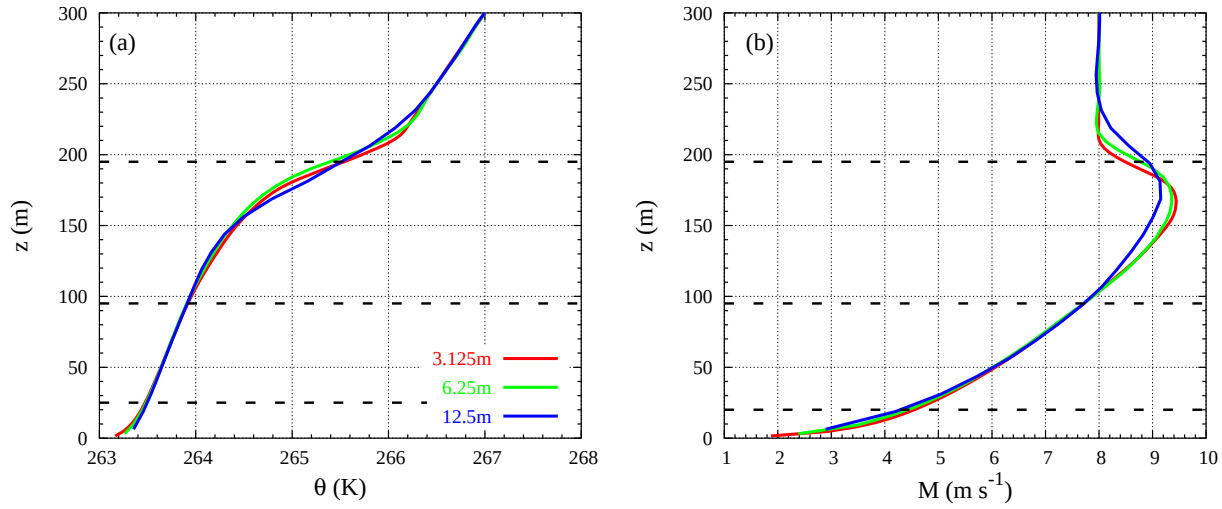

Figure 6.5: (a) Mean potential temperature (K) and (b) Mean wind (m s^{-1}) profiles for the GABLS LES case at: 3.125 m, 6.25 m and 12.5 m resolution. The horizontal discontinuous lines indicate the levels where the PDFs have been computed

sections for the u component of the wind are displayed in Figure 6.9, together with a vertical cross-section.

For the 3 levels considered, the PDFs are computed for the three components of the wind (u, v, w) and θ , taking one field every minute during the eight hour of integration. Therefore 128×128×60 different points are used to construct each PDF. In Figure 6.6 the resulting PDFs for the wind components (B(u), B(v) and B(w)) and the temperature (B(θ)) are given. The corresponding moments for u, v, w and θ are shown in Table 6.1.

The mean value and the standard deviation are almost equal to the values provided by the standard method of computing them in LES, that is, the sum of all the values divided by the number of points, considering that all of them have the same probability. The sensitivity to the bin size is also indicated in Table 6.1 where the error indicates the variation of each moment when a bin size is changed. In this case, it is found that the mean values are not sensitive to the bin size if the PDFs are built with approximately more than 10 intervals (i.e. $\frac{(X_{max}-X_{min})}{\Delta x} \geq 10$ where X_{max} and X_{min} are the maximum and minimum values of the field and Δx the considered bin size). Nevertheless, the shape of the PDFs changes when the number of intervals decreases, as Figure 6.7 points out.

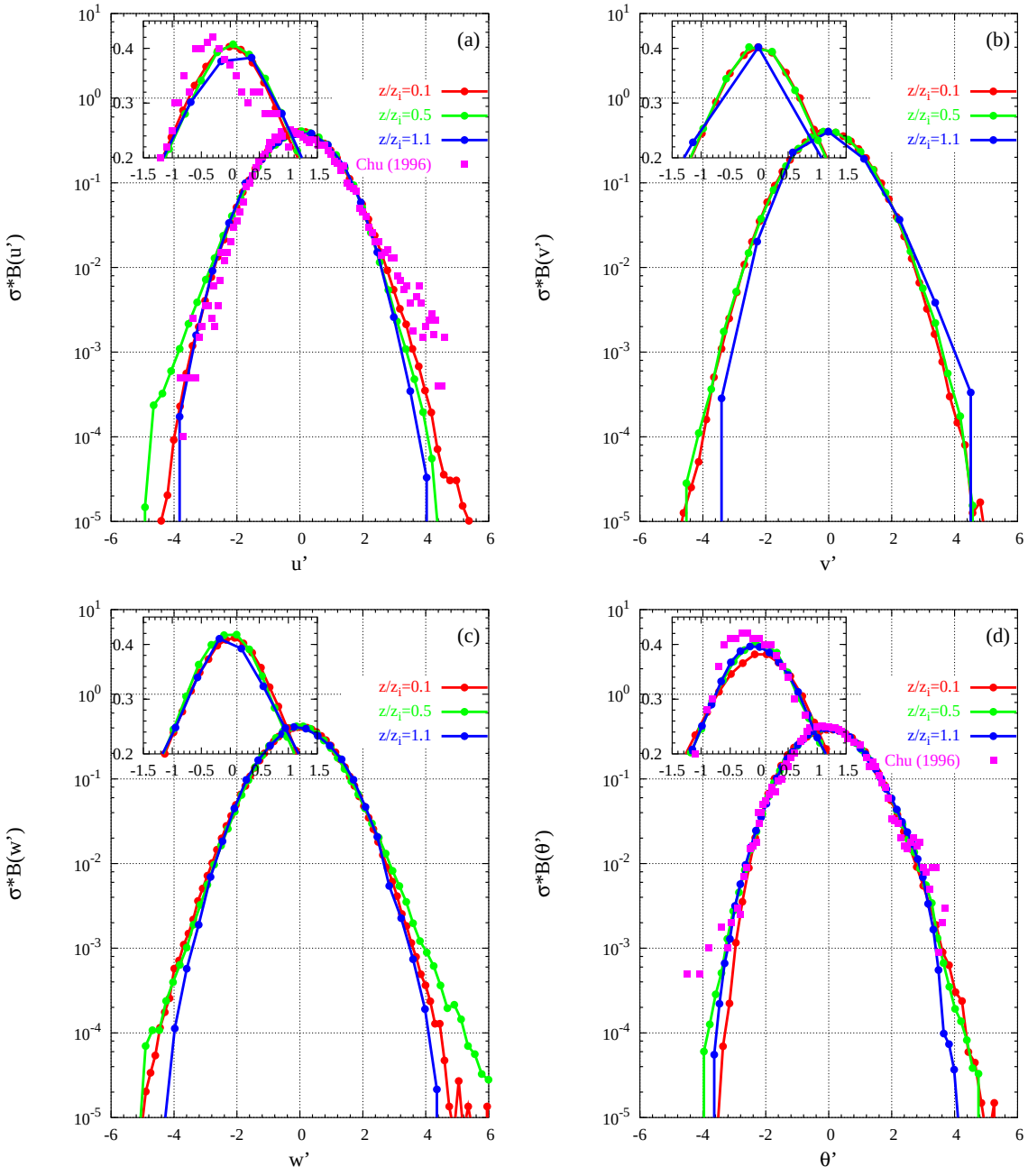

Figure 6.6: Normalized PDFs for (a) u, (b) v, (c) w and (d) θ obtained from the 3.125 m resolution GABLS LES case at the three studied levels. The PDFs computed from observations near the ground by Chu et al. (1996) are indicated in empty squares. In the top left of both figures there is a zoom of the upper part of the PDFs

Table 6.1: u, v, w **and** θ **statistics of the 3.125 m resolution stable GABLS LES case computed from PDF for each level studied. The error is due to the change of the bin sizes in the computation of the PDFs**

	z/z_i=0.1	z/z_i=0.5	z/z_i=1.1
$\bar{u}$ (m s^{-1})	3.859±0.000	7.032±0.000	8.480±0.001
σ_u (m s^{-1})	0.501±0.003	0.362±0.004	0.191±0.007
S_u	0.038±0.001	-0.168±0.005	-0.099±0.002
K_u	3.081±0.006	3.195±0.003	2.846±0.004
$\bar{v}$ (m s^{-1})	2.559±0.000	3.094±0.000	0.151±0.001
σ_v (m s^{-1})	0.413±0.003	0.251±0.006	0.084±0.015
S_v	0.021±0.001	0.055±0.002	0.369±0.030
K_v	3.018±0.002	3.119±0.004	3.231±0.050
σ_w (m s^{-1})	0.266±0.001	0.184±0.001	0.106±0.003
S_w	-0.044±0.001	0.127±0.002	0.020±0.003
K_w	3.260±0.003	3.524±0.010	2.973±0.005
$\bar{\theta}$ (K)	263.677±0.000	264.136±0.000	265.589±0.001
σ_θ (K)	0.097±0.001	0.108±0.001	0.121±0.003
S_θ	0.125±0.003	0.123±0.008	0.020±0.004
K_θ	2.842±0.006	3.021±0.004	2.974±0.004

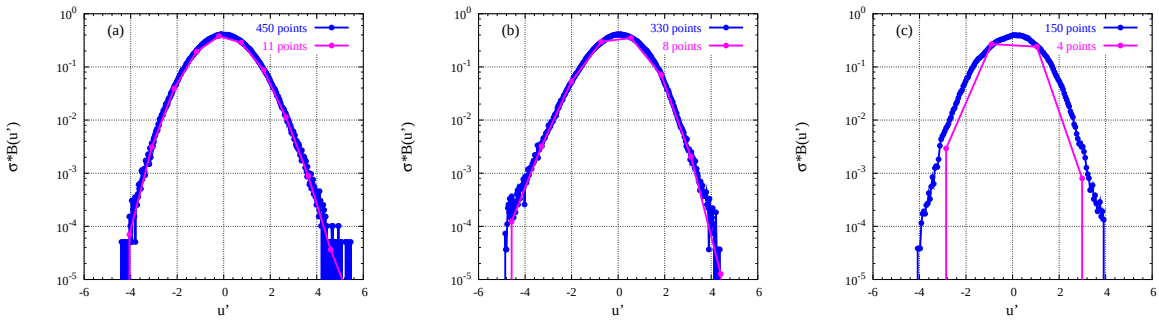

Figure 6.7: Sensitivity of the PDFs to the bin sizes. PDFs computed at the three considered levels: (a) $z/z_i = 0.1$, (b) $z/z_i = 0.5$ and (c) $z/z_i = 1.1$. Two different number of intervals have been considered ($\Delta u = 0.5$ m s^{-1} and $\Delta u = 0.01$ m s^{-1}) to change the number of intervals that the PDF is constructed

6.4.2 Gaussianity of the Probability Density Functions

The Kolmogorov-Smirnov test (Wilks, 1995) is used to check the Gaussianity of the computed PDFs in the same way as Larson et al. (2001). This test is applied to the cumulative distribution function (CDF) which is defined as:

$$B(\xi) = \frac{dC(\xi)}{d\xi} \tag{6.11}$$

where B(ξ) is the PDF, C(ξ) is the CDF and ξ any variable. The fit of the PDF to a Gaussian shape for any variable ξ is $G(\xi) = C\exp(-\frac{(\xi-\overline{\xi})^2}{\sigma_\xi^2})$. In the Kolmogorov-Smirnov test, the parameter D is computed to evaluate if the PDF is Gaussian or not:

$$D = max\sum_i |C(\xi) - G(\xi)| \tag{6.12}$$

where C(ξ) is the CDF and $G(\xi)$ the Gaussian fit. The goodness of the Gaussian fit is evaluated comparing D to a given values that are found in statistical tables depending on the rejection level (μ). Therefore, the distribution is considered Gaussian if D is smaller than the tabulated value, for a given μ.

If a rejection level of 5% is taken, the test considers B(u), B(v), B(w) and B(θ) Gaussian at every studied level. Fields as different as those shown in Figure 6.9.a and 6.9.c are considered Gaussian, although the first presents more elongated structures.

The Gaussian fits for the B(u), B(v), B(w) and B(θ) for the GABLS LES case are shown in Figure 6.8. Although the Kolmogorov-Smirnov test considers B(u), B(v), B(w) and B(θ) to be Gaussian, the tails slightly depart from the Gaussianity, especially in the levels where S and K are not exactly equal to the Gaussian values (S=0, K=3), as Table 6.1 indicates. Near the ground, the shape and the tails of the PDFs as well as their corresponding Gaussian fits, are similar to those obtained in Chu et al. (1996).

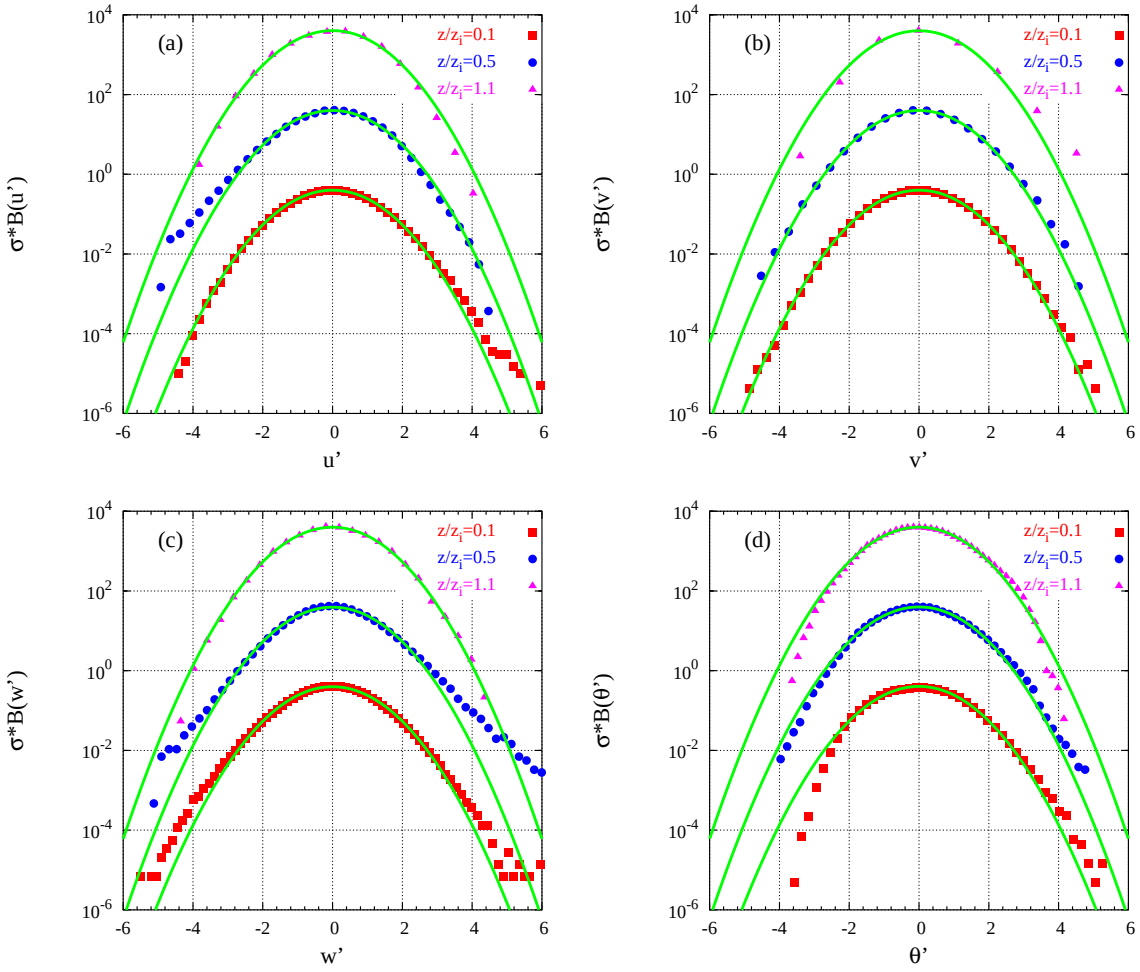

Figure 6.8: Gaussian fit of the PDFs obtained from (a) u, (b) v, (c) w and (d) θ for the 3.125 m resolution GABLS LES case at each studied level. The upper two curves have been shifted up 2 and 4 decades to clarify the intercomparison

6.4.3 Eddy structures and spectra

Within the SBL, the structures are characterized by the appearance of alternating streaks of high and low speed aligned approximately in the mean flow direction near the surface (Figure 6.9), a level where the eddies are smaller than in the middle of the SBL.

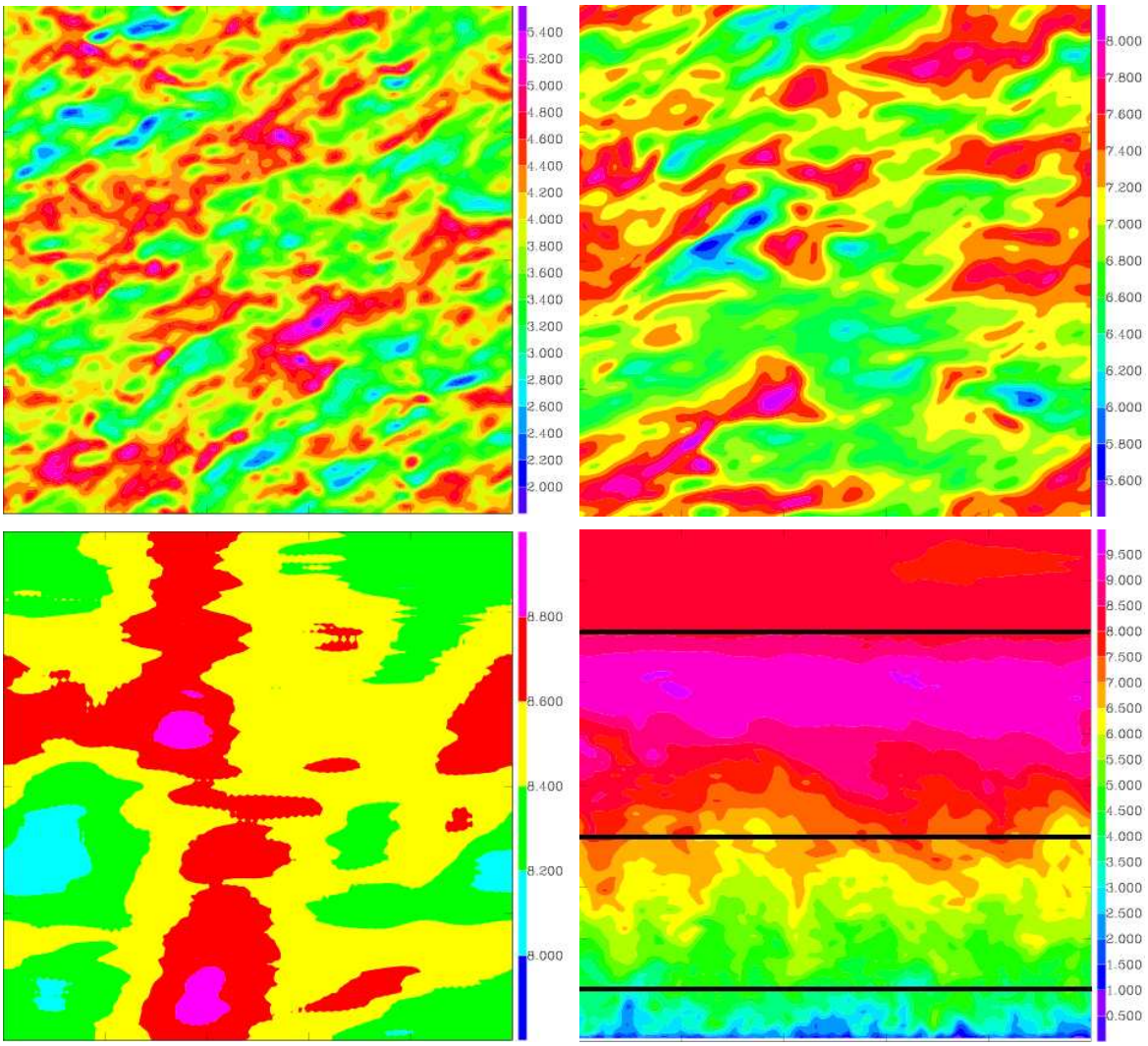

Figure 6.9: Horizontal cross-sections for u (m s^{-1}) for the 3.125 m resolution GABLS LES case at: (top left) z/z$_i$=0.1, (top right) z/z$_i$=0.5, (bottom left) z/z$_i$=1.1 (interval: 0.2 m s^{-1}). In (bottom right) a vertical cross-section for u in the transversal direction (interval: 0.5 m s^{-1}). Horizontal black lines indicate the levels where the horizontal cross-sections are plotted

The TKE spectra corresponding to the levels of the horizontal cross-sections in Figure 6.9 and averaged over one hour are shown in Figure 6.10. The spectra is only inspected until the cut-off wavenumber as in Adams and Stoltz (2002) and here $k_c = 32$. Therefore, below these numbers it is better not to extract conclusions from the spectra. The estimated value of the Ozmidov scale (L_{oz}, see equation 3.5), used here as an indication of

the upper limit of the inertial subrange, is only close to k_c in the middle of the boundary layer where the stability is smaller than at the other considered levels. The spectra also indicate that the buoyancy subrange is well captured within the boundary layer but not above it (z/z_i =1.1) probably because of too small a domain size. There is no evidence of an inertial subrange in any of the levels where the spectra are computed.

The peaks in the spectra also point out the sizes of the most energetic horizontal eddies. At z/z_i =0.1 their size is about 100 m and it becomes larger as height increases (the peak is shifted to lower k values at z/z_i=0.5). Finally, at the top of the boundary layer there is not any peak in the TKE spectrum because the most energetic eddies are of the same order as the domain size. This is in good agreement with the horizontal cross-sections (Figure 6.9).

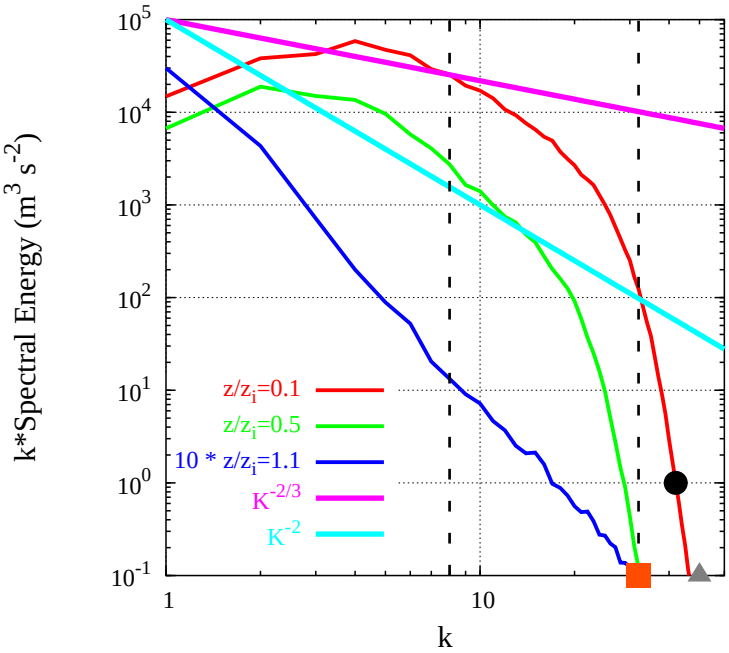

Figure 6.10: TKE spectra for each studied level. The TKE spectrum at z/z_i=1.1 has been shifted up 1 decade. The points indicate k_{oz} at z/z_i=0.1 (dot), at z/z_i=0.5 (square) and at z/z_i=1.1 (triangle). The horizontal discontinuous line indicates the cut-off wavenumber. The power laws of the inertial ($k \cdot S(k) \propto k^{-2/3}$) and the buoyancy ($k \cdot S(k) \propto k^{-2}$) subranges are also indicated

6.4.4 Description of the Probability Density Functions

Near the ground, there is a large number of structures as the horizontal cross-section of u (Figure 6.9.a) indicates. The PDFs computed from u, v, w and θ (Figure 6.6) are Gaussian, according to the Kolmogorov-Smirnov test. However, the skewness and the

kurtosis differ slightly from the Gaussian values, as the tails for $B(\theta)$ or $B(w)$ depart from Gaussianity. Nevertheless, this departure is smaller compared to a convective case. The shapes of $B(u)$ and $B(\theta)$ are similar to those of Chu et al. (1996). The zooms in Figure 6.6 show that the observations are less Gaussian than the PDFs computed from the LES, although one may note that they correspond to a high-frequency time series measurements at a single point. Therefore they consider a different range of eddies from the LES, that only capture the resolved motions. The LES structures depend on the subgrid-scale scheme used, and this might partially explain the differences with the results of Chu et al. (1996).

In the middle of the SBL, there are less u and θ structures (Figure 6.9.b) and each one occupies a larger area than those near the ground (Figure 6.10). At this level S_u and K_u are slightly different to the Gaussian values (Table 6.1) and there is a small departure from the Gaussianity in the tails (Figure 6.8).

The top of the SBL is much layered and there are not many structures (Figure 6.9.c); as the spectrum (Figure 6.10) indicates the most energetic structures in the model are as wide as the domain size. The PDFs are still Gaussian and the tails do not depart much from Gaussianity. The u values are not much spread around the mean and σ_u is smaller than at lower levels, giving a narrower $B(u)$. The structures in the horizontal cross-sections of u and θ are very similar at this level, giving σ, S and K very close for both quantities, with $B(u)$ and $B(\theta)$ having similar shapes. The width of $B(\theta)$ remains nearly constant at the three considered levels since the variation of σ_θ with height is not as large as σ_u.

6.5 Joint probability density functions

The probability density of two variables simultaneously is the joint probability density. In this section we will focus on the joint PDFs of w and θ ($B(w,\theta)$, Figure 6.11) which is normalized as before $\int_{-\infty}^{\infty}\int_{-\infty}^{\infty} B(w,\theta)dwd\theta = 1$. The vertical temperature flux is the first joint moment (covariance or correlation) computed from $B(w,\theta)$

$$\overline{w\theta} = \int_{-\infty}^{\infty}\int_{-\infty}^{\infty}(w-\overline{w})(\theta-\overline{\theta})B(w,\theta)dwd\theta \tag{6.13}$$

Following Mahrt and Paumier (1984) the geometry of the joint PDF is explored. Completely random motions (phase lags of 90°) yield a joint PDF formed by a variety of circles so that the density function depends only on the distance from the origin. Periodic motions with phases other than 0°, 90°, 180° and 270° correspond to partial correlation and elliptical patterns of the joint PDF, which is the expected case for the turbulent

stratified flows. The most vigorous events are associated with the largest distances to the origin, but the significance of those events is determined by their probability of occurrence, which decreases or is small at large distances.

The joint PDFs for the stable GABLS LES case and for the zero-wind CBL are shown in Figure 6.11 and they can be compared to Mahrt and Paumier (1984, Figure 3) and interpreted in terms of quadrants. The upper right quadrant ($w' > 0$, $\theta' > 0$) corresponds to warm updrafts, the upper left one ($w' > 0$, $\theta' < 0$) to cold updrafts and so on. For a given distance from the origin, the flux is greatest for an angle of 45°, 135°, 225° or 315° (since these are the axes of maximum correlation), and the flux is expected to be near zero when the tilt is 0°, 90°, 180°, or 360°. For a given angle, the generation of flux increases with the radial distance. Nevertheless, the contribution to the total flux depends on the joint probability of occurrence of w and θ.

Regarding the stable GABLS LES joint PDFs, near the ground and in the middle of the SBL, they are tilted about 7° towards the bottom right quadrant, corresponding to the predominance of warm downdrafts and cold updrafts. In the inversion layer, there is almost no tilt, corresponding to a very small correlation between w and θ. If the values of the fluxes are computed, they are very similar to those given by the standard LES method (Figure 6.11), slightly weaker near the ground, practically equal in the middle of the SBL and a 33% stronger at the inversion layer. This point will be discussed in section 6.7.

Near the ground, the joint PDF of w and θ for the zero-wind CBL is more tilted than in the stable case and therefore the absolute value of the flux is larger. Contrarily to the stable case, the joint PDF is tilted towards the bottom left quadrant ($w' > 0$, $\theta' > 0$) and the resulting flux is positive. Close to the ground, the thermals plumes move upward and therefore the temperature of the plume decreases as it mixes with the surrounding cold air. This is in good agreement with the LES results and the joint PDFs computed in Mahrt and Paumier (1985), Deardorff and Willis (1985) and Chu et al. (1996),

Above the boundary layer height, the joint PDF of w and θ for the zero-wind CBL is close to the one obtained from the stable case in since both joint PDFs there is almost no tilt corresponding to a very small correlation between w and θ. Nevertheless, in the zero-wind CBL the joint PDF is tilted towards the bottom right quadrant, and then the vertical temperature flux obtained is negative due to the large downdrafts motions.

Figure 6.11 also highlights that the joint PDFs for the zero-wind CBL are much more assimetric than for the stable case. The vertical motions are suppressed in stably stratified conditions whereas the plumes can easily grow in the CBL.

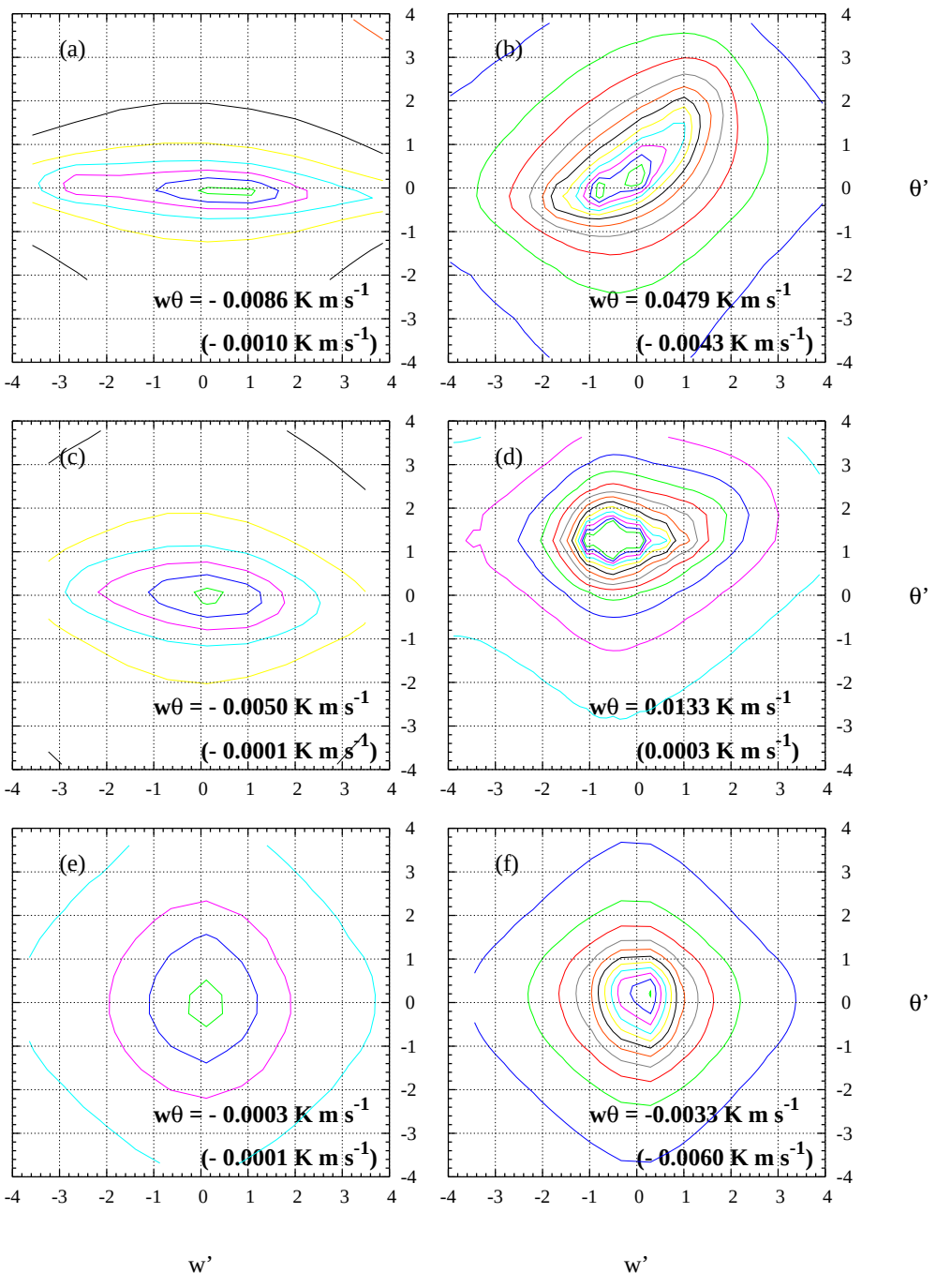

Figure 6.11: Normalized joint PDFs of w and θ obtained from (left figures) the 3.125 m resolution GABLS LES case and from (right figures) the zero-wind CBL at (top) z/z_i=0.1,(middle) z/z_i=0.5 and (bottom) z/z_i=1.1. The contours start at 0.002 level with increments of 0.002 in each case. The vertical temperature flux ($\overline{w\theta}$) computed for each PDF is also indicated and in the brackets ($\overline{w\theta}_{PDFs}$ - $\overline{w\theta}_{LES}$)

6.6 Ergodicity

When the LES results are compared to observational data (as in chapter 4), the assumption of ergodicity is implicitly made since the averaged LES profiles are compared to those measured at a specific point. The applicability of the ergodic theorem for the LES under study will be now checked. The following quantities for any ivariable χ are considered for the three levels of analysis:

• the approximate **"ensemble average"** operator, $\mathcal{M}_{x,t}(\chi)$, constructed using the complete fields at each level and using one output every minute for a whole hour

• the approximate **"spatial average"** operator, $\mathcal{M}_{x=fix,t}(\chi) = \mathcal{M}_x(\chi)$, which takes a field at each level for one single instant (three levels are considered $z/z_i = 0.1$, 0.5, 1.1)

• the approximate **"temporal average"** operator, $\mathcal{M}_{x,t=fix}(\chi) = \mathcal{M}_t(\chi)$, which takes all the values during one hour each time step ($\Delta t = 0.2$ s for the stable case and $\Delta t = 2$ s for the zero-mean CBL case) for one specific location

$\mathcal{M}_{x,t}(\chi) = \mathcal{M}_t(\chi)$ means that the variable (χ) is homogeneous, whereas $\mathcal{M}_{x,t}(\chi) = \mathcal{M}_x(\chi)$ implies stationarity. Ergodicity occurs when stationarity and homogeneity take place simultaneously.

B(u), B(v) and B(θ) for the stable LES GABLS case using these three different operators are shown in Figures 6.12 and 6.13, corresponding to the ensemble average, the spatial operator applied at three different instants of the eighth hour (15', 30' and 45' minutes) and the temporal operator at two different points of the domain. The corresponding averages are written in Table 6.2.

As is shown in Beare et al. (2005), the regime is stationary from the seventh hour on. This is confirmed here by the fact that the PDFs for the different instants ($\mathcal{M}_{x,15}$, $\mathcal{M}_{x,30}$ and $\mathcal{M}_{x,45}$) are very similar to that for the ensemble over one hour ($\mathcal{M}_{x,t}$). However the PDFs and the mean values obtained for the temporal series ($\mathcal{M}_{x_1,t}$ and $\mathcal{M}_{x_2,t}$) at two different locations (x_1 and x_2) diverge significantly (with differences between mean values of up to 0.5 m s^{-1} for the wind and 0.1 K for the temperature). Nevertheless, the homogeneity is slightly lost at $z/z_i = 0.1$ and $z/z_i = 0.5$ for the temperature field, although it becomes homogeneous at $z/z_i = 1.1$. This is probably related to the updrafts/downdrafts motions within the SBL that are much weaker than in the CBL. It is concluded that the field is not homogeneous and therefore the ergodic theorem is not fulfilled for such a regime.

For the convective regime, the pair of updrafts-downdrafts are more intense as the cross-sections (Figure 6.2) and the joint PDFs (Figure 6.11) point out. Therefore, the field is less homogeneous than for the SBL and it is even further away from the ergodicity.

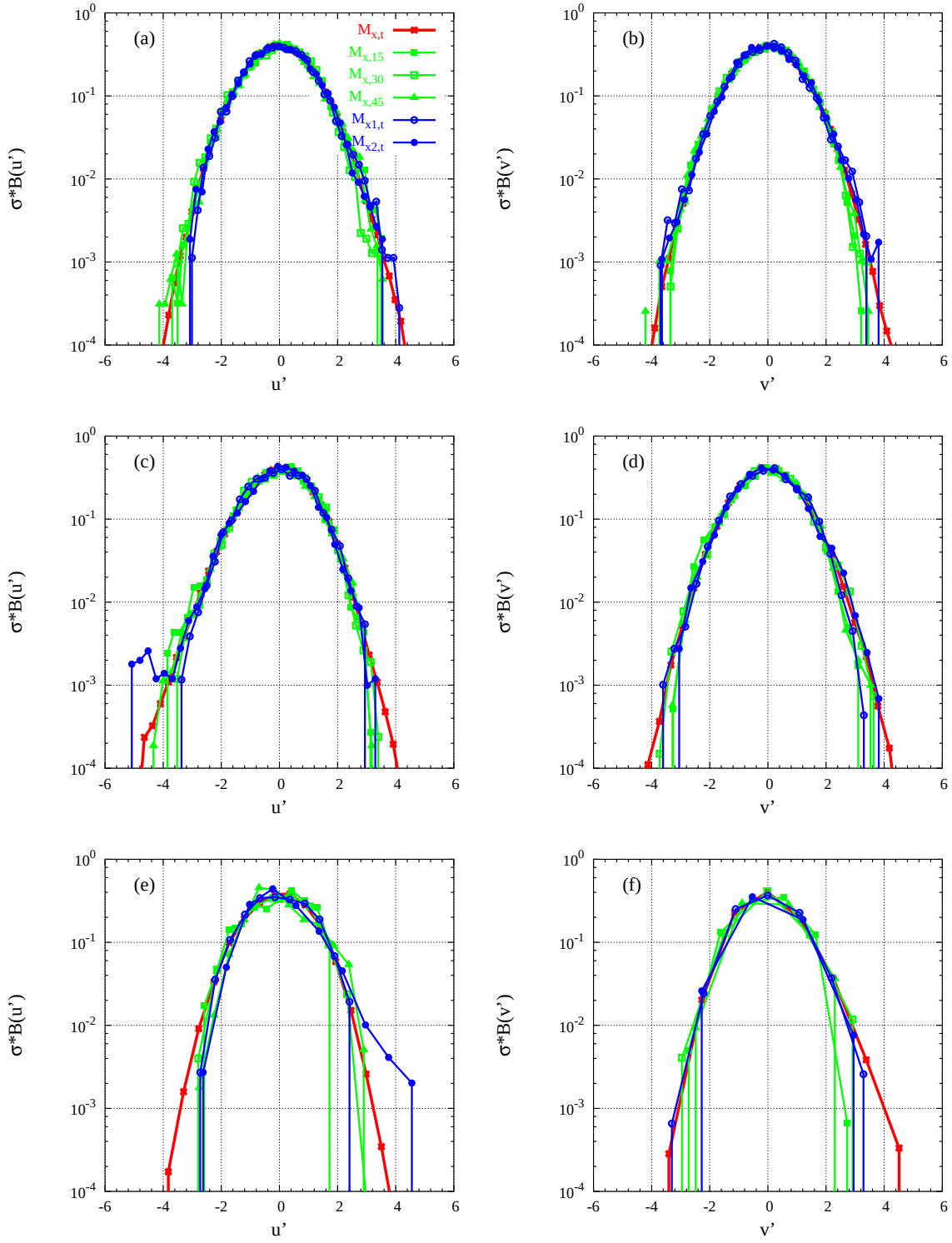

Figure 6.12: Normalized PDFs for (left) u and (right) v computed with the operators $\mathcal{M}_{x,t}$, $\mathcal{M}_x$ and $\mathcal{M}_t$, (ensemble, space and time averages, respectively) at (a) and (b) z/z$_i$=0.1; (c) and (d) z/z$_i$=0.5; (e) and (f) z/z$_i$=1.1

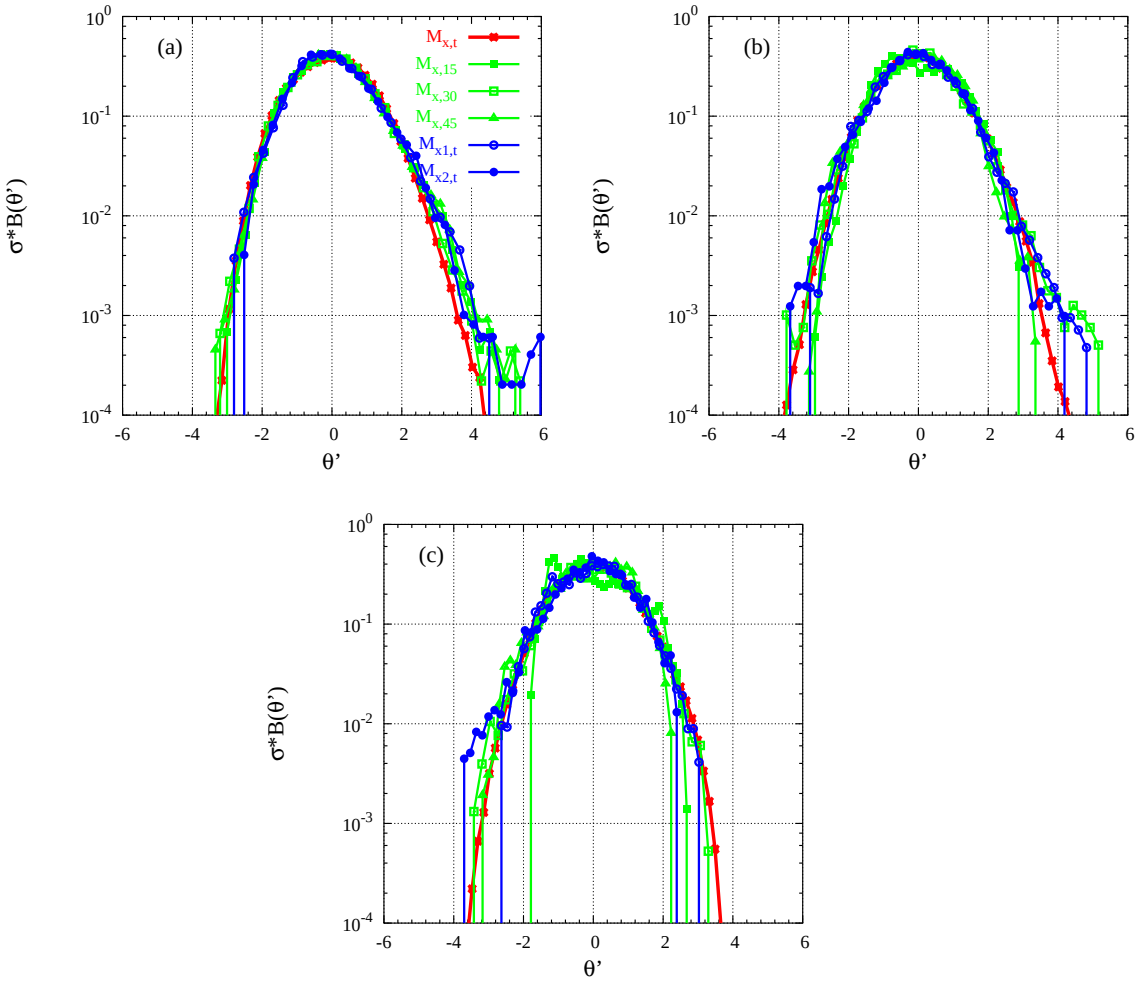

Figure 6.13: Normalized PDFs for θ computed with the operators $\mathcal{M}_{x,t}$, $\mathcal{M}_x$ and $\mathcal{M}_t$, (ensemble, space and time averages, respectively) at (a) z/z$_i$=0.1, (b) z/z$_i$=0.5 and (c) z/z$_i$=1.1

Table 6.2: **Ergodicity for the stable LES case. $\overline{u}$ and $\overline{v}$ (in m s^{-1}) and $\overline{\theta}$ computed from the ensemble, space and time averages ($\mathcal{M}_{x,t}$, $\mathcal{M}_x$ and $\mathcal{M}_t$, respectively)**

	z/z$_i$=0.1	z/z$_i$=0.5	z/z$_i$=1.1
$\mathcal{M}_{x,t}(u)$	3.859	7.032	8.480
$\mathcal{M}_{x_1,t}(u)$	3.868	7.024	8.481
$\mathcal{M}_{x_2,t}(u)$	4.338	7.368	8.079
$\mathcal{M}_{x,15}(u)$	3.800	7.061	8.450
$\mathcal{M}_{x,30}(u)$	3.885	7.023	8.486
$\mathcal{M}_{x,45}(u)$	3.849	7.077	8.487
$\mathcal{M}_{x,t}(v)$	2.599	3.094	0.151
$\mathcal{M}_{x_1,t}(v)$	2.562	3.090	0.151
$\mathcal{M}_{x_2,t}(v)$	2.768	3.006	0.081
$\mathcal{M}_{x,15}(v)$	2.583	3.172	0.200
$\mathcal{M}_{x,30}(v)$	2.537	3.061	0.150
$\mathcal{M}_{x,45}(v)$	2.508	3.021	0.106
$\mathcal{M}_{x,t}(\theta)$	263.676	264.136	265.589
$\mathcal{M}_{x_1,t}(\theta)$	263.570	264.036	265.574
$\mathcal{M}_{x_2,t}(\theta)$	263.634	264.097	265.894
$\mathcal{M}_{x,15}(\theta)$	263.734	264.206	265.602
$\mathcal{M}_{x,30}(\theta)$	263.681	264.143	265.585
$\mathcal{M}_{x,45}(\theta)$	263.619	264.090	265.589

Although the 3.125 m resolution GABLS LES case is Gaussian, it is non-homogeneous. If the corresponding real field was not homogeneous either, this would have deep consequences, especially when a comparison between measurements in a single vertical and LES ensemble averaged results was made. However, the assumption of ergodicity is implicitly made when the LES results are compared to observations, as it is described in chapter 4. This also highlights how difficult is to compare LES to measurements.

6.7 Sensitivity of the Probability Density Functions to resolution

The sensitivity of the PDFs from the stable GABLS LES case to the chosen resolution is studied here. As the resolution decreases without changing the domain size, the PDFs are calculated with a smaller number of points. Until now, the results shown correspond to the 3.125 m case, where the PDFs are computed using 128×128=16384 points for a single instant. At a resolution of 12.5 m, the PDFs are computed only with 32×32=1024 points each instant, but still enough to compute significantly statistical PDFs.

Despite the fact that the mean profiles do not change very much for each resolution

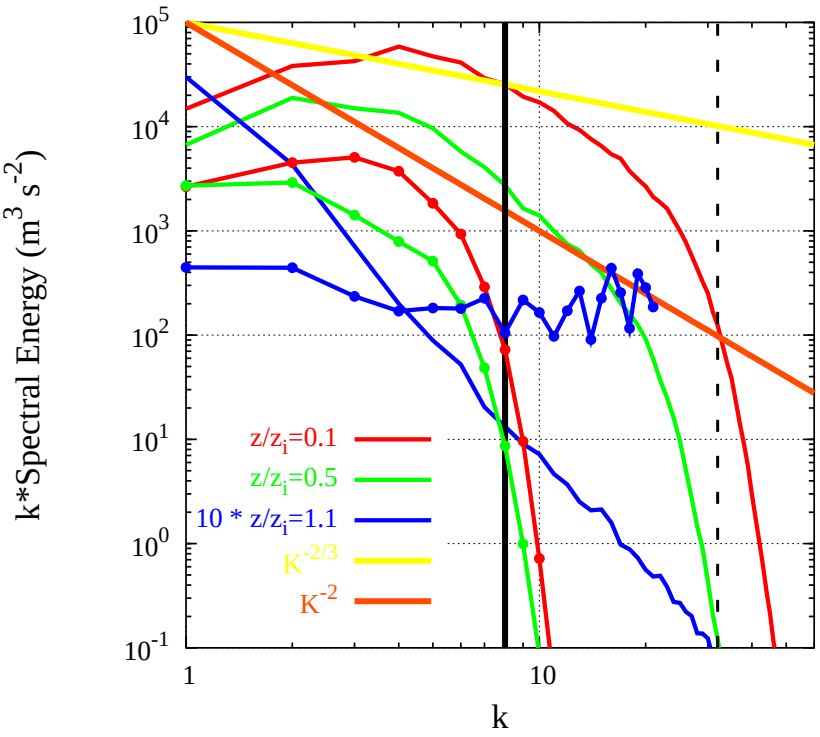

Figure 6.14: TKE spectra computed for the stable GABLS case at two resolutions 3.125 m (solid lines) and 12.5 m (lines and points) for each studied level. The inertial and buoyancy subranges are also indicated as well as the cutoff wavenumbers (vertical lines) depending on the chosen resolution

(Figure 6.5), the structures do. The TKE spectra for the 3.125 m and 12.5 m resolutions is shown in Figure 6.14. For the coarser case, the horizontal cross-sections and also the spectra indicate that the structures at 12.5 m resolution are larger than at 3.125 m resolution. This fact might affect the shape of the PDFs and consequently the value of their corresponding moments.

The PDFs of u, v, w and θ computed for each resolution are shown in Figures 6.15 and 6.16. When the resolution is decreased, the PDFs are still Gaussian, according to the Kolmogorov-Smirnov test, but the tails also experience a small departure from Gaussianity, especially for w and θ. This is most noticeable near the ground, where the skewness and kurtosis values depart from the Gaussian values more than at higher resolutions (Figure 6.17). Another feature is that the field is more nearly homogeneous than in higher resolutions and then ergodicity is more closely approximated.

Figure 6.18 shows how the shape of the PDFs changes when the resolution is decreased. Since the eddy structures are coarser represented, the values are more concentrated to the mean one and then the joint PDF is more regular than in higher resolution. The fluxes computed from the joint PDFs also decrease since the w and θ values are less correlated.

The largest differences between the fluxes computed from the PDFs and those from LES take place at the top of the boundary layer, for any of the resolutions considered.

The profiles of $\overline{w\theta}$, $\overline{uw}$, $\overline{u^2}$ and $\overline{w^2}$ computed from the LES and those obtained from the PDFs and joint PDFs, respectively, at the three considered levels are shown in Figure 6.19. It is known that, for LES, the subgrid contribution is larger when the resolution is coarser, especially near the ground, a level where the most energetic eddies are smaller. The subgrid contribution of the moments in the 3.125 m resolution case is very small, and then the resolved moments are approximately equal to the total ones (Figure 6.19). On the contrary, the subgrid contribution becomes very large for the 12.5 m resolution case, making clear that the PDF computation of the turbulence moments corresponds to the resolved fluxes in the classical LES computation (Figure 6.19). Finally, when the structures are coarser, for instance at the top of the SBL for any resolution, the PDFs have lesser statistical signification and they might overestimate the fluxes computed from them. This is the case for $\overline{w\theta}$ at z/z_i =1.1 in Figure 6.11.

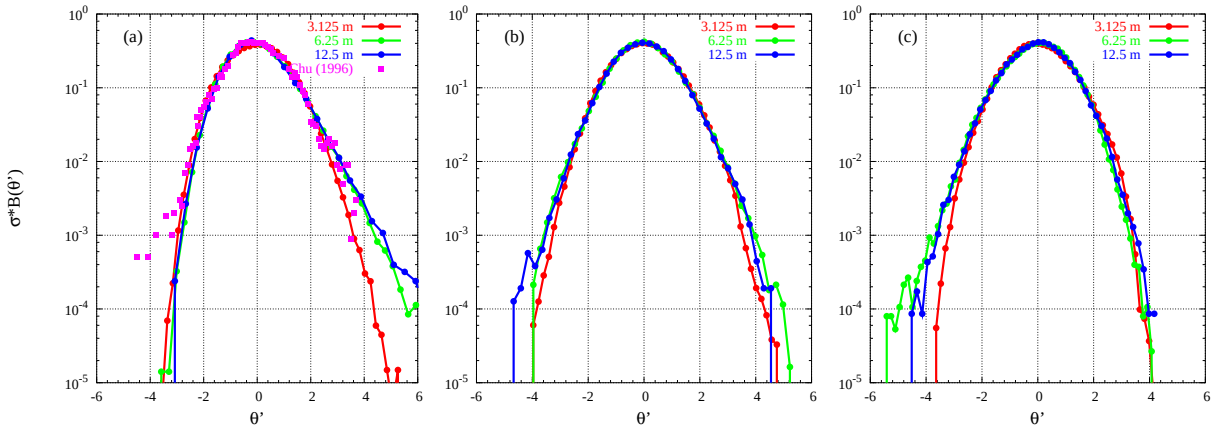

Figure 6.15: Normalized PDFs for θ obtained from GABLS LES case for the three resolutions considered at the three studied levels: (a) z/z_i=0.1, (b) z/z_i=0.5 and (c) z/z_i=1.1

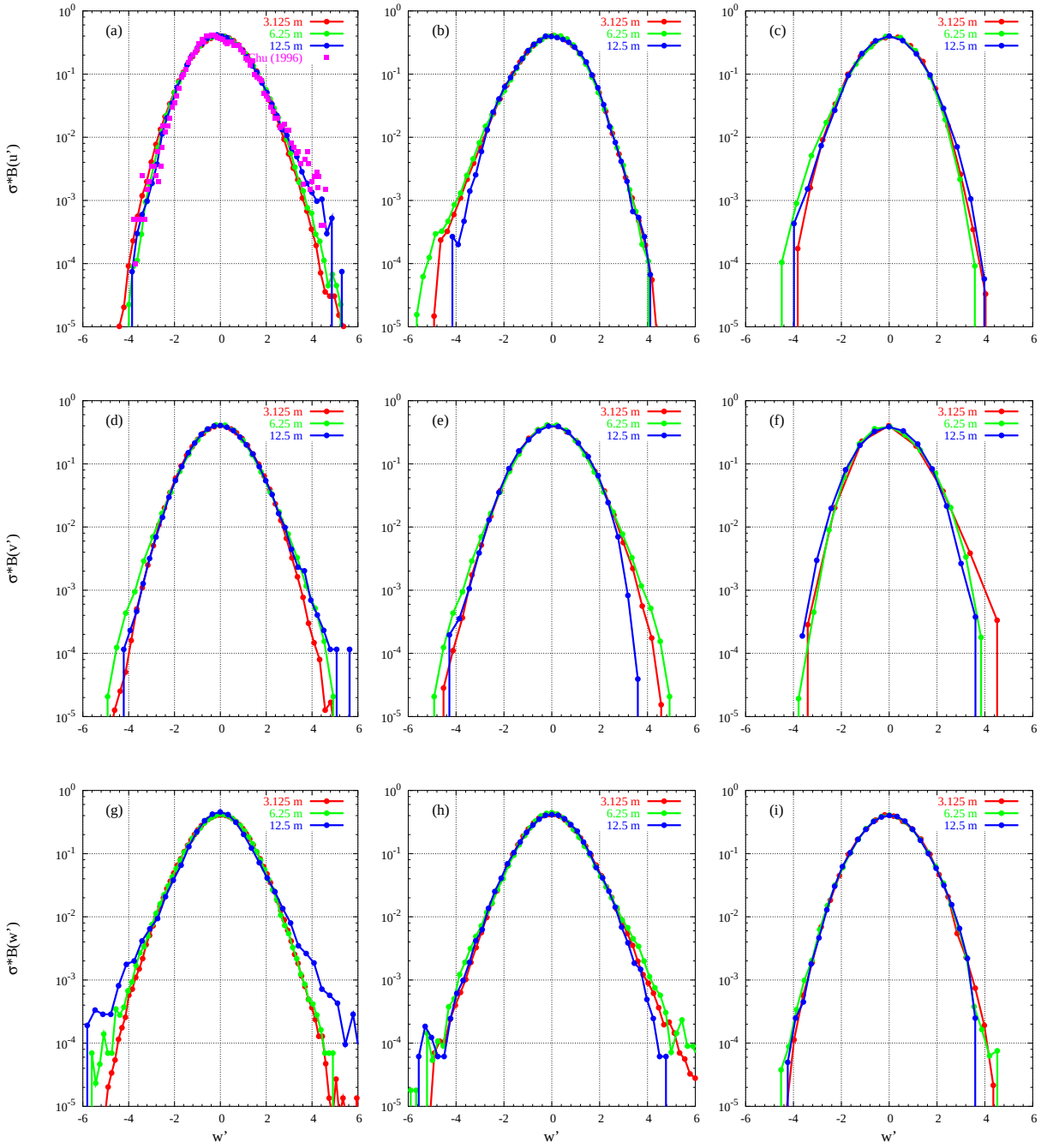

Figure 6.16: Normalized PDFs for (top) u, (middle) v and (bottom) w obtained from GABLS LES case for the three resolutions considered at the three studied levels: (a), (d) and (g) z/z_i=0.1; (b), (e) and (h) z/z_i=0.5; (c), (f) and (i) z/z_i=1.1. The PDFs computed from observations near the ground by Chu et al. (1996) are indicated in empty squares

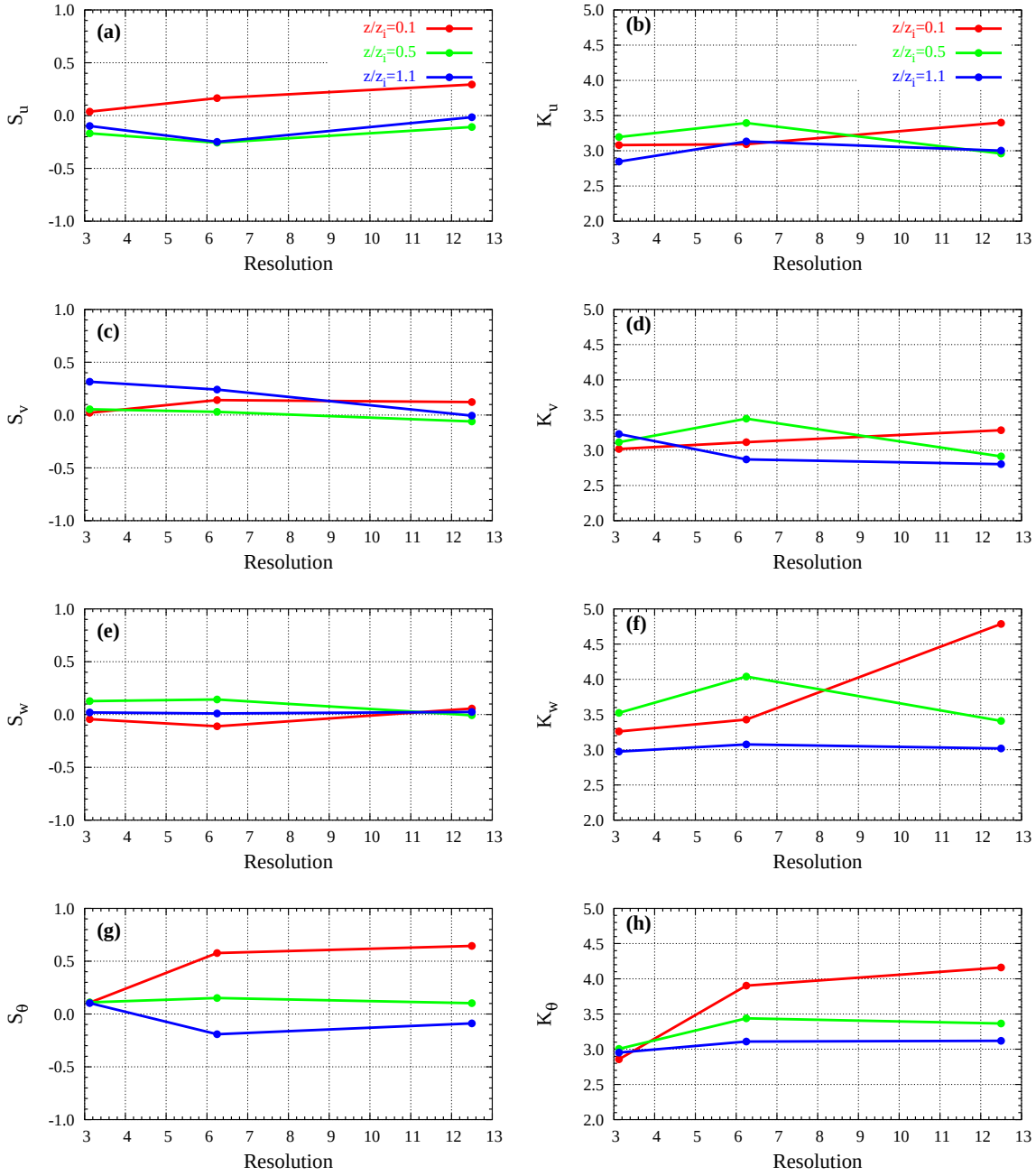

Figure 6.17: Skewness and kurtosis values as a function of the resolution chosen computed from: (a) and (b) u; (c) and (d) v; (e) and (f) w; (g) and (h) θ

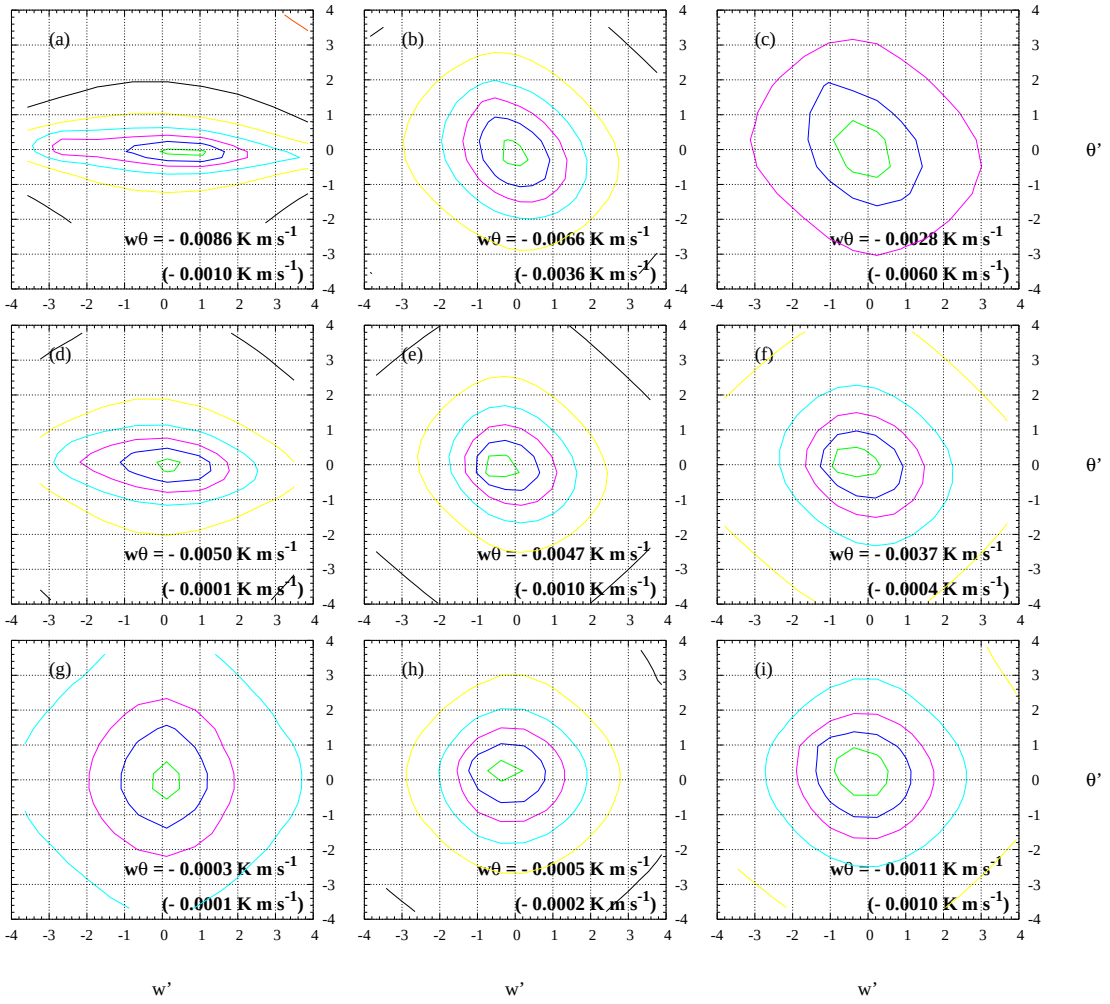

Figure 6.18: Normalized joint PDFs of w and θ obtained from (left) the 3.125 m, (middle) 6.25 m and (right) 12.5 m resolution GABLS LES case at (top) z/z_i=0.1,(middle) z/z_i=0.5 and (bottom) z/z_i=1.1. The contours start at 0.002 level with increments of 0.002 in each case. The vertical temperature flux ($\overline{w\theta}$) computed for each PDF is also indicated and in the brackets ($\overline{w\theta}_{PDFs}$ - $\overline{w\theta}_{LES}$)

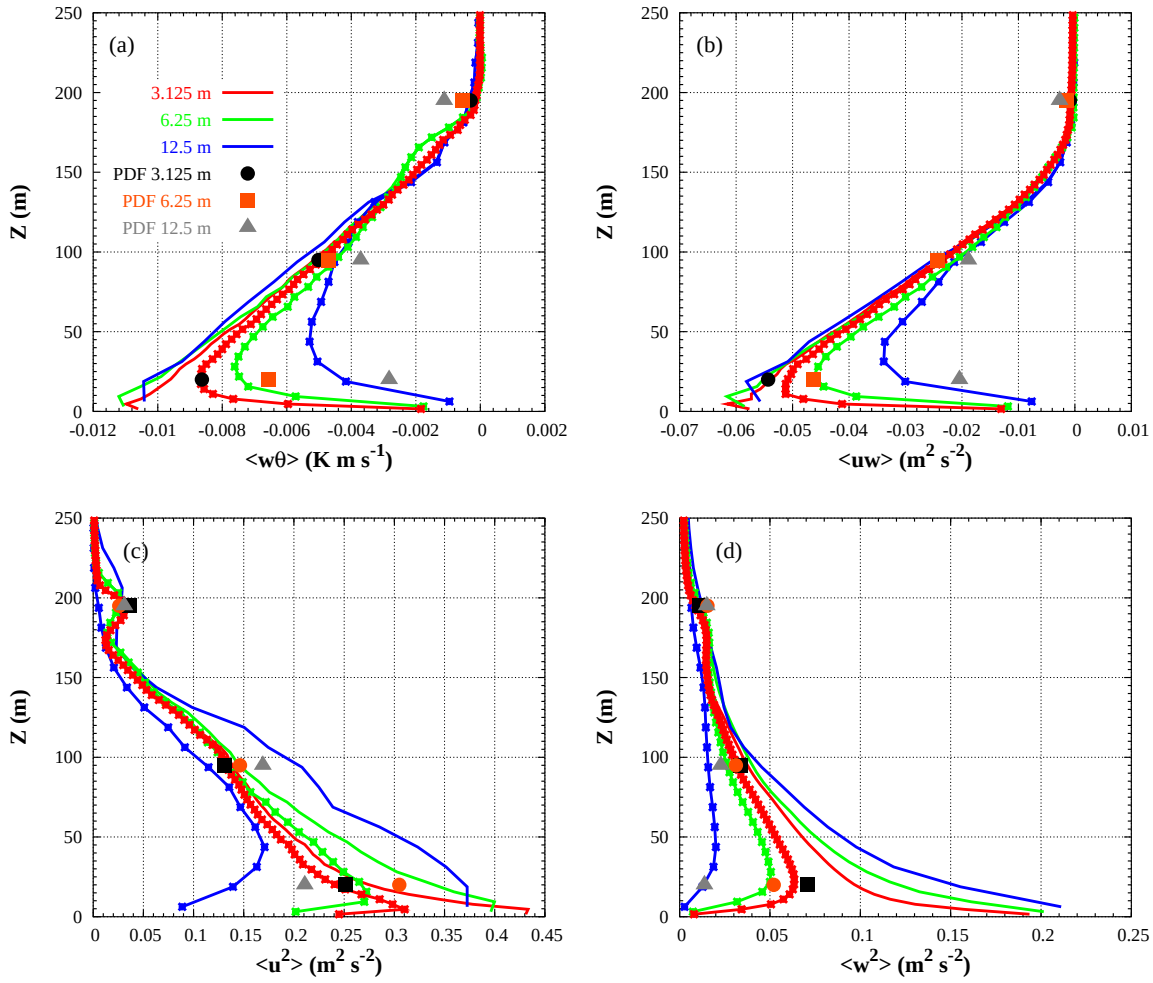

Figure 6.19: LES profiles for the three resolutions considered (total contribution in lines and resolved in lines and points) for (a) $\overline{w\theta}$, (b) $\overline{uw}$, (c) $\overline{u^2}$ and (d) $\overline{w^2}$ and those computed from the PDFs (bigger symbols) at the three computation levels

6.8 Conclusions

It is found that the PDFs are a useful tool to study the eddy structures present in the flow. This methodology has been checked through the inspection of the PDFs computed from an LES of a zero-mean wind CBL and then applied to the LES of the SBL case described in chapter 5. The shapes of the PDFs computed from a CBL or a SBL case are quite different since in the first one the pairs of updrafts/downdrafts are much more intense than in the SBL, where the vertical motions are suppressed because of the stable conditions. As a result, the PDFs computed from the SBL case are much more Gaussian than the CBL ones, which have values of skewness and kurtosis largely departing from those Gaussian.

Following the methodology to construct a PDF, the shape is quite sensitive to the number of points considered in the computation. Nevertheless, the mean values are not dependent of the number of points considered. On the other hand, the PDFs only contain the information of the resolved motions computed from the LES. Therefore, the fluxes computed from the PDFs correspond to those LES resolved. However, the eddy structures indirectly depend on the turbulence scheme used.

The attention is focused on the inspection of the tails of the PDFs, which correspond to weak probability events, that might not be well represented by the model. For instance, the tails in the joint PDFs for a CBL case can give an idea of the intensity and probability of the pairs of updrafts/downdrafts. When the PDFs are computed from a lower resolution case, the main differences take place near the tails because the eddy structures are coarser represented. Therefore, although the PDFs of the SBL are Gaussian, the ergodic theorem is not fulfilled since the field is stationary but not homogeneous. The CBL is still less homogeneous and consequently less ergodic. The ergodicity assumption is implicitly made when the LES profiles are compared to single point measurements. Assuming it might explain some of the differences between the LES results and observations.

PDFs can also be a tool to compare LES results to observations, as it is used in the next chapter, beyond the mean profiles. In fact, different eddy structures can produce similar mean profiles but in this case the processes are not well represented. It is worth mentioning that not all the observed eddy scales are represented in an LES and this fact might explain some differences between the PDFs computed from LES results and observations.

On the other hand, the PDFs can be used as a supplementary diagnostic to compare different LES models (such as the GABLS intercomparison described in the previous chapter). Therefore, the eddy structures are compared beyond the classical LES averages. Furthermore, the PDFs can be useful to identify observed intermittencies, especially the

tails, as well as to find a parameterization through the characteristic function.

Chapter 7

STUDY OF AN OBSERVED LOW-LEVEL JET[1]

This chapter is devoted to study an observed Low-Level Jet (LLJ), which is one of the most typical phenomena observed within the SBL, through the analysis of the observations and LES modelling. The LES results in chapter 3 correspond to ideal situations and when they are compared to observations in chapter 4, the whole data of the campaign is taken. Therefore, the LES do not exactly reproduce the observations and the comparison of the LES results to observations is difficult.

To partially overcome this problem, an LES of an observed LLJ within an stationary period is performed. Now, the LES model is initialized with observed profiles and surface fluxes but the surface is still flat. The main objective is to understand the basic processes that take place within this regime as well as the structure of the associated turbulence. The attention is focused on the mixing across the inversion height and on the elevated turbulence.

Although the simulated conditions now are more based on real observations than for the LES described in chapter 3, the large scale forcings, such as the ones produced by the orography, are still not fully included in the LES. To do so, mesoscale modelling is needed and the local effects are further studied in the next chapter.

To study the mixing across the inversion level, two scalars are introduced above and below the maximum of the wind. Time series of the evolution of the scalar concentrations, as well as the vertical profiles, give a complete picture of the processes that take place there. The sensitivity of the results on the resolution and the prescribed surface boundary condition are also analyzed. Finally, the results are compared to observations through

[1]This chapter is based on: Cuxart, J., and Jiménez, M.A., 2005a: Mixing processes in a nocturnal low-level jet, submitted to *Journal of the Atmospheric Sciences*.

the PDFs methodology described in the previous chapter.

7.1 Introduction

Although the wind at ground level is frequently lighter or calm at night under clear-sky and weak synoptic winds conditions, the winds some tens of meters aloft may have supergeostrophic values. A Low-Level Jet (LLJ), or nocturnal jet, is a thin stream of fast moving air usually located close to the ground. It is usually formed during the night and reaches its peak during the predawn hours.

LLJs can be produced by a number of mechanisms and they are very important for a variety of applications, including wind energy and nocturnal transport of atmospheric quantities. LLJs are also important for generating shear between the level of the jet and earth's surface, and this shear is likely to have a role in controlling fluxes between the surface and the atmosphere. However, current Numerical Weather Prediction (NWP) models do not predict properties of these LLJs very well. Mesoscale models, which may have sufficient vertical resolution to explicitly simulate these LLJs, have difficulty predicting their direction and strength, probably because of the crude representation of subgrid mixing in stable conditions. Large-scale models, which have coarser vertical resolution, are not able to simulate the LLJs, and their effects are not currently part of any parameterization schemes in these models.

7.1.1 Main features of a Low-Level Jet

Several LLJs have been further studied such as in the Baltic Sea (Smedman et al., 1993) or in the south-eastern Kansas (USA) during the CASES-99 campaign (Banta et al., 2002). It is worth mentioning the climatological studies over north-central Oklahoma by Whiteman et al. (1997) and more recently in the Weddell sea (Antarctica) by Andreas et al. (2000).

The term LLJ has been used to refer to any low-level speed maximum in the vertical profile of the wind. A large number of mechanisms can produce a LLJ and this has led to use ambiguously this term in the literature. As Stull summarizes (1988, and references therein), there are several conditions that favour the formation of the LLJ. The first proposed formation mechanism of the LLJs was given by Blackadar (1957), analysing the inertial oscillation resulting from the departure from the geostrophic equilibrium within the boundary-layer at the end of the day. A temperature inversion at the surface may decouple the surface winds from the winds aloft, that due to the Coriolis force turn around the geostrophic value forming a LLJ.

However, other factors are often also involved in the generation of this nocturnal feature. Horizontal temperature gradients generate a variation of the geostrophic wind with height (the thermal wind) and the resulting pressure gradient can induce a LLJ. These temperature gradients can be generated by a sloping terrain (see, for example, Lenschow et al., 1988), or by surface heterogeneities. Bonner (1968) suggested that the baroclinicity causing the LLJ could be either of thermal or dynamical origin, the latter in his case induced by the Rocky Mountains. Whiteman et al. (1997) also consider LLJs after a cold front passage.

7.1.2 Description of an observed Low-Level Jet during SABLES-98

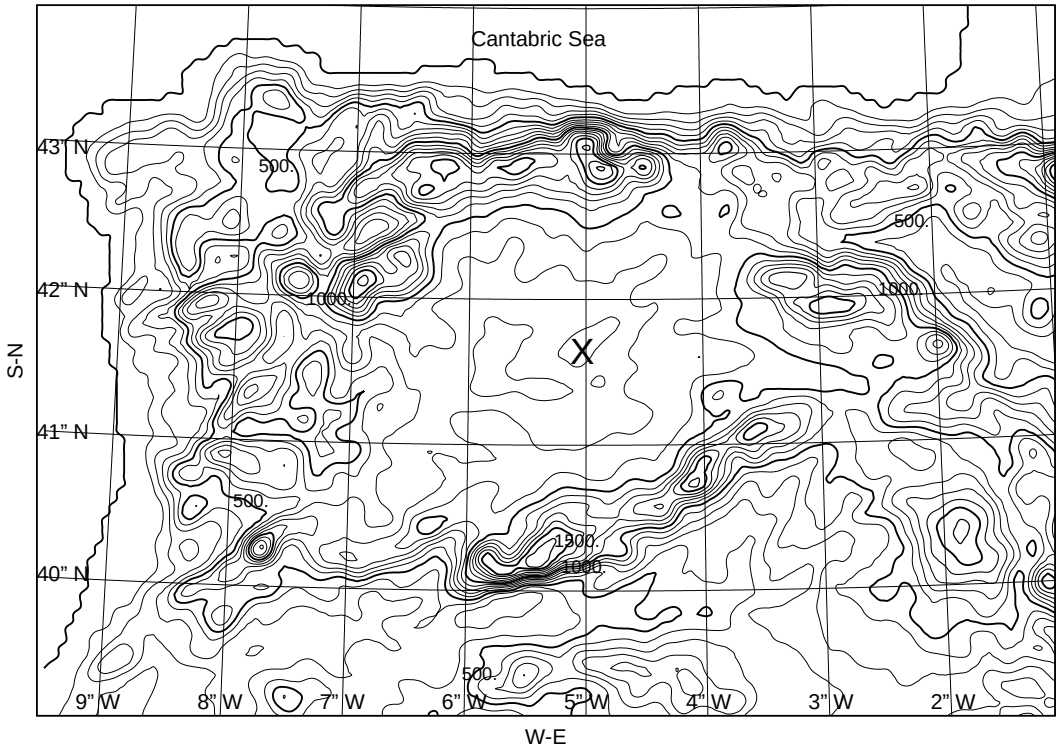

Figure 7.1: Location of the place where the SABLES-98 campaign took place. The cross indicates the position of the main tower

The Stable Atmospheric Boundary Layer Experiment in Spain-1998 (SABLES-98, Cuxart et al. 2000b) took place during 14 days in September 1998 on the Northern Spanish Plateau (see location in Figure 7.1). This is the upper part of the Duero River Basin, an elevated flat area with a radius of about 150 km and a height of about 800 m above sea-level (ASL) surrounded by mountain ranges with peaks up to 2500 m ASL.

Nevertheless, the basin has a slight slope of about 300 m from the northern and southern parts to the central area, where the Duero river flows from east to west. A 100 m tower was setup, with sonic anemometers at its lower part. Captive balloons were released continuously when the synoptic wind was weak. More details of the campaign are found in chapter 4 where the observations are compared to the LES results of chapter 3. Different static stabilities were sampled, ranging from near neutral to very stable during the 12 hour-long nights.

In most of the more stable nights, LLJs were observed and their main features are analysed in Conangla and Cuxart (2005, CC2005 from now on). Basically, they consisted of a flow from the East, with the maximum around 8-9 m s^{-1} located somewhere between 60 and 100 m above ground level (AGL). The synoptic situation located the study area near the center of a high pressure system, with a very weak pressure gradient and a very weak flow from the eastern sector. The basin diverted the synoptic flow and allowed basin-scale flows to develop during night. The observed LLJs seem to be due to a combination of some factors mentioned above, with an initial phase of inertial oscillation, followed by a less regular pattern that might involve baroclinicity related to the sloping terrain and also the presence of locally generated katabatic flows.

In CC2005, one of the observed LLJ was chosen for a more detailed study using a single-column model (described in Cuxart et al, 2000b). The soundings measured during the night of 20-21 September 1998 as well as the time series taken from the main tower are shown in Figures 7.2 and 7.3, respectively. The wind speed profile indicates the development of a LLJ at 0030 UTC, which remains until 0330 UTC, with the nose of the jet located at a height of around 60 m, with a speed of about 8 m s^{-1}. The direction of the wind was from the eastern quadrant and the surface cooling was about 11°. The peak in the TKE time series (Figure 7.3.c) occurred quite early in the night (200UTC) and it was related to an increase of the wind speed (see Figure 7.3.a). However, the consequences of this turbulent event are only reflected in the temperature field at the lowest level (Figure 7.3.b), where its associated downward heat flux produced a significant increase of temperature near the ground. A further study of the data measured during this night is found in Cuxart et al. (2000b).

The main purpose in CC2005 was to see if the model was able to generate turbulent motions at the upper part of the LLJ (above the maximum) as the low-values of the Richardson number computed from the soundings seemed to indicate. The model showed that conditions are met for turbulence mixing in that layer, basically due to shear production combined with a weak temperature gradient. An elevated layer of turbulence at a height between 1 and 3 times the height of the wind maximum (h_{LLJ}) was found,

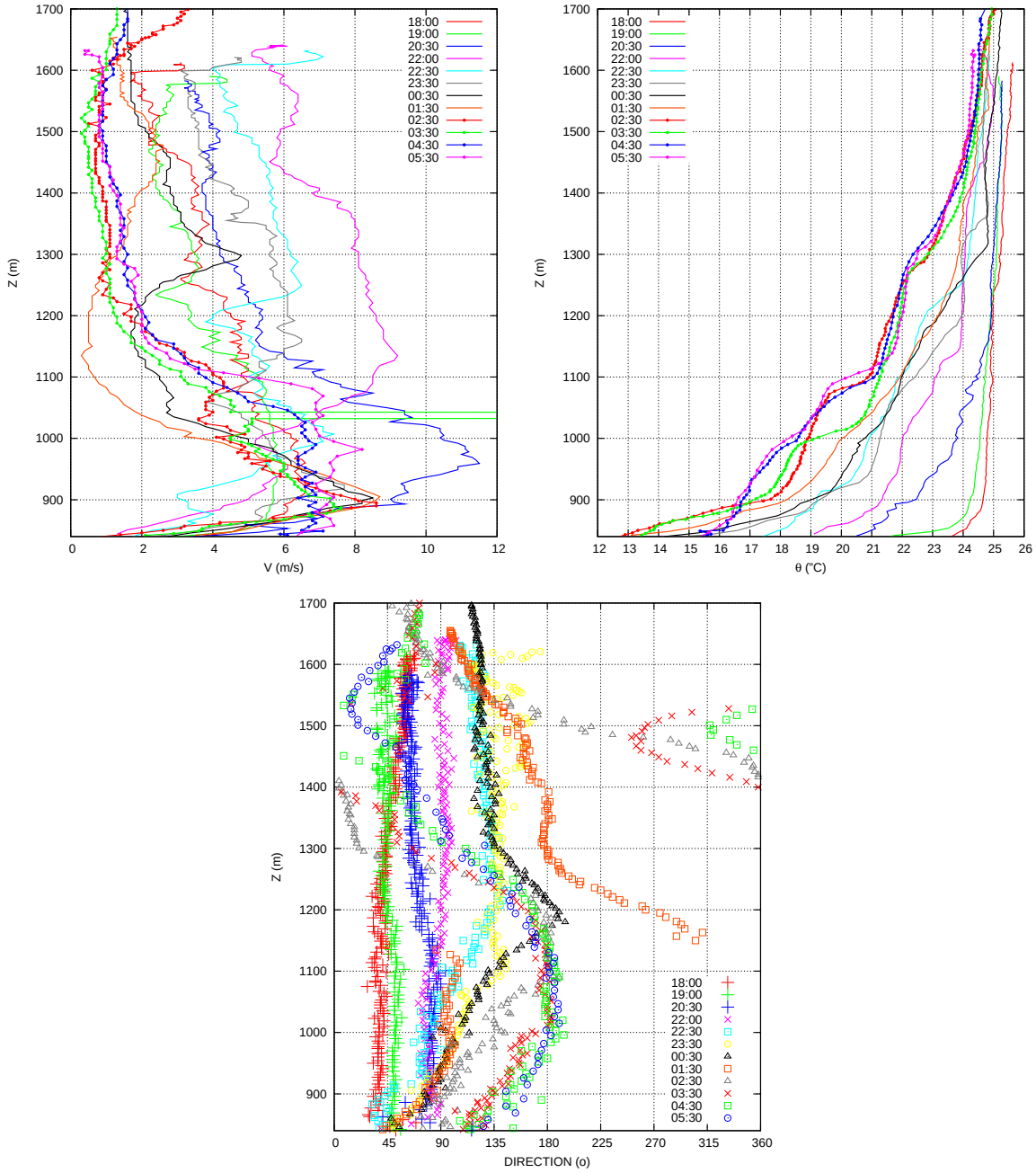

Figure 7.2: Evolution of the (a) wind speed, (b) temperature and (c) direction measured from the tethered balloon during the night of the 21st September during the SABLES-98 campaign. The ground is about 820 m (ASL)

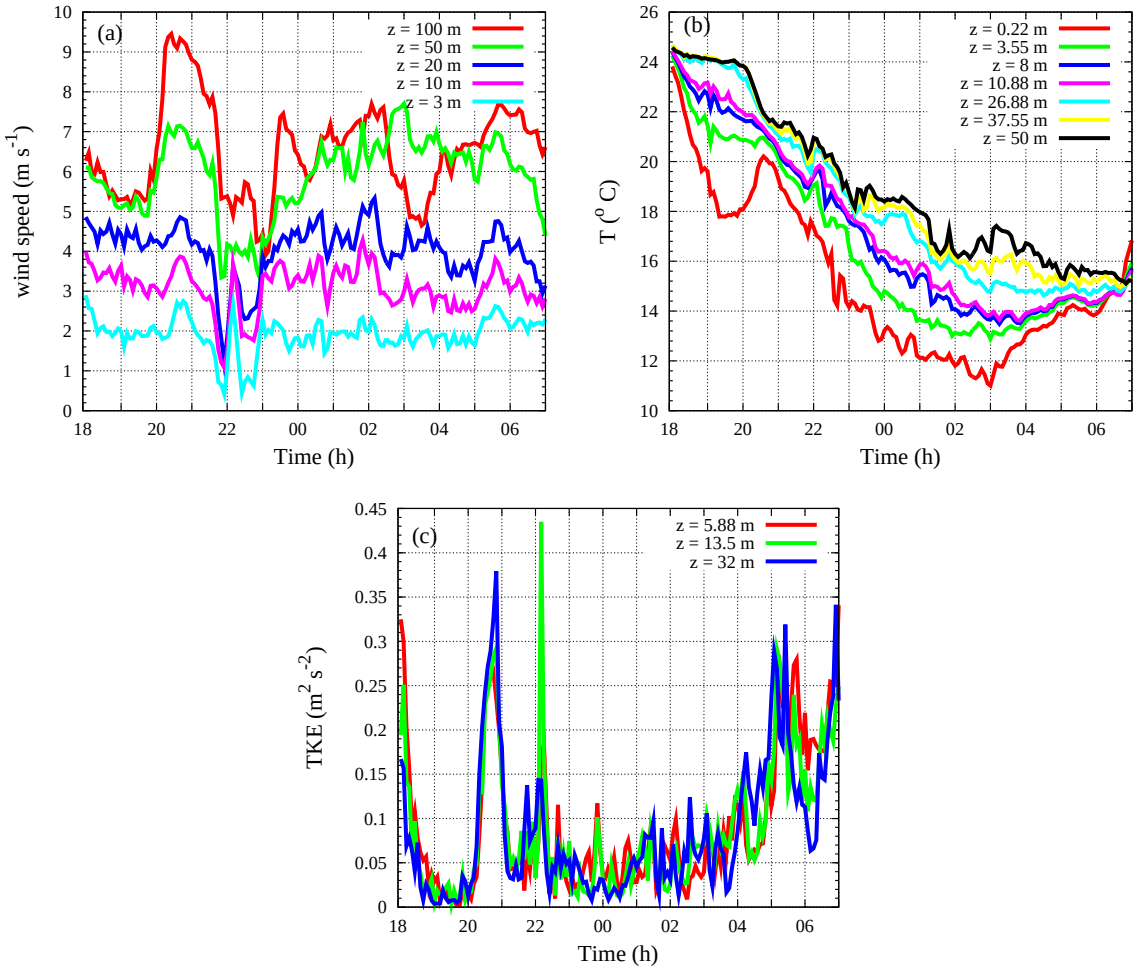

Figure 7.3: Evolution of the (a) wind speed, (b) temperature and (c) TKE measured from the main tower during the night of the 21st September during the SABLES-98 campaign

similarly to what Smedman et al. (1993) had previously indicated. In the CC2005 simulation, the elevated layer of turbulence was practically decoupled from the turbulence below h_{LLJ}, with the layer of wind maximum having an absolute minimum of turbulence kinetic energy (TKE).

However, a single-column model is just a parameterization of the turbulence processes. The present work is an attempt to look at the same case but using a more realistic tool, a Large-Eddy Simulation (LES) model. The aim is to inspect up to what level the features indicated by the single-column model are effectively reproduced by a LES model provided that it is run in conditions that it can handle. The distribution of the turbulent layers and the rate of transport through the inversion at the wind maximum are the major points of study. To proceed, a simulation of a stationary LLJ observed in SABLES-98 from midnight to 0200 UTC of the 21st September is made, and two passive scalars are used, one above and one below the wind maximum. As in CC2005, the LLJ will be maintained by the prescription of a vertical variation of the geostrophic wind. The results confirm most of the findings of CC2005 and provide supplementary information about the details of the mixing processes.

7.2 Modelling configuration and strategy

The Meso-NH model (Lafore et al., 1998) is run in LES configuration (Cuxart et al. 2000b), taking a domain size of 600×400×700 m, using 100×100×150 grid points in the x, y, and z directions, respectively. The horizontal grid spacing is 6 m for x and 4 m for y. A horizontally anisotropic grid has been chosen to better resolve the streamwise streak-like structures present near the wall in shear-driven boundary layers. The vertical grid spacing changes with height; the vertical resolution is larger near the ground, constant (2 m) until 100 m, stretched until 400 m where it is about 5 m, and stretched further until 700 m, where it is about 30 m.

The latitude (43°) and the roughness length (z_0=0.035 m) correspond to the SABLES-98 site (Cuxart et al., 2000b). Since the observed LLJ is stationary between 0030 UTC and 0200 UTC, the initial temperature and wind profiles for the LES model are taken from the average of the soundings (see Figure 7.2) within this period. This will allow to compare the LES results to measurements, after the spin-up of the simulation is over (about half-an-hour). The measured humidity during this night was below 50% and therefore, effects of moisture are not considered in this study. Initially, the wind has a maximum of 8.8 m s^{-1} at 62 m and values near 2 m s^{-1} above 300 m, whereas the potential temperature near the ground is 286 K, has a vertical gradient of about 0.09 K m^{-1} below the wind

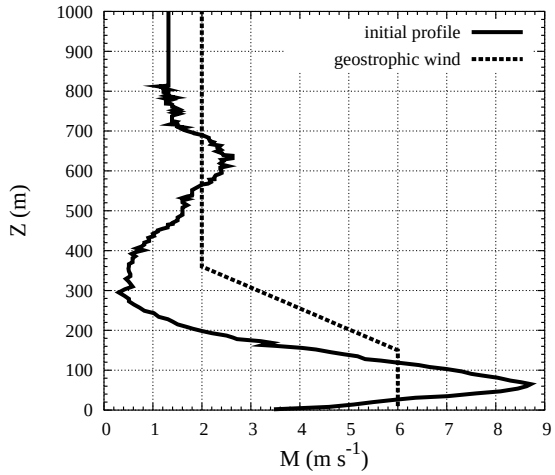

Figure 7.4: Initial wind profile for the LES and the imposed variation on the geostrophic wind

maximum, and of 0.01 K m^{-1} above it.

As in CC2005, the geostrophic wind is prescribed constant (6 m s^{-1}) below the maximum of the wind and decreases linearly above it up to 350 m, from where it is constant again (2 m s^{-1}) until the top of the domain, as Figure 7.4 points out. This vertical variation of the geostrophic wind is consistent with the thermal wind associated with the climatologically observed temperature difference across the northern Duero basin. A small random perturbation is added to all velocity components to initiate the resolved motions.

To allow feedbacks between the soil and the atmosphere, a very simple energy budget equation (Van der Wiel et al., 2002) has been considered, where the three terms that balance are the turbulent heat flux, the flux from the soil and the longwave radiative flux. This is the same energy budget equation used in chapter 3. From this energy budget equation, the averaged surface vertical flux converges to about -0.011 K m s^{-1}, larger than the one measured during the stationary period (-0.006 K m s^{-1}); this stronger cooling flux sustained during four hours leads to a smaller surface temperature than observed at the end of the run.

Tests made using different surface boundary conditions, such as prescribing the observed surface fluxes, vary much the profiles within the layer below the inversion, as it will be shown later. However, none of them is able to reproduce well its observed characteristics, since either the temperature or the wind are not well captured. The upper layer and the rate of mixing across the inversion do not seem affected by the chosen surface conditions. Some sensitivity is found to the resolution below the inversion, at a smaller vertical resolution of 5m , the surface flux converges to more negative heat fluxes and

there is even more mixing in that layer.

The run lasts 4 h; one hour after the start, two scalars are introduced, one below (S_1) and one above (S_2) the wind maximum. They are used to inspect the mixing above, below and across the LLJ maximum.

7.3 Description of the mean state

In Figure 7.5 the profiles of the wind, potential temperature, Brunt-Väisälä frequency (N_{BV}) and Richardson number (Ri) are shown, averaged over the horizontal domain and over 0.5 h. The wind profile (Figure 7.5.a) has a stationary maximum at z = h_{LLJ} = 65 m, and the wind shear is very intense below and above this level. This feature compares very well with the observations. Above the wind maximum, the wind rotates with time both in the simulation and in reality. In the simulation, the rotation is due to the inertial oscillation, but in the observations other effects can contribute.

The model develops a temperature inversion at the wind maximum (Figure 7.5.b), slightly stronger than the one observed at the end of the run. As a result of a too large surface heat flux, the model has more mixing below the inversion than observed, as indicated by the TKE. This excess of mixing reduces the temperature gradient in the lower layer and increases the inversion strength. On the other hand, the stability near the ground is close to the observed one, as well as above the inversion, where the simulated potential temperature is very close to the observed profiles.

The Meso-NH model as a LES for the SBL has showed in chapter 3 that it was trustworthy within the range of Derbyshire's formula (Equation 3.1). The present simulation has a surface heat flux well below the Derbyshire maximum (using G=6 m s^{-1} and Ri_c=0.25, would allow a maximum value of $< w\theta >_s$=-0.015 K m s^{-1}). Therefore, no runaway cooling is presented in the runs.

Another way to check the goodness of the simulation and to understand it is to inspect the Brunt-Väisälä frequency (N_{BV}) and the gradient Richardson number (Ri, computed by finite differences) derived from the mean profiles. These quantities are shown in Figures 7.5.c and 7.5.d, compared to one sounding of the simulated period. The sounding (as the others not shown) has large values for N_{BV} close to the ground and a secondary maximum just below the wind maximum. Above it, N_{BV} is smaller, almost constant and equal to 0.02 s^{-1}. Similar arguments can be given for Ri, noting here that almost all the column is below the critical values allowing for mixing except near the inversion and close to the ground. Equivalent results were found in Mahrt et al. (1979) from sounding measurements. As a first approximation, we consider that the simulation is able to capture

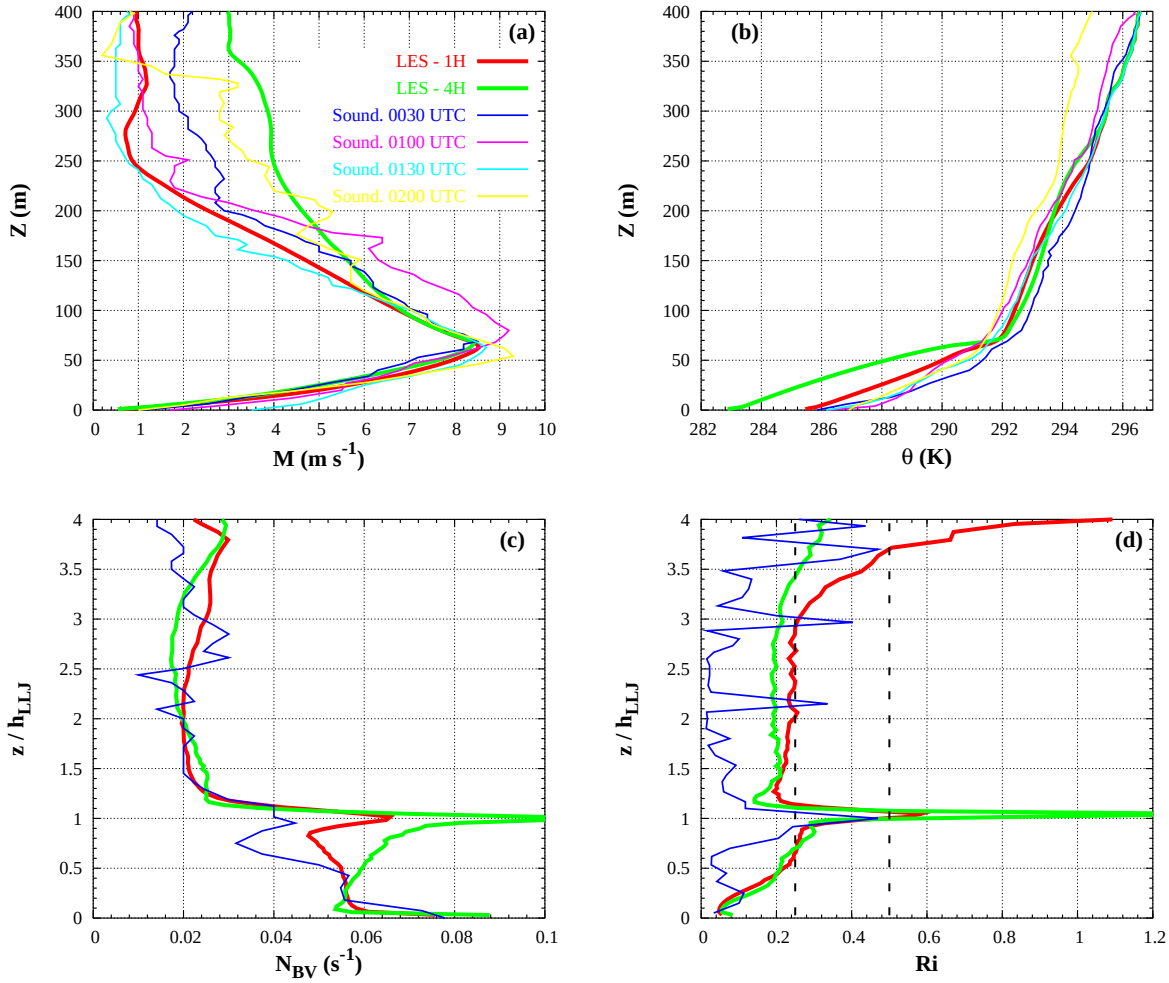

Figure 7.5: Averaged LES outputs at 1h and 4h (thick lines) and some soundings (thin lines) for (a) wind speed; (b) potential temperature; (c) Brunt-Väisälä frequency and (d) gradient Richardson number. In (c) and (d) only the 0130 UTC sounding is plotted

the main characteristics of the observed case, especially above the wind maximum.

7.4 Turbulence generated by the Low-Level Jet

The profiles of some turbulence quantities are shown in Figure 7.6. This Figure highlights that all variables are minimum at the LLJ height. It is very interesting to note that the model seems to prevent any exchange of heat across the wind maximum due to vertical turbulence transport, since both the resolved and the subgrid averaged heat fluxes are zero at that level, indicating a decoupling between the upper and the lower part of the LLJ. More hints are given by the profiles of the TKE and the horizontal variance of the wind. The resolved TKE budget shows that model sees the LLJ as a decoupled system

of two layers. The inspection of the variances shows that the horizontal components contribute more than the vertical one everywhere except near the inversion, where there is a minimum for the horizontal ones and a small secondary maximum for the vertical ones.

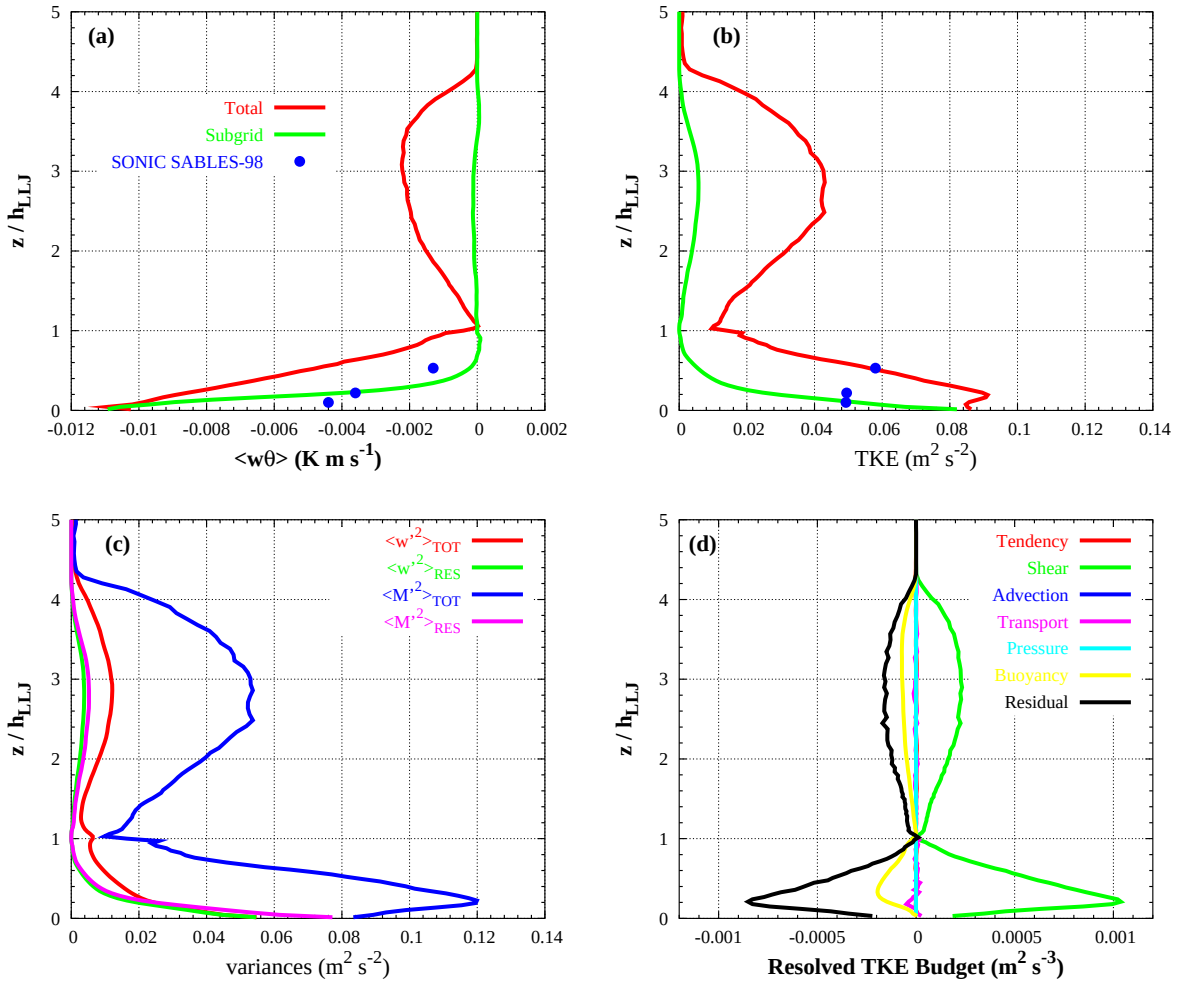

Figure 7.6: Averaged LES outputs at 4h: (a) vertical temperature flux; (b) Turbulence Kinetic Energy; (c) horizontal ($< M'^2 >$) and vertical ($< w'^2 >$) velocity variances; (d) resolved TKE budget. The symbols in (a) and (b) are averages from sonic anemometers

The layer above the inversion deserves special attention. There are very few measurements of turbulence in that layer (see Smedman et al., 1993 or Conangla and Cuxart, 2005) and the evidence of turbulence above the jet is basically indirect, observing minimum values of Ri from soundings. Although the values of the modelled turbulence are not very large, the LES generates TKE above the LLJ of the same order of the measures near the ground, showing a maximum above two times h_{LLJ}, as already pointed out Smedman et al. (1993) from aircraft observations of a LLJ over the Baltic Sea. Most of the TKE at

these levels comes from resolved motions. The production by shear is almost completely balanced by the dissipation, since the stratification is weak, contrary to the budget below the wind maximum.

7.5 Mixing across the wind maximum

The inspection of the averaged profiles of the turbulent fluxes seems to indicate that there is (almost) no mixing across the LLJ maximum where the inversion develops. Nevertheless, this could be a numerical artifact that provided a zero mean. In order to see how the model treats this level, two scalars are introduced after the spin-up of the simulation is over (1 hour after the start). This methodology was previously applied in Wyngaard and Brost (1994) where the use of two scalars in a convective boundary layer was useful to determine the top-down and bottom-up diffusion across the inversion.

The scalars are initialized as shown in Figures 7.7.a and 7.7.b, slightly distant from the wind maximum. In the same figure, the concentrations of the scalar four hours later can be seen. The model has diffused the scalars until the wind maximum but has not allowed almost any of it to cross the inversion, except maybe a little amount of under-inversion scalar being able to cross the layer.

To check the dependence of the scalar diffusion to the resolution considered, the same run is done taking the same horizontal resolution but a lower vertical resolution (now $\Delta z = 5$ m). The sensitivity test at coarser (5 m) vertical resolution allows more scalar to cross the inversion, as it is seen in Figures 7.7.c and 7.7.d, although the TKE and heat flux profiles do not change practically (not shown). The comparison of the time series at different heights of the scalar concentration for the lower and higher runs are shown in Figure 7.8. For instance, below the LLJ height $< S_1 >$ slightly decreases at the higher resolution whereas it is transported in the coarser resolution run, as Figures 7.7.c and 7.8.a point out. Similar results are found for the concentration of $< S_2 >$.

It might be that it is the advection scheme (leapfrog, flux-corrected) that allows the scalar to cross the ondulating version, an effect that diminishes with the increase of the resolution. The effects of the advection scheme are more important when the resolution is coarser, as it was stated in the GABLS intercomparison exercise described in chapter 5.

Figure 7.9 shows the diffusivities for heat and momentum computed dividing the total turbulence flux by the gradient:

$$K_M = -\frac{< uw >}{\partial < u > /\partial z} \tag{7.1}$$

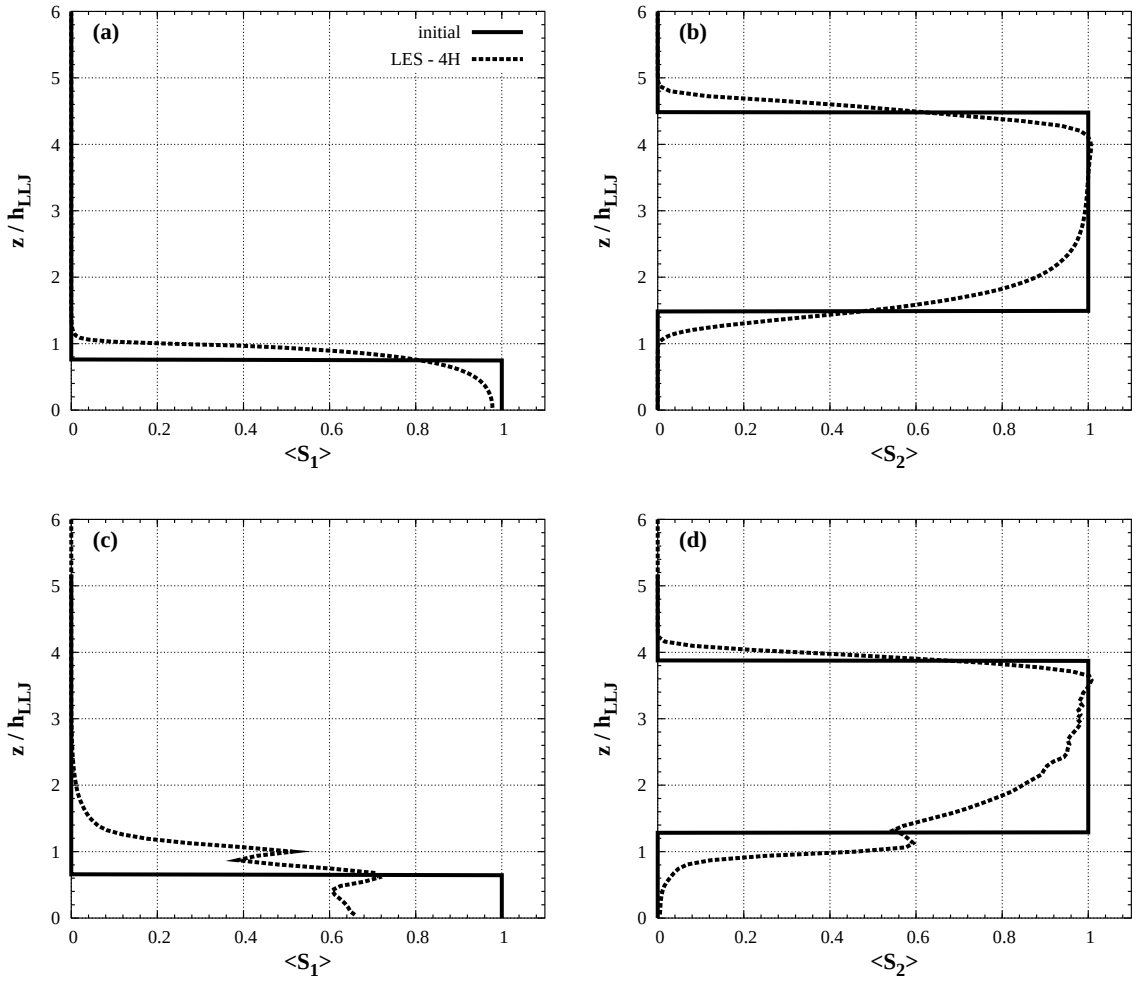

Figure 7.7: Averaged scalar concentrations of S_1 and S_2 after 1h (solid lines) and after 4h (dotted lines) from the beginning of the run. (a) and (b) correspond the standard run (Δz =2 m) whereas (c) and (d) to the lower resolution run (Δz =5 m)

$$K_H = -\frac{< w\theta >}{\partial < \theta > /\partial z} \tag{7.2}$$

where K_M and K_H are the diffusivities for momentum and heat, respectively, and $Pr = \frac{K_M}{K_H}$ is the Prandtl number.

The values near the inversion are very close to zero, although the values just below the inversion are slightly larger than just above, which might also help explaining why there is some low-level scalar crossing the inversion and not the contrary. The values of the diffusivities are one order of magnitude smaller than for a classically surface shear-driven stable case, such as in Beare et al. (2005). However it is interesting to note the values are larger in the upper part of the low-level jet than under the inversion, with somewhat larger values for heat than for momentum. This can be seen in the curve for the turbulence

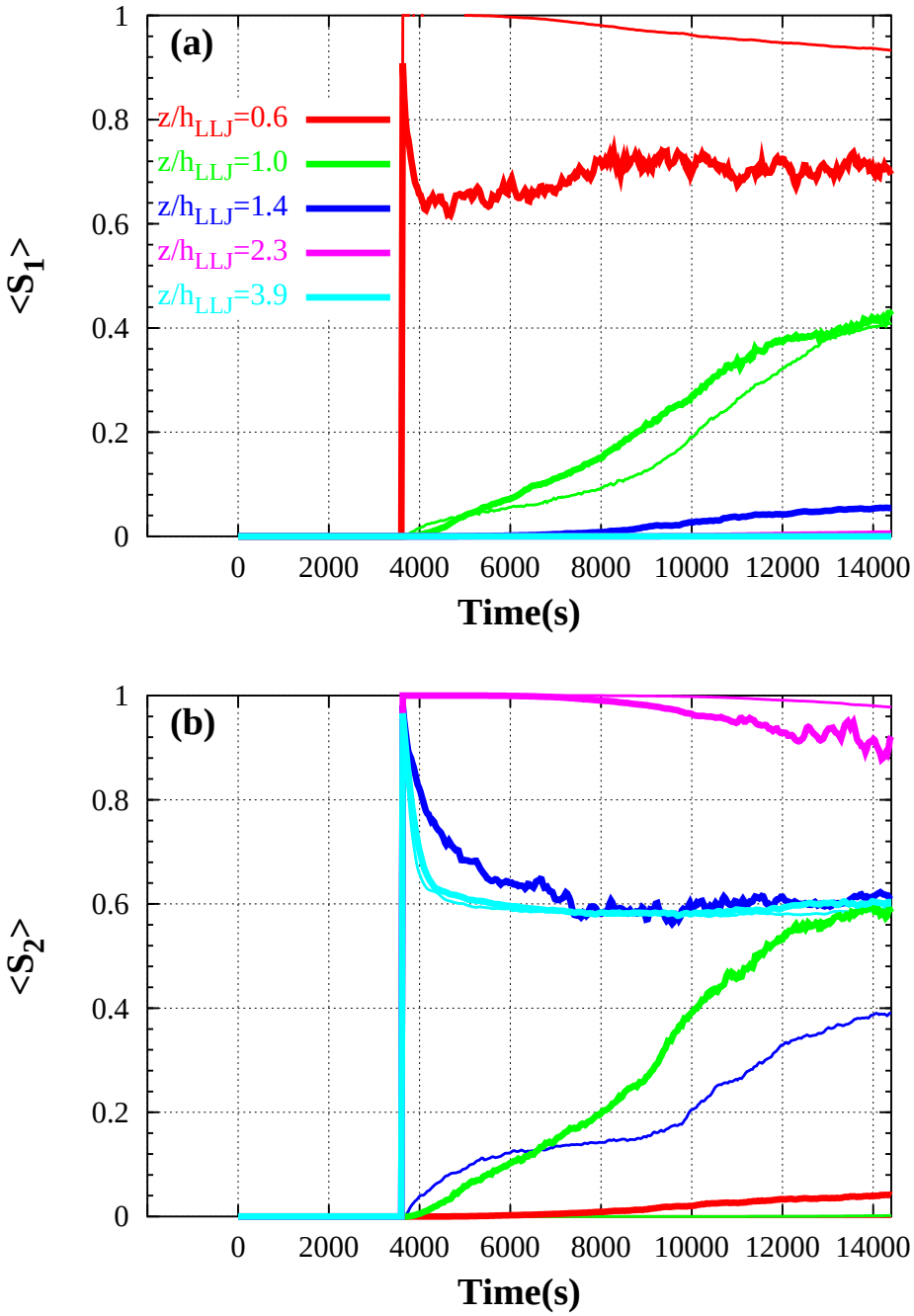

Figure 7.8: Time series for the scalar concentrations of (a) S_1 and (b) S_2 at different heights. Thick lines represent the lower resolution run (Δz =5 m) whereas the thinner ones the the standard run (Δz =2 m)

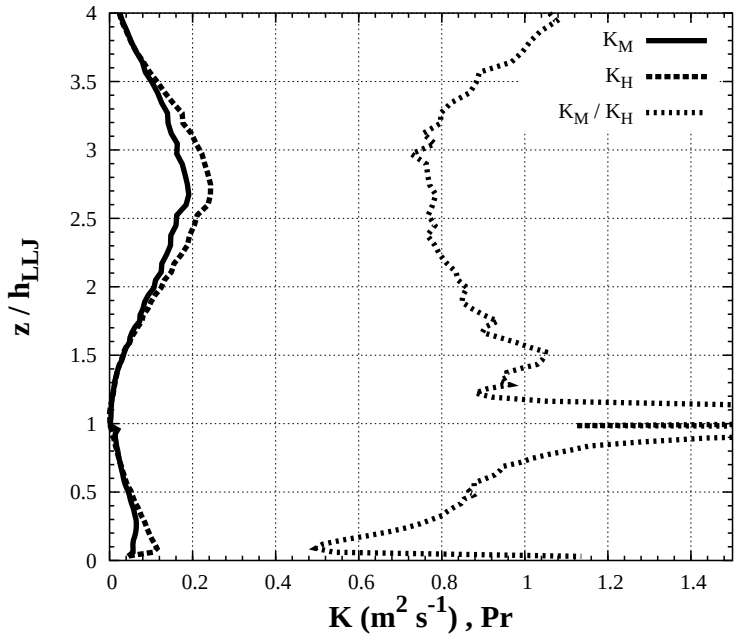

Figure 7.9: Eddy diffusivities for heat and momentum (K_M, K_H) and turbulence Prandtl number averaged during the 4th hour of the simulation

Prandtl number, which has an average value of 0.8 above the wind maximum and varies much below. The computation at the jet height is doubtful, because it is a zero divided by zero operation.

7.6 Eddy structures

The simulated regime can be seen as a two-layered regime, separated by a very well defined interface, the inversion at the wind maximum. In order to inspect how the turbulence regime is in each of these layers, the downwind and crosswind TKE spectra are analysed in Figure 7.10 at five different heights (0.6, 1, 1.4, 2.3 and 3 times h_{LLJ}). The spectra for wavenumbers larger than a certain cut-off number are not commented (Adams and Stoltz, 2002).

The downwind spectra show that, at every level, the most energetic structures are at the lowest wavenumbers, indicating that the eddies are elongated in the direction of the wind. Note also that the eddies are more energetic away from the inversion. From the comparison with the -2/3 slope, there seems to exist a short inertial subrange at every layer except the inversion, in the approximate range of wavenumbers 2 to 6. However, these scales (of about 100 m or more) seem far too large to indicate the beginning of any isotropic mixing, furthermore when the Ozmidov scale (L_{oz}) (an estimation of the upper

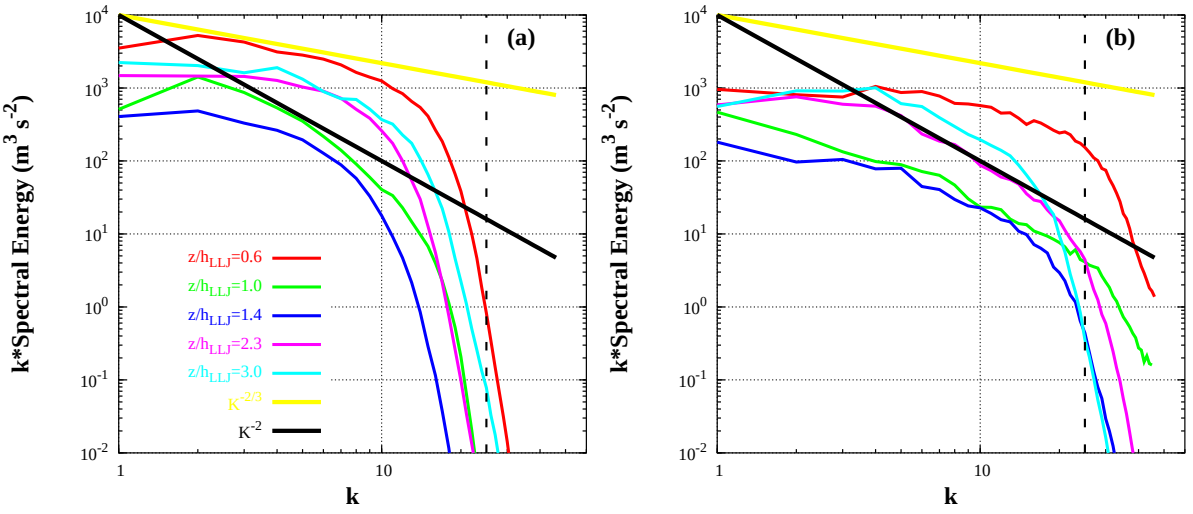

Figure 7.10: (a) Downwind and (b) crosswind TKE spectra obtained from the LES at $z/h_{LLJ} =$ 0.6, 1, 1.4, 2.3 and 3.0 after 4 h (dotted line: cut-off wavenumber)

limit of the inertial subrange, computed here at each level using the averaged subgrid dissipation and N_{BV}), gives values below 5 m. It does not seem likely that this range corresponds in any case to an inertial subrange.

The buoyancy subrange in the downwind spectra is approximately between wavenumbers 4 and 8 above and below the jet maximum and between 3 and 5 at the inversion level. In the physical space this would imply wavelengths on the range 50-100 m far from the inversion and 100-300 m close to it. The corresponding frequencies, obtained using the downwind velocity at each level, show that these waves would correspond to the largest supported at each level, as indicated by N_{BV} in Figure 7.5.c, with higher frequency oscillations at the inversion layer.

The crosswind spectra seem to show an inertial subrange between wavenumbers 7 to 22 (15 to 50 m) below the inversion and nothing clearly identifiable in the other levels. These wavenumbers are closer to the Ozmidov scale and could indicate effectively the existence of an inertial subrange starting at some scale around 20 m, even if this is larger than the Ozmidov scale, already an estimation itself. There also seems to exist a buoyancy subrange at the inversion and above, basically between wavenumbers 4 and 12, that converted to frequencies using the speeds of the crosswind also yield values very close to N_{BV} at each level.

The energy peaks of the crosswind spectra show a size of about 80-100 m away from the inversion, which can be seen as the separation between the alternating streaks, whereas close to the inversion the maximum is the first wavenumber, showing that maybe such a structure is not found in the inversion.

7.7 Comparison to observations

As mentioned above, during the period 0030-0200 UTC of September 21th, 1998, the LLJ was very steady, with the maximum well defined at about 65 m AGL. Although there were only sonic anemometer measurements up to 32 m, there were more conventional sensors in the tower recording at a rate of 5 Hz, up to 50 m for the temperature and up to 100 m for the wind. In order to see up to what point the LES simulation is realistic beyond the comparison of averaged values, we inspect here the probability density functions (PDFs) measured by those sensors and those produced by the LES at the same levels, the latter computed taking a complete horizontal field every minute during the last hour of the simulation. This comparison will inform if the LES is behaving similarly to the reality or not.

As it is described in the previous chapter, the PDFs are normalized such that $\int_{-\infty}^{\infty} B(x)dx = 1$ for any variable x. To allow for a clear comparison to other series, they are customarily plotted using $\sigma_x B(x')$ where $x' = \frac{x-\overline{x}}{\sigma_x}$. Here, $\overline{x}$ is the mean value and σ_x the standard deviation; a logscale is chosen for the y-axis to better inspect the tails (Figure 7.11).

Figure 7.11.a compares the PDFs for the fluctuations of the wind speed at 3 levels and also to some measurements by Chu et al. (1996) in the stably stratified surface layer. The LES model at 10 m fits better to Chu et al. (1996) data than to SABLES-98 data. This can be explained by the fact that Chu et al. (1996) measured in a classical surface-induced shear-driven SBL, well described by the similarity theory, which is imposed in the first level of the LES model. SABLES-98 data, with a LLJ, surely does not fit very well with the standard similarity theory, as the tails show. Moreover, Figure 7.12 shows that both observations and LES at this level have a large departure of the Gaussianity for the skewness and kurtosis values. At 50 m (not far from the above analyzed 0.6 h_{LLJ} level), the LES generates a quasi-Gaussian distribution, whereas the data show asymmetry (see Figure 7.12), with the largest values more frequent than the smallest. At 100 m, above the wind maximum, the simulation and the data compare fairly well, although some discrepancies still exist at the tails. Moreover, near the mean value the PDF computed from data have some slight fluctuations as the departure from the Gaussianity of the kurtosis value indicate (Figure 7.12). Nevertheless, this comparison gives support to the idea that the simulation is more realistic above than below the wind maximum.

The fluctuations of temperature at 10 and 50 m are compared in Figure 7.11.b. In the surface layer, again the LES compares better to the data by Chu et al. (1996) than to the present LLJ conditions, supposedly by construction. However it is very worthy to note here that the observed data show a very clearly defined binormal distribution, both at 10

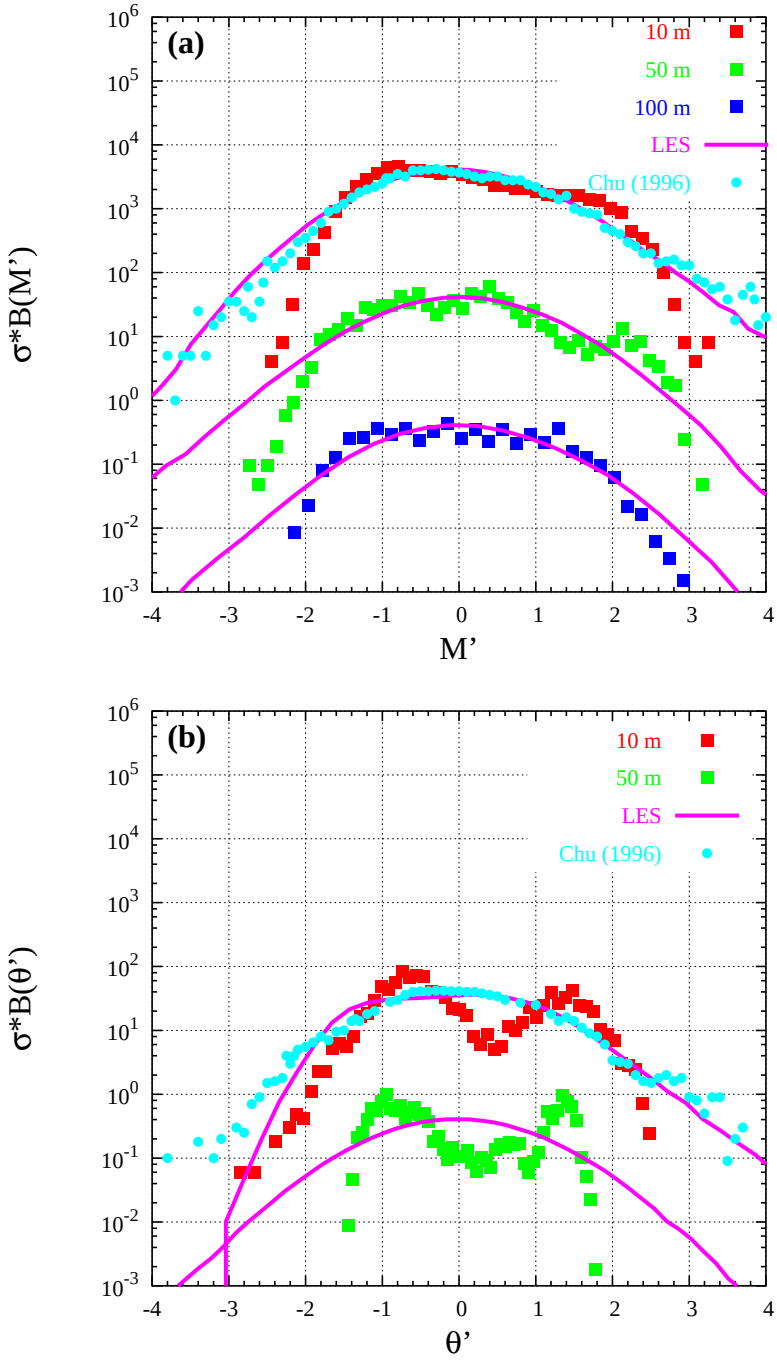

Figure 7.11: Normalized PDFs for (a) wind speed and (b) potential temperature computed from data (points) and from the LES (lines) at 10 m, 50 m and 100 m. The PDFs at 50 m and 100 m have been shifted up two and four decades respectively to clarify the intercomparison. In circles PDFs obtained from data measurements in Chu et al. (1996)

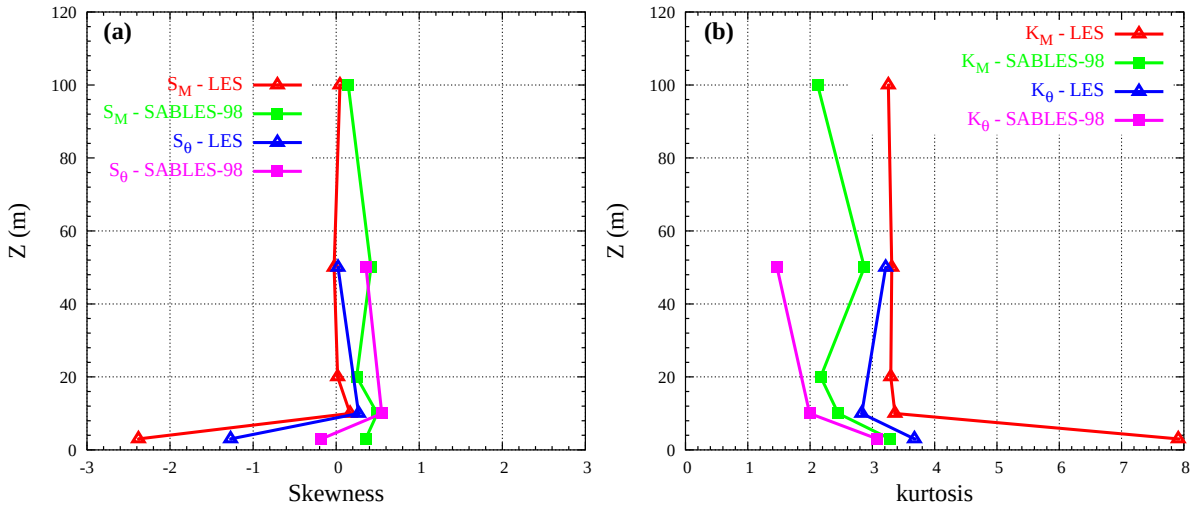

Figure 7.12: (a) skewness and (b) kurtosis values obtained from the PDFs computed through the LES results (triangles) and the observations (squares)

and at 50 m, with values as significant as ± 0.5 K. This is in good agreement with Figure 7.12 where the kurtosis values obtained from the data are smaller than those Gaussian. However, the kurtosis and skewness values obtained from the simulations are very close to the Gaussian values.

The observations could therefore indicate that the mixing below the LLJ maximum is performed either by large eddies, suddenly bringing warmer air to the surface that cools until a new event takes place, or that there could be intrusive bursts from above with a certain periodicity. The LES is clearly not able to produce this kind of distribution, and acts more as a system immediately reducing any too large gradient that is formed in the layer. The difference could also be due to a wrong placement of the inversion, which would excessively restrict the mixing across the wind maximum in the LES, whereas the reality could be less restrictive, as Banta et al. (2002) show. In fact, the observations sometimes show larger TKE at 32 m than at 5.8 m during this "steady state" period.

To sum up, Figure 7.11 points out that the PDFs computed from LES results and observations are similar but the tails are not properly captured by the LES, especially near the surface. These differences can be explained considering that:

• only the resolved motions are presented in the PDFs from the LES whereas in the PDFs from the measurements all scales of motion are included,

• the LES results depend on the turbulence scheme considered as well as the advection scheme,

• the ergodicity hypothesis is made since the PDFs of a single point (measurements) are compared to the ones computed taking all the horizontal field (LES),

• other forcings than the ones taken into account in the LES might be present in the observations.

Figure 7.13 shows the comparison of the LES profiles to the mean values considering the PDFs. The PDFs again highlight that the LES reproduce well the mean wind but not the near-the-ground temperature. Therefore, some sensitivity test are presented in the next section.

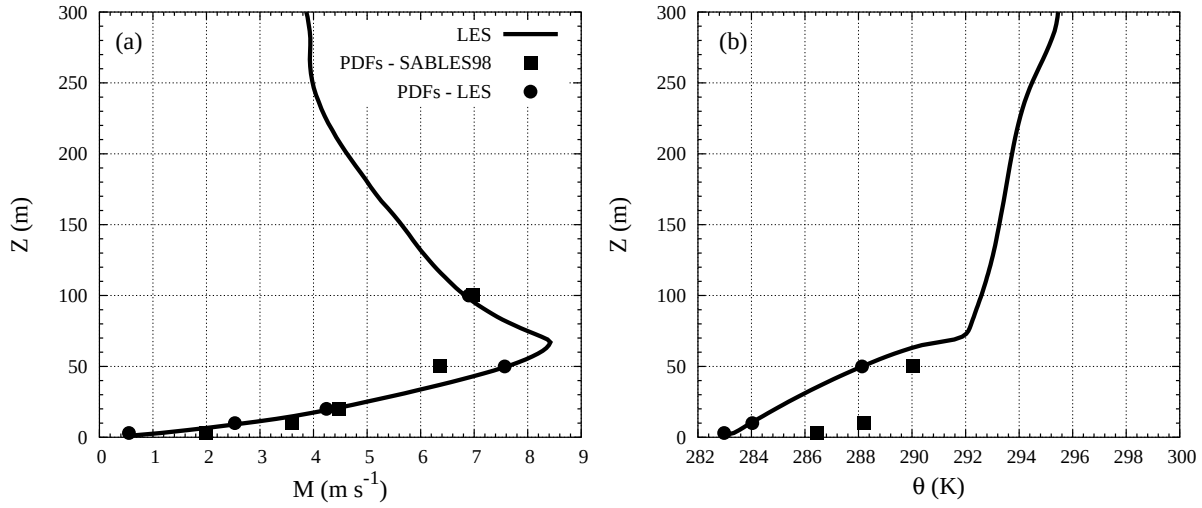

Figure 7.13: Mean profiles for (a) wind speed and (b) potential temperature obtained from the LES (lines) and those computed from the PDFs (points)

7.8 Sensitivity to the surface prescribed condition

From the comparison of the LES to observations through the PDFs it is found that the surface temperature is not well captured by the LES although at upper levels the LES results are closer to the observations. Moreover, when other quantities are considered instead of the temperature the LES results and the observations behave similarly. Several sensitivity tests have been performed to better capture the near-the-ground profiles. Since the LES is computationally very expensive, the tests have been performed using the lower resolution ($\Delta z = 5$ m).

Figures 7.14 and 7.15 shows the results for each sensitivity test labelled as:

• **energy budget equation**: coarser resolution run considering the energy budget equation that allows feedback between the soil and the atmosphere,

• $< w\theta >_s$= **-0.005 K m s^{-1}**: the surface vertical temperature flux is prescribed,

• **observed fluxes**: the surface vertical temperature and momentum fluxes are prescribed ($< w\theta >_s$= -0.005 K m s^{-1}, $< uw >_s$= -0.003 m^2 s^{-2} and $< vw >_s$= 0.0003 m^2 s^{-2}),

• **high resolution**: a 2 m resolution run considering the the energy budget equation.

The observed values from the tower are also indicated in Figure 7.14. From the energy budget equation, the averaged surface vertical temperature flux converges to a value larger than the one observed. Therefore, the same conditions are run using a prescribed surface vertical temperature flux ($< w\theta >_s$= -0.005 K m s^{-1}) instead of the energy budget equation. The maximum of the wind reaches higher levels whereas the temperature profile is less stable allowing more mixing. There is still turbulence above the LLJ and the TKE presents a similar shape. The inversion is less strong and therefore there is slightly more transport of scalar through the inversion. Nevertheless, the results above the LLJ do not change significantly.

However, the prescribed surface vertical temperature flux does not improve the results of the temperature near the surface. Another sensitivity test is performed prescribing the surface vertical temperature flux ($< w\theta >_s$= -0.005 K m s^{-1}) as well as the momentum fluxes ($< uw >_s$= -0.003 m^2 s^{-2} and $< vw >_s$= 0.0003 m^2 s^{-2}), corresponding to observed values. Now the temperature profile near the surface is better captured but the wind has less shear below the LLJ. This fact makes the turbulence below the LLJ weaker than in previous runs, although above the LLJ the turbulence is not affected. There is less upward transport of scalar since the inversion is stronger and more decoupled but the downward transport slightly increases.

Regarding the mixing, when the surface cooling is imposed there is more scalar transported through the inversion layer (Figure 7.15), especially in the case where the observed forcings are included in the LES. There is more downward transport of S_2 in the prescribed observed forcings than in the imposed surface forcing but an opposite behaviour is found for the upward transport of S_1. Therefore, the inversion height has different characteristics depending on the surface condition applied in the LES.

These tests highlight how difficult is to simulate the surface conditions and this is still a problem not solved. Nevertheless, the results above the LLJ are almost independent of the surface forcing imposed.

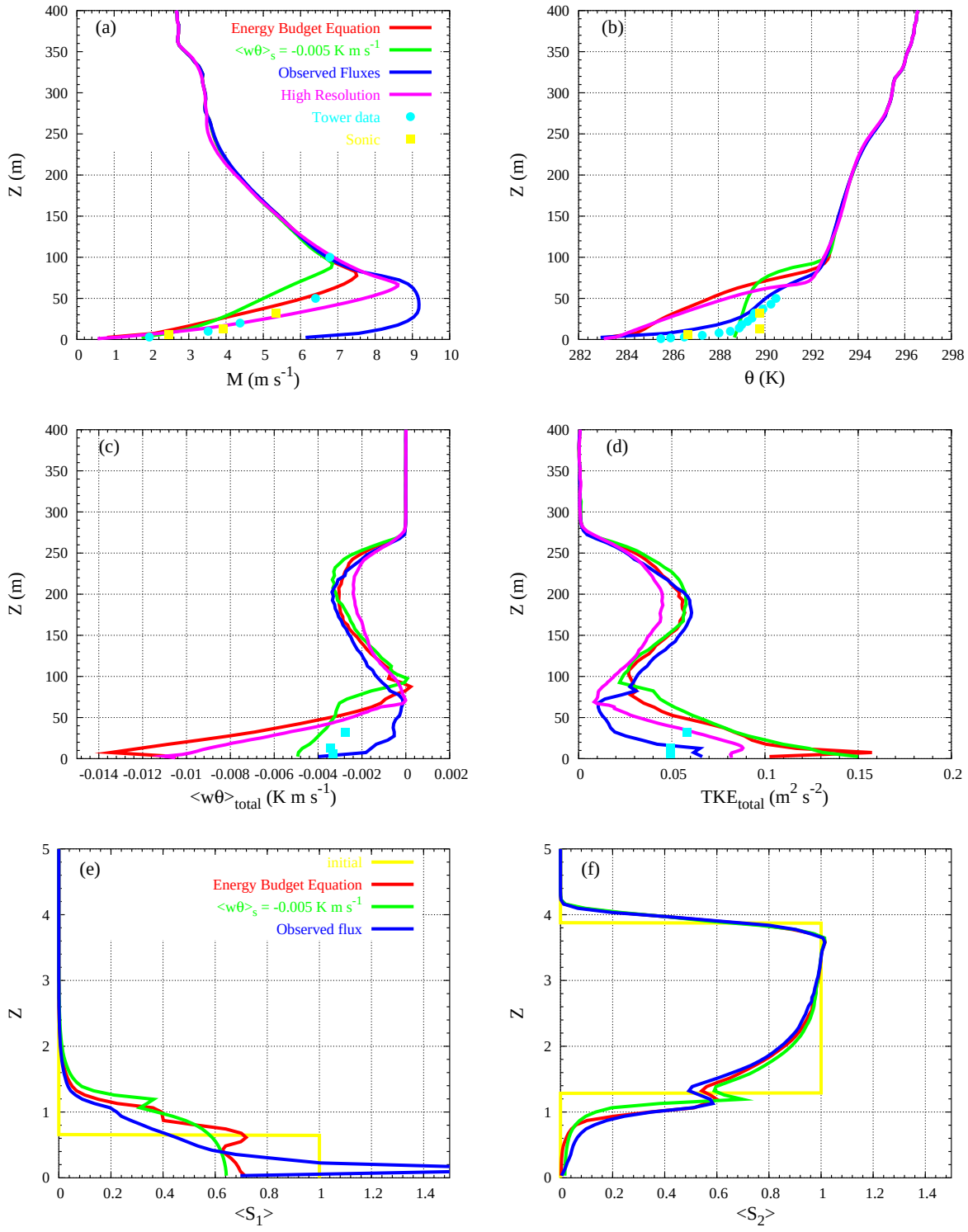

Figure 7.14: Profiles obtained for each of the sensitivities to the surface prescribed condition studied: (a) wind speed; (b) potential temperature; (c) heat flux; (d) Turbulence Kinetic Energy and the scalar concentrations of (e) S_1 and (f) S_2. The symbols show the measurements from the tower. Theses profiles correspond to averages over the last 0.5 h of the run. For the scalar concentration profiles, the initial profile is also shown

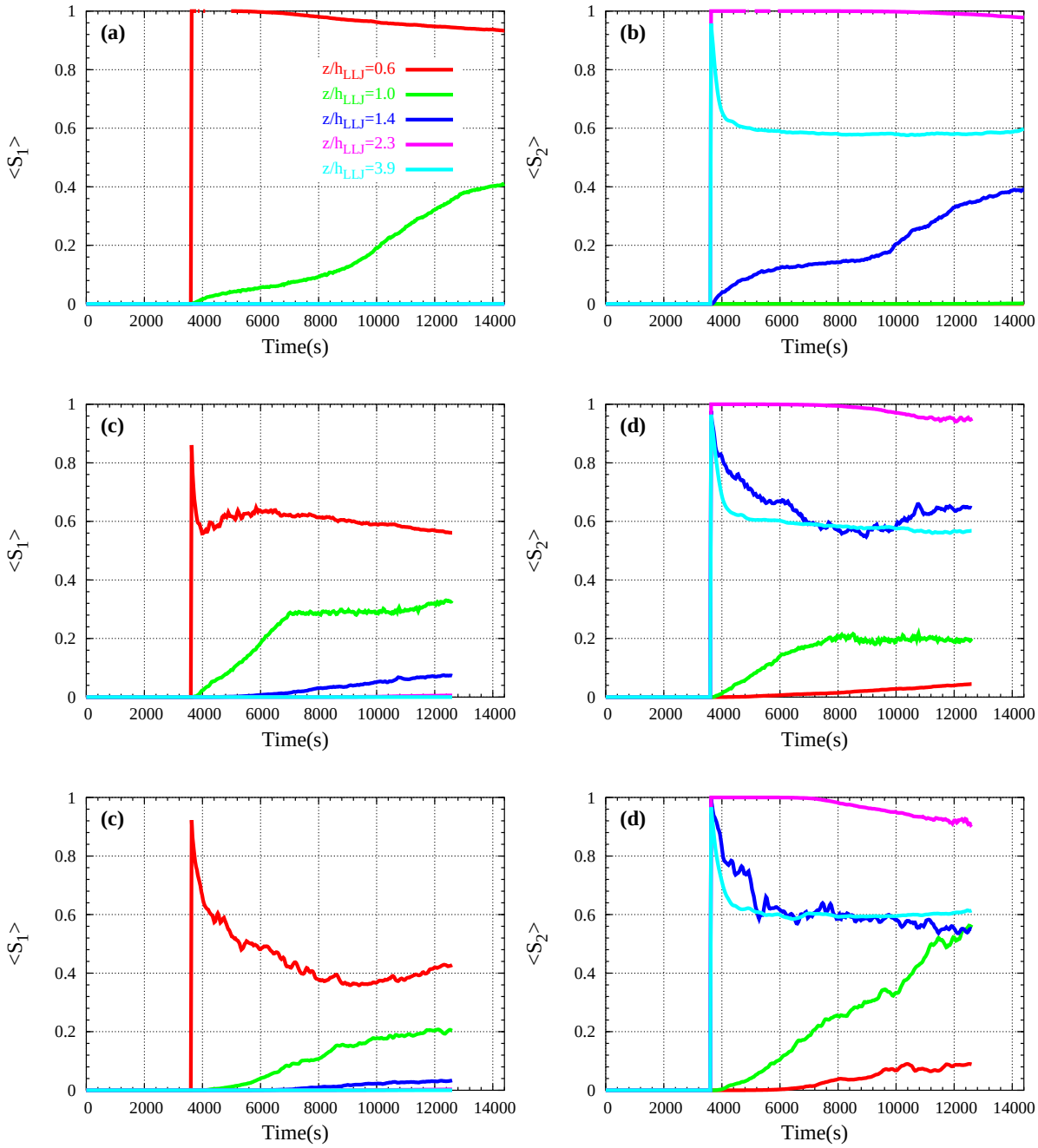

Figure 7.15: Time series for the scalar concentrations (left) S_1 and (right) S_2 for each of the sensitivity tests. (a) and (b) the **high resolution case (Δ = 3 m)**; (c) and (d) the **prescribed heat flux ($< w\theta >_s$ = -0.005 K m s^{-1})** run; (e) and (f) where the **observed momentum and heat fluxes** are prescribed

7.9 Conclusions

An observed Low-Level Jet (LLJ) during the SABLES-98 campaign has been undertaken with the aim of understanding the basic processes taking place in the regime and the structure of the associated turbulence. An LES of the LLJ is performed initialsed with data from soundings and the results are compared to those measured by the tower and the soundings through the inspection of the mean profiles and the PDFs methodology explained in chapter 6.

The model distinguishes between two separated layers, one above the maximum of the wind, with weak stable stratification and strong shear and the other below, with stronger stratification and shear. Both layers have significant turbulence, of similar intensity, with the upper part extending as high as 3 times the height of the maximum of the wind. An inversion is formed at the wind maximum (slightly stronger than the observed one) that decouples both layers. The use of passive scalars shows that the transport across the interface is small. The model, forced to behave accordingly to the surface layer similarity theory, runs more smoothly in the lower layer than the observations, that indicates a more intermittent behaviour.

The exploration of the spectra seems to confirm the existence of wave-like motions within the simulations, well characterized by the values of N_{BV} at each level, that the model captures precisely. The waves are of larger frequency and apparent wavelength in the layers close to the inversion. There also seems to exist a short inertial subrange below the inversion, seen only in the crosswind spectra, starting at scales of about 20 m.

The comparison of the LES results to the main tower data is made through the computation of the PDFs, whereas the soundings are compared to the averaged LES profiles over the horizontal within the stationary period. Therefore, the ergodic hypothesis explained in the previous chapter is implicitly made. The simulation behaves closely to the observations, especially in the upper layer. The temperature gradient in the lower layer is somewhat too large. The differences might be due to the imposed surface boundary conditions, other forcings that might be ignored, the dynamic forcing used, or a too coarse grid resolution near the ground that might rely more than advisable on the turbulence scheme. Nevertheless, sensitivity test highlight that the results above the LLJ do not depend on the imposed surface boundary conditions which is still a subject of study.

Nevertheless, the effects on the results from the largest scales are not taken into account in the LES. This fact compels us to study the contribution of the larger scales in the SBL profiles and how they can influence it. This is the subject of the next chapter, where mesoscale modelling is undertaken.

Chapter 8

LOCAL CIRCULATIONS WITHIN THE NOCTURNAL BOUNDARY LAYER[1]

In previous chapters it has been seen that many eddy scales are presented in the observations of the SBL. However, the LES results contain only the information from the scales smaller than the simulation domain. Since the larger scales are not taken into account in the LES, they could explain the differences between the LES results and the observations. For instance, in chapter 6 it is shown that the PDFs computed from LES results diverge to those computed from observations only in the tails. The tails can be associated to events of lower scales (that are parameterized in the LES) or events to larger scales (that are not taken into account in the LES runs).

Therefore, here mesoscale modelling is used to explore the contribution of the largest scales within the SBL. Contrarily to the LES of the previous chapters, mesoscale modelling includes the information of the orography as well as the soil uses to make the simulated conditions closer to the reality.

The study of the locally generated circulations at the basin scale is of primary importance to characterize the local wind regimes, but also to be able to understand point measurements at meteorological stations. Precisely, the study of the stably stratified nocturnal boundary layer is very much determined by the presence of katabatic flows, that can be organized at the scale of the basin. Observed time series show sudden changes of the wind direction, bursts of turbulence, and a posterior slower pace of the surface cooling rate, that seem difficult to explain without considering slope flows. Therefore, this fact

[1]This chapter is based on: Cuxart, J., and Jiménez, M.A., 2005b: Local nocturnal circulations on the Majorca Island. submitted to *Monthly Weather Review*.

highlights the importance of mesoscale modelling to complement the information given by measurements and LES results.

To start with, a simple case over the Majorca Island is chosen and a mesoscale run is performed. This is a closed system consisting of basins surrounded by mountains and the sea. More complex orographic system will be analysed in the future such as the Duero basin to understand some of the features observed during the SABLES-98 campaign. Therefore, vertical and horizontal cross-sections, as well as some time series at a single point, are used to analyze the complete picture. To validate the runs, they are compared to NOAA satellite images and available data from automatic surface weather stations. The difficulties appeared when the mesoscale runs are validated are discussed but this is a work still in progress in the frame of a research project.

8.1 Introduction

The study of the atmospheric boundary layer normally assumes horizontal homogeneity, which is implicitly imposed in any work related to data analysis, or single-column or Large-Eddy Simulation modelling exercises. This approximation is fair when the synoptic scale flows and the turbulence response to forcings are the dominant factors and the orographic features are not too important. But when the orography is showing significant variations it must be taken into account.

Furthermore, in stably stratified conditions, such as in the nocturnal boundary layer with synoptic light winds and clear skies, the role of the orography becomes extremely important, say dominant (see, for instance, the VMTX campaign in the Salt Lake Valley, Doran et al., 2002). The lack of turbulence mixing allows large temperature gradients to develop near the ground, of different intensity depending on the location. The coldest particles of air start their descent downhill, but are compressed and heated during their way until they become neutrally buoyant.

During the diurnal cycle in mountainous regions, three-dimensional circulations can form within and just above the valleys. Two different kinds of geographically generated flows can be distinguished: cross-valley-axis flows (anabatic/katabatic slope winds) and along-valley-axis flows (mountain-valley valley winds). During the night, radiative cooling of the mountains surfaces cools the air adjacent, resulting in cold downslope or katabatic winds. These winds are very shallow (2 to 20 m) and have velocities of the order of 1 to 5 m s^{-1}. Above the layer floor, there is a gentle return circulation of upward moving air that diverges towards the ridges. The anabatic winds appear after sunrise when the heating warms the air close to the ground but this is a subject of another study because here

we will only study the nocturnal boundary layer. At night, the orographically generated circulations are a combination of the katabatic winds with the valley winds. This last one consists of a flow down the valley onto the plains with depths between 10 to 400 m and velocities of 1 - 8 s^{-1}.

The quasi-horizontal motions generated in this way transport air to locations that can be very distant of their sources, especially if they are combined with larger scale temperature gradients, such as a sea-land discontinuity or baroclinicity at the scale of the basin (see Stull, 1988). At one particular point, for instance at a meteorological station, the arrival of these currents may result in sudden changes in the wind speed and direction, changes in the surface cooling rate or turbulence bursts. Blumen (1984) studied how the arrivals of gravity flows were seen in the 300m-tower at the Boulder Atmospheric Observatory in the foothills of the Rocky Mountains, as Cuxart et al. (2000b) for the CIBA site in the Duero basin.

With this in mind, it seems obvious that any study on stably stratified nocturnal boundary layers based on point or column measurements would need an estimation of the orographically generated flows that reach that particular point. Not only for academic reasons, but also for practical purposes since, depending on the variability of those currents, the measurements at that station could be very different from those at another point, not necessarily very distant.

The direct study of the orographically generated flows at the scale of a basin is currently out of reach because only punctual observations can be made. Some observational hints could be obtained through the use of doppler radar (for instance as in CASES-99 campaign) or inferences from satellite images, but a complete picture seems difficult to obtain. The most easily available alternative is the mesoscale modelling, which is the approach taken here.

Mesoscale modelling of the nocturnal boundary layer is difficult for a number of reasons. The horizontal resolution chosen is normally not larger than 1 km and the turbulent motions at these scales have to be fully parameterized, thus relying on assumptions that many times are not very adequate for the night-time turbulence. The physiographical characteristics of the underlying terrain are very relevant and must be adequately represented in the model, both by an adequate soil-vegetation scheme and by a good initial soil temperature and moisture. The longwave radiation must be well represented, especially in the lowest layers of the atmosphere, where the vertical divergence of the radiative flux is larger. The terrain has to be well characterized, using an adequate coordinate apt to capture the downhill motions. These problems are also shared by Zhong and Fast (2003) where a high resolution mesoscale run is performed using three different mesoscale models

for one of the intense observed periods during the VTMX campaign.

The observational work has shown that the most relevant features in the SBL are concentrated in the first hundreds of meters of the atmosphere, and the slope flows have all their features in the first tens of meters or even in the first ten meters (Mahrt et al., 2001). This circumstance forces the modeller to prescribe a very fine vertical resolution close to the ground, restricting much the time step and producing simulations that are very costly computationally. This leads to the use of relatively coarse horizontal resolution, resulting in strongly anisotropic grid boxes.

However, this approach suffers of two major drawbacks: the existence of runaway cooling when the turbulence scheme is not able to mix and decouples the surface and the atmosphere (see further details in chapter 3), and the difficulties to verify the goodness of the produced fields, due to the absence of adequate observed data with sufficient spatio-temporal representativity. In this work, the simulations do not fall into a situation of runaway cooling and preliminary efforts have been made towards a methodology of verification using satellite images.

The simulation that is presented here is focussed on the isle of Majorca, belonging to the Balearic Islands archipelago in the Western Mediterranean Sea. The isle, of a characteristic length of 100 km and with important mountain ranges and several well-distinguished basins is a good test location for the suggested methodology. Later it will be presented how the flows are organized at the scale of the island at an advanced stage of the night and how the simulation compares to the available direct and remote sensed data. The analysis will be centered on the phenomena at the basin scale, inspecting how the flows behave and relating their characteristics to the theoretical prescriptions given in the bibliography (Fleagle, 1950; Mahrt, 1982). Some considerations will be made on the representativeness of a given station.

8.2 The simulation setup

The Balearic archipelago is located in the western Mediterranean Sea, 200 km offshore of the east coast of the Iberian Peninsula (Figure 8.1). It is composed of four islands (Majorca, Minorca, Eivissa and Formentera) and a number of smaller isles. The largest island is Majorca, which has a characteristic size of 100 km, whereas Eivissa and Minorca have a characteristic size of 40 km and Formentera of 15 km. This work is part of a larger study on the local winds on the Balearic archipelago, but here the main purpose will be to describe the nocturnal circulations on the Majorca isle, putting emphasize on the characteristic sizes of the circulations (depth and horizontal scale) and the difficulty

Figure 8.1: Location of the Balearic Islands in the Western Mediterranean Sea

of simulating and verifying such cases.

Majorca is, therefore, the largest island. It has a large mountain range at its north-western side (Serra de Tramuntana), with an average height of 700 m above-sea-level (ASL) and the central part has several peaks between 1200 and 1500 m. On the opposite side (SE) there is a discontinuous lower mountain range (Serra de Llevant), with an average height of 300 m, not really opposing much resistance to a perpendicular flow. The center of the island is relatively flat, although elevated at the central part (200 m ASL), with a small central mountain (Randa, 400 m). This orographical configuration results in three main basins: the Palma basin at the SW part, the Campos basin at the SE, the Alcudia basin at the N, plus two coast narrow basins between the mountain ranges and the sea at NW and E. (Figure 8.2)

The island has a population of about 750000 inhabitants and more than 370000 live in the city of Palma de Majorca and its surroundings, located in the Palma basin. This basin has a characteristic size of 20 km and it is completely surrounded by mountain ranges and elevations that make a semi-closed basin, except at the coast, a wide bay. In the center of the basin, at about 10 km N of the city, there is an installation where residuals are burnt that is upwind when drainage flows occur. On the other hand, the inland is mostly agricultural and there is interest in a good characterisation of the cold areas at night. A study of the daytime part of the cycle was made by Ramis et al. (1990).

To perform this study, the Meso-NH model of the French community has been used

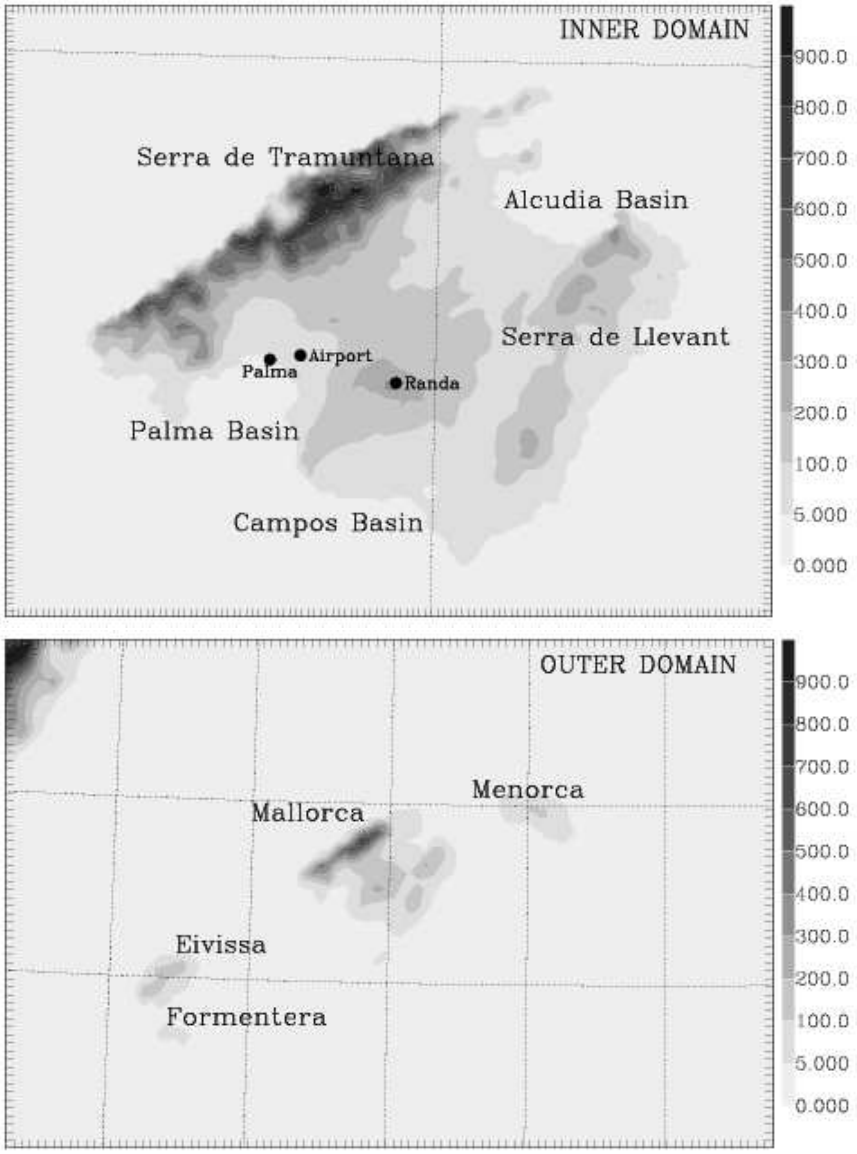

Figure 8.2: (top) Inner and (bottom) outer domains considered in the run. Some towns as well as the three main basins and the two mountain ranges are also indicated

(Lafore et al., 1998). The model can be used in a large variety of configurations (from Large-Eddy simulations to synoptic scales). Its performance for boundary layer regimes has been tested successfully (Cuxart et al., 2000a) and the stable boundary layer has received special attention lately (see previous chapters). It has been shown that the model is able to simulate moderate to relatively strong stabilities without experiencing runaway cooling, which is also the case for this modelling study.

A case with a very weak synoptic pressure gradient is chosen: the archipelago is very close to the center of a winter high pressure system, with a very weak flow coming from the southeast (of about 4 m s^{-1} over the sea at 10m), thus normal to main mountain range at the NW. The skies were cloudless and the humidity was below 60%. The situation is steady at the synoptic scale during all the run. Two domains are chosen (Figure 8.2). The largest one has a resolution of 5 km and the inner one of 1 km, covering only Majorca. The initial and boundary conditions are provided by the ECMWF analyses. The simulation runs from 12 UTC (12 local solar time) on January 5th, 1999 to the dawn of the next day, thus covering completely the 15-hour-long night. It has been run on the ECMWF supercomputers.

The vertical grid mesh has been chosen as very fine near the ground, to be able to capture all the details of the low level flows. Therefore, the vertical resolution is close to 3 m near the ground, with a stretching factor that leads the resolution to about 8 m at 500 m ASL and to 500 m at the model top. Such a fine vertical resolution implies very short timesteps (below 2 s), especially at mountain slopes.

The relevant physical processes in this simulations are the dynamics -basically the advection scheme, here a flux corrected second order centered scheme-, the turbulence scheme (only the vertical part of the complete 3D turbulence scheme of Cuxart et al., 2000a is activated, using the Bougeault-Lacarrere mixing length (1989) as the closure parameter), a two-layered soil scheme (Noilhan and Planton, 1989), and the radiation scheme (adapted from Morcrette, 1990).

8.3 General description of the flow

The general flow in the area is from the SE. In Figure 8.3, the streamlines at several heights are shown: near the surface (z = 10 m), within the boundary layer (z = 100 m) and in the free atmosphere (z = 1000 m). It is clear that at a height of 1000 m, the flow barely sees the island as it flows over it. However at 100 m ASL, the NW mountain range (Serra de Tramuntana) is clearly blocking and diverting the flow around it, with a bifurcation point near the centre of the isle. The estimated Froude number Fr is defined as:

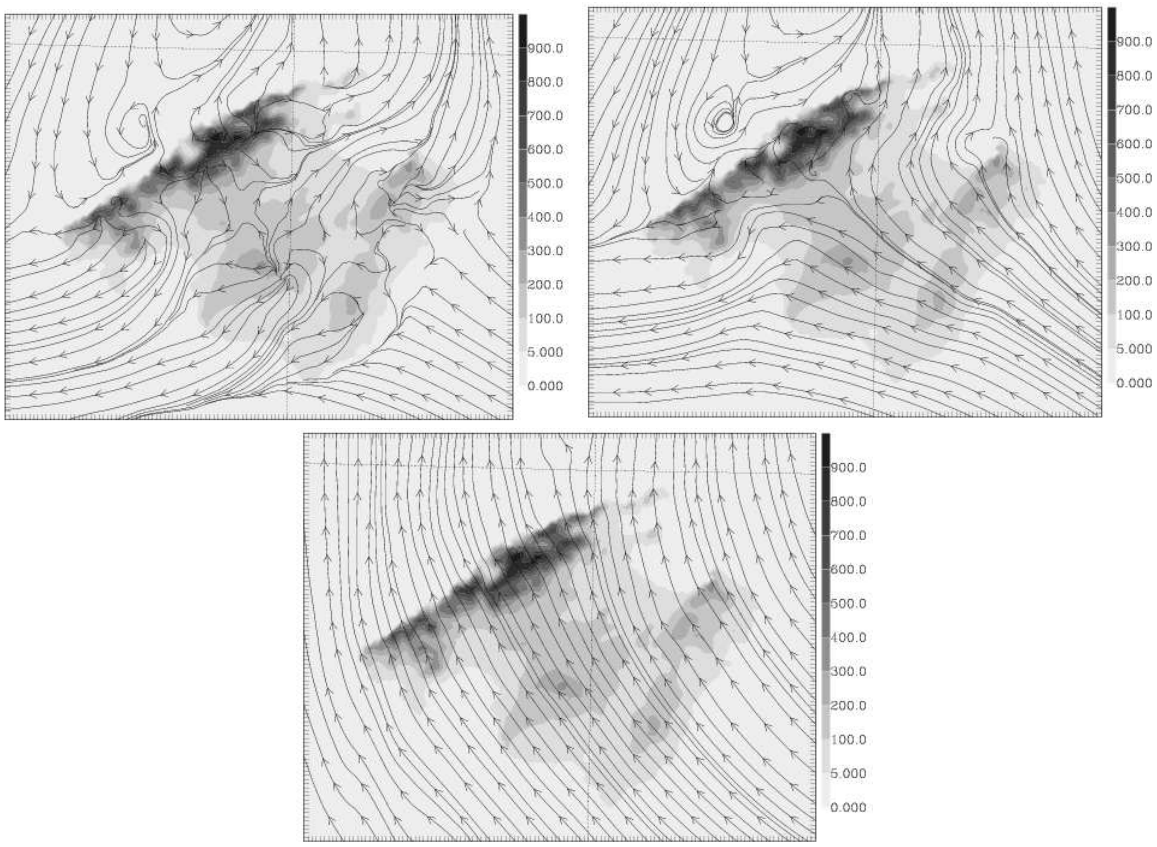

Figure 8.3: Streamlines at different heights: (top-left) 10 m, (top-right) 100 m and (bottom) 1000 m at 0400 UTC

$$Fr = \frac{UN_{BV}}{h} \tag{8.1}$$

where U is the mean wind speed, N_{BV} the Brunt-Väisälä frequency and h the average mountain height. Taking $U = 4$ m s^{-1}, $N_{BV} = 0.01$ s^{-1} and $h = 800$ m the Froude number is about 0.6, indicating that some of the air flows over the top of the hill, while air at lower altitudes separates to flow around the hill. Therefore the center of the isle is an area of minimum wind speeds, able to develop freely winds determined basically by the topographical configuration. This is clearly seen in the streamlines at 10 m above ground level (AGL).

The simultaneous exploration of the streamlines at 100 and 10 m ASL shows that in the SW part of the island the flow diverted by the mountain and the low level drainage flow have the same direction and result in a relatively deep flow out of the island, whereas the same phenomenon takes place at the N part of the island, but less intense since the mountain range is less compact at that part. It can be seen that the flow is out of the island at the three main basins at the lower levels. Similar results are found in Zhong and

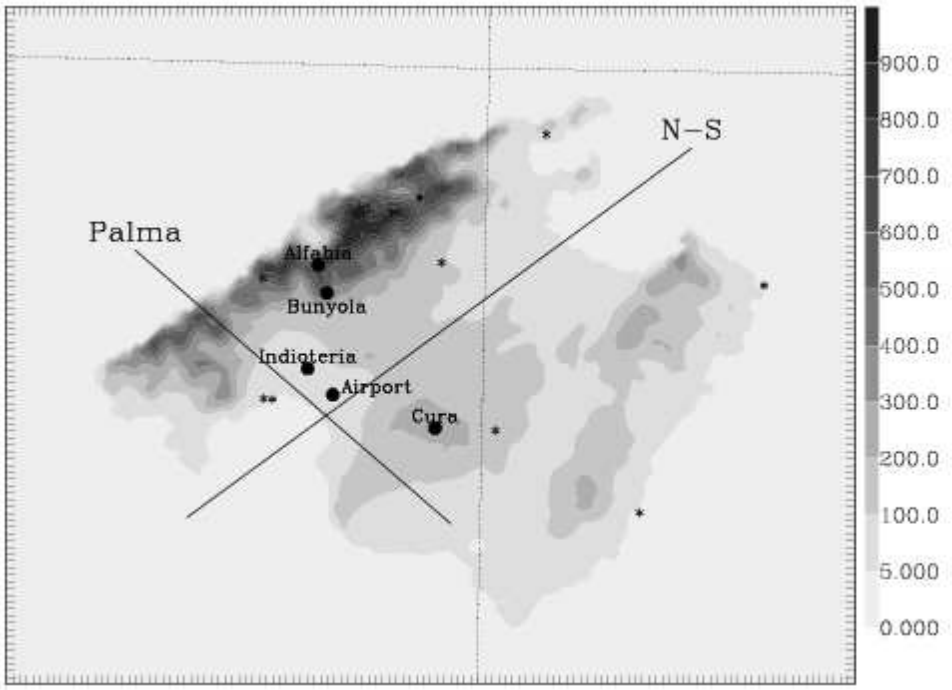

Figure 8.4: Vertical cross-sections that have been considered as well as some of the locations that later will be studied further. The locations of the automatic surface weather stations are presented with an asterisk

Fast (2003) for a mesoscale run of a period during the VTMX campaign.

To inspect with some more insight the details of the circulations several vertical cross sections are shown, following the lines given in Figure 8.4, at 0400 UTC. The section "Palma" (Figure 8.5) shows that the maximum winds are at the eastern part of the island and are reduced as the flow progresses inland. There are several areas of minimum wind speeds at the center of the island and behind the Tramuntana mountain range. At low level at the central part of the basin the winds blow from the north with speeds of about 4 m s^{-1}, and at height of 500 m from the east and weaker, thus almost normal to the general SE flow, indicating the existence of a land-sea circulation. The streamlines show that air cumulates in the low levels from the mountains around and the temperatures are minimal near the ground. Other sections show similar patterns: accumulation of cold air in the valleys, where the speeds are minimal, and outflow to sea at the shore.

A cold pool is also found in the center of the valley. A cold pool is a topographically confined, stagnant layer of air that is colder than the air above. Cold pools can be characterized as diurnal, forming during the evening or night and decaying following sunrise the next day, or persistent lasting longer than a normal night-time temperature inversion. In our case, the cold pool will be destroyed during the sunrise. Observed cold

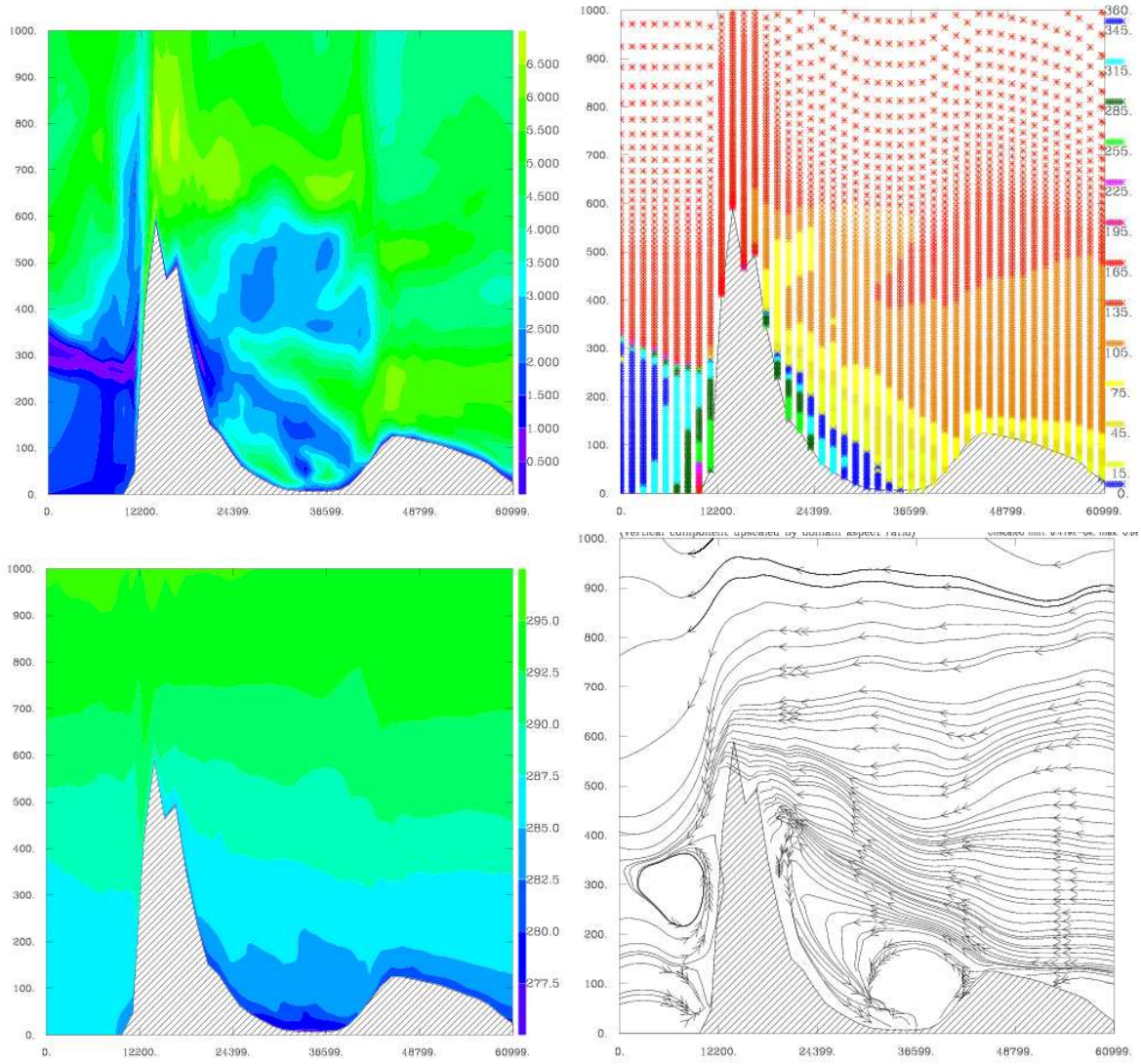

Figure 8.5: Vertical cross-section labelled as 'Palma' in Figure 8.4 at 0400 UTC. (Top-left) Wind speed (in m s^{-1}), (Top-right) wind direction (in degrees), (Bottom-left) potential temperature (in K) and (Bottom-right) streamlines. The city of Palma is located approximately in the middle of the valley

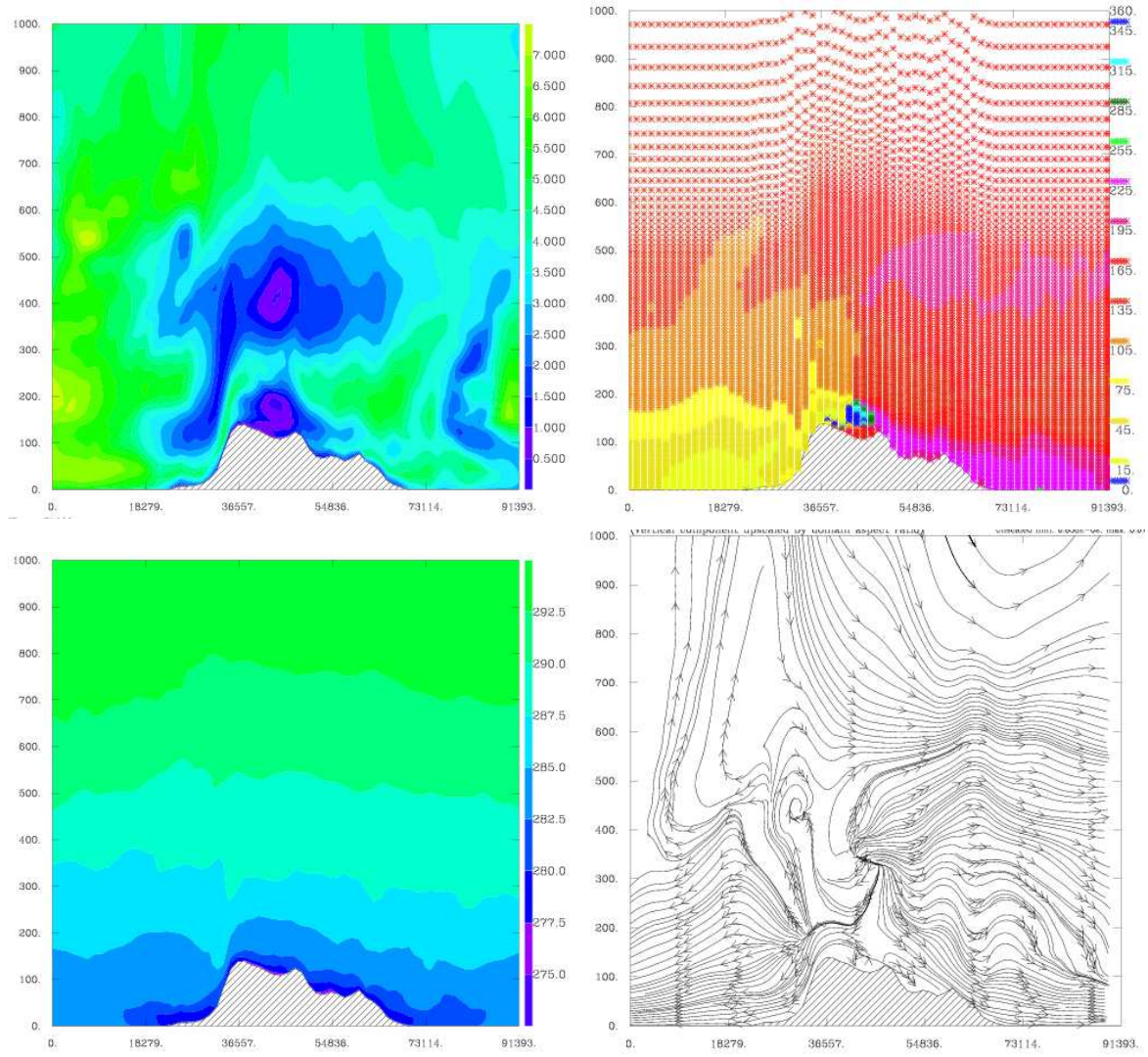

Figure 8.6: Vertical cross-section labelled as 'N-S' in Figure 8.4 at 0400 UTC (plots as in Figure 8.5)

pools in the Columbia River basin are further explained in Whiteman et al. (2001) and a mesoscale results in Zhong et al. (2001).

Figure 8.6 shows the cross-section labelled as 'N-S' in Figure 8.4 running from Palma to the Alcudia basins, crossing the central elevated part of the island. It is seen that the flow runs downhill from the center to both valleys with speeds over 5 m s^{-1} at heights below 50 m AGL and much weaker about 200 m above. The temperature gradients are very strong close to the ground, especially in the little valleys, allowing the development of cold pools. The streamlines do not show a well defined return flow above, as pointed out Whiteman et al. (1999) and the basins seem to function unconnected. At the Palma basin (on the left-hand side in Figure 8.6) the wind veers from the north near the ground towards the synoptical wind (SE) at heights about 600 m. This is not observed in the Alcudia basin where the direction of the outflow wind near the surface corresponds to the synoptical wind at higher levels.

In Figure 8.7 the time series of some selected parameters are shown for one point in the Tramuntana range, one point in Randa and two points in the valley. The locations are indicated in Figure 8.4. It is noteworthy that, except at the beginning of the night, the winds are strong at the valley than in the mountains, with a larger cooling rate in the valley (in the mountains it is not present) and much larger heat flux and TKE in the mountain, showing that the valleys are acting like quiescent pools of cool air.

The time series at the same locations between 1900 UTC and 2030 UTC are shown in Figure 8.8. The wind speed and direction remain nearly constant in the mountains (Bunyola and Cura) whereas they significantly change in the locations within the valley (Airport and Indioteria) because of the orographically generated effects. In fact, the changes of the wind in the airport between 19 and 20 h are very similar to those seen by Blumen (1984) in the foothills of the Rocky Mountains and that he describes as arrivals of gravity flows. The temperature also decreases in the valley points remaining nearly constant in the locations at the mountains. The TKE is also larger in the mountains because the downslope wind generates shear. Since this is not constant during the whole night, the TKE can have some fluctuations due to a period of intense shear, for instance.

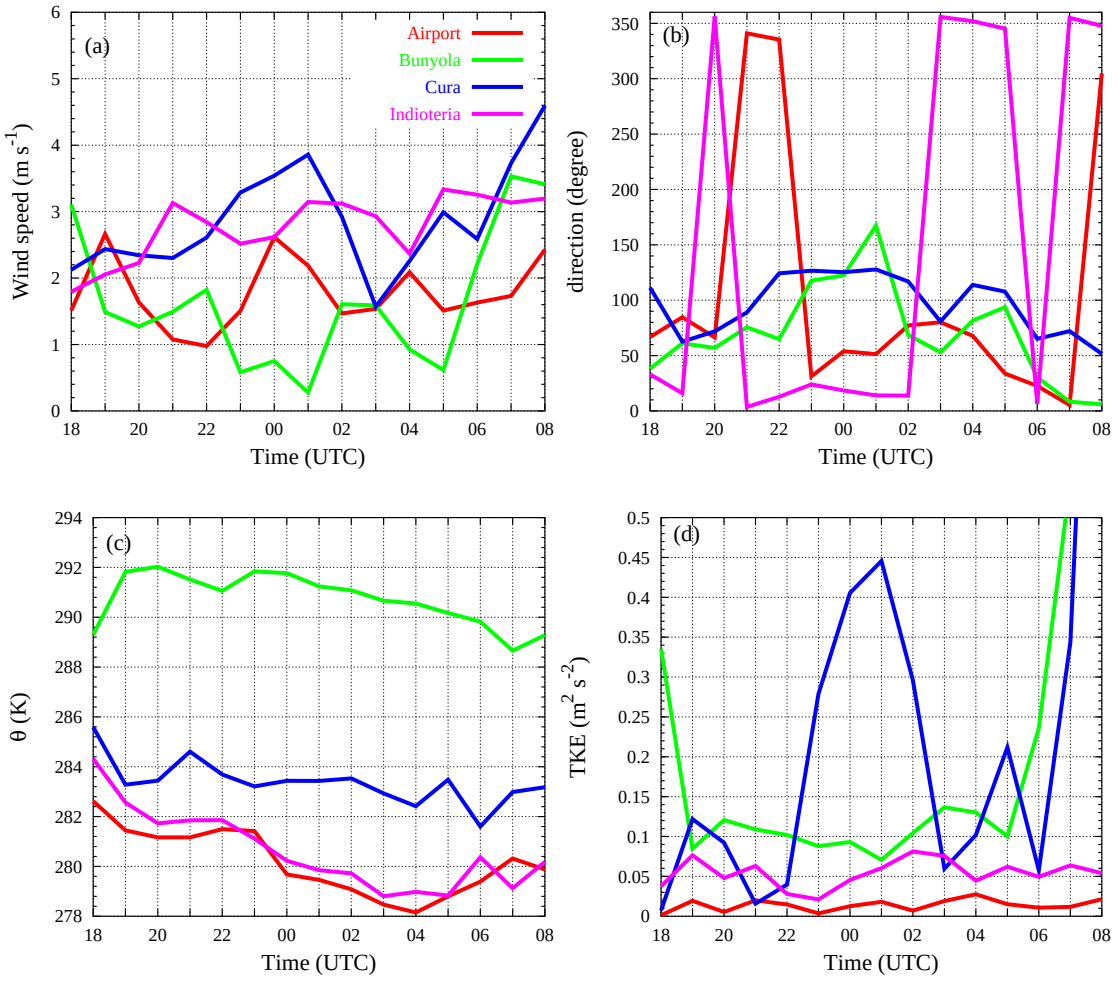

Figure 8.7: Time series obtained from the model at 10 m during the whole night at different locations: within the basin (Airport and Indioteria) and in the mountains that close the basin (Cura and Bunyola). The position of all these points is shown in Figure 8.8. (a) Wind speed (m s^{-1}), (b) wind direction (in degrees where the north corresponds to 0°), (c) potential temperature (K) and (d) Turbulent Kinetic Energy (m^2 s^{-2}). One point every hour is plotted

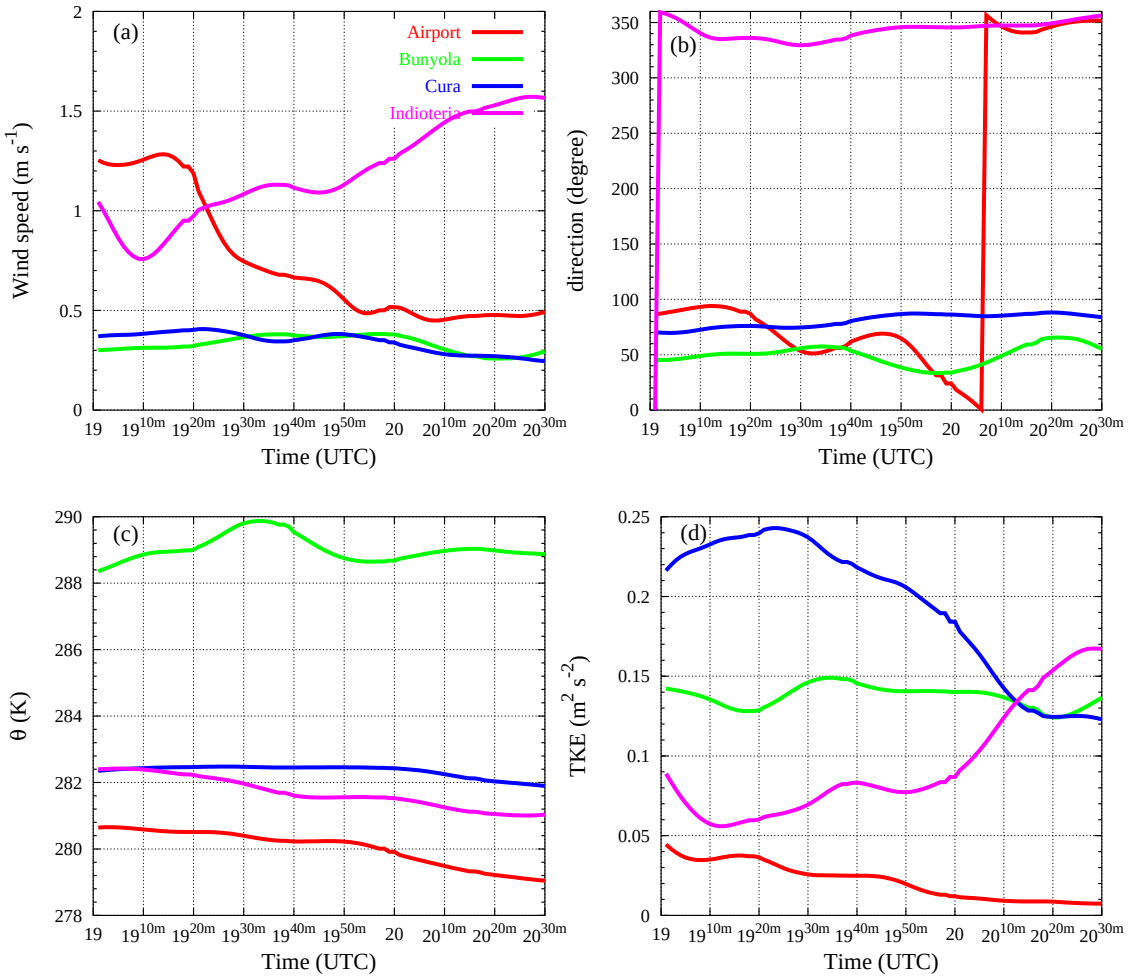

Figure 8.8: Time series obtained from the model at different locations as in Figure 8.7 between 1900 UTC and 2030 UTC. One point every minute is plotted

8.4 Verification of the mesoscale run

Figure 8.9 shows the horizontal cross-sections of the wind (at a height of 10 m) and potential temperature at 1.5 m, with the available observations from the automatic weather stations (AWS) at 0400 UTC. The wind speed and direction are approximately well captured at this moment of the night. Although the measurement points are not uniformly distributed over the island, the coldest and hottest areas showed by the model match with those measured.

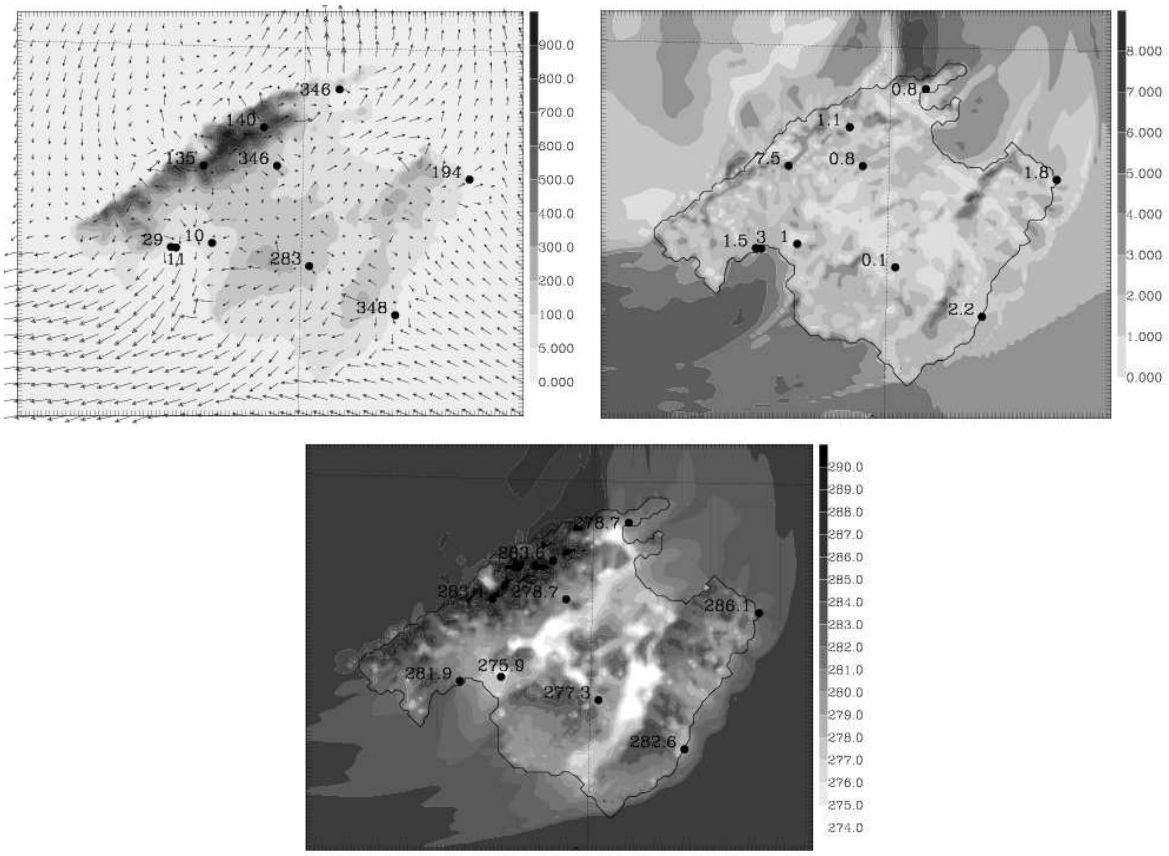

Figure 8.9: Horizontal cross-sections at 0400 UTC at a height of 10 m for (top-left) wind direction, (top-right) wind speed (m s^{-1}), and (bottom) potential temperature (K) at 1.5 m. The surface weather stations are indicated with a point and the figures represent the measured value at this time. In the wind direction cross-section there is one arrow each 3 grid points

To see if the evolution of the variables is realistic, some time series measured by the surface weather stations and obtained from the model are shown in Figure 8.10. The direction of the wind is well captured by the model in the valley (Airport) as well as at the mountain top (Alfabia). The temperature and the wind speed are slightly overestimated in the Airport and an opposite behaviour is found in Alfabia. Within these weak pressure gradient conditions, the wind is very calm and it might be not enough to the sensor to

take a measurement. Therefore, some of the automatic surface weather stations measure 0 m s^{-1} at a height of 10 m in points where there is wind but extremely calm. On the contrary, it is very difficult that the model have a zero-mean wind in a single point. Summarizing, it can be said that the results in the valley tend to give too high winds, resulting in temperatures warmer than the observed of the order of 2 to 4 K. The results in the coast and in the mountains do not show such large differences.

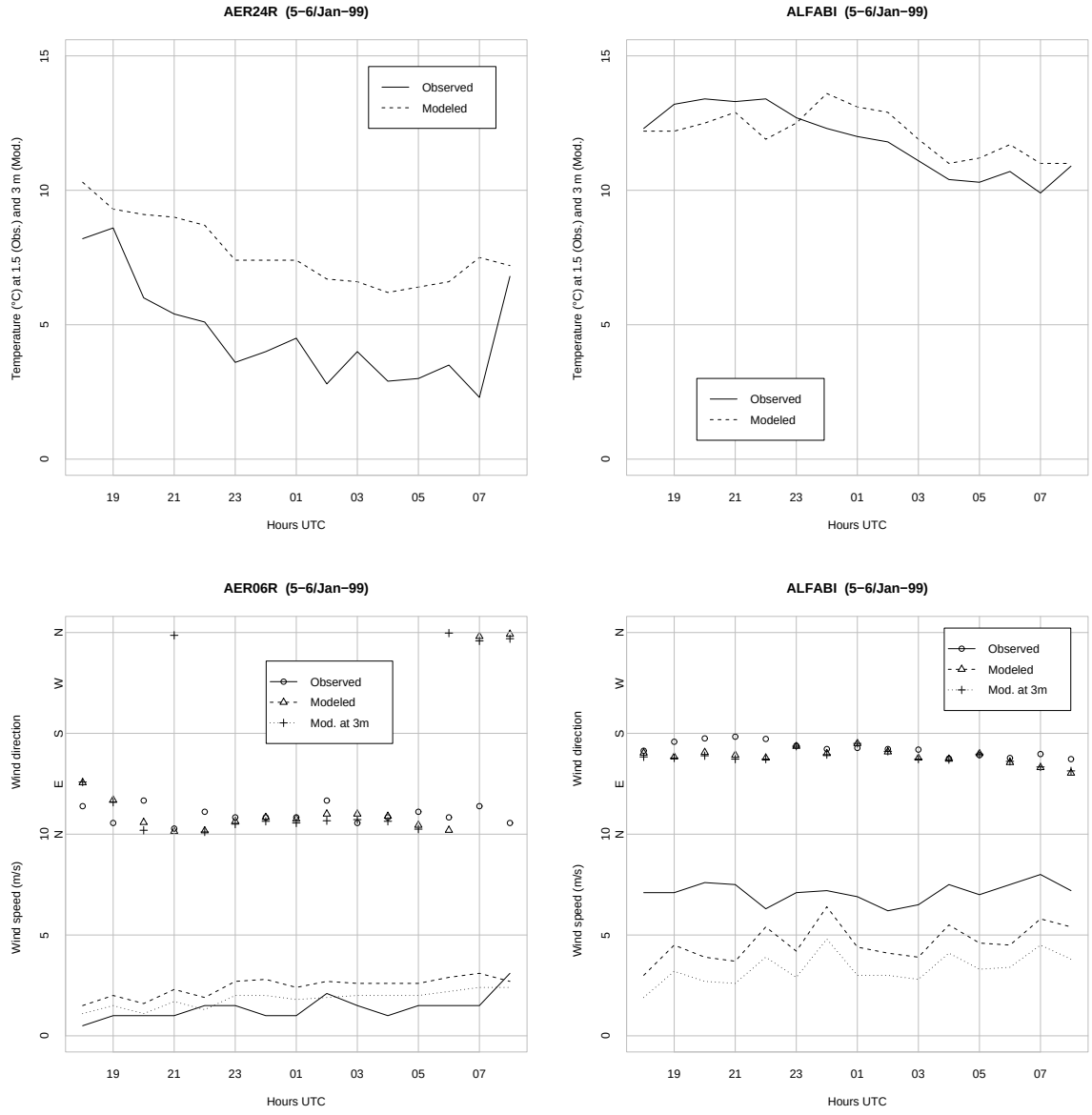

Figure 8.10: Comparison of the time series measured and obtained from the model for one point within the basin (Airport, labelled as AER24R and AER06R) and one point on the top of a mountain in the NW mountain range (Alfabia)

Figure 8.11 shows a first try of comparison between the radiative surface temperature

as computed by the model and as estimated from the NOAA image of the same night. The model creates a cold area in the center of the island and in some areas of the three main basins. These characteristics are also found in the satellite image, except north of Campos, where the image seems to show some fog, not accounted in the model because no condensation scheme was activated. There is a bias between the model and the satellite (warmer), but the main structures seem captured. The comparison of model and satellite is the subject of another work (Mira et al., 2004). However, it is important to notice that both plots do not have the same spatial resolution since the resolution for the NOAA image is coarser than the modelled one (1 km). It is also worth mentioning that the NOAA image has been corrected to plot the radiative temperature and the results might be sensitive to the different corrections applied. In this case, the NOAA image has been corrected geometrically and by the emissivity and water vapor. Not all the images taken during the simulated period are "good" for the comparison. In fact, only pictures taken in the zenith angle will be considered because the others have coarse spatial resolutions.

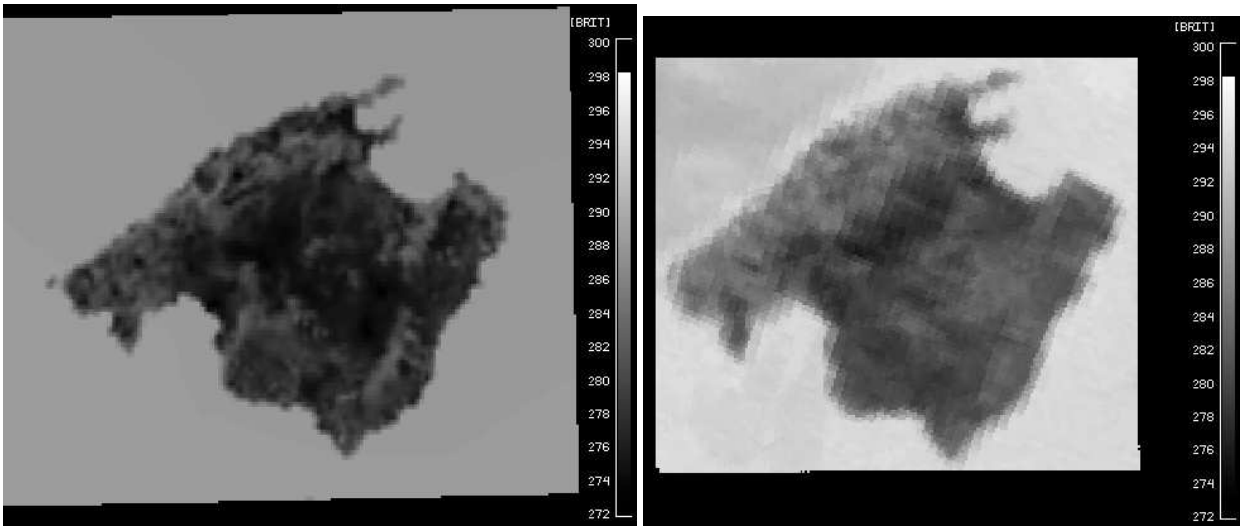

Figure 8.11: Radiative temperature (K) obtained from the model (left) and from the NOAA satellite image (right) at 0400 UTC

8.5 Description of the flows in a basin

The Palma basin is almost closed. At the north and the west it is limited by mountain ranges peaking at about 1000 m ASL, at the east there is the Randa Mountain and an elevated area, resulting in a slope of almost constant angle during several kilometers. The south part is open to the sea. Thus, the west side of the basin is bounded by many valleys that generate night-time outflows to the plain, whereas the east side is basically a slope parallel to the sea coast.

This configuration offers the chance to study how two different types of mountain flows behave under similar meteorological conditions and to inspect how they interact when they merge at the center of the basin. The steep side will be represented by the line Bunyola-Indioteria and the gentle slope by the line Cura-Airport. Bunyola is in the northern mountains, Indioteria in the valley, close to Palma, Cura at the Randa mountain and the Airport in the valley, very nearby the end of the slope. These locations are indicated in Figure 8.4.

The vertical cross-section following the Cura-Airport line (gentle slope) shows successive areas of acceleration and deceleration of the near-the-surface flow (see Figure 8.12). In the zones where the flow goes more slowly, the air is warmer, thus fitting well with the picture of compression and warming already pointed out by Fleagle (1950) or McNider (1982). The maximum speeds are around 5 m s^{-1} at a height of 30-50 m AGL. The height estimated by the formula of Manins and Sawford (1979), $h = 0.75Es$, where s is the slope distance and E the entrainment at the top ($E = 0.05sin(\alpha)^{0.66}$, Briggs 1981) is of about 30 m for an average slope of 1.2°. At 250 m AGL there exists a minimum in the wind velocity. The turbulence is weak, mostly confined close to the ground, but with some areas of elevated turbulence above the wind maximum, in conformity with the studies of Blumen (1984), Conangla and Cuxart (2005) and chapter 6. The cold air reaches the valley and cumulates there, where the Airport is.

If the analysis of Mahrt (1982) is performed on this simulated flow, with parameters estimated as 4 m s^{-1} for the downslope velocity, 10000 m for the downslope scale and a depth scale for the slope wind of 40 m, together with a slope angle around 1.2°, it can be seen that a Froude number defined as $Fr = \frac{U^2}{gH}$ is very small (0.04) and it can be considered that it is a regime where the buoyancy and the thermal wind contribution balance, due to increasing depth and temperature deficit in the slope direction, which can be observed in Figure 8.12. We find that this is a "tranquil flow" as Mahrt defines it ("the thermal wind term resulting from increasing depth and/or temperature deficit in the direction of the flow acts to oppose the buoyancy acceleration causing the flow to be relatively weak and retain its small Froude number").

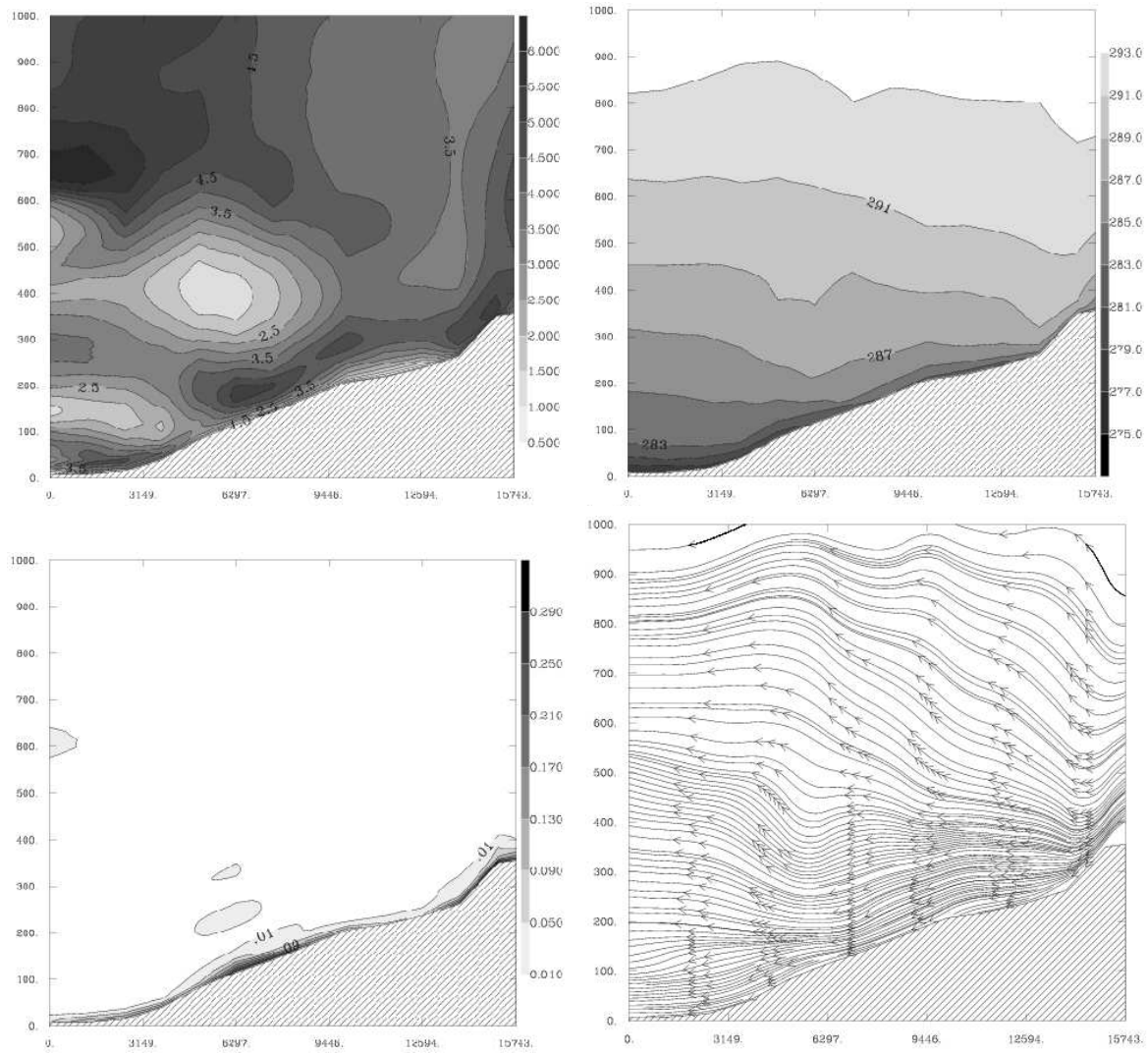

Figure 8.12: Vertical cross-section along the slope CURA-AIRPORT at 0400 UTC: (top-left) wind speed (m s^{-1}), (top-right) potential temperature (in K), (bottom-left) Turbulent Kinetic Energy (m^2 s^{-2}) and (bootm-right) streamlines

The line Bunyola-Indioteria is steeper (Figure 8.13), but the parameters of the downslope flow are very similar, although the slope angle is double (2.6°). Following Mahrt (1982) it is also a tranquil flow. Nevertheless, some differences are noteworthy. First, in the steepest part, there is relatively strong turbulence extending some hundreds of meters AGL because of the large shear. It disappears when the slope diminishes and a similar pattern as for the other case is formed, in this case with stronger elevated turbulence in the valley, disconnected from the one generated by friction near the ground. The behaviour of the wind near the ground is less oscillatory and seems to be continuously accelerating as the flow progresses downhill, the stratification near the ground is very strong and the wind is like slipping over the ground radiative inversion. In this case the streamlines seem

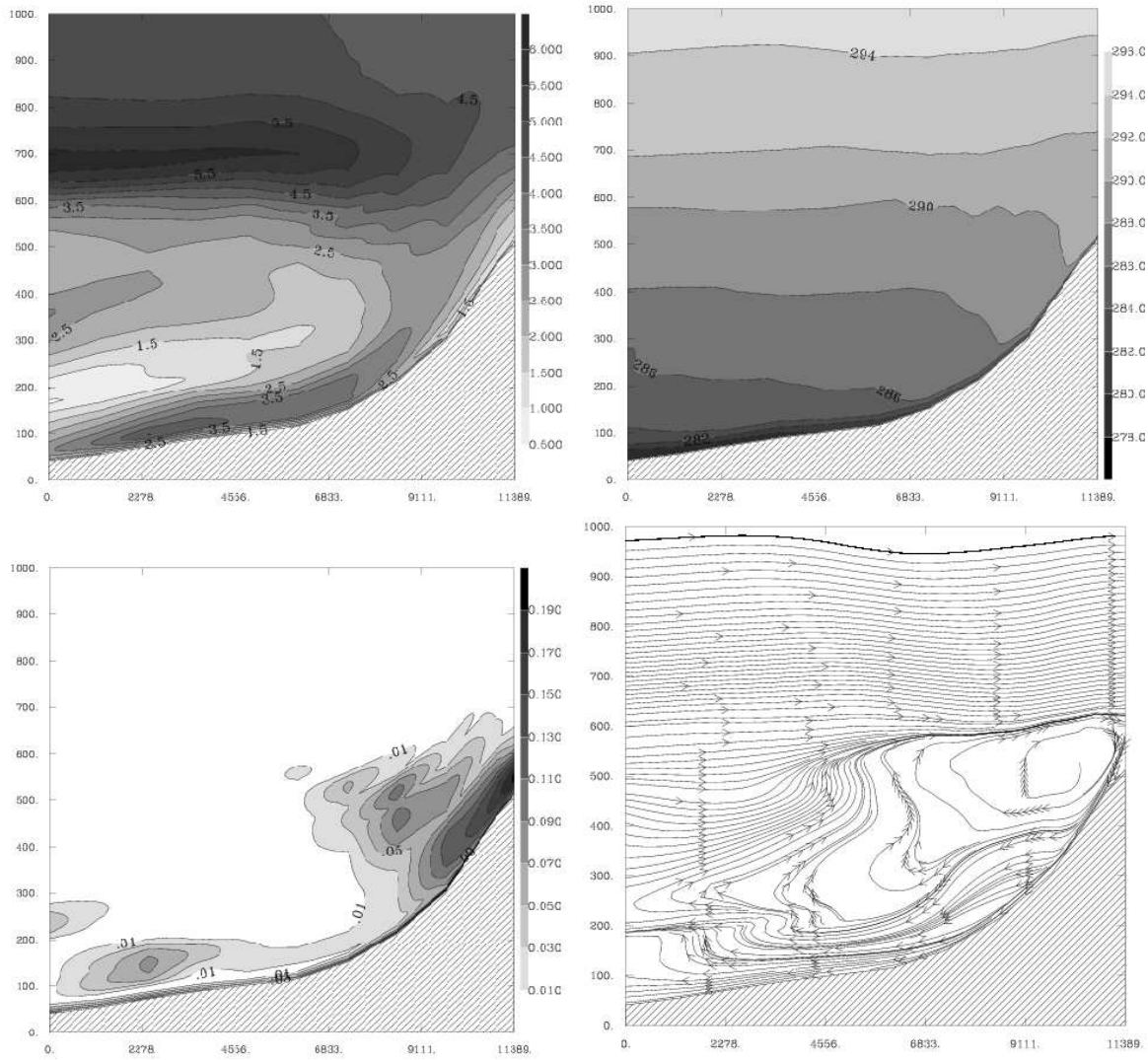

Figure 8.13: The same as in Figure 8.12 but for the slope BUNYOLA-INDIOTERIA

to trace well an elevated return current coupled with the synoptic flow at a height about 500 m ASL.

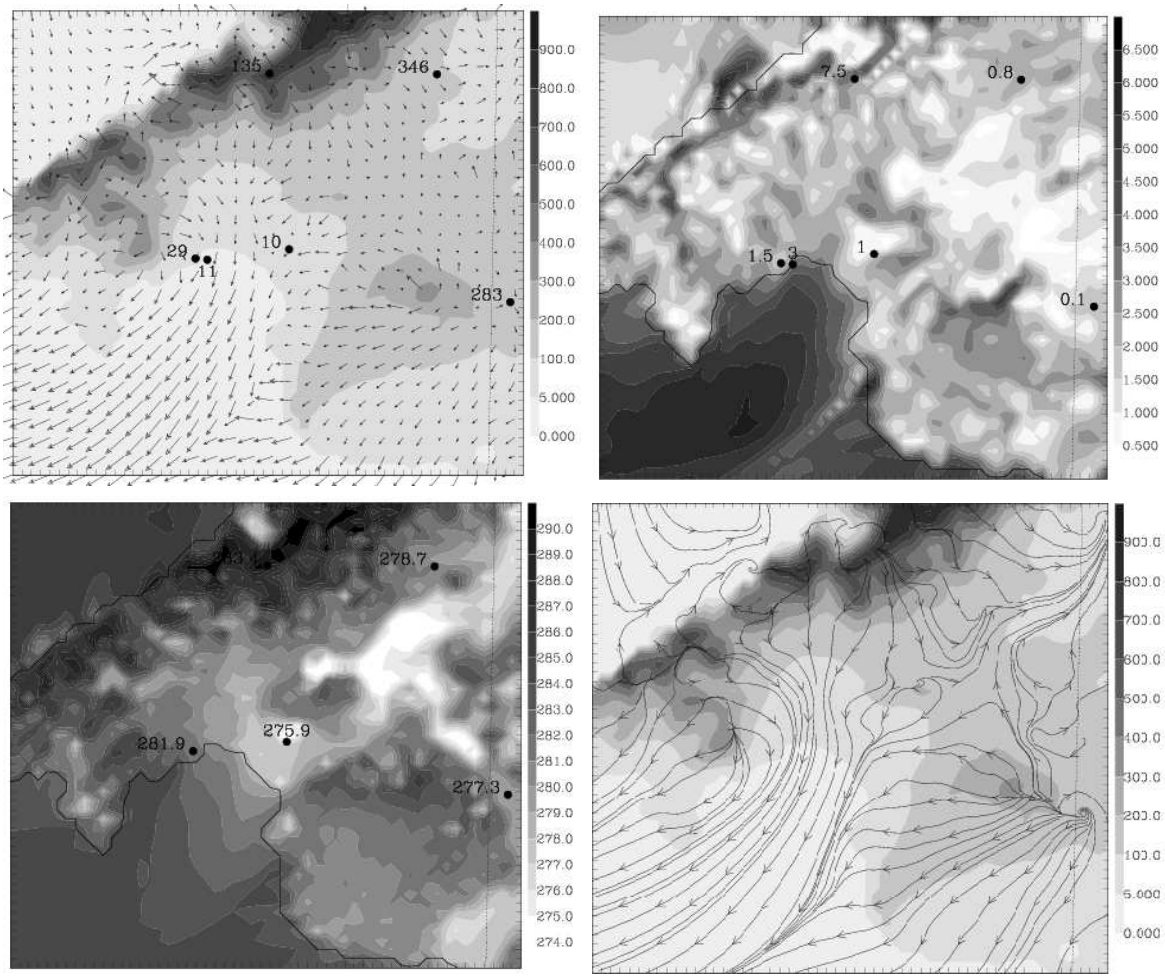

Figure 8.14: Horizontal cross-sections at a height of 10 m and at 0400 UTC in the Palma basin. (Top-left) wind direction, (top-right) wind speed (m s^{-1}) and (bottom-left) potential temperature (K) at 1.5 m and (bottom-right) streamlines. The surface weather stations are indicated with a point and the figures represent the measured value at this time

Figure 8.14 shows several horizontal cross sections at a height of 10 m focused on the Palma basin. The streamlines show clearly how the low level flows converge in the center of the basin and flow offshore in the SW direction. The wind speed is maximum following certain lines and areas of almost calm wind are well identified. The later in the valley are the zones where the lowest temperatures occur. The measurements at 0400 UTC are also plotted showing that the model is able to reproduce the wind (speed and direction) and the potential temperature. In order to inspect the realism of these fields, the radiative surface temperatures of the model and of the NOAA image are compared (Figure 8.11). It can be seen that most of the features are common in both fields, thus giving some

confidence in the simulation results.

However, some reflexions are inspired by these fields. Two points as close as Indioteria and the Airport, both at the center of the basin at a distance of about 5 km have large differences, as it is seen in the vertical profiles at 0400 UTC in Figure 8.15. The wind between these two points at 10 m can differ more than 60° and more than 2 m s^{-1}, and the temperature about 3 K. What would be a criterion to choose one of these points as a representative point of the basin? Both are distant from nearby obstacles, are located over characteristic terrain of the area, but show large differences related to the presence of drainage flows. It does not seem a question that can be easily answered.

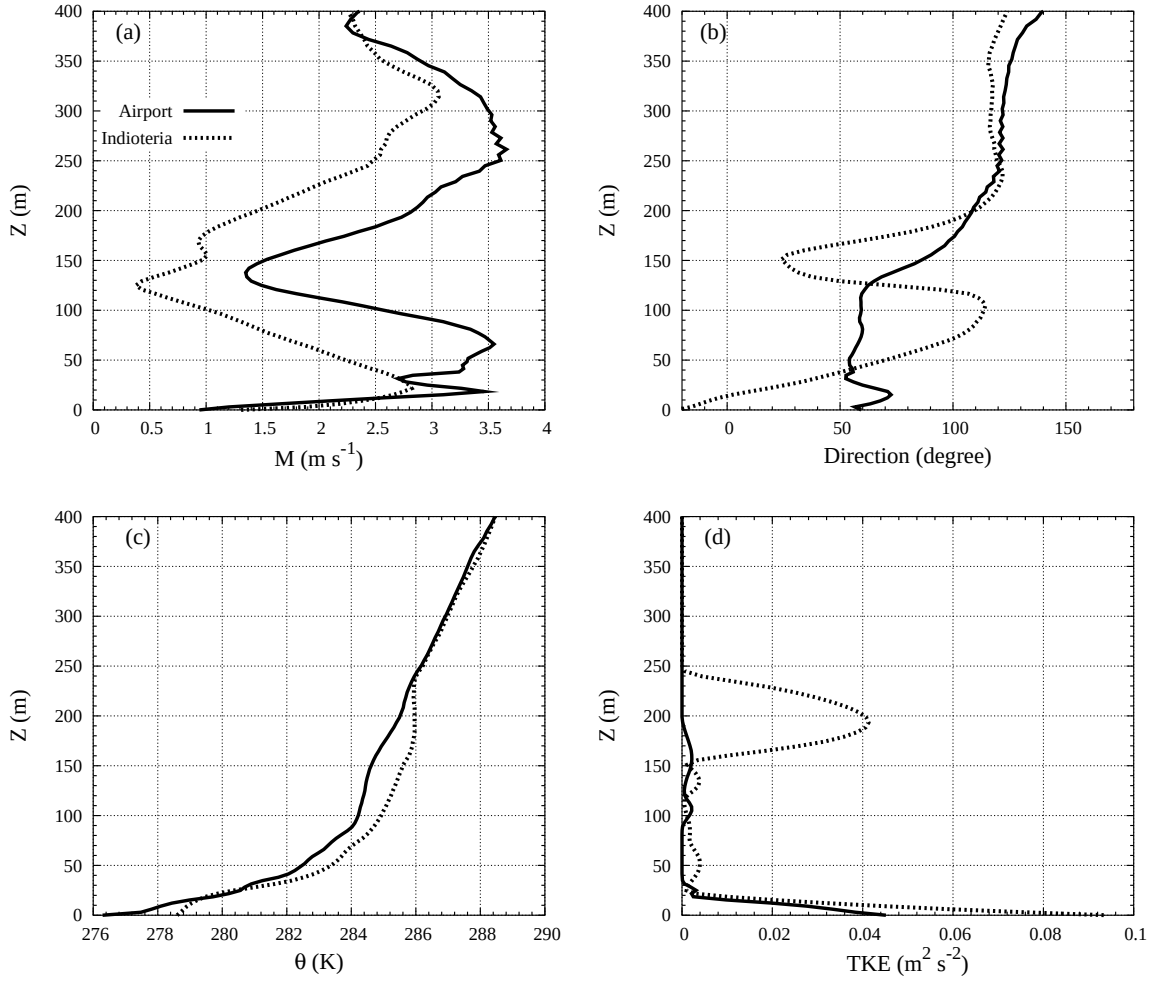

Figure 8.15: Vertical profiles at 0400 UTC in Indioteria and the Airport of (a) wind speed (m s^{-1}), (b) direction (degrees), (c) potential temperature (K) and (d) Turbulence Kinetic Energy (m^2 s^{-2})

8.6 Conclusions

In this chapter, the orographically generated flows in the SBL have been studied over the Majorca Island through mesoscale modelling. It has been shown that the island - of a relatively small dimension - is able to create a system of nocturnal local winds. These are mostly related to the orography and follow a certain pattern at the lower levels particular of each location. More simulations should be performed under slightly different situations to confirm the late assertion.

The model generates the low-level flows in a slow continuous manner, with non sudden changes, contrarily to the observations. For instance, chapter 7 shows that the tails of the PDFs computed from observations only differ from those computed from the LES results in the tails. Tails in the PDFs computed from observations contain all the scales of motions but when the LES is considered, only the resolved scales are taken into account.

The verification of such clear air simulations is difficult and a first try has been made using a NOAA radiative surface temperature field. The preliminary comparison of structures shows an approximate correspondence between the model and the satellite in what refers to cold and warm areas, but this subject deserves further work. The simulated fields are also compared to those measured by the automatic surface weather stations (AWS). The AWS are not uniformly distributed along the island and most of they are very close and located near the coast. Nevertheless, the simulated patterns near the surface agree with the observations.

To end, the simulation shows that very nearby stations in the center of a basin can give large differences in the basic meteorological variables, such as the wind or the temperature. This makes the authors wonder about the actual concept of the representativeness of a meteorological station, that should maybe be reviewed incorporating some information on the surrounding topography. Finally, the mesoscale modelling complements the information given by the LES to better understand the processes that take place within the SBL.

Chapter 9

CONCLUSIONS

The main objective in this work has been to study the processes that take place in the stably stratified atmospheric boundary layer (SBL). It has been shown that the SBL is a complex and turbulent regime difficult to study and this makes it the less understood boundary layer regime. For instance, the observations studied in chapter 4 highlight that all scales of motion may exist within the SBL and usually, under very stable conditions, the spectral gap is not present. Since the stability tends to suppress the vertical motions, the turbulence is not homogeneous neither isotropic. Nevertheless, there is still no widely accepted theory to deal with the turbulence in stably stratified conditions. Besides, local effects, such as the orography or the soil uses, are important and they can even modify the SBL mean features.

Modelling is a useful tool to study the SBL but models can suffer runaway cooling when they are working under very strongly strably stratification. On the other hand, to better represent the main observed SBL features, all scales of motion should be included in the model. Isotropic eddies are very small but the largest eddies, generated from the mesoscale motions, are also important. Therefore, a study of the SBL has been made here using Large-Eddy Simulation (LES) and mesoscale modelling to cover a large range of eddy motions. Finally, these runs are compared the observations to better understand the processes that take place there.

Following the main objectives given in the introduction, first of all, it is checked if the LES is able to work under stably stratified conditions. As it is described, the turbulence scheme in the LES model used considers the Kolmogorov theory for the dissipation of energy, which assumes homogeneity and isotropy, but these conditions are not always fulfilled within the SBL. An LES of the SBL has been performed and it has shown that the range of stabilities, in which the model is able to produce realistic results, is from weakly to moderately stable conditions. The simulated conditions correspond to a very

simple SBL where the terrain is flat and the turbulence is only generated by shear near the surface.

The most stable cases suffer runaway cooling, that is, the surface is cooled too much and the boundary layer becomes too stable reducing the downward heat flux and making the surface even colder. In these cases, the model does not mix enough at the lowest levels giving unrealistic values of the surface temperature. This confirms that modelling the SBL is difficult and runaway cooling is a well-known limitation. It is worth mentioning that the simulated cases which present runaway cooling have values of surface thermal conditions and geostrophic winds that do not fulfil the criterion proposed by Derbyshire. These conditions would be observable when the effect of the large scale forcings is included in the observations, but not in the LES.

The realism of these runs is inspected through the comparison to data obtained from two experimental field campaigns (SABLES-98 and CASES-99). Although there is not a well defined methodology in the literature to compare LES results to observations, it is presented here an attempt. Data of both campaigns are classified in categories and the simulated profiles are compared to the observed ones for each category. It is found that the mean features of the SBL are well represented by the LES model, especially the thermal structure. Nevertheless, the shear near the surface is overestimated by the model. This fact might be explained because the Monin-Obukhov similarity is applied in the LES in the first computation level and probably the observations do not behave in this way. Other differences between the observations and the LES runs can be explained as:

(i) the simulated conditions do not exactly correspond to the observed ones. Other external forcings than those prescribed in the model (the geostrophic or the surface cooling) might exist in the observations and they can modify the mean characteristics of the SBL.

(ii) the LES results only contain the information of the scales up to the resolved motions whereas in the observations all the scales are included. This is especially important in the SBL where the size of the smallest eddies can be 1 m or smaller. In fact, the largest scales (from mesoscale effects) are also not included in the LES results. Therefore, mesoscale modelling is needed to complement the information found through the LES. It is worth mentioning that in mesoscale runs, the smallest scales of motions are computationally parameterized.

(iii) turbulence quantities are only measured in discontinuous manner and at low levels (for instance, up to 50 m for the field campaigns used here). Then, it is shown that modelling is a useful tool, for instance, to characterize the elevated turbulence.

(iv) the LES results are averaged profiles over the horizontal domain and over a period

of time where the fields are stationary. On the other hand, data from towers used here correspond to a time series at a single location and at different levels averaged over an interval of time (here 5 min). When the comparison of the LES results to observations is performed, two completely different types of data are compared. Besides, the assumption of ergodicity (field homogeneous and stationary) is implicitly made.

The model joined the GABLS intercomparison exercise, where different turbulence schemes ran the same SBL conditions (similar to the ones described before) to check similarities or differences with other proposals. This intercomparison has highlighted that the LES results are quite sensitive to the turbulent and the advection schemes, especially near the inversion level. On the other hand, all models behave similarly (the surface is cooled and a maximum of the wind is developed near the inversion) but the results are quantitative different, especially near the inversion. The results are sensitive to the resolution and the 12.5 m resolution results are very spread and tend to cluster as the resolution increases. Furthermore, the models that use modified turbulence schemes do not present significant improvements compared to those that use the standard Kolmogorov theory.

To further explore the LES results, the PDFs have been used to study the eddy structures, to supplement the information given by the LES mean profiles. The shape of the PDFs computed from a SBL case is quite different from those computed from a Convective Boundary Layer (CBL), since the main processes that take place in both regimes are largely different. For instance, it has been found that within the CBL the updrafts and downdrafts make bimodal PDFs whereas in the SBL the vertical motions are suppressed and the PDFs are more Gaussian. Moreover, the shape of the PDFs also depends on the height where they are computed, in any of the considered regimes. From the PDFs it has been also possible the compute the fluxes, which correspond to those resolved in the LES. Nevertheless, the attention has been focused on the tails, which correspond to fluctuations of values far away from the mean one and with small probability. It has been found that the PDFs are Gaussian but this is not the case for the PDFs computed from observations, since all scales of motions are present and the tails largely depart from those computed from the LES. Although the PDFs for the SBL are Gaussian, contrarily to other boundary layer regimes, the ergodic theorem is not fulfilled, because the field is stationary but not homogeneous.

It has been shown that the PDFs are also a useful tool to compare LES results to observations, taking into account the eddy structures beyond the classical mean profiles. The differences between the PDFs computed from LES results or observations occur especially in the tails. The fluctuations that are represented in the tails of the observed

PDFs can come from the smallest or largest eddies but in the LES smallest eddies are not completely well represented whereas the largest are not included. This fact highlights a limitation when the SBL is studied through LES and opens the door to a new tool, mesoscale modelling, to better understand the contribution of the largest scales. Besides, the PDFs can also be used as an extra diagnostic in an LES intercomparison exercise such as GABLS or to characterize the observed intermittencies of a quantity of interest.

To advance further, the study of an observed Low-Level Jet (LLJ) has been undertaken. The attention has been focused on the mixing across the inversion (corresponding to the LLJ height) and the turbulence above it, where it is difficult to get high-frequency or time series measurements. The LES results show that there is no mixing across the inversion and the layer above and below the LLJ are decoupled. As it has been observed, a maximum of turbulence is found above the LLJ at a height about two times the height of the maximum of the wind.

The LES mean profiles behave similarly to soundings. Nevertheless, the comparison is also done through PDFs to see if the eddy structures are similar. The tails from the PDFs computed from the LES results differ from those computed from the observations, since the smallest structures are much more difficult to reproduce from the LES. On the contrary, the contribution of the smallest eddies are included in the data. The comparison also highlights that it is difficult to fix the prescribed surface boundary condition and this is a problem not solved yet. However, the results above the LLJ do not change when different prescribed surface boundary conditions are used. Therefore, further work will consist on improving the results near the surface (for instance, modifying the turbulence scheme to reduce the mixing) but also including other forcings, such as the radiation, which might be present in these stably stratified conditions.

It has been seen that from the observed LLJ study that the surface forcings are important to better understand the observations and the processes that take place within the SBL. The orographic effects are very important within the SBL, especially in the generation of local winds such as katabatic winds or valley winds. Since the LES runs consider the terrain flat, far away from reality, mesoscale modelling has been used to study these effects. These orographic effects should be taken into account when a location of a measured point (i.e. a tower) is considered. In fact, points distant 5 km can measure different SBL mean features near the surface and this fact highlights the importance of determining the orographic contribution of the data. In the same way the orographic effects can explain some differences between the LES results and the observations. It is worth mentioning that mesoscale runs do not suffer from runaway cooling since the locally generated flows avoid that the surface cools in excess. Therefore, runaway cooling can

be a numerical artifact which is present in the models under strongly stably stratified conditions over flat terrain.

Some steps to validate the mesoscale runs against observations have been undertaken but further work is still needed to develop a methodology. The results are validated against NOAA satellite images and it is found that the model is able to reproduce the cold and warm surface areas. The comparison of the time series observed from surface weather stations to those obtained from the simulation have shown that the model tends to overestimate the wind when they are weak and also to underestimate the surface cooling in some places. This is probably due to some processes that are not well represented by the model.

Nevertheless, there are still some questions still not solved and further work will be needed:

(i) It has been found that it is difficult to classify the observations to compare them to the LES runs and this is a problem still not solved. Therefore, the methodology described here should be improved, for instance adding an extra classification parameter. But, which are the key parameters to classify the data to compare the LES results to observations?

(ii) The validation of the mesoscale runs against observations is a work that has just started in our group and only the preliminary results are given here. How can the mesoscale runs be validated? The study of the locally generated flows must be pursuit.

(iii) As it is described, the runaway cooling is a limitation to simulate very stable conditions and it is shared by most of the models. Which modifications on the turbulence scheme should be done to avoid to cool the surface too much (runaway cooling) in very stable conditions? Further work is needed on the modification of the turbulence scheme (i.e. increase the mixing for more stable situations) to overcome this limitation.

(iv) From the comparison to observations it has been found that the surface Monin-Obukhov similarity theory should be revised to deal with very stable conditions because data seem not to behave in this way. Is the Monin-Obukhov similarity theory, included in the LES, adequate to deal with the stably stratified conditions?

(v) It has been found that the LES results are quite sensitive to the advection and turbulence schemes, especially in the inversion layer. Are the physical processes that take place in the inversions well represented by the models? What are doing the advection and turbulence schemes there? To address the physics of mixing at inversion layers, a saline water tank will be used to study the physical processes that take place in the inversion, in collaboration with the Delft University of Technology, The Netherlands. One of the advantages of using the water tank is that the forcings are controlled in the laboratory, as in the LES, but also no numerical artifacts are presented in the flow.

Nowadays works on SBL are still in progress to improve the description of this boundary layer regime in the numerical prediction models. In fact there is not still a widely accepted theory to describe the anisotropy and the inhomogeneities of the stably stratified conditions. A tool or a theory might be found in the future but a complete description of the processes that take place within the SBL should be studied with the present tools in the range where they seem to work properly.

References

Adams, N. A., and Stolz, S.: 2002, A Subgrid-Scale Deconvolution Aprroach for Shock Capturing, *J. Comput. Phys.* **178**, 391-426.

André, J.C., and Mahrt, L.: 1982, The nocturnal surface inversion and influence of clear-air radiative cooling, *J. Atmos. Sci.* **39**, 864-878.

Andreas, E.L., Claffey, K.J., and Makshtas, A.P.: 2000, Low-level atmospheric jets and inversion over the western Weddell sea, *Boundary-Layer Meteorol.*, **97**, 459-486.

Andrén, A., Brown, A. R., Graf, J., Mason, P. J., Moeng, C.-H., Nieuwstadt, F. T. M., and Schumann, U.: 1994, Large-eddy simulation of a neutrally stratified boundary layer: A comparison of four computed codes, *Quart. J. Roy. Meteorol. Soc.* **120**, 1457-1484.

Andrén, A.: 1995, The structure of stably stratified atmospheric boundary layers: A large-eddy simulation study, *Quart. J. Roy. Meteorol. Soc.* **121**, 961-985.

Armenio, V., and Sarkar, S.: 2002, An investigation of stably stratified turbulent channel flow using large-eddy simulation *J. Fluid Mech.* **459**, 1-42.

Banta, R.M, Newsom, R.K., Lundquist, J.K., Pichugina, Y.L., Coulter, R.L., Mahrt, L.: 2002, Nocturnal low-level jet characteristics over Kansas during CASES-99, *Boundary-Layer Meteorol.*, **105**, 221-252.

Beare, R.J., MacVean, M.K., Holtslag, A.A.M., Cuxart, J., Esau, I., Golaz, J.-C., Jiménez, M.A., Khairoutdinov, M., Kosović, B., Lewellen, D., Lund, T.S., Lundquist, J.K., McCabe, A., Moene, A.F., Noh, Y., Raash, S., and Sullivan, P.: 2005, An intercomparison of Large-eddy simulations of the stable boundary layer, *Accepted to Bound.-Layer Meteorol.*.

Blackadar, A.K.: 1957, Boundary layer wind maxima and their significance for the growth of nocturnal inversions, *Bull. Amer. Meteor. Soc.*, **38**, 283-290.

Blumen, W.: 1984, An observational study of instability and turbulence in night-time drainage winds, *Bound.-Layer Meteorol.*, **28**, 245-269.

Bonner, W.D.: 1968, Climatology of the low-level jet, *Mon. Wea. Rev.*, **96**, 833-850.

Bougeault, P., and Lacarrère, P.: 1989, Parameterization of orography-induced turbulence in a mesobeta scale model, *Mon. Weather Rev.*, **117**, 1872-1890.

Bretherton, C.S., MacVean, M.K., Bechtold, P., Chlond, A., Cotton, W.R., Cuxart, J., Cuijpers, H., Khairoutdinov, M., Kosović, B., Lewellen, D., Moeng, C.-H., Siebesma, P., Stevens, B., Stevens, D.E., Sykes, I., and Wyant, M.C.: 1999a, An intercomparison of radiatively- driven entrainment and turbulence in a smoke cloud, as simulated by different numerical models, *Quart. J. R. Meteor. Soc.*, **125**, 391-423.

Bretherton, C. S., Krueger, S.K., Wyant, M.C., Bechtold, P., van Meijgaard, E., Stevens, B., and Teixeira, J.: 1999b, A GCSS boundary layer model intercomparison study of the first ASTEX Lagrangian experiment, *Bound.-Layer Meteor.*, **93**, 341-380.

Briggs, G. A.: 1981, Canopy effects on predicted drainage flow characteristics and comparison with observations. *Proceedings 5th AMS symp on Turbulence and diffusion.*

Brown, A. R., Cederwall, R. T., Chlond, A., Duynkerke, P. G., Golaz, J. C., Khairoutdinov, M., Lewellen, D. C., Lock, A. P., Macvean, M. K., Moeng, C.-H., Neggers, R. A. J., Siebesma, A. P., and Stevens, P.: 2002, Large-eddy simulation of the diurnal cycle of shallow cumulus convection over land, *Quart. J. Roy. Meteorol. Soc.* **128**, 1075-1094.

Brown, A. R., Derbyshire, S.H., and Mason, P.J.: 1994, Large-eddy simulation of stable atmospheric boundary layer with revised stochastic subgrid model, *Quart. J. Roy. Meteorol. Soc.* **120**, 1485-1512.

Businger, J.A., Wyngaard, J.C., Izumi, Y., and Bradley, E.F.: 1971, Flux profile relationships in the atmosphere surface layer, *J. Atmos. Sci.*, **28**, 181-189.

Canuto, V. M.: 2002, Critical Richardson number and gravity waves, *Astronomy & Astrophysics* **384**, 1119-1123.

Cederwall, R. T.: 2002, Large-Eddy Simulation of the Evolving Stable Boundar y Layer over Flat Terrain, *Ph. D. Dissertation, Stanford University, CA*, pp. 231.

Chu, C.R., Parlange, M.B., Katul, G.G. and Albertson, J.D.: 1996, Probability density functions of turbulent velocity and temperature in the atmospheric surface layer, *Water Resources Research*, **32**, 1681-1688.

Clarke, R.H., Dyer, A.J., Brooke, R.R., Reid, D.G., and Troup, A.J., 1971: The Wangara experiment. Boundary layer data, *Paper No. 19, Division of Meteorol. Phys.*, CSIRO, Australia, 21p and data Tables (316p).

Conangla, L. and Cuxart, J.: 2005, On the turbulence at the upper part of the LLJ: an experimental and numerical study, *Accepted to Bound.-Layer Meteorol.*.

Cuijpers, J.W.M., and Duynkerke, P.G.: 1993, Large-eddy simulation of trade wind cumulus clouds, *J. Atmos. Sci.*, **50**, 3894-3908.

Cuxart, J., Holtslag, A.A.M., Beare, R.J., Bazile, E., Beljaars, A., Conangla, L., Ek, M., Freedman, F., Hamdi, R., Kerstein, A., Kitagawa, A., Lenderink, G., Lewellen, D., Mailhot, J., Mauritsen, T., Perov, V., Schayes, G., Steeneveld, G.-J., Svensson, G., Taylor, P., Weng, W., Wunsch, S., and Xu, K.-M: 2005, Single-column model intercomparison for a stably stratified atmospheric boundary layer, *Accepted to Bound.-Layer Meteorol.*

Cuxart, J., Morales, G., Terradellas, E. and, Yagüe, C.: 2002, Study of Coherent Structures and Estimation of the Pressure Transport Terms for the Nocturnal Stable Boundary Layer, *Bound.-Layer Meteorol.*, **105**, 305-328.

Cuxart, J., Bougeault, P., and Redelsperger, J.-L.: 2000a, A turbulence scheme allowing for mesoscale and large-eddy simulations, *Quart. J. Roy. Meteor. Soc.*, **126**, 1-30.

Cuxart, J., Yagüe, C., Morales, G., Terradellas, E., Orbe, J., Calvo, J., Fernandez, A., Soler, M. R., Infante, C., Buenestado, P., Espinalt, A., Joergensen, H. E., Rees, J. M., Vilá, J., Redondo, J. M., Cantalapiedra, I. R., and Conangla, L.: 2000b, Stable Atmospheric Bound.-Layer Experiment in Spain (SABLES-98): A report, *Bound.-Layer Meteor.*, **96**, 337-370.

Cuxart, J.: 1997, Planetary Boundary Layer simulation: from LES to general circulation models, *thesis*, Dpt. d'astronomia i meteorologia, Universitat de Barcelona, Spain.

Deardorff, J.W. and Willis, G.E.: 1985, Further results from a laboratory model of the convective planetary boundary layer, *Boundary-Layer Meteorol.*, **32**, 205-236.

Deardorff, J. W.: 1980, Stratocumulus-capped mixed layers derived from a three-dimensional model, *Bound.-Layer Meteor.*, **18**, 495-527.

Deardorff, J.W.: 1973, Three-dimensional numerical modeling of the planetary boundary layer, *Workshop on Micrometeorology*, Boston, 14-18 August, American Meteorol. Society, Science Press, pp. 271-311.

Deardorff, J.W.: 1972, Numerical investigation of neutral and unstable planetary boundary layer, *J. Atmos. Sci.*, **29**, 91-115.

Derbyshire, S. H.: 1995, Stable boundary layers: Observations, models and variability. Part I: Modelling and measurements, *Bound.-Layer Meteor.*, **74**, 19-54.

Derbyshire, S. H.: 1990, Nieuwstadt's stable boundary layer revisited, *Bound.-Layer Meteorol.* **116**, 127-158.

Doran, J.C., Fast, J.D., and Horel, J.: 2002, The VTMX 2000 campaign. *Bull. Amer. Met. Soc.*, **83**, 537-551.

Duynkerke, P.G., Jonker, H.J.J., Chlond, A., Van Zanten, M.C., Cuxart, J., Clark, P., Sanchez, E., Martin, G., Lenderink, G., and Teixeira, J.: 1999a, Intercomparison of three- and one-dimensional model simulations and aircraft observations of stratocumulus, *Bound.-Layer Meteorol.* **92**, 453-487.

Duynkerke, P.G.: 1999b, Turbulence, Radiation and Fog in Dutch stable boundary layers, *Bound.-Layer Meteorol.* **90**, 447-477.

Dyer, A.J.: 1974, A review of flux-profile relations, *Bound.-Layer Meteorol.* **1**, 363-372.

Essau, I.: 2004, Simulation of Ekman boundary layers by large eddy model with dynamic mixed subfilter closure, *J. Env. Fluid Mech.*, **4**, 273 - 303.

Estournel, C., Vehil, R., and Guedalia, D.: 1986, An observational study of radiative and

turbulence cooling in the nocturnal boundary layer (ECLATS experiment), *Bound.-Layer Meteorol.* **34**, 55-62.

Farge, M.: 1992, Wavelet transforms and their implications to turbulence *Ann. Rev. Fluid Mech.*, **24**, 395-457.

Flamant, C., Drobinski, P., Nance, L., Banta, R., Darby, L., Dusek, J., Hardesty, M., Pelon, J., and Richard, E.: 2002, Gap flow in an Alpine valley during a shallow south fohn event: Observations, numerical simulations and hydraulic analogue, *Quart. J. Roy. Meteor. Soc.*, **128**, 1173-1210.

Fleagle, R.G.: 1950, A theory of air drainage, *J. of Meteor.*, **7**, 227-232.

Fox, D.G., and Orszag S.A.: 1973, Pseudospectral approximation to two-dimensional turbulence, *J. Comput. Phys.*, **11**, 612-619.

Garratt, J. R.: 1992, The Atmospheric Boundary Layer, Cambridge University Press, Cambridge, 316 pp.

Garratt, J. R., and Brost, R.A.: 1981, Radiative cooling effects within and above the nocturnal boundary layer, *J. Atmos. Sci.* **38**, 2730-2746.

Garratt, J. R., and Ryan, B.F.: 1989, The structure of the stably stratied internal boundary layer in offshore fow over the sea, *Bound.-Layer Meteorol.* **47**, 17-40.

Germano, M., Piomelli, U., Moin, P. and Cabot, W. H.: 1991, A dynamic subgrid-scale eddy viscosity model, *Physics of fluids A* **3**, 1760-1765.

Hodur, R.M.: 1997, The Naval Research Laboratory s Coupled Ocean/Atmosphere Mesoscale Prediction System (COAMPS), *Mon. Wea. Rev.*, **125**, 1414-1430.

Holton, J.R.: 1979, Introduction to Dynamic Meteorology, Second Edition, *Academic Press*, 391pp.

Holtslag, A.A.M.: 2003, GABLS initiates intercomparison for stable boundary layer *GEWEX news* **13**, 7-8.

Izumi, Y.: 1971, Kansas 1968 Field Program Data Report, *Environmental research papers*, **No 369**, AFC RL-72 0041, Air Force Cambridge Research Lab., Bedford, USA.

Izumi, Y., and Caughey, J.S.: 1976:, Minnesota 1973 Atmospheric boundary Layer Experiment Data Report, *Environmental research papers*, **No 547**, Air Force Cambridge Research Lab., Bedford, USA, 79p.

Jaubert, G., Bougeault, P., Berger, H., Chimani, B., Flamant, C., Häberli, C., Lothon, M., Nuret, M., and Vogt, S.: 2005, Numerical simulation of meso-gamma scale features of föhn at ground level in the Rhine valley, *Quart. J. Roy. Meteor. Soc.*, **131**, 1339-1361.

Kampé de Fériet, J.: 1939, Les Fonctions aléatoires stationnaires et la théorie statistique de la turbulence homogène, *Ann. Soc. Sci. Bruxelles*, **59**, 145-194.

Khairoutdinov, M.F., and Randall, D.A.: 2003, Cloud resolving modelling of the ARM Summer 1997 IOP: Model formulation, results, uncertainities and sensitivities, *J. Atmos. Sci.*, **60**, 607-625.

Kolmogorov, A. N.: 1941, Dissipation of energy in a locally isotropic turbulence, *Doklady Akad. Nauk SSSR* **32**, 141.

Kosović, B., and Curry, J. A.: 2000, A Large-Eddy Simulation Study of a Quasi- Steady, Stably Stratified Atmospheric Boundary Layer, *J. Atmos. Sci.*, **75**, 1052-1068.

Kosović, B.: 1997, Subgrid-scale modelling for the large-eddy simulation of high-Reynolds-number boundary layers, *J. Fluid Mech.*, **336**, 151-182.

Lafore, J. P., Stein, J., Asencio, N., Bougeault, P., Ducrocq, V., Duron, J., Fisher, C., Héreil, P., Mascart, P., Pinty, J. P., Redelsperger, J.-L., Richard, E., and Vilá-Guerau de Arellano, J.: 1998, The Meso-NH atmospheric simulation system. Part I: Adiabatic formulation and control simulation, *Ann. Geophys.*, **16**, 90-109.

Lapworth, A.A.: 2003, Factors determining the decrease in surface wind speed following the evening transition, *Quart. J. Roy. Meteor. Soc.*, **129**, 11945-1968.

Larson, V.E., Wood, R., Field, P.R., Golaz, J.-C., Vonder, T.H and Cotton, W.R.: 2001, Small-scale and mesoscale variability of scalars in cloudy boundary layers: one-dimensional probability density functions, *J. Atmos. Sci.*, **58**, 1978-1994.

LeMone, M.A.: 1990, Some observations of vertical velocity skewness in the convective planetary boundary layer, *J. Atmos. Sci.*, **47**, 1163-1169.

Lenschow, D.H., Li, X.S., Zhu, C.J., and Stankov, B.B.: 1988, The stably stratified boundary layer over great plains. I. Mean and turbulence structure, *Bound.-Layer Meteorol.* **42**, 95-121.

Lenschow, D.H., Wyngaard, J.C., Pennell, W.T.: 1980, Meanfield and second-moment budgets in a baroclinic convective boundary layer, *J. Atmos. Sci.*, **37**, 1313-1326.

Lettau, H.H., and Davidson, B.: 1957, Exploring the atmosphere's first mile, *Pergamon press*, UK, 578p.

Lewellen, D.C., and Lewellen, W.S.: 1998, Large-eddy boundary layer entraintment, *J. Atmos. Sci.*, **55**, 2645-2665.

Mahrt, L., and Vickers, D.: 2002, Contrasting vertical structures of nocturnal boundary Layers, *Bound.-Layer Meteorol.* **105**, 351-363.

Mahrt, L., Vickers D., Nakamura R., Soler M.R., Sun J.L., Burns S., Lenschow D.H.: 2001, Shallow drainage flows, *Bound.-Layer Meteor.*, **101**, 243-260.

Mahrt, L.: 1999, Stratified atmospheric boundary layers, *Bound.-Layer Meteor.*, **90**, 375-396.

Mahrt, L., Sun, J., Blumen, W., Delany, T. and Oncley, S.: 1998, Nocturnal Boundary-layer regimes, *Bound.-Layer Meteorol.* **88**, 255-278.

Mahrt, L. and Paumier, J.: 1984, Heat transport in the atmospheric boundary layer, *J. Atmos. Sci.*, **41**, 3061-3075.

Mahrt, L.: 1982, Momentum balance of gravity flows. *J. Atmos. Sci.*, **39**, 2701-2711.

Mahrt, L., Heald, R.C., Lenschow, D.H., Stankov, B.B., and Troen, I.B., 1979: An observational study of the structure of the nocturnal boundary layer, *Bound.-Layer Meteorol.*, **17**, 247-264.

Manins, P.C., and Sawford, B.L., 1979: Katabatic winds: A field case study *Quart. J. Roy. Meteor. Soc.*, **105**, 1011-1025.

Mason, P. J., and Thomson, D. J.: 1992, Stochastic backscatter in large-eddy simulations of boundary layers', *J. Fluid Mech.* **242**, 51-78.

Mason, P. J., and Derbyshire, S. H.: 1990, Large-eddy simulation of the stably-stratified atmospheric boundary layer, *Bound.-Layer Meteorol.* **53**, 117-162.

McNider, R.T.: 1982, A note on velocity fluctuations in drainage flows, *J. of Atmos. Sci.*, **39**, 1658-1660.

Millionshchikov, M.D.: 1939, Decay of homogeneous isotropic turbulence in viscous incompressible fluids, *Doklady AN SSSR*, **22**, 236-240.

Mira, A., Cuxart, J., Jiménez, M.A., and Guijaro, J.A.: 2004, Verification of high-resolution simulations for the Majorca Island using satellite images, *EMS Annual Meeting Abstracts*, **Vol. 1**, 00292.

Moeng, C.-H., Cotton, B., Stevens, B., Bretherton, C.S., Rand, H., Chlond, A., Khairoutdinov, M., Krueger, S., Lewellen, W., MacVean, M., Pasquier, J., Siebesma, A., and Sykes, R.: 1996, Simulation of the statocumulus-topped planetary boundary layer: intercomparison among different numerical codes, *Bull. Amer. Meteor. Soc.*, **77**, 261-278.

Moeng, C.-H., and Sullivan, P.P.: 1994, A comparison of shear-and buoyancy-driven planetary boundary layer, *J. Atmos. Sci.*, **51**, 999-1022.

Moeng, C.-H., and Rotunno, R.: 1990, Vertical-velocity Skewness in the Buoyancy-Driven Boundary Layer, *J. Atmos. Sci.*, **47**, 1149-1162.

Moeng, C.-H., and Wyngaard, J.C.: 1989, Spectral analysis of Large-Eddy Simulations

of the Convective Boundary Layer, *J. Atmos. Sci.*, **45**, 3573-3587.

Moeng, C.-H.: 1984, A large-eddy simulation model for the study of the boundary-layer turbulence, *J. Atmos. Sci.*, **41**, 2052-2062.

Monin, A.S. and Yaglom, A.M.: 1971, Statistical Fluid Mechanics. Vol. I, *The Massachusetts Institute of Technology*, 769pp.

Monin, A.S., and Obuhkov, A.M.: 1954, Basic laws of turbulence mixing in the atmosphere near the ground, *Tr. Akad. Nauk SSSR Geofiz. Ins.*, **46**, 2311-2330.

Morcrette, J.-J.: 1990, Impact of changes to the radiation transfer parameterizations plus cloud optical properties in the ECMWF model. *Mon. Wea. Rev.*, **118**, 847-873.

Nai-Ping, L., Neff, W.D., and Kaimal, J.C.: 1983, Wave and turbulence structure in a disturbed nocturnal inversion, *Bound.-Layer Meteorol.*, **26**, 141-155.

Nakanishi, M.: 2000, Large-eddy simulation of radiation fog, *Bound.-Layer Meteorol.*, **94**, 461-493.

Nieuwstadt, F.T.M., Mason, P.J., Moeng, C.-H. and Schumann, U.: 1993, Large-eddy simulation of the convective boundary layer: A comparison of four computer codes, *Turbulent shear flows 8*, Durst et al., Eds. Springer-Verlag, 343–367.

Nieuwstadt, F. T. M.: 1985, A model for the stationary, stable boundary layer, *Turbulence and diffusion in stable environments*, J.C.R. Hunt, Ed., Clarendon Press, 149-179.

Nieuwstadt, F. T. M.: 1984, The turbulent structure of the stable, nocturnal boundary layer, *J. Atmos. Sci.*, **41**, 2202-2216.

Noilhan, J., and Planton S.: 1989, A simple parameterization of land surface processes for meteorological models. *Mon. Wea. Rev.*, **117**, 536-549.

Ozmidov, R.V.: 1965, Energy distribution between oceanic motions of different scales, *Bull. Acad. Sci., U.S.S.R., Atmos. and Oceanic Phys.*, **1**, 257-261.

Piacsek, S.A., and Williams, G.P.: 1970, Conservation properties of convection difference schemes, *J. Comp. Phys.*, **6**, 392-405.

Poulos, G. S., Blumen, W., Fritts, D. C., Lundquist, J. K., Sun, J., Burns, S. P., Nappo, C., Banta, R., Newson, R., Cuxart, J., Terradellas, E., Balsley, B., and, Jensen, M.: 2002, CASES-99: A comprehensive investigation of the stable nocturnal boundary layer, *Bull. Amer. Meteor. Soc.*, **83**, 555-581.

Raasch, S., and Schröter, M.: 2001, PALM - A large-eddy simulation model performing on massive parallel computers, *Meteorol. Z.*, **10**, 363-372.

Ramis C., Jansa A., Alonso S.: 1990, Sea breeze in Mallorca - A numerical study, *Meteor. and Atmos. Phys.*, **42**, 249-258.

Reynolds, O.: 1895, On the dynamical theory of incompressible viscous fluids and the determination of the criterior, *Phil. Trans. Roy. Soc. London*, **A186**, 123-164.

Reynolds, O.: 1883, An experimental investigation of the circumstances which determine whether the motion of water shall be direct or sinuous, and of the law of resistance in parallel channels, *Phil. Trans. Roy. Soc. London*, **A174**, 935-982.

Saiki, E. M., Moeng, C.-H., and Sullivan, P.: 2000, Large-eddy simulation of the stably stratified planetary boundary layer, *Bound.-Layer Meteorol.*, **95**, 1-30.

Sánchez, E., and Cuxart, J.: 2004, A buoyancy-based mixing length proposal for cloudy boundary layers, *Quart. J. Roy. Meteor. Soc., in press.*

Sánchez, E.: 2002, Nubes de capa límite atmosférica: estudio numérico y experimental, *thesis*, Dpt. de Física de la Tierra, Astronomia y Astrofísica I, Universidad Complutense de Madrid, Spain.

Schumann, U.: 1995, Stochastic backscatter of turbulence energy and scalar variance by random subgrid-scale fluxes, *Proc. Roy. Soc. London*, **A 451**, 293-318 and 811.

Siebesma, A.P., Bretherton, C.S., Brown, A., Chlond, A., Cuxart, J., Duynkerke, P.G., Jiang, H., Khairoutdinov, M., Lewellen, D., Moeng, C.-H., Sanchez, E., Stevens, B., and

Stevens, D.E.: 2003, A Large Eddy Simulation Intercomparison Study of Shallow Cumulus Convection, *J. Atmos. Sci.*, **60**, 1201-1219.

Smagorinsky, J.: 1963, General circulation experiments with the primitive equations. Part I: the basic experiment, *Mon. Wea. Rev.*, **91**, 99-164.

Smedman, A. S., Tjernström, M., and Högström, U.: 1993, Analysis of the turbulence structure of a marine low-level jet, *Boundary-Layer Meteorol.*, **66**, 105-126.

Smolarkiewicz, P. K., and Grabowski W.W.: 1990, The multidimensional positive definite advection transport algorithm: nonoscillatory option. *J. Comput. Phys.*, **86**, 355-375.

Soler, M. R., Infante, C., Buenestado, P. and Mahrt, L.: 2002, Observations of nocturnal drainage flow in a shallow gully, *Bound.-Layer Meteorol.* **105**, 253-273.

Stevens, B., Ackerman, A.S., Albrecht, B.A., Brown, A., Chlond, A., Cuxart, J., Duynkerke, P.G., Lewellen, D., MacVean, M.K., Neggers, R.A.J., Sanchez, E., Siebesma, A.P., and Stevens, D.E.: 2001, Simulations of Trade Wind Cumuli under a Strong Inversion *J. Atmos. Sci.*, **58**, 1870-1891.

Stull, R. B.: 1988, An Introduction to Boundary Layer Meteorology, Kluwer Academic Publishers, Dordretch, 666 pp.

Sullivan, P. P., Mc Williams, J. C. and Moeng, C.-H.: 1994, A subgrid Scale model for Large-Eddy simulations of Planetary Boundary-Layer flows, *Bound.-Layer Meteorol.* **71**, 247-276.

Svensson, G., and Holtslag, A.A.M.: 2005, Impact of turbulence in the stable boundary layer on the synoptic scale flow, *Submitted to Bound.-Layer Meteorol.*

Taylor, G.I., and Green, A.K., 1937: Mechanisms of the production of small eddies from large ones, *Proc. of the Royal Society of London*, **A158**, 499-521.

Tennekes, H. and Lumley, J.L.: 1982, A First Course in Turbulence, *The Massachusetts Institute of Technology*, 300pp.

Thoroddsen, S.T. and Van Atta, C.W.: 1992, Exponential tails and skewness of density-gradient probability density functions in stably stratified turbulence, *J. Fluid Mech.*, **244**, 547-566.

Van de Wiel, B. J. H., Ronda, R. J., Moene, A. F., De Bruin, H. A. R. and Holtslag, A. A. M.: 2002, Intermittent turbulence and oscillations in the Stable boundary layer over land. Part I: A bulk model, *J. Atmos. Sci.* **59**, 942-958.

Viterbo, P., Beljaars, A.C.M., Mahfouf, J.-F., and Teixeira, J.: 1999, The representation of soil moisture freezing and its impact on the stable boundary layer, *Quart. J. Roy. Meteorol. Soc.*, **125**, 2401-2426.

Wang, S. and Stevens, B.: 2000, Top-Hat representation of turbulence statistics in cloud-topped boundary layers: A large eddy simulation study, *J. Atmos. Sci.*, **57**, 432-441.

Whiteman, C. D., Zhong, S., Shaw, W.J., Hubbe, J.M., Bian, X., and Mittelstadt, J.: 2001, Cold Pools in the Columbia Basin, *Weather and Forecasting*, **16**, 432-447.

Whiteman, C. D., Bian, X., and Zhong, S.: 1999, Wintertime evolution of the temperature inversion in the Colorado plateau basin, *J. Appl. Meteor.* , **38**, 1103-1117.

Whiteman, C.D., Bian, X., and Zhong, S.: 1997, Low-level jet climatology from enhanced rawinsonde observations at a Site in the Southern Great Plains, *J. Appl. Meteor.*, **36**, 1363-1376.

Wilks, D.S.: 1995, Statistical methods in the atmospheric sciences, *Academic Press*, 467pp.

Willis, G.E., and Deardorff, J.W.: 1974, A laboratory model of the unstable planetary boundary layer, *J. Atmos. Sci.*, **31**, 1297-1307.

Wyngaard, J.C.: 1988, Structure of the PBL, *Lectures on Air Pollution Modelling*, Eds., A. Venkatrem and J.C. Wyngaard. Amer. Meteor. Soc., Boston, 385pp.

Wyngaard, J.C. and Brost, R.A.: 1984, Top-Down and Bottom-Up diffusion of a scalar in the Convective Boundary Layer, *J. Atmos. Sci.* **41**, 102-112.

Zhong, S., and Fast, J.D.: 2003, An Evaluation of MM5, RAMS, and Meso Eta at Sub-Kilometer Resolution Using VTMX Field Campaign Data in the Salt Lake Valley, *Mon. Wea. Rev.*, **131**, 1301-1322.

Zhong, S., Whiteman, C.D.,Bian, X., Shaw, W.J., and Hubbe, J.M.: 2001, Meteorological Processes Affecting Evolution of a Wintertime Cold Air Pool in a Large Basin, *Mon. Wea. Rev.*, **129**, 2600-2613.

Articles

• Jiménez, M.A., and Cuxart, J., 2005a: Large-eddy Simulations of the Stable Boundary Layer: study of applicability using experimental data, Boundary-Layer Meteorology, 115, 241-261.

• Jiménez, M.A., and Cuxart, J., 2005b: Study of the probability density functions from a Large-eddy simulation for a stably stratified boundary layer, Boundary-Layer Meteorology, in Press.

• Cuxart, J., and Jiménez, M.A., 2005a: Mixing processes in a nocturnal low-level jet, submitted to Journal of the Atmospheric Sciences.

• Cuxart, J., and Jiménez, M.A., 2005b: Local nocturnal circulations on the Majorca Island. submitted to Monthly Weather Review.

• R. J. Beare, M.K. MacVean, A.A.M Holtslag, J. Cuxart, I. Esau, J.-C. Golaz, M.A. Jiménez, M. Khairoutdinov, B. Kosovic, D. Lewellen, T.S. Lund, J.K. Lundquist, A. McCabe, A.F. Moene, Y. Noh, S. Raasch and P. Sullivan, 2005: An intercomparison of Large-Eddy simulations of the Stable Boundary Layer, Boundary-Layer Meteorology, in Press.